Dissertation

Cenozoic magma-assisted continental rifting and crustal block rotations in an extensional overlap zone between two rift segments, Southwest Ethiopia, East Africa

von

Asfaw Erbello Doelesso

2023

Dissertation

Cenozoic magma-assisted continental rifting and crustal block rotations in an extensional overlap zone between two rift segments, Southwest Ethiopia, East Africa

von

Asfaw Erbello Doelesso

zur Erlangung des akademischen Grades
Doctor rerum naturalium
»Dr. rer. nat.«
in der Wissenschaftsdisziplin Geologie

eingereicht an der
Mathematisch-Naturwissenschaftlichen Fakultät
der Universität Potsdam

Potsdam, den 13. Juni 2023

betreut von:
Prof. Manfred R. Strecker, PhD
Institut fur Geowissenschaften
Universitat Potsdam

Prof. Dr. Bodo Bookhagen
Institut fur Geowissenschaften
Universitat Potsdam

Published online on the
Publication Server of the University of Potsdam:
https://doi.org/10.25932/publishup-61096
https://nbn-resolving.org/urn:nbn:de:kobv:517-opus4-610968

Allgemeine Zusammenfassung

Wie Kontinentalverschiebung funktioniert und das Auseinanderbrechen von Kontinenten vonstatten geht, sind nach wie vor offene Fragen in den Geowissenschaften. In dieser Studie untersuche ich das Auseinanderbrechen von Afrika im Rahmen der tektonischen Prozesse im Ostafrikanischen Grabensystem von Süd-Äthiopien. Einige Studien legen nahe, dass ein Mantelquellenauftrieb von partiell geschmolzenem Mantelmaterial eine thermisch bedingte Krustenschwächung und -dehnung verursachen, die zur Bildung des vulkanisch und seismisch aktiven Rifts in Ostafrika führt. Vor diesem Hintergrund wurde in dieser Studie insbesondere die komplexe tektonische Geschichte in einer Übergangszone zwischen dem südlichen äthiopischen Rift und dem nördlichen Kenia-Rift eingehend, sowie unter besonderer Berücksichtigung der magmatischen Entwicklung untersucht. Die Übergangszone, auch Broadly Rifted Zone oder BRZ genannt, wurde zunächst mit Hilfe satellitengestützter morphometrischer Charakterisierungen beschrieben und hinsichtlich ihrer tektonischen Aktivität untersucht. Weiterhin wurde die Hebungs- und Exhumationsgeschichte von Horstblöcken mittels sogenannter thermochronologischer Untersuchungen analysiert, die Auskunft über die thermische Geschichte bzw. über die tektonisch kontrollierte Abkühlung von Blöcken des Sockelgesteins geben können. Schließlich wurden paläomagnetische Untersuchungen durchgeführt, um den Grad langfristig wirksamer Rotationsprozesse zu quantifizieren, die für die regionale Deformation von känozoischen Krustenblöcken in der BRZ verantwortlich sind. Die Untersuchungen zeigen, dass Deformation in Verbindung mit der Bildung von Verwerfungen um etwa 22 Ma begann - nach dem Ende ausgeprägter vulkanischer Aktivität zwischen 45 und 27 Ma. Die anfänglich räumlich verteilte Deformation wanderte danach auf eine schmale Zone im Grabenbereich zu und breitete sich entlang der Gofa-Provinz nach Norden aus, bevor sich die aktuell stattfindende Deformation in der südlichen Gofa-Provinz und im Chew Bahir-Becken während einer späten Phase Krustendehnung um 15 bis 9 Ma lokalisierte. Die räumliche Änderung in der Deformation geht einher mit einer weiteren Phase ausgeprägter magmatischer Aktivität. Paläomagnetische Messungen und radiometrische Datierungen weisen auf eine gegen den Uhrzeigersinn gerichtete Rotationsbewegungen um vertikale Achsen innerhalb der Übergangszone zwischen dem südlichen äthiopischen Rift und dem nördlichen Kenia-Rift hin, die allerdings im Laufe der Zeit abnahm. Die Abnahme der vertikalen Blockrotation in Verbindung mit der räumlichen und zeitlichen Veränderung der Deformationsprozesse könnte auf eine charakteristische Evolutionsphase dieser Region hinweisen, die den Übergang von einer räumlich verteilten anfänglichen Deformation bis hin zur Lokalisierung der Bildung von Verwerfungen in der Spätphase der Grabenbildung reicht, die nun durch magmengestützte Deformationsprozesse des Ostafrikanischen Riftsystems gekennzeichnet ist und einen Nord-Süd-gerichteten Gradienten der tektonischen Aktivität aufweist

Abstract

Continental rifts are key geodynamic regions where the complex interplay of magmatism and faulting activity can be studied to understand the driving forces of extension and the formation of new divergent plate boundaries. Well-preserved rift morphology can provide a wealth of information on the growth, interaction, and linkage of normal-fault systems through time. If rift basins are preserved over longer geologic time periods, sedimentary archives generated during extensional processes may mirror tectonic and climatic influences on erosional and sedimentary processes that have varied over time. Rift basins are furthermore strategic areas for hydrocarbon and geothermal energy exploration, and they play a central role in species dispersal and evolution as well as providing or inhibiting hydrologic connectivity along basins at emerging plate boundaries.

The Cenozoic East African rift system (EARS) is one of the most important continental extension zones, reflecting a range of evolutionary stages from an early rift stage with isolated basins in Malawi to an advanced stage of continental extension in southern Afar. Consequently, the EARS is an ideal natural laboratory that lends itself to the study of different stages in the breakup of a continent. The volcanically and seismically active eastern branch of the EARS is characterized by multiple, laterally offset tectonic and magmatic segments where adjacent extensional basins facilitate crustal extension either across a broad deformation zone or via major transfer faulting. The Broadly Rifted Zone (BRZ) in southern Ethiopia is an integral part of the eastern branch of the EARS; in this region, rift segments of the southern Ethiopian Rift (sMER) and northern Kenyan Rift (nKR) propagate in opposite directions in a region with one of the earliest manifestations of volcanism and extensional tectonism in East Africa. The basin margins of the Chew-Bahir Basin and the Gofa Province, characterized by a semi-arid climate and largely uniform lithology, provide ideal conditions for studying the tectonic and geomorphologic features of this complex kinematic transfer zone, but more importantly, this area is suitable for characterizing and quantifying the overlap between the propagating structures of the sMER and nKR and the resulting deformation patterns of the BRZ transfer zones.

In this study, I have combined data from thermochronology, thermal modeling, morphometry, paleomagnetic analysis, geochronology, and geomorphological field observations with information from published studies to reconstruct the spatiotemporal relationship between volcanism and fault activity in the BRZ and quantify the deformation patterns of the overlapping rift segments. I present the following results: (1) new thermochronological data from the en-échelon basin margins and footwall blocks of the rift flanks and morphometric results verified in the field to link different phases of magmatism and faulting during extension and infer geomorphological landscape features related to the current tectonic interaction between the nKR and the sMER; (2) temporally constrained paleomagnetic data from the BRZ overlap zone between the Ethiopian and Kenyan rifts to quantitatively determine block rotation between the two segments. Combining the collected data, time-temperature histories of thermal modeling results from representative samples show well-defined deformation phases between 25–20 Ma, 15–9

Ma, and ~5 Ma to the present. Each deformation phase is characterized by the onset of rapid cooling (>2°C/Ma) of the crust associated with uplift or exhumation of the rift shoulder. After an initial, spatially very diffuse phase of extension, the rift has gradually evolved into a system of connected structures formed in an increasingly focused rift zone during the last 5 Ma. Regarding the morphometric analysis of the rift structures, it can be shown that normalized slope indices of the river courses, spatial arrangement of knickpoints in the river longitudinal profiles of the footwall blocks, local relief values, and the average maximum values of the slope of the river profiles indicate a gradual increase in the extension rate from north (Sawula basin: mature) to south (Chew Bahir: young). The complexity of the structural evolution of the BRZ overlap zone between nKR and sMER is further emphasized by the documentation of crustal blocks around a vertical axis. A comparison of the mean directions obtained for the Eo-Oligocene (Ds=352.6°, Is=-17.0°, N=18, α_{95}=5.5°) and Miocene (Ds=2.9°, Is=0.9°, N=9, α_{95}=12.4°) volcanics relative to the pole for stable South Africa and with respect to the corresponding ages of the analyzed units record a significant counterclockwise rotation of ~11.1°± 6.4° and insignificant CCW rotation of ~3.2° ± 11.5°, respectively.

Zusammenfassung

Kontinentale Rifts sind herausragende geodynamische Regionen, in denen das komplexe Zusammenspiel von Magmatismus und Störungstätigkeit untersucht werden kann, um die treibenden Kräfte der Extension und die Bildung neuer divergenter Plattengrenzen zu verstehen. Eine gut erhaltene Riftmorphologie kann außerdem eine Fülle von Informationen über das Wachstum, die Interaktion und die Verknüpfung von Abschiebungssystemen im Laufe der Zeit liefern. Wenn Riftbecken über längere geologische Zeiträume erhalten bleiben, können die bei den Extensionsprozessen generierten Sedimente die tektonischen und klimatischen Einflüsse auf Erosion- und Sedimentation archivieren, die sich aufgrund von Ratenänderungen im Laufe der Zeit variieren können. Riftbecken sind weiterhin strategische Gebiete für die Erkundung von Kohlenwasserstoffen und geothermischer Energie, und sie spielen eine zentrale Rolle bei der Ausbreitung und Entwicklung von Arten und der hydrologischen Konnektivität entlang der entstehenden Plattengrenzen. Das känozoische ostafrikanische Grabensystem ist eine der bedeutendsten kontinentalen Extensionszonen, die eine Reihe von Entwicklungsstadien widerspiegelt - von einem frühen Grabenstadium mit isolierten Becken in Malawi bis zu einem fortgeschrittenen Stadium kontinentaler Extension im südlichen Afar. Das känozoische ostafrikanische Rift ist demzufolge ein ideales natürliches Labor für die Untersuchung unterschiedlicher Stadien beim Auseinanderbrechen eines Kontinents. Der vulkanisch und seismisch aktive östliche Zweig der EARS ist durch mehrere, seitlich versetzte tektonische und magmatische Segmente gekennzeichnet, bei denen benachbarte Extensionsbecken entweder über eine breite Deformationszone oder über eine größere Transferstörung hinweg Krustendehnung ermöglichen. Die Broadly Rifted Zone (BRZ) im südlichen Äthiopien ist ein integraler Bestandteil des östlichen Zweigs des EARS; in dieser Region propagieren Riftsegmente des südlichen äthiopischen Rifts (sMER) und des nördlichen kenianischen Rifts (nKR) in entgegengesetzter Richtung in einer Schlüsselregion mit einer der frühesten Manifestationen von Vulkanismus und Extensionstektonik in Ostafrika. Die nach Westen abfallenden Beckenränder des Chew-Bahir-Beckens und der Gofa-Provinz, die sich durch ein semiarides Klima und eine weitgehend einheitliche Lithologie auszeichnen, bieten gute Voraussetzungen für die Untersuchung der tektonischen und geomorphologischen Merkmale dieser komplexen kinematischen Transferzone, vor allem aber eignet sich dieses Gebiet dafür, die Überlappung zwischen den propagierenden Strukturen des sMER und des nKR und der dabei entstehenden Deformationsmuster der zu charakterisieren und zu quantifizieren. In dieser Arbeit habe ich Daten aus Thermochronologie, thermischer Modellierung, Morphometrie, Paläomagnetik, Geochronologie und geomorphologischen Feldbeobachtungen mit Informationen publizierter Studien kombiniert, um die räumlich-zeitliche Beziehung zwischen Vulkanismus und Störungstätigkeit in der BRZ zu rekonstruieren und die Deformationsmuster der sich überlappenden Riftsegmente zu quantifizieren. Im Folgenden stelle ich die folgenden Ergebnisse vor: (1) neue thermochronologische Daten von den en-échelon-Beckenrändern und Liegendblöcke der Riftflanken sowie vor Ort verifizierte morphometrische Ergebnisse, um die Verbindung zwischen unterschiedlichen Phasen von Magmatismus und Verwerfungen während der Extension

herzustellen und geomorphologische Landschaftsmerkmale abzuleiten, die mit der aktuellen tektonischen Interaktion zwischen dem nKR und dem sMER zusammenhängen; (2) zeitlich begrenzte paläomagnetische Daten aus einer Überlappungszone zwischen dem äthiopischen und kenianischen Rift, um quantitativ eine Blockrotation zwischen den beiden Segmenten zu bestimmen. Kombiniert man die erhobenen Daten, so zeigen die Zeit-Temperatur-Verläufe der thermischen Modellierungsergebnisse aus repräsentativen Proben gut definierte Deformationsphasen zwischen 25–20 Ma, 15-9 Ma und 5 Ma bis zur Gegenwart. Jede Deformationsphase ist durch den Beginn einer raschen Abkühlung der Kruste (>2°C/Ma) in Verbindung mit der Hebung bzw. Exhumation der Riftschulter gekennzeichnet. Nach einer initialen, räumlich sehr diffusen Phase der Extension hat sich das Rift allmählich zu einem System mit verbundenen Strukturen entwickelt, die sich in den letzten 5 Ma in einer zunehmend fokussierten Riftzone gebildet haben. Hinsichtlich der morphometrischen Analyse der Riftstrukturen kann gezeigt werden, dass normalisierte Steilheitsindizes der Flussläufe, die räumliche Anordnung von Knickpunkten in den Fluss-Längsprofilen der Liegendblöcke, lokale Reliefwerte und die durchschnittlichen Maximalwerte der Steigung der Flussprofile eine allmähliche Zunahme der Extensionsrate von Norden (Sawula-Becken: ausgereift) nach Süden (Chew Bahir: jung) anzeigen. Die Komplexität der strukturellen Entwicklung der BRZ-Überlappungszone zwischen nKR und sMER wird weiterhin deutlich durch die Dokumentation von Krustenblöcken um eine vertikale Achse. Die paläomagnetischen Untersuchungen zeigen, dass ein Vergleich der mittleren Richtungen, die für das Eo-Oligozän (Ds=352,6°, Is=-17,0°, N=18, α_{95}=5,5°) und das Miozän (Ds=2,9°, Is=0,9°, N=9, α_{95}=12,4°) relativ zum Pol für das stabile Südafrika und in Bezug auf die entsprechenden Zeitalter gemessen wurden, in einer signifikanten Drehung gegen den Uhrzeigersinn von 11,1°± 6,4° bzw. einer unbedeutenden Drehung gegen den Uhrzeigersinn von 3,2° ± 11,5° resultiert.

To my parents

Acknowledgement

I would like to thank my advisor Manfred Strecker for his whole-hearted guidance, and support, as this work was financed through the German Academic Exchange Services (DAAD), funds provided by the Faculty of Mathematics and Natural Sciences of the University of Potsdam to Manfred Strecker, and Potsdam University Graduate School (PoGs). Additionally, I thank Bodo Bookhagen, Daniel Melnick and Guillaume Dupont-Nivet for their support, and contributions to the different manuscripts presented in this thesis.

I thank all my co-authors and colleagues that shared in many ways their expertise and helped me during lab work, and scientific discussions at the different stages of this dissertation and having given me this opportunity to work with them.

I acknowledge my colleagues, professors, secretaries and administrative staff of the Institute of Geosciences at the University of Potsdam who contributed in many ways to enrich my time here.

I also thank the administrative staff of section 4.3 at Deutsches GeoForschungsZentrum (GFZ) for allowing me to use the paleomagnetic lab and guidance by Norbert Nowaczyk.

Thanks to my friends Heiko Pingle and Cody Colleps having been close, and supportive. This thesis would not have been possible without the unconditional support and love of my parents. I am extremely grateful to my mother Genet Suraj and my father Erbello Doelesso. Thanks to my brother Meseret Erbello and all family members of Ameha Muluneh. Finally, thanks to the almighty God

Contents

List of Figures

List of Tables

Chapter 1

Thesis organization and author contributions

This cumulative dissertation comprises one published paper, one rived manuscript in review, and one manuscript to be submitted. Chapters 3, 4, and 5 are manuscripts where I am the first author. The numbering of the figures and tables was adjusted to the consecutive chapters. The bibliography for chapters 2 and 6 is provided at the end of the dissertation; the bibliography for chapters 3, 4 and 5 is at the end of each chapter. The supplementary information and related bibliography for the three manuscripts are presented at the end of the dissertation.

After a brief introduction concerning rifting and extensional deformation processes the structural, geodynamic, and geologic setting of the East African Rift System and the Broadly Rifted Zone in southern Ethiopia is presented in Chapter 2 in light of the relevant research questions and hypotheses to be tested; in addition, I present a brief summary of the different methods that were applied in this study. A detailed account of the research methods is given in the individual research chapters 3, 4 and 5.

Chapter 3: "Magma-assisted continental rifting: The Broadly Rifted Zone in SW Ethiopia, East Africa", revised manuscript in review in the journal Tectonics of the American Geophysical Union (A. Erbello et al.), is co-authored by C. Colleps , D. Melnick, E. R. Sobel, B. Bookhagen, H. Pingel, G. Zeilinger, P. van der Beek, and M. R. Strecker. AE, DM and MS developed the research design; DAAD and MRS provided funding. AE did the analysis, thermal modeling, and interpretation and prepared the manuscript under the supervision of MS and ES, and CC participated in the thermal modeling. All co-authors contributed to the reviewing and editing of the paper.

Chapter 4: "Geomorphic expression of a tectonically active rift-transfer zone in S. Ethiopia", Geomorphology, v. 403, 108162, doi:10.1016/j.geomorph.2022.108162, 2022 (A. Erbello et al.) is co-authored by D. Melnick, G. Zeilinger, B. Bookhagen, H. Pingel, and M. R. Strecker. AE, MS, DM, GZ, and BB developed the research design. AE did the analysis, and interpretation and prepared the manuscript under the supervision of MS, BB and GZ, and BB participated in the analysis. All co-authors contributed to the reviewing and editing of the paper. DAAD and MRS provided funding.

Chapter 5: "Temporal variation in counterclockwise vertical-axis block rotations across a rift overlap zone, southwestern Ethiopia, East Africa", the manuscript is ready to be submitted to the American Geophysical Union's journal Geochemistry, Geophysics, Geosystems (Erbello et al.), is co-authored by G. Dupont-Nivet, T. Kidane, N. Nowaczyk, M. Sudo, D. Melnick, B. Bookhagen, S. Brune, G. Corti, G. Gecho, and M.R. Strecker. AE, GD, TK and MRS developed the research design. AE did the analysis, and interpretation and prepared the manuscript under the supervision of GD and MRS, and GD participated in the analysis. AE and MS carried out the $^{40}Ar/^{39}Ar$ dating. All co-authors contributed to the reviewing and editing of the paper. DAAD and MRS provided funding.

Chapter 2

Introduction

2.1 Motivation

Continental rift basins are elongated depressions bounded by normal faults. While they can form in mountain belts at high elevations during the late-stage evolution of crustal shortening and uplift (Dewey, 1988; Jademec *et al.*, 2007; Göğüş and Psyklywec, 2008; Kapp *et al.*, 2008), rift basins typically develop under conditions of a protracted tensional stress field that affects the entire lithosphere and causes crustal extension at a variety of scales (Olsen, 1995; Buck, 2006; Brune, 2014; Beniest *et al.*, 2017; Armitage *et al.*, 2018). Not only are present-day rift zones and the vestiges of paleo-rift basins that are inherited from the geological past important areas for natural resources such as hydrocarbons, mineral deposits, freshwater, and geothermal prospects, rift basins have also played a pivotal role in biotic evolution and in providing efficient migration corridors during the dispersal and interchange of species (deMenocal, 2004; Dommain *et al.*, 2022; McCune *et al.*, 1984; Prömmel *et al.*, 2013; Zappettini *et al.*, 2017). Furthermore, the inherited extensional structures of paleo-rifts often guide tectonic inversion processes in orogenic forelands, thus modifying the width and style of deformation of mountain belts (Mora *et al.*, 2009; Parra *et al.*, 2010; Arnous *et al.*, 2021), and appear to play a role in controlling rupture during seismogenesis in slowly deforming continental interiors (Clark and Leonard, 2003; Landgraf *et al.*, 2017; Zoback, 2010). Clearly, these different phenomena constitute important areas of academic, economic, and societal relevance; therefore, a better understanding of the spatiotemporal characteristics, deformational styles, and topographic influence of faulting in extensional geodynamic settings an important task for geoscientists.

Continental rift formation is mainly controlled by the interplay between extensional driving forces and the mechanical strength of the different sectors of the lithosphere (Kirby, 1980; Bott and Kusznir, 1984; Porth, 2000). For example, in geodynamic settings involving continental collision and mountain building, magma-poor, passive rifts such as the Rhine Graben system in Europe (Dèzes *et al.*, 2005) or the Baikal Rift in Asia (Petit and Déverchère, 2006; Sengör and Burke, 1978) may develop in the orogenic foreland and evolve into a series of linked

extensional basins. Conversely, decompression melting during the ascent and impingement of a mantle plume at the asthenosphere-lithosphere boundary causes magmatic underplating (KRISP working group, 1987), the generation of dynamic topography (Ebinger and Sleep, 1998; Moucha and Forte, 2011; Nyblade and Sleep, 2003), and the development of a tensional tectonic stress field. This active rifting process causes normal faulting (Withjack and Scheiner, 1982), which is accompanied by pronounced volcanic activity (McKenzie, 1978; Sengör and Burke, 1996; Bosworth *et al.*, 2015). Ultimately, the mantle-driven processes of extension will lead to the formation of magma-assisted continental rifts (Buck, 2006; Wright *et al.*, 2006; Bastow *et al.*, 2010). Magmatism during decompression melting may occur over long episodes involving millions of years (Bialas *et al.*, 2010) or during a very short period of <1 Ma (Courtillot and René, 2003; Wolfenden *et al.*, 2004, 2005), but generally magmatism occurs prior to the onset of upper-crustal deformation (Aitken *et al.*, 2013; Corti, 2008). Overall, magmatic processes involving differentiation, crustal assimilation, dike injections and the eruptions of flows will lead to crustal weakening and subsidence (Hinz, 1981; White and McKenzie, 1989; Hill, 1991; Buck, 2006; Bialas *et al.*, 2010; Kendall and Bertelloni, 2016), which may be further facilitated by extensional reactivation of pervasive lithospheric heterogeneities inherited from previous deformation events (*e.g.*, Rosendahl, 1987; Morley, 1999; Corti, 2012; Buiter and Torsvik, 2014). The combination of a present-day tensional stress field superposed on pre-existing zones of weakness may influence the architecture, propagation, and overall evolution of continental rifts, as observed in the East African Rift System (EARS) (Strecker *et al.*, 1990; Shackleton, 1993; Hetzel and Strecker, 1998; Chorowicz, 2005; Vetel and Le Gall, 2006; Corti *et al.*, 2008; Brune *et al.*, 2017).

Following initial rifting, extensional basins generally evolve from limited areas of tectonic subsidence into large, often linear zones of extension with major basin-bounding normal faults, which may interact kinematically and ultimately become linked (Morley *et al.*, 1990; Nelson *et al.*,1992, 1992; Gupta *et al.*, 1998). Normal-fault growth, interaction, and linkage may involve seismogenic, aseismic, and magmatic processes and generate a characteristic topography and tectono-geomorphic signature on the landscape that includes closely spaced normal faults bounding second-order horsts and grabens as well as fault zones with obliquely slipping normal faults (*e.g.*, Penck, 1924; Strecker *et al.*, 1990; Gawthorpe and Leeder, 2000; Densmore *et al.*, 2007; Ebinger and Scholz, 2012).

On a larger regional scale, however, the kinematic interaction between different rift basins may occur via a transfer fault or a wide zone of overlap between two fault strands of opposing polarity (*e.g.*, Morley *et al.*, 1990), leading to a microplate between the overlapping rift segments (*e.g.*, Macdonald *et al.*, 1991). In such a setting, a drag force acting on the margins of the rift causes the microplate to rotate about a vertical axis. The angular velocity of the microplate may vary with the size of the affected crustal block and the extension rate (*e.g.*, Schouten *et al.*, 1993; Katz *et al.*, 2005).

In general, the first-order principles defining the different stages of rift evolution are well known from detailed geological and geophysical investigations of mature Cenozoic rift basins and the vestiges of extensional basins from the distant geological past where extension was

either aborted or continued to evolve into oceanic spreading centers (*e.g.*, Milanovsky, 1983). In addition, analog and numerical modeling studies have highlighted the spatiotemporal characteristics and geometries of rifted regions and identified similarities between extensional processes that can be used to assess the degree of extension and predict future behavior of linked faults and their associated tectonic and thermal subsidence patterns (Buck, 1991; Corti *et al.*, 2003; Buiter and Torsvik, 2014).

Based on available geological and geophysical data obtained in East Africa and the distribution of extensive, rift-related volcanic sequences, upwelling mantle impinging at the base of the lithosphere initiated rifting in East Africa by thermally weakening and preconditioning the lithosphere (Fairhead and Girdler, 1969; Burke, 1996). Furthermore, the continual uplift and creation of dynamic topography in East Africa, possibly accompanied by mantle-drag forces (*e.g.*, Buck, 2006), generated a tensional tectonic stress field within the African plate that caused extensional fracture systems, propagation of normal faults, and emplacement of dikes and voluminous lava flows. This is in contrast to other studies that did not attribute a defining role to mantle processes and plume formation but rather proposed that far-field stresses related to collisional processes such as those between Arabia and Eurasia may have initiated rifting in East Africa (Courtillot, 1982; Reilinger and McClusky, 2011).

These contrasting views highlight the need for structural, geochrononological, and thermochronologic studies in East Africa to better constrain the character and timing of extensional processes at different timescales. On long, i.e., geological timescales, for example, the relationship between the emplacement of volcanic flows and dikes and the onset or termination of regional-scale normal faulting is still largely enigmatic, although advanced, magma-assisted stages of rifting have been inferred in some parts of the rift (Ebinger and Sleep, 1998; Keir *et al.*, 2006; Riedl *et al.*, 2019). While the present-day geophysical and structural signatures of extensional Cenozoic processes in East Africa are quite well-known, little data is available on the early stage of continental rifting (*e.g.*, Roecker *et al.*, 2017); this particularly applies to the transition between individual faults and linked normal-fault arrays, spatial changes in normal faulting within the larger rift depressions, as well as the rotations of crustal blocks and their interaction in light of reactivated basement heterogeneities (*e.g.*, Morley *et al.*, 1992; Bosworth and Morley, 1994; Chorowicz, 2005; Brune *et al.*, 2017; Emishaw and Abdelsalam, 2019). On shorter timescales, many questions also remain concerning the details of regional rifting processes and fault activity, and yet these issues are important given their relevance to hazard analysis (Zielke and Strecker, 2009) and the assessment of geothermal resources (Estefanny and Daniel, 2023; Hutchison *et al.*, 2023).

In light of the short summary of rifting processes provided in the preceding paragraphs, the Cenozoic EARS is an ideal location for studying the relationship between magmatism, faulting, interaction between adjacent rift basins, and associated deformation phenomena in time and space. Extending more than ~3000 km from a tectono-magmatic active deformation zone in southern Afar to the magma-poor Malawi Rift and zones of initial extension in Mozambique, this rift system documents deformation features and magmatic characteristics that reflect different

evolutionary stages of extensional processes (*e.g.*, Chorowicz, 2005; Ebinger and Scholz, 2012; Rooney, 2017). The EARS comprises several spatially offset rift basins where deformation between them is accommodated by obliquely oriented transfer faults at different spatial scales (*e.g.*, Rosendahl, 1987; Morley *et al.*, 1990), but linkage also occurs between en échelon zones of extension within the larger rift basins (*e.g.*, Riedl *et al.*, 2020). A prominent transfer zone links the southern Main Ethiopian Rift (sMER) and the northern Kenya Rift (nKR), defining a broadly rifted zone (BRZ) of deformation between both sectors of the EARS (Davidson, 1983; WoldeGabriel and Aronson, 1987; Ebinger *et al.*, 2000). Despite numerous studies conducted in this region to uncover a link between massive volcanism and rifting (*e.g.*, Levitte *et al.*, 1974; WoldeGabriel and Aronson, 1990; Davidson, 1983; George *et al.*, 1998; Ebinger *et al.*, 2000; Bonin *et al.*, 2005; Pik *et al.*, 2008; Steiner *et al.*, 2021), some details, such as the spatiotemporal relationship between regional magmatic pulses and faults, are not yet clear. Also uncertain is the nature of tectonic interaction between propagating rift segments and the resulting complexity of deformation across overlapping extensional zones, particularly in the context of reactivated basement shear zones related to paleo-tectonic events.

Based on the results achieved in previous studies and the remaining research gaps identified above, the motivation of my thesis is based on two main objectives. Under the hypothesis that volcanism and rifting in Southern Ethiopia are closely related, the first objective is to establish a link between the pulses in regional magmatism and rifting across the BRZ in space and time. For this purpose, data was first compiled from well-dated, regionally distributed volcanic rocks; in a second step, new low-temperature thermochronologic data from the left-stepping en-échelon footwall flanks of the rift basins in the BRZ were synthesized and analyzed. In a third step, thermal modeling results based on new low-temperature thermochronologic data were combined with geologic, geomorphic, structural, and seismicity data. The second objective of my study is to determine temporally constrained quantitative deformation in areas within a rift overlap zone. To this end, a total of 40 paleomagnetic sites (4–8 standard core samples per site) were selected within a ~75 to 125-km-long and a ~20 to 40-km-wide zone of a rift overlap between the Chew Bahir Basin-Gofa Province and the sMER. Additionally, ten samples from key sites recording deformation were collected for $^{40}Ar/^{39}Ar$ dating to complement the age constraints for the sampled volcanic units. To address the above overarching research issues,

To address the overarching research issues mentioned above, answers were sought in particular to questions that probe the relationship between magmatism and rifting in space and time, and the extent and nature of tectonic interaction between adjacent rift segments, namely:

- When did crustal uplift and exhumation initiate across the BRZ?
- Is there a relationship between the onset of rift-shoulder uplift and exhumation and pulses in regional volcanism?
- How did initially isolated rift basins grow laterally, interact kinematically, and link over time, and what was the role of inherited basement fabrics during rift-basin evolution?

- How does the rigid block between the Chew Bahir Basin-Gofa Province and the sMER influence deformation over time?

Below, I briefly summarize the most relevant aspects of previous studies on the geologic and tectonic setting of the BRZ, followed by a brief introduction of the methods applied in my research. The subsequent three chapters constitute independent research papers that have either been published, reviewed, or are ready to submit. Each chapter is preceded by an introduction to the specific research problem addressed in that chapter, followed by a description of the geologic and tectonic setting of the area investigated, a detailed section on methods and results, and a discussion and a summary of the main conclusions and implications.

2.2 Tectonic setting of the study area

The Cenozoic EARS (Fig. 2.1) is an ideal geodynamic setting to study continental rifting. The rift extends more than ~3000 km from a tectono-magmatic active deformation zone in southern Afar where the transition from advanced continental separation to oceanic spreading occurs, to the magma-poor rift segments in Malawi and Mozambique (Tiercelin *et al.*, 2002; Corti, 2009; Koptev *et al.*, 2015; Njinju *et al.*, 2019). The EARS exhibits different stages of extension and varying levels of seismicity and seismogenic faulting (Parsons *et al.*, 1992; Ibs-von Seht *et al.*, 2001; Keir *et al.*, 2006; Calais *et al.*, 2008; Stamps *et al.*, 2014; Muirhead *et al.*, 2015; Oliva *et al.*, 2019; Muluneh *et al.*, 2020; Craig and Jackson, 2021). The rift system hosts volcanically active, and virtually non-magmatic sectors (Ebinger and Scholz, 2012; Njinju *et al.*, 2019); and it includes regions with pronounced differences in crustal composition and geophysical anomalies that reflect multiple geodynamic processes in the past that have culminated in the ongoing Cenozoic extension associated with pronounced mantle anomalies (Shackleton, 1976, 1993; Green *et al.*, 1991; Birt *et al.*, 1997; Ebinger and Sleep, 1998; Dugda *et al.*, 2005; Pik *et al.*, 2006; Ayalew and Gibson, 2009; Rooney, 2010; Civiero *et al.*, 2015; Hassan *et al.*, 2020).

In the eastern branch of the EARS the BRZ between the sMER and nKR exhibits imprints of multiple tectonic events that have affected this region since the Neoproterozoic. NW-SE-striking Mesozoic lineaments obliquely cut an older NE-SW-striking Neoproterozoic basement fabric (Morley *et al.*, 1992; Bosworth and Morley, 1994; Brune *et al.*, 2017; Emishaw and Abdelsalam, 2019), which may have been repeatedly reactivated during the Cenozoic (Chorowicz, 2005; Mamo, 2012). The well-developed N-S to NE-SW-striking Cenozoic rift-related principal basin-bounding faults strike sub-parallel to the Neoproterozoic basement fabrics of the pan-African Belt (Corti, 2009; Kendall and Bertelloni, 2016), while the NW-SE-striking lineaments are associated with the Melut and Muglade basins in Sudan and South Sudan and the Anza Rift in northern Kenya are thought to be of Paleogene-Cretaceous age (Bosworth and Morley, 1994). Often, the surface expression of the Mesozoic lineaments is obscured by well-developed Quaternary rift structures and basin-fill sediments, yet the rift basins appear to be connected in the subsurface by shorter E-W-oriented lineaments (*e.g.*, Ebinger *et al.*, 1993; Mamo, 2012; Emishaw and Abdelsalam, 2019).

The Neoproterozoic and Mesozoic lineaments have been suggested to control the growth of normal faults in southern Ethiopia and northern Kenya (*e.g.*, Chorowicz, 2005; Boone *et al.*, 2019). Extensional deformation related to Nubia-Somalia plate motion initiated in northern Kenya during the Eo-Oligocene (e.g., Boone *et al.*, 2019) and propagated toward the north in the Gofa Province at ~10 Ma (*e.g.*, WoldeGabriel and Aronson, 1987; Bonini *et al.*, 2005; Balestrieri *et al.*, 2016) via the Chew Bahir Basin by ~20 Ma (Pik *et al.*, 2008). To the east of the Chew Bahir Basin and the Gofa Province of the sMER, major normal faults bounding the Chamo and Abaya basins started activity during the Miocene between 18 and 14 Ma, and faulting migrated farther to the south and toward the axial zone of the rift during the late Miocene and early Pliocene (*e.g.*, Ebinger *et al.*, 2000; Bonini *et al.*, 2005), prior to the current tectonic interaction between the Chew Bahir Basin and the Gofa Province and the sMER.

In the EARS, differences in seismicity between magmatically active versus inactive areas have been noted (*e.g.*, Parsons and Thompson, 1991; Foster and Jackson 1998; Meghraoui *et al.*, 2016). The eastern branch of the EARS is one of the most volumetrically important magmatic extensional provinces on Earth (Latin and White, 1993) and this magmatic character may determine the frequency and magnitude of seismicity. For example, in a global survey of rift-related seismicity and magmatism, Parsons and Thompson (1991) convincingly showed that magmatic rift zones, such as the Ethiopian and Kenyan rifts, are characterized by low levels of seismicity. These authors explained the phenomenon of reduced faulting activity by stress equalization associated with a build-up of magma pressure counteracting tectonic stresses and thus suppressing seismicity. In such a scenario, rift extension is thought to be accomplished by a combination of magmatic dike intrusion and normal faulting, accompanied by small, but frequent earthquakes. This behavior characterizes the seismicity of the Ethiopian and Kenyan rifts. In contrast, higher seismicity levels that reach magnitudes as large as Mb 7.4 characterize the virtually amagmatic western branch of the EARS and the Tanzania rift zone (Parsons and Thompson, 1991; Foster and Jackson 1998; Meghraoui *et al.*, 2016). In line with this is a study by Craig and Jackson (2021) who showed that earthquake-depth distributions unrelated to magmatic diking vary significantly along the EARS. The authors indicate that earthquake depths in the northernmost section of the rift are clustered at shallow depths, whereas in the western branch earthquake hypocenters extend to depth of ~40-km.

2.3 Geologic setting

The oldest unit in the study region comprises Neoproterozoic basement rocks that are mainly exposed in the footwall flanks of the Chew Bahir Basin and the southern Gofa Province (Davidson, 1983). Well-indurated, thin basal conglomeratic sandstone beds unconformably overlie the crystalline basement rocks (Davidson and Rex, 1980; Ebinger *et al.*, 2000). The age of the sandstone layer is uncertain, however, Levitte (1974) has correlated the unit with petrographi-

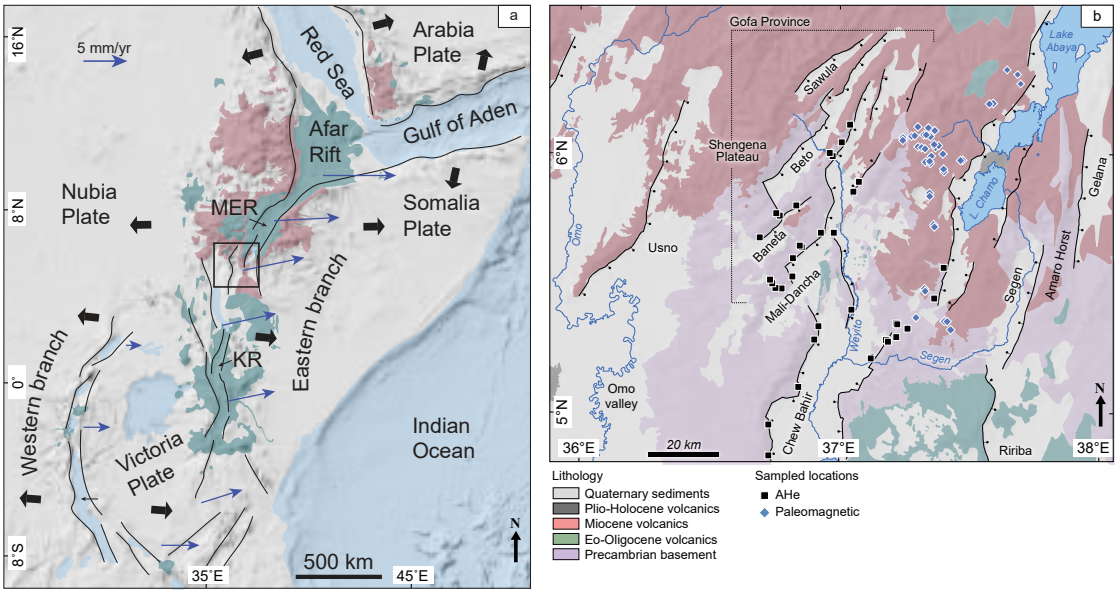

Figure 2.1: Tectonic setting of the East African Rift System

cally similar lower unit of the Turkana Grits in northern Kenya of Cretaceous inferred age (*e.g.*, Owusu Agyemang *et al.*, 2019).

The subsequently deposited Eo-Oligocene volcanics are mainly exposed along the rift margins that reflect a progressive thickening to about more than a kilometer toward the north (Davidson, 1983; Ebinger *et al.*, 1993; 2000; George *et al.*, 1998). This early phase of volcanism occurred between 45 and 35 Ma (Davidson and Rex, 1983). Rooney (2017) correlated the Eo-Oligocene Gamo-Amaro basalts with the regional Mekonnen basalts (35-28 Ma; Davidson, 1983), and reclassified them as Gamo-Makonnen basalts, representing the main phase of flood basalt emplacement between 38 and 27 Ma (Steiner *et al.*, 2021).

The ~500-m-thick Getera-Kela basalt with an age range between 18 and 12 Ma (Ebinger *et al.*, 1993) covers the Eo-Oligocene volcanics. South of the Amaro Horst in the northern Segen Basin, WoldeGabriel *et al.*et al. (1991) dated a petrographyically similar basalts at ~11 Ma. Furthermore, phonolitic eruptive centers located along the strike of the Mali-Dancha and Bala-Kela basins record emplacement age between 16 and 12 Ma (Davidson, 1983).

During the Pliocene, thin lava flows of the Gombe Group were emplaced along the Omo-Turkana Depression, extending farther to the north along the Usno Basin in the Omo Valley (Watkins, 1983; Brown *et al.*, 1985; Davidson, 1983; Haileab *et al.*, 2004; Erbello and Kidane, 2018). Following the emplacement of the Gombe Group basalts, volcanic activity shifted toward the east in the Ririba rift during the late Pliocene (Ebinger *et al.*, 2000; Bonini *et al.*, 2005; Corti *et al.*, 2019).

Quaternary volcanics are restricted to the axial zone of the sMER in the northern sector of the Chamo Basin and to areas to the west of the Omo Valley (*e.g.*, Ebinger *et al.*, 1993; Jicha and Brown, 2014)

2.4 Techniques to determine onset of rift shoulder uplift, to infer Quaternary deformation and a ridged block rotation

Thermochronology and thermal history modeling are advanced tools to investigate the history of cooling in rocks of the Earth's crust in the context of tectono-thermal and erosional processes (Reiners and Ehlers, 2005). Low-temperature apatite (U-Th-Sm)/He and zircon (U-Th-Sm)/He (AHe and ZHe) thermochronology is based on the decay of U, Th, and Sm isotopes, producing α-particles, which are only partially retained in a temperature range referred to as partial retention zone (PRZ) (Dodson, 1973). The AHe and ZHe PRZ range from ~40–70°C (Gautheron *et al.*, 2012) and ~140–220°C (Guenthner *et al.*, 2013), respectively. Assuming a mean surface temperature of ~20°C and a geothermal gradient of ~40°C/km (Pik *et al.*, 2003), the range of thermal sensitivity of AHe and ZHe in this part of Africa corresponds to a depth of about 1 to 5.5 km. Hence, these thermochronologic systems can potentially document the thermal history associated with tectonic and erosional processes in the uppermost part of the crust.

Morphometric indices from 89 catchments and their main stream channels draining the footwalls of the rifted Chew Bahir Basin and the Gofa Province were analyzed using the TanDEM-X WorldDEM (Rizzoli *et al.*, 2017; Wessel *et al.*, 2018), which has a resolution of 12 m. The computed results were subsequently verified in the field. Additionally, the character of regional seismicity, the distribution of mean annual rainfall, and the potential influence of the vegetation cover on erosional processes were considered to identify process gradients, prominent regional geomorphic markers, and different stages in the tectonic evolution of a structurally complex rift zone.

Due to the ubiquitous presence of minerals with magnetic properties in magmatic rifts, volcanic and sedimentary rocks deposited in subsiding rift basins can be exploited as archives to characterize the character of Earth's magnetic field on a variety of timescales (*e.g.*, Butler, 1998), because the rock units acquire magnetic-field signatures of the prevailing normal or reverse magnetic polarity directions shortly after lava-flow emplacement or the deposition of sedimentary strata. Through the identification of chrons, which can be thought of as magnetic polarity-rock units, these measurements enable developing a magnetic stratigraphy (Butler, 1998); additionally, the magnetic properties may be used to define paleo-latitudinal positions of plates or rotations or crustal blocks in tectonically deforming regions (Butler, 1998). The latter approach was used in this study; in particular, Eo-Oligocene and Miocene volcanics and sedimentary rock samples were collected from locations across the Gidole-Chencha Horst to extract the magnetic field acquired during cooling and deposition with the aim to identify the effects of regional rotations of crustal blocks on the rifting process. Alternative Field (AF) and thermal demagnetization

techniques were applied to remove secondary components of magnetization. For each group of the collected rock units, a paleomagnetic pole was calculated and compared relative to the pole for stable South Africa at corresponding ages (Vaes *et al.*, 2022). The analysis of the results and their relevance for tectonic models for rift evolution was aided by statistical analysis (*e.g.*, Butler, 1998).

Chapter 3

Magma-assisted continental rifting: The Broadly Rifted Zone in SW Ethiopia, East Africa

Erbello, A., Colleps, C., Melnick, D., Sobel, E.R., Bookhagen, B., Pingel, H., Zeilinger, G., van der Beek, P., and Strecker, M.R., in review, Magma-assisted Continental Rifting: The Broadly Rifted Zone in SW Ethiopia, East Africa.

This chapter has been submitted to Tectonics and is in review

---

Abstract

The Gofa Province and Chew Bahir Basin in the Broadly Rifted Zone (BRZ) between the southern Main Ethiopian Rift (sMER) and the northern Kenya Rift (nKR) record early volcanism and associated faulting in East Africa; however, the spatiotemporal relationships between volcanism and faulting remain poorly constrained. We applied apatite (U-Th)/He (AHe) and zircon (U-Th)/He (ZHe) thermochronometry to Neoproterozoic basement rocks from exhumed footwall blocks of the extensional Gofa Province and Chew Bahir Basin and analyzed our result in the context of well-dated regional volcanic units in the BRZ to unravel the interplay between tectonic exhumation, faulting, and volcanism. Weighted-mean (AHe) ages ranging from 77.3 to 3.0 Ma were recorded in 28 samples; the youngest ages were obtained from the Chew Bahir Basin and the narrow deformation zone of the Gofa Province. Mean ages from ZHe data range between 320.5 and 150 Ma. Our thermal modeling results reflect little or no significant tectonically related regional crustal cooling prior to extensive volcanism, which started at about 45 Ma. Conversely, time-temperature histories based on our samples record widespread crustal cooling related to tectonism at ~22 Ma. After initial spatially diffuse extensional deformation during the late Oligocene and early Miocene, faulting accompanied by rapid crustal cooling shifted toward a narrow zone of the Gofa Province and Chew Bahir Basin during the middle to late Miocene (15–9 Ma) and Pliocene (<5 Ma), respectively. The crustal cooling phases follow a regional trend in episodes of volcanic eruptions. For example, the initial cooling between 25 and 20 Ma corresponds with the end of widespread flood-basalt volcanism (45–27 Ma), suggesting that spatially diffuse normal faulting may have initiated shortly after the emplacement of voluminous and areally extensive flood basalts. The Miocene and Pliocene shifts in deformation along the Mali-Dancha and Bala-Kela basins in the Gofa Province and the Chew Bahir Basin, respectively, may

indicate strain localization during the late stage of rifting and ongoing tectonic interaction between the sMER and the nKR. Our results support the notion of crustal weakening by massive volcanism prior to initial rifting as a precursor to widespread extensional faulting, and thus offer further insights into magma-assisted deformation processes in the East African Rift System.

3.1 Introduction

Continental rift basins are elongated depressions bounded by normal faults and areally extensive flexures that evolve during extensional tectonism affecting the entire lithosphere (*e.g.*, Olsen, 1995; Ebinger *et al.*, 1999). The depositional record of these basins is an important archive of the combined impacts of magmatic, tectonic, and climatic forcing on erosion and sedimentation processes, which may vary over time as rifting is sustained over long timescales (*e.g.*, Ebinger and Scholz, 2012; Buiter *et al.*, 2022). Commonly, rift basins are strategic sites for hydrocarbon and geothermal-energy exploration and also play a pivotal role in biotic evolution, hydrological connectivity, and the dispersal of species at continental scales (McCune *et al.*, 1984; deMenocal, 2004; Prömmel *et al.*, 2013; Dommain *et al.*, 2022).

Magmatic continental rifts are often associated with extensive areas of volcanic rocks that were emplaced prior to the onset of widespread upper crustal extensional deformation and tectonic subsidence (McKenzie, 1978; White and McKenzie, 1989; Corti, 2008; Aitken *et al.*, 2013; Kendall and Bertelloni, 2016); examples include the Red Sea Rift (Bosworth *et al.*, 2005; Bosworth and Stockli, 2016), the North and South Atlantic rifts (Saunders *et al.*, 1997; Courtillot *et al.*, 1999; Courtillot and Renne, 2003; Torsvik and Cocks, 2005), and the East African Rift (Wolfenden *et al.*, 2004; Kendall and Bertelloni, 2016). Over time, both magmatism and extensional deformation migrate toward the interior of these tectonic depressions, and a narrow, volcanically and tectonically active area develops during more advanced stages of extension (*e.g.*, Morton *et al.*, 1979; Ebinger *et al.*, 1993; Corti, 2008; Richter *et al.*, 2021; Riedl *et al.*, 2022).

2D numerical modeling studies indicate that upwelling of hot asthenospheric material may cause a reduction in lithospheric thickness, ultimately leading to crustal weakening and thus promoting extension as observed in the East African Rift System (EARS, Buck, 2006). Furthermore, efficient crustal extension can be further facilitated by the reactivation of inherited basement heterogeneities, such as suture zones, deep-seated crustal-scale shear zones, metamorphic fabrics, and structures associated with paleo-rifts (Vauchez *et al.*, 1997; Corti, 2008; Kendall and Bertelloni, 2016).

Typically, large continental rift zones evolve from isolated tectonic basins during the early stages of extension into larger, throughgoing, and topographically linked depressions (*e.g.*, Ebinger *et al.*, 1999; Ebinger and Scholz, 2012 and references therein). Before this connectivity between individual basins is achieved, the kinematic transfer of extension between these basins is accommodated within structurally complex transfer zones by the generation of closely spaced normal faults, the formation of local transfer faults, and pronounced magmatic activity accom-

panied by diking (Bosworth and Morley, 1994; Morley *et al.*, 1992; Riedl *et al.*, 2022). The Broadly Rifted Zone (BRZ) in northern Kenya and southern Ethiopia is such a transfer zone, where the southern Main Ethiopian Rift (sMER) and the northern Kenya Rift (nKR) segments propagate toward each other (Ebinger *et al.*, 2000; Bonini *et al.*, 2005; Chorowicz, 2005; Brune *et al.*, 2017). Although the chronology of ubiquitous volcanism and normal faulting, as well as the influence of inherited basement fabrics on guiding extensional faulting have been documented in East Africa (*e.g.*, Morley *et al.*, 1992; Ebinger *et al.*, 2000; Corti, 2008; Brune *et al.*, 2017), the synergies and mutual influences of these different forcing factors are not yet fully understood.

The BRZ comprises multiple, N-S to NE-SW-oriented parallel rift basins between the sMER and the nKR (Fig. 3.1a). In Ethiopia, these areas comprise the Omo Valley and the Sawula, Beto, Bala-Kela, Baneta, Mali-Dancha, Chew Bahir, Segen, Gelana, and Chamo basins. The basins are filled with Tertiary and Quaternary sediments and volcanics, while the rift flanks are mainly characterized by Neoproterozoic basement rocks and overlying Eo-Oligocene flood basalts (Fig. 3.1b, *e.g.*, Davidson, 1983; Steiner *et al.*, 2022).

Concerning the temporal patterns of rifting in the sMER, low-temperature thermochronological studies at the uplifted margins of the Chew Bahir and the Beto (northern Gofa Province) basins in southern Ethiopia indicate that rifting and tectonic exhumation initiated at ~20 Ma (Pik *et al.*, 2008) and ~12 Ma (Philippon *et al.*, 2014; Balestrieri *et al.*, 2016), respectively. Although studies have proposed a propagation of rifting from northern Kenya toward the Gofa Province via the Chew Bahir Basin in Ethiopia (WoldeGabriel *et al.*, 1990; Bonini *et al.*, 2005; Chorowicz, 2005), Balestrieri *et al.* (2016) suggested that synchronous deformation along the basin-bounding faults of the Beto Basin and the eastern margin of the Amaro Horst occurred between ~12 and 10 Ma. Boone *et al.* (2019) also suggested synchronous rift initiation across the BRZ, but with an onset between 20 and 17 Ma (Fig. 3.1b). A proper assessment of the timing of rifting in the sMER is further complicated by shifts in the locus of tectonic activity. For example, tectonic activity in the northern Gofa Province in the late Miocene to early Pliocene has subsequently shifted toward the now seismically active Chew Bahir Basin (Ebinger *et al.*, 2000). Furthermore, whereas WoldeGabriel and Aronson (1987) considered the Gofa Province as a failed rift segment and the Chew Bahir Basin in the south as an early-stage rift, Erbello *et al.* (2022) recently demonstrated the existence of active Quaternary normal faults, young tectonic landforms, and tectonically forced drainage networks in the northern Gofa Province along the Bala-Kela Basin margin.

From these different views, it can be concluded that the spatiotemporal characteristics of rifting in the Chew Bahir Basin and the Gofa Province are ambiguous and still poorly constrained. In addition, despite previous thermochronological studies and the availability of geochronological data, potential relationships between clustered volcanic and tectonic activity in the sMER remain unclear. In this study, we therefore attempt to clarify these ambiguities and hypothesize that pulses in volcanism are intimately linked with phases of tectonic activity. Using new low-temperature thermochronological data in combination with a synopsis of radiometrically dated volcanic rocks and existing thermochronological data, we examine the spatiotemporal relationships between volcanism, rifting, and the evolution of topography in the BRZ.

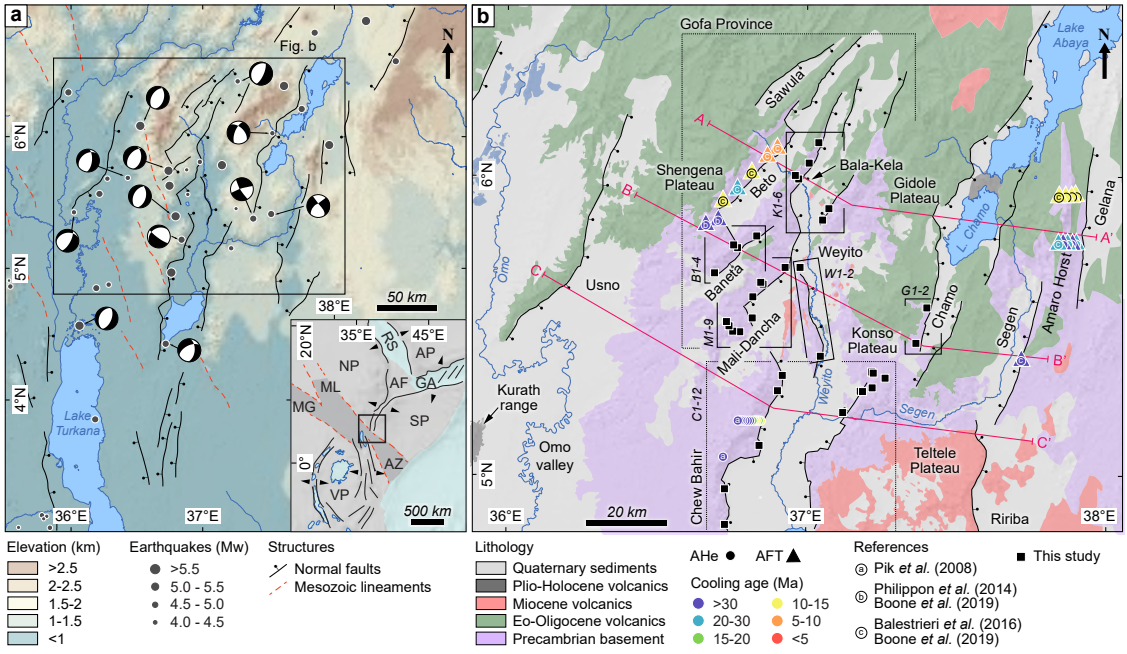

Figure 3.1: Tectonic setting of the southern Main Ethiopian Rift and the northern Kenya Rift, (a) NW-SE striking Mesozoic lineaments (Chorowicz, 2005), and Quaternary NNE-SSW-striking faults (Balestrieri *et al.*, 2016; Erbello *et al.*, 2022) superposed on hill-shaded relief derived from a TanDEM 30-m resolution Digital Elevation Model. Inset map at the bottom left shows undifferentiated tectonic lineaments associated with the late Cretaceous to early Paleogene South Sudan Rift and the northern Kenya Rift (AZ: Anza Rift basin; ML: Melut Basin; MG: Muglad Basin), and the Tertiary East African, Gulf of Aden and Red Sea plate boundaries (AP: Arabia plate; SP: Somalia plate; NP: Nubia plate; AF: Afar Rift; GA: Gulf of Aden Rift; VP: Victoria plate) with the location of the study area, (b) Geological map superposed on hill-shaded relief showing principal stratigraphic units (Davidson, 1983; Balestrieri *et al.*, 2016; Erbello *et al.*, 2022), AHe and AFT cooling ages are from (a: Pik *et al.*, 2008; b: Boone *et al.*, 2019; triangles: Balestrieri *et al.*, 2016 and Boone *et al.*, 2019; squares: this study), and across-rift profile lines (red lines). Earthquake focal mechanisms (Harvard CMT catalogue; Asfaw, 1990; Ayele and Arvidsson, 1997; Foster and Jackson, 1998), and seismic events (gray dots) are from the International Seismological Center (ISC: https://www.isc.ac.uk). Boxes indicate isolated rift basins across the BRZ and range of samples collected from each of the basins (C1-11: Chew Bahir, M1-9: Mali-Dancha, B1-4: Baneta, K1-6: Bala-Kela, and G1-2: Chamo basins).

3.2 Tectonic and geologic setting

3.2.0.1 Tectonic setting

The BRZ is a structurally complex extensional deformation zone with imprints of multiple tectonic events. NW-SE-striking tectonic lineaments inherited from Cretaceous-Paleogene paleo-rifts obliquely cut NNE-SSW-striking Neoproterozoic basement fabrics (Morley *et al.*, 1992; Bosworth and Morley, 1994; Brune *et al.*, 2017; Emishaw and Abdelsalam, 2019; Fig. 3.1a). While the well-developed N-S to NE-SW-striking Cenozoic rift structures are closely aligned with the regional basement fabrics (Corti, 2009; Kendall and Bertelloni, 2016), the Cretaceous-Paleogene NW-SE-striking lineaments are associated with the Melut and Muglade basins in Sudan and South Sudan, and the Anza Rift in northern Kenya (*e.g.*, Bosworth and Morley, 1994). These rift basins are connected in the subsurface; however, the well-developed N-S to NE-SW-trending rift basins associated with the active EARS obscure these features (*e.g.*, Ebinger *et al.*, 1993; Mamo, 2012; Emishaw and Abdelsalam, 2019). More recently, Kounoudis *et al.* (2021) imaged a NW-SE-trending area of high wave-speed at a depth of <200 km, suggesting that the pervasive band of crustal heterogeneity may have controlled rift localization in the BRZ during the Mesozoic and Cenozoic.

The Chew Bahir Basin and the Gofa Province comprise a 10 to 50-km-wide zone of N-NE-trending en-échelon rift basins (Davidson, 1983) bounded by Miocene faults (WoldeGabriel *et al.*, 1991; Ebinger *et al.*, 1993, 2000; Bonini *et al.*, 2005; Philippon *et al.*, 2014; Boone *et al.*, 2019), and these structural basins are kinematically linked by shorter NW-SE-striking normal faults (Ebinger *et al.*, 2000; Philippon *et al.*, 2014; Brune *et al.*, 2017).

Earthquakes recorded across the sMER since 1913 have clustered along a narrow zone between the lower Omo Valley and the Baneta, Mali-Dancha, Chew Bahir, and Segen basins (Gouin, 1979); the earthquake hypocenters are mainly at depths <15 km and are characterized by normal faulting kinematics with a minor oblique-slip component (Asfaw, 1990; Ayele and Arvidsson, 1997; Foster and Jackson, 1998). Earthquakes between January 2019 and September 2020 across the Turkana Depression and the BRZ clustered along a narrow sector in the Omo Valley and the Baneta, Mali-Dancha, Chew Bahir, and Segen basins. The majority of these events were characterized by normal faulting with a minor oblique-slip component (Musila *et al.*, 2022).

3.2.0.2 Geologic setting

Neoproterozoic basement rocks are the oldest exposed units in the region; they consist of high-grade amphibolite and layered granulites that are exposed across the entire width of the BRZ (Gichile, 1992). The spatially extensive basement rocks were metamorphosed during collisional Pan-African orogenic processes between 750 and 550 Ma (Asrat and Barbey, 2003) and are characterized by NNE-SSW-striking foliations (Davidson, 1983). The granulites are mainly exposed along the southwestern margin of the Chamo Basin, on the Konso Plateau (Kazmin *et al.*, 1978), and northeast of the Chew Bahir Basin (Davidson, 1983) (Fig. 3.1b). The outcrops

in the Konso Plateau are characterized by E-W-striking foliations (Davidson, 1983; Asrat and Barbey, 2003), reflecting effects of post-Pan-African tectonic events (de Wit and Chewaka, 1981).

Radiometric age determinations of plutonic rocks in the Konso Plateau document that the pluton was emplaced around 449 ± 2 Ma (Asrat and Barbey, 2003). Compositionally similar intrusive rocks west of the Konso Plateau (Davidson, 1983), dated between 526 ± 5 Ma and 554 ± 23 Ma (Gichile, 1992; Worku and Schandelmeier, 1996; Teklay *et al.*, 1998; Yibas *et al.*, 2002), highlight major structural and metamorphic events in Ethiopia (*e.g.*, Asrat and Barbey, 2003). Based on their structural, geochronologic, and compositional similarities, Yibas et al. (2002) interpreted the intrusions in the context of plutonic episodes following the Pan-African orogeny.

Well-indurated, thin basal conglomeratic sandstone beds unconformably overlie the crystalline basement rocks (Davidson and Rex, 1980; Ebinger *et al.*, 1993). A 5 to 30-m-thick conglomeratic sandstone layer, silicified at the top, is exposed along the margin of the Amaro Horst (Wolde-Gabriel, 1991; Ebinger *et al.*, 1993) but is absent west of the BRZ (Moore and Davidson, 1978; Davidson, 1983; Philippon *et al.*, 2014). The age of the sandstone layer is uncertain; however, studies have correlated the sediments with the petrographically similar lower unit of the Turkana Grits of inferred Cretaceous age in northern Kenya (Murray-Hughes, 1933; Arambourg and Wolff, 1969; Walsh and Dodson, 1969; Levitte, 1974; Savage and Williamson, 1974; Owusu Agyemang *et al.*, 2019). In contrast, Davidson (1983) suggested an early Paleogene depositional age based on sediment composition and the nature of contact with the overlying Eo-Oligocene volcanics. The undeformed conglomeratic sandstone layer lacks organic remains and is thought to represent sedimentation across a peneplain surface prior to the emplacement of the voluminous Eo-Oligocene volcanics (Davidson and Rex, 1980; Davidson, 1983).

The subsequently deposited Eo-Oligocene volcanic successions are exposed mainly along the rift shoulders, with thicknesses ranging from several hundred meters to a kilometer in places (Davidson, 1983; Ebinger *et al.*, 1993; 2000; George *et al.*, 1998). The composition of these units ranges from primitive basalts to more evolved TiO2-enriched alkaline basalts (Rooney, 2017; Steiner *et al.*, 2022), emplaced between 45 and 35 Ma (Davidson and Rex, 1983). Spatially restricted thick sequences belonging to the Amaro Basalt overlie the ubiquitous conglomeratic sandstone layer and have been dated to 44.9 ± 0.7 Ma (Ebinger *et al.*, 1993). The thickness of the Amaro Basalt increases toward the north along the Amaro Horst, where the full sequence is exposed (Levitte, 1974; Fig. 3.1b). To the south of the Amaro Horst, petrographically similar basalts overlying the crystalline basement rocks yielded a K-Ar age of 42.5 ± 0.7 Ma (*e.g.*, WoldeGabriel *et al.*, 1991). To the west of the Amaro Horst, along the margin of the Chamo and Beto basins, the stratigraphically lower Gamo Basalt overlies the widespread Amaro Tuff dated between 37.9 and 35.1 Ma (Davidson, 1983; Ebinger, 1993). Rooney (2017) correlated the Amaro and Gamo basalts with the Mekonnen basalts (35–28 Ma; Davidson, 1983), and reclassified them as the Gamo-Mekonnen basalts; these volcanics represent the main phase of flood-basalt volcanism between ca. 38 and 27 Ma (Steiner *et al.*, 2022).

The Amaro Tuff covers the Gamo-Mekonnen Basalt and separates the 500-m-thick Getera-Kela Basalt from the older basaltic units (18–12 Ma; Ebinger *et al.*, 1993). South of the Amaro Horst, a

petrologically similar basaltic unit was dated at ~11 Ma (WoldeGabriel *et al.*, 1991). Radiometric dating of phonolite eruptive centers located along-strike of the Mali-Dancha and Bala-Kela faults provided ages between 16 and 12 Ma (Davidson, 1980).

During the early to middle Pliocene, thin lava flows of the Gombe Group were emplaced along the Omo-Turkana Depression (Watkins, 1983; Brown *et al.*, 1985). The lava flows extend farther north toward the Usno Basin in the lower Omo Valley and crop out in the form of erosional remnants along the western margin of the Chew Bahir Basin (Davidson, 1983). Based on petrographic analysis and K-Ar dating, Haileab *et al.*, (2004) correlated these units with the Gombe Group basalts along the northeastern sectors of the Lake Turkana Basin (Watkins, 1983). These widely distributed basalt flows erupted during a short period between 4.05 and 4.18 Ma (Erbello and Kidane, 2018).

During the late Pliocene, volcanic activity shifted toward the southeast of the BRZ along the Ririba Rift segment (Corti *et al.*, 2019). Outcrops of Quaternary volcanics are restricted to the northern sector of the Chamo Basin and to areas west of the Omo Valley (Fig. 3.1b). The Quaternary Bobem (0.66 ± 0.02 Ma) and the Nech Sar basalts (0.99 ± 0.10 Ma) in the northern Chamo Basin capped southwest-dipping fluvio-lacustrine deposits. Both units were subsequently cut by N-S-striking normal faults (Ebinger *et al.*, 1993). N-S aligned Quaternary volcanic fields of the Kurath range in the Omo Valley were emplaced at 91.5 ± 15 ka (Jicha and Brown, 2014).

With respect to the rift-related magmatic evolution of the study area, it can be concluded that the volcanic rocks in the BRZ were emplaced in three major eruption periods during the Eo-Oligocene, Miocene, and Pliocene-Holocene. Interestingly, these distinct eruptive episodes were virtually coeval with phases of tectonic activity in the Red Sea Rift (*e.g.*, Bosworth and Stockli, 2016), the eastern Tanzanian Craton (*e.g.*, Rooney, 2020c), and the nKR (Muirhead *et al.*, 2022; Riedl *et al.*, 2022).

3.3 Methods

Low-temperature (U-Th-Sm)/He apatite and zircon (AHe and ZHe) thermochronology is based on the decay of U, Th, and Sm isotopes, producing α-particles retained below system-specific closure temperatures that vary with cooling rate (Dodson, 1973), grain size (Farley, 2000; Reiners *et al.*, 2002), and the amount of radiation damage in a crystal (*e.g.*, Flowers *et al.*, 2009; Gautheron *et al.*, 2012; Guenthner *et al.*, 2013). Temperature ranges in which particles are only partially retained are referred to as partial retention zones (PRZ). The AHePRZ and ZHePRZ range from ~40–70 °C (Gautheron *et al.*, 2012) and ~140–220 °C (Guenthner *et al.*, 2013), respectively. Assuming a mean surface temperature of 20 °C and a geothermal gradient of 40 °C/km (Pik *et al.*, 2003), the range of thermal sensitivity of AHe and ZHe in this part of Africa corresponds to a depth of about 1 to 5.5 km. Hence, these thermochronologic systems can potentially document

the thermal history associated with tectonic and erosional processes in the uppermost part of the crust.

Following standard magnetic and heavy liquid mineral separation, a total of 182 apatite and 10 zircon single grains were carefully handpicked, their dimensions measured, and packed in Pt (for apatite) and Nb (for zircon) tubes for isotope analyses at the University of Potsdam (He) and GFZ-German Research Centre for Geosciences (U, Th, Sm), according to methods described in Zhou *et al.* (2017) and Galetto *et al.* (2021).

Additionally, high-resolution TanDEM-X (12 m) digital topographic data were used to identify lineaments of inferred tectonic origin from a rift-overlap zone between the Chew-Bahir Basin and the sMER.

3.3.1 Sample collection

Assuming that the recently well-established AHe thermochronometeric system can potentially archive crustal cooling patterns in space and time during rifting, 35 bedrock samples were collected from exhumed amphibolite and granulite basement rocks from footwall blocks adjacent to the Chew Bahir, Mali-Dancha, Baneta, Bala-Kela, and Chamo basins (Fig. 3.2a). As the extent of basement exposures diminishes laterally north of the Chew Bahir Basin (Davidson, 1983)(Fig. 3.3), we collected samples from both elevation profiles and along-strike of the exposed footwall blocks similar to the approach chosen by Mortimer *et al.* (2016). Rock samples from six elevation profiles were collected from regions with sufficiently uplifted footwall blocks (Fig. 3.4). A set of samples from the NW-SE-striking Mali-Dancha Basin margin was collected between 880 m and 1,500 m asl. Two elevation profiles, spaced ~10 km apart, were obtained along a transect across the northeastern margin of the Chew Bahir Basin. A single sample was also collected from the base of the exposed footwall farther south. Additionally, two samples from different structural positions were collected from transects across the flanks of the Baneta, Mali-Dancha, and Bala-Kela basins. At locations where exhumed Neoproterozoic basement rocks were characterized by insufficient relief (<200 m), single samples were collected from the base of the exposed footwall margin.

3.3.2 Thermal history modeling

Thermal modeling was performed using both QTQt (Gallagher, 2012) and HeFTy (Ketcham, 2005) inversion programs. QTQt employs a Bayesian trans-dimensional Markov Chain Monte Carlo algorithm to search time-temperature paths that are compatible with observed data based on a posterior probability, whereas HeFTy employs a Frequentist approach using a random, non-learning Monte Carlo time-temperature search algorithm to determine thermal histories that agree with observed data based on a goodness-of-fit statistical test. The contrasting modeling and visualization outputs from QTQt and HeFTy each have their own unique advantages (Vermeesch and Tian, 2014; Gallagher and Ketchman, 2018; Murray *et al.*, 2022, and Abbey *et al.*, 2023), which

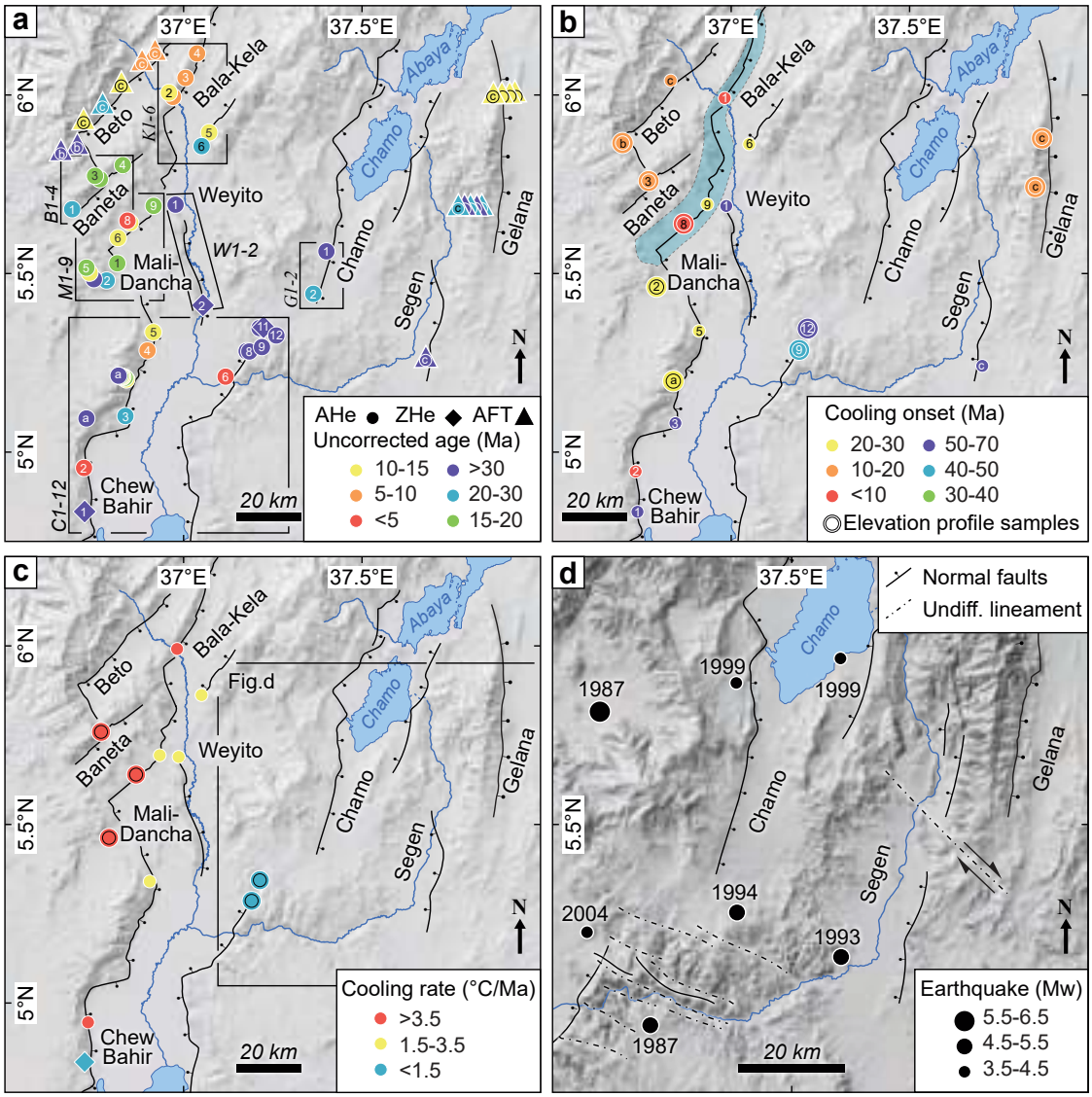

Figure 3.2: AHe age data and representative thermal modeling results from the BRZ superposed on hill-shaded relief. (a) Weighted-mean AHe age (uncorrected), (b) onset of cooling, (c) cooling rate calculated from the slope of the tT-path in specified time interval, and (d) inferred lineaments, and earthquakes in the sMER and the Chew Bahir Basin superposed on a 12-m resolution DEM generated from TanDEM-X data. The transparent envelope shown in (b) represents a narrow zone of deformation during the late stage (<10 Ma) of rifting. Seismicity data are from the International Seismological Center (https://www.isc.ac.uk).

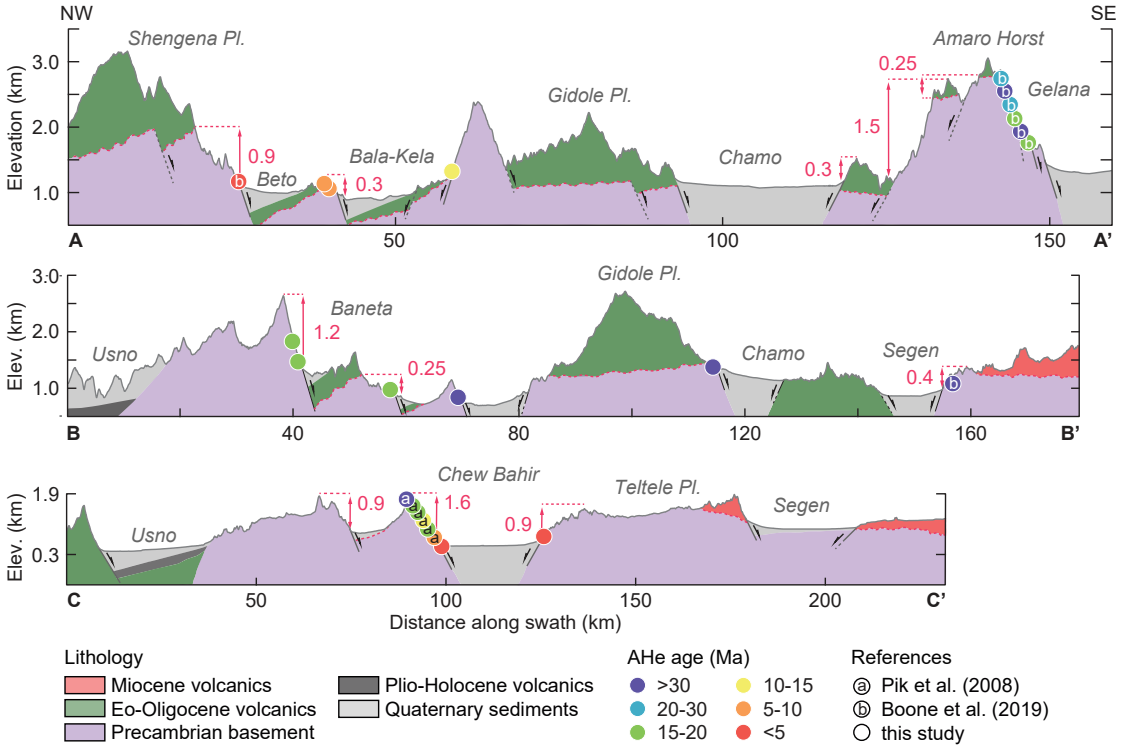

Figure 3.3: AHe cooling ages (uncorrected) superposed on across-rift geological cross sections (A-A'; B-B'; C-C'; locations shown in Fig. 3.1b). AHe cooling ages are from Pik *et al.*, (2008) (a), Boone *et al.*, (2019) (b), and this study (circles). The indicated apparent displacement was estimated from the DEM.

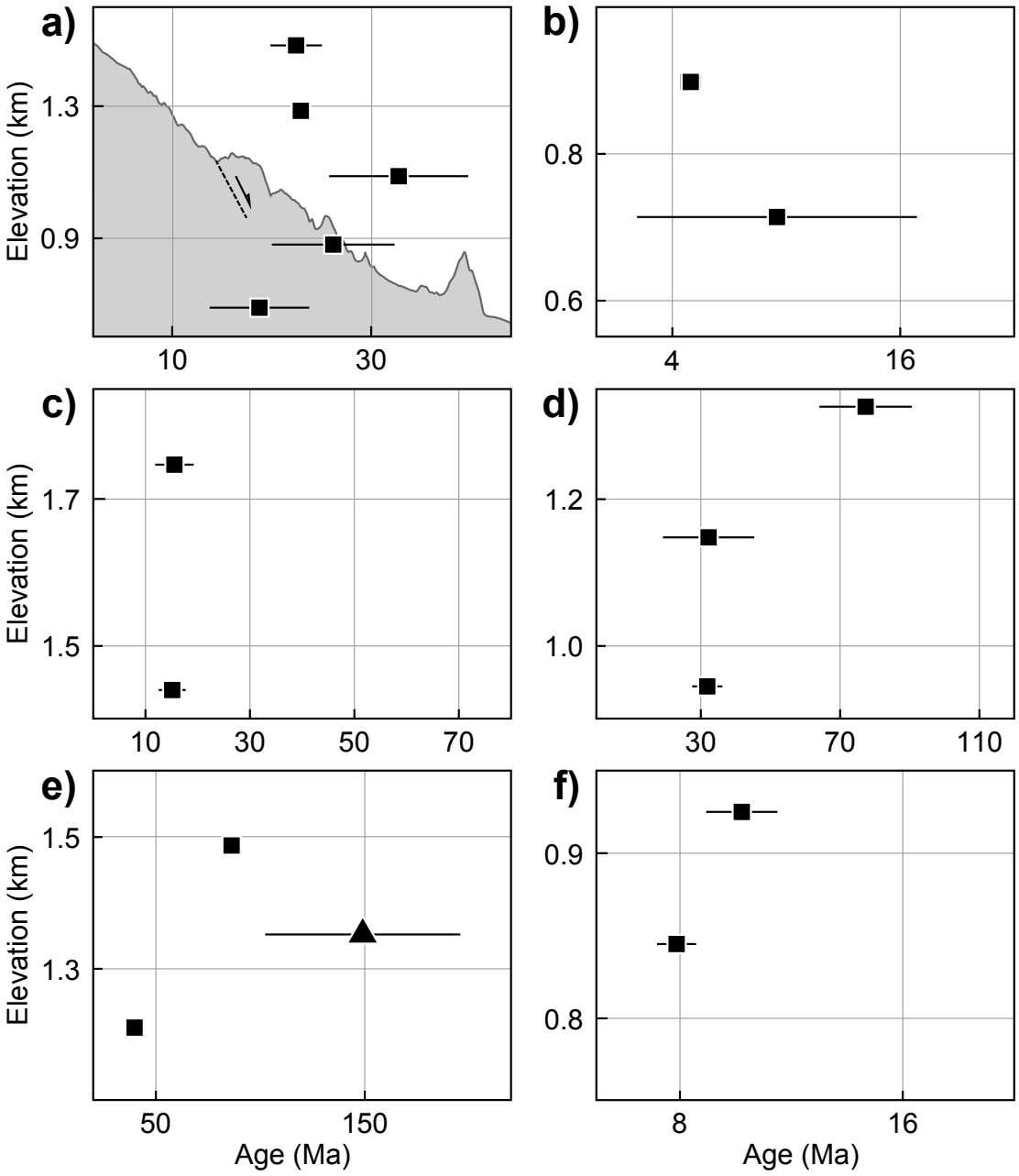

Figure 3.4: Weighted-mean ages plotted against elevation for samples from the Mali-Dancha (a and b), Baneta (c), Chew Bahir (d and e) and Bala-Kela (f) basins. The weighted-mean ages (AHe: filled square; ZHe: filled triangle) with the 95% confidence interval were estimated based on a minimum of three single-grain ages using IsoplotR v.9 (Vermeesch, 2018). A topographic profile with a broken line and an arrow (a) indicate inferred normal fault.

we strategically exploited through a systematic and iterative modeling approach to thoroughly assess and interpret our (U-Th)/He dataset.

To account for the impact of radiation damage on He diffusivities, the accumulation of radiation damage and annealing models of Flowers et al (2009) and Guenthner et al. (2013) for the AHe and ZHe systems, respectively, were applied in all QTQt and HeFTy inversions. Single-grain AHe data from each sample were first scrutinized for outliers by assessing potential age-eU-grain size relationships. Individual samples revealing distinctive age-eU-grain size relationships within all grains over a comparatively broad range of eU concentrations (>10 ppm) were first identified, and data from these samples were considered robust inputs for thermal modeling. Potential outliers based on first-order age-eU relationships from each sample were first noted, and model sensitivities to the inclusion or exclusion of such grains were evaluated. Potential outliers were determined to be excluded if their inclusion as inputs (1) significantly obscured the resulting thermal history in QTQt with poor age predictability, and/or (2) prevented HeFTy from finding any sufficient time-temperature histories. All excluded data points are identified in the Supporting information A. 11–14 and A. 16–19.

Thermal histories for each individual sample were first modeled in QTQt, followed by multiple-sample modeling of compiled data from individual elevation profiles. All models initiated at high temperature (450 ± 50 °C) in the late Neoproterozoic (525 ± 25 Ma) to represent the Pan-African orogenic event (Davidson, 1983; Yibas *et al.*, 2002; Asrat and Barbey, 2003). Because the stratigraphic thickness for the Paleogene sediments and the Eo-Oligocene volcanics on top of the basement rocks is so variable, with the units even absent at some places (*e.g.*, Davidson, 1983; Ebinger *et al.*, 2000; Philippon *et al.*, 2014), a broad range of temperature constraints extending from 120 to 20 °C and covering a time interval between 80 and 30 Ma was applied. For elevation-profile samples, a regionally estimated geothermal gradient of 40 °C/km (Pik *et al.*, 2003) was used. A final constraint (20 ± 10 °C at 0 Ma) was applied to all models simulating present-day conditions. After implementing these time-temperature constraints, all models were allowed to search for solutions between 550 Ma and the present. We used 50,000 burn-in and 200,000 post-burn-in sampling iterations for individual inverse modeling experiments. The resulting expected thermal history model was constructed from all possible time-temperature paths weighted by their posterior probabilities (*e.g.*, Gallagher, 2012). A summary of thermal modeling input parameters and the model setup is presented in the Supporting information Tables A. 15 and A. 19–20.

The probability distribution from the expected output of the time-temperature models from QTQt was used to set up the HeFTy model thermal history inversions. Samples that contained single-grain AHe data spanning a range of eU concentrations >10 ppm with a comparatively distinctive age-eU relationship were explicitly selected for thermal inversions in HeFTy. The motivation to additionally model these data in HeFTy models was twofold: (1) to confirm the thermal histories produced in QTQt for robust interpretation, and (2) to permit the forward modeling of each individual and reasonably fitting thermal history in order to visually compare predicted age-eU patterns to observed data (*e.g.*, Guenthner, 2021). For each HeFTy inversion,

a near-identical constraint box to that used in QTQt was imposed from 80–30 Ma and 120–20 °C, followed by a second overlapping constraint universally applied from 70–1 Ma and 125–20 °C to allow the model to explore potential post-80 Ma reheating and cooling scenarios. Each HeFTy inversion was also unconstrained during the Phanerozoic to permit the exploration of varying radiation-damage accumulation histories that may have a direct influence on observed AHe data (*e.g.*, Colleps *et al.*, 2021), and thus impact the post-80 Ma thermal history. The details of each QTQt and HeFTy inversions, including justifications for geological constraints and data inputs, are presented in the Supporting information S1. Following each HeFTy inversion, the model output was exported to forward model age-eU and grain-size trends for each "good" t-T pathway using a modified Matlab script from Guenthner (2021), and the forward models were compared to the observed data.

The timing of the onset of cooling was determined based on the shape of the 95% credible interval, marking early and late required onset of cooling for a modeled sample (*e.g.*, Murray *et al.*, 2022; Abbey *et al.*, 2023). The cooling rate for each model was also estimated from the slope of the weighted-mean expected time-temperature path between specified time intervals.

3.4 Results

3.4.1 Apatite (U-Th)/He ages

Where possible, two to twelve single grains ranging in size from 38 to 145 µm (ESR-equivalent spherical radius) were analyzed from each sample in an attempt to quantify intra-sample age dispersion. Unfortunately, only one grain could be analyzed from samples B-1, B-4, C-3, and C-12 due to their poor apatite yield and quality. A summary of the data is presented in appendix A; Tables 1 and 2.

Apparent (uncorrected) AHe single-grain ages range between 0.86 ± 0.08 Ma and 109.4 ± 3.5 Ma (A.1–A.4). Effective uranium ($eU = U + 0.235 \times Th$, Flowers *et al.*, 2009) concentrations for the analyzed samples are generally low. Weighted-mean ages calculated using IsoplotR (Vermeesch, 2018) exhibit a range between 3.1 ± 1.9 Ma (C-2) and 77.3 ± 15.1 Ma (C-9) (Fig. 3.2a); however, a single-grain age obtained from sample C-12 located at the top of the northeastern flank of the Chew Bahir Rift records a much older age (86.3 ± 0.4 Ma).

ZHe ages measured from sample C-11, collected at a structural position between C-10 (AHe age 39.8 ± 6.2 Ma) and C-12, yielded a mean age of 149.3 ± 46.8 Ma (Fig. 3.2b). Additional ZHe ages measured from samples C-1 and W-2, collected at the southwestern flank of the Chew Bahir and Weyito basins, yielded mean ages of 265.7 ± 14.5 Ma and 219.3 ± 26.5 Ma, respectively (A.5).

The intra-sample age-dispersion in our data set is large, with values from ~4 to 158%. Only a few of the analyzed samples (C-10, K-1, M-3, and W-3) exhibit dispersion within 20% of the weighted mean age. Individual sample plots depicting apparent age against ESR and eU concentration are presented in the Supporting Information S2. The apparent ages plotted against eU or ESR in some samples exhibit a weak correlation; however, some others, for example,

K-1, K-6, B-3, M-1 and M-6, taken from the foot of the Bala-Kela, Baneta and Mali-Dancha basin margins, show a strong to moderate correlation. Despite the moderate positive correlation between apparent age and eU in sample M-6, the variation in eU ranges only between ~3 and 5 ppm (see Supporting information S2). In light of the significant grain-size variation between ~60 and 130 µm in sample K-1, apparent intra-sample age dispersion would be expected, assuming that the sample cooled slowly through the AHePRZ (*e.g.*, Reiners *et al.*, 2002).

Data from elevation profile across the southern margin of the Mali-Dancha Basin exhibit older weighted-mean ages at increasingly higher elevation for samples located close to the base of the rift flank; however, ages from structurally higher positions do not follow this trend (Fig. 4a). This interruption in the age-elevation trend is likely related to the presence of a subsidiary fault with unknown displacement, expressed as a slope-break in a topographic profile (Fig. 4a). Sample pairs from the northeastern margin of the Chew Bahir and Bala-Kela basins reflect a consistent age-elevation relationship (Figs. 3.4d, e and f). Sample pairs located at different structural positions across the flanks of the Baneta and Mali-Dancha basins exhibit overlapping weighted-mean ages within the 95% confidence interval (Figs. 3.4b and c). Weighted-mean ages obtained from samples located at higher structural positions from the Baneta (15.1 ± 3.2 Ma and 15.6 ± 4.5 Ma) and Bala-Kela (7.9 ± 0.8 Ma and 10.2 ± 1.5 Ma) basin flanks are older than samples collected from the base of the rift flanks (Fig. 3.4). Single-grain ages from along the foot of the Baneta Basin flank farther south (B-1; 15.1 ± 4.2 Ma) and north (B-4; 16.2 ± 1.0 Ma) overlap with weighted-mean ages of sample pairs located at different structural positions across the flank. Similarly, along the margin of the northward-narrowing Mali-Dancha and Bala-Kela basins, weighted-mean ages range between 15.5 ± 10.3 Ma and 4.9 ± 1.1 Ma. In contrast, sample mean ages along the Chew Bahir Basin flank record a narrow distribution between 10.3 ± 4.8 Ma and 3.1 ± 1.9 Ma, and the single-grain age from a sample located at the base of the footwall yields a significantly older age of 32.7 ± 0.8 Ma.

3.4.2 Thermal-history modeling results

Thermal modeling was carried out for individual samples and sets of elevationl-profile samples from the region . Thermal modeling results from laterally offset vertical profiles C7-9 (AHe) and C10-12 (C-11: ZHe) collected from the northeastern flank of the Chew Bahir Basin record the onset of protracted slow cooling (~0.7–1.2 °C/Myr) between ~55 and 41 Ma (Fig. 3.5b). Similar characteristics of slow cooling throughout the Cenozoic is reflected by samples C-3 and W-1, which were collected from the base of the southwestern Chew Bahir Basin margin and the NW-SE-striking Weyito Basin flank, respectively (Supporting information A. 21).

Spatially distributed samples from the Chew Bahir Basin and the Gofa Province exhibit an onset of cooling (>~2 °C/Myr) between 27 and 21 Ma. For example, individually modeled samples M-1 and M-2, collected at different structural positions across the NW-SE-striking Mali-Dancha Basin flank, record an onset of rapid cooling (>~2.3 °C/Myr) between ~25 and 14 Ma (Fig. 3.5a). Jointly modeled samples M-1 and M-2 exhibit an episodic onset of cooling at ~27 and

4 Ma (Fig.3.5b). Farther southeast along the margin of the Mali-Dancha Basin, sample C-5 from a transition zone between the Mali-Dancha and Chew Bahir basins records well-constrained, protracted cooling after ~23 Ma (A.10). Additionally, samples M-9 and K-6, collected from a transition zone between the Mali-Dancha and Bala-Kela basins and the eastern flank of the Bala-Kela basin, respectively, exhibit an onset of cooling between ~23 and 21 Ma (Fig. 3.5a and A.10).

Samples B-2 and B-3 from different structural positions of the NE-SW-striking Baneta margin document that rapid cooling started between ~15 and 12 Ma (Fig. 3.5a and A.10). A consistent onset of rapid cooling (~5 °C/Myr) at ~15 Ma was recorded by jointly modeled samples B-2 and B-3 (Fig. 3.5b). Toward the east, samples M-7 and M-8 from different structural positions of the Mali-Dancha Basin margin (Baneta halfgraben) record that rapid cooling initiated at ~9 Ma (Fig. 3.5b). In the Gofa Province, sample K-1 collected from the base of the Bala-Kela basin records a positive correlation between age and grain size (A.7) and exhibits slow cooling through the AHePRZ prior to more rapid cooling (~5 °C/Myr) commencing at ~6 Ma (Fig. 3.5a). In summary, thermal modeling results for samples from the BRZ and from the base of the rift flanks indicate an onset of cooling in time intervals between 55–40 Ma, 27–21 Ma, and 15–6 Ma. More recent (<6 Ma) rapid cooling (~6 °C/Myr) is documented from sample C-2, which was collected at the base of the Chew Bahir Basin margin, and elevation-profile samples M-1 and M-2 from the Mali-Dancha basin margin (Figs. 3.2b, 3.5a and b).

The time-temperature history results of some samples analyzed in this study exhibit a progressive increase in temperature between the Eocene and Oligocene (Figs. 3.5a and b). From ~49 to 35 Ma, thick layers (>1.5 km; Davidson, 1983) of basaltic flows covered much of the BRZ (Davidson, 1983; Ebinger *et al.*, 1993; Steiner *et al.*, 2022), suggesting that the recorded increase in temperature possibly reflects the influence of reheating associated with stratigraphic burial. A coeval reheating event documented from the adjacent flanks of the Beto and Gelan basins (Balestrieri *et al.*, 2016; Boone *et al.*, 2019) is interpreted to constrain the regional extent of the emplaced volcanic products during the Eocene and Oligocene.

The predicted ages from thermal histories fit the observed data reasonably well. For example, multiple single-grain ages from samples M-1, M-2, B-3, K-1, and K-6 were predicted within <~20% error of the observed ages. In contrast, some of the predicted ages from samples C-2, K-1, M-1, and M-2 range between ~30 and 50% of the observed ages (Fig. 3.5a). The predicted ages from the jointly modeled samples C7-9, M1-2, B2-3, and M7-9 range between 5 and 50%, with few ages exceeding 50% of the observed ages (Fig. 3.5b). Except for two single-grain ages, all the predicted ages for the elevation-profile samples C10-12 were predicted within ~20% of the observed ages (Fig. 3.5b). The age-eU patterns predicted from individual "good" thermal history outputs for each sample modeled by HeFTy demonstrate that the modeling results obtained are robust despite the dispersion in the observed data (Fig. 3.5a). While there are many factors that can influence AHe ages reproducibility (zoning, radiation damage, chemistry; *e.g.*, Fitzgerald *et al.*, 2006; Kohn *et al.*, 2009), the fact that the sampled bedrock is Neoproterozoic, and was subjected to multiple tectonic overprints between the Cretaceous and Tertiary periods

(Morley, 1992; Bosworth and Morley, 1994; Ebinger *et al.*, 2000; Chorowicz, 2005) indicates that the analyzed apatite grains must have experienced a complex thermal history that may have amplified the variable effects of damage accumulation, zonation, and grain chemistry on AHe data disparities.

3.5 Discussion

3.5.1 History of vertical movements prior to the emplacement of flood basalts

Thermal modeling results of new AHe and ZHe data from the BRZ record little or insignificant tectonically induced crustal cooling shortly prior to massive volcanism in southern Ethiopia (35–45 Ma; Davidson, 1980; Ebinger *et al.*, 2000). Conversely, time-temperature histories obtained from samples located mainly along and across the NW-SE-striking footwall flanks document a temporally consistent onset of slow cooling, likely recording the onset of denudation between ~65 and 60 Ma (Fig. 3.6). Denudation associated with the onset of slow cooling may reflect Paleogene extension related to the opening of the Anza Rift in northern Kenya (Morley *et al.*, 1990, 1992; Bosworth and Morley, 1994), regional uplift documented farther to the east in the Ogaden Basin (Mége *et al.*, 2015), and ensuing erosion. For example, the elevation-transect samples from the northeastern footwall block of the Chew Bahir Basin reveal an onset of slow cooling between ~55 and 40 Ma (Fig. 3.5b). Likewise, sample W-1 from the base of the NW-SE-striking Weyito Basin margin records protracted slow cooling throughout the Cenozoic, which may be related to vertical crustal motion in the context of extensional tectonism in the Anza Rift. A similar prolonged residence close to the surface and slow cooling from shallow crustal levels can be inferred from the analysis of sample C-3 from the base of the southwestern margin of the Chew Bahir Basin. Farther to the northeast, a sample from the Segen Basin margin with a central AFT age of ~65 Ma (Balestrieri *et al.*, 2016) and a mean AHe age of ~61 Ma (Boone *et al.*, 2019) exhibits a consistent thermal history of prolonged residence close to the surface during the Cenozoic (Boone *et al.*, 2019). Additionally, this thermal history may further indicate that crustal cooling was associated with the attainment of NW-SE-trending local relief during the early Paleogene, assuming that adjacent regions were low-relief surfaces during this period (Davidson and Rex, 1980). Based on thermal modeling results from a set of vertical-profile samples from the NW-SE-striking Beto Basin margin and AFT cooling ages ranging between 75 and 60 Ma, Philippon *et al* .(2014) inferred a period of rapid crustal cooling during the Cretaceous and Paleogene due to regional uplift documented in northern Kenya (Foster and Gleadow, 1996; Spiegel *et al.*, 2007; Torres Acosta *et al.*, 2015; Boone *et al.*, 2019). Combining the AFT data from Philippon *et al.* (2014) with new AHe ages, Boone *et al.* (2019) also inferred rapid crustal cooling (~2.5–5 °C/Myr) across the NW-SE-striking flank of the Beto Basin during the Cretaceous. Rapid cooling may have been linked with the formation of the Anza Rift and associated NW-SE-oriented lineaments that appear to be present-day vestiges of these early extensional processes in the BRZ (Morley, 1992; Bosworth and Morley, 1994). This interpretation is compatible with a fault-kinematic

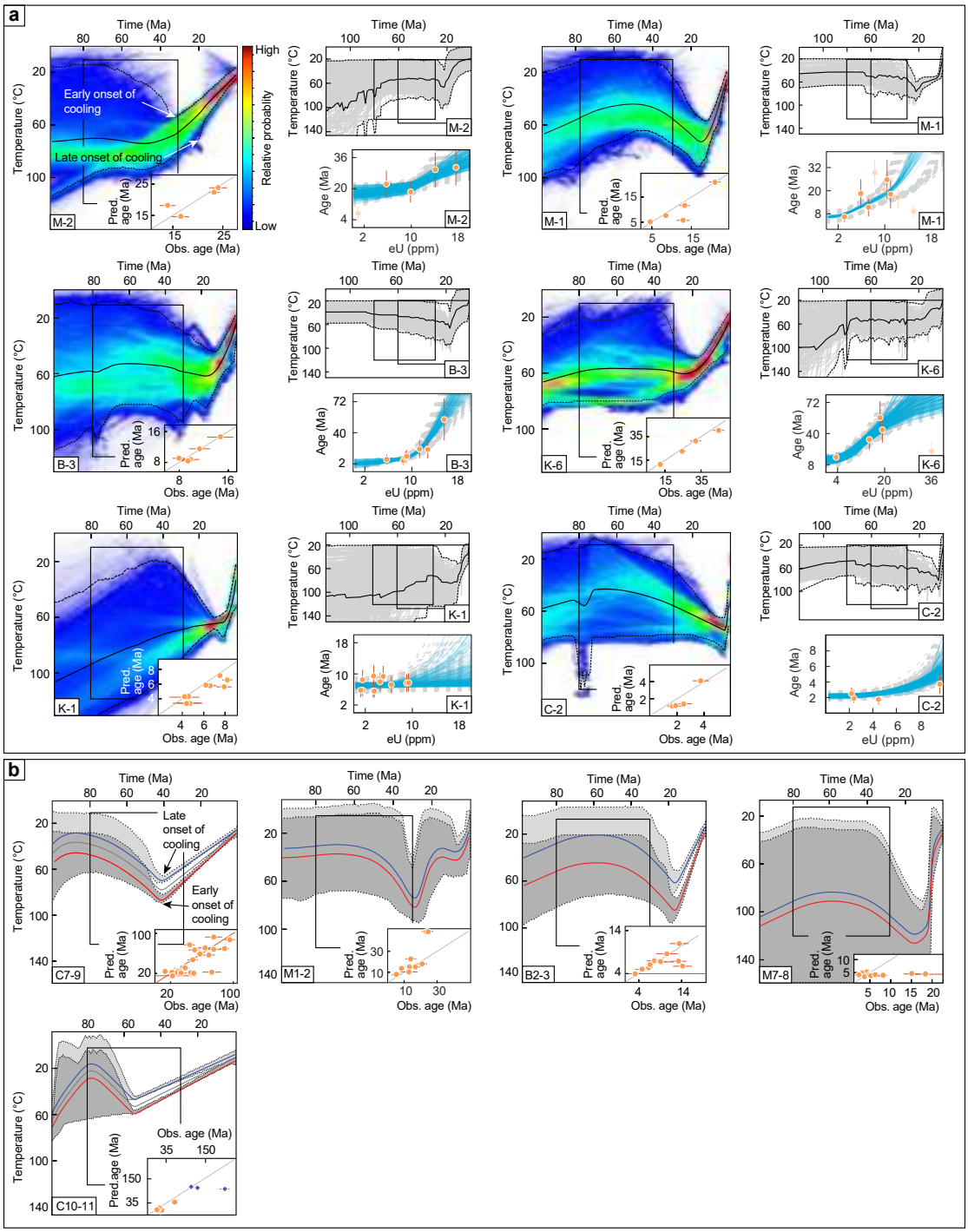

Figure 3.5: Expected thermal histories, relative probability, and their 95% credible interval obtained from QTQt (Gallagher, 2012) and HeFTy (Ketcham, 2005) modeling for individual samples (a) and multiple samples (b). The expected thermal history represents the weighted-mean of all the models sampled (solid lines). (b) The thermal history models for elevation-profile samples, the topmost sample is plotted in blue and the thermal history of the lowermost sample is plotted in red. The thermal histories for samples in between are shown in gray (a and c). For individual and elevation profile samples, the 95% credible interval is drawn as a stippled line. The relative probability is shown in color scale (a). The black boxes are the thermal history constraints.

analysis of structures in the Turkana Grits of northern Kenya that documents a NE-SW-oriented extensional period during the Paleogene (Vetel and Le Gall, 2006). Flank uplift associated with activity in the Anza Rift might have generated the source rock for the petrographically correlated and up to 30-m-thick Cretaceous-early Paleogene (?) conglomeratic sandstones exposed in the southern sMER (WoldeGabriel*et al.*1991) and in the Turkana area of northern Kenya (Arambourg and Wolff, 1969; Levitte *et al.*, 1974).

3.5.2 Implication for interaction between the southern Main Ethiopian and northern Kenya rifts

Rapid Plio-Pleistocene cooling along the footwall flanks of the Chew Bahir and the Mali-Dancha basins reflects the current tectonic interaction between the sMER and nKR (Fig. 3.5a and b: C-2 and M1-2); this interaction is likely to have involved a reactivated, NW-SE-striking inherited basement fabric via the seismically active Segen Basin (Fig. 3.2d). Interestingly, the reactivated basement fabrics and the structurally associated Segen River suggest that the current hydrologic connectivity between lakes Abaya, Chamo, and Turkana via the Chew Bahir Basin might have been influenced by tectonic processes that were established during the Pleistocene. The aborted propagation of the sMER toward the Ririba Rift during the early Pleistocene (*e.g.*, Corti *et al.*, 2019), the current active tectonism of the southern Gofa Province and the Chew Bahir Basin (Philippon *et al.*, 2014; Erbello *et al.*, 2022), as well as seismicity clusters along the Omo Valley, the southern Gofa Province, and the Chew Bahir and Segen basins (Musila *et al.*, 2022) support our interpretation. Recent geodetic surveys from across the basins (Knappe *et al.*, 2020) reveal a strain rate of ~4.5 mm/yr within in a narrow zone between the Chew Bahir and Segen basins (Fig. 3.7), thus further supporting the inferred tectonic interaction between the sMER and the nKR (Fig. 3.8e).

Our thermal modeling results from a set of elevation profiles across the northeastern margin of the Chew Bahir Basin (C7–9 and C10–12) reflect an early Paleocene to late Eocene (~55–41 Ma) onset of slow cooling (~0.7–1.2 °C/Myr). Conversely, elevation-profile samples M-1 and M-2 and a sample C-2 from across the NW-SE striking Mali-Dancha Basin margin and the western flank of the Chew Bahir Basin, respectively, record rapid cooling that began during the early Pliocene (~5 Ma) (Fig. 3.5a and b). Furthermore, sample C-6 collected farther south along the eastern margin of the Chew Bahir Basin close to SW flowing Segen River, records a weighted-mean age of ~3 Ma, indicating a recent onset of crustal cooling in the southern Gofa Province and the Chew Bahir Basin. In light of these observations, recent seismicity (Musila *et al.*, 2022), historical earthquake records (https://www.isc.ac.uk), and structural data (Fig. 3.2d) suggest that the current kinematic interaction between the sMER and the Chew Bahir Basin (Ebinger *et al.*, 2000, Philippon *et al.*, 2014, Erbello *et al.*, 2022) began during the early Pliocene, following reactivation of NW-SE-striking inherited basement fabrics.

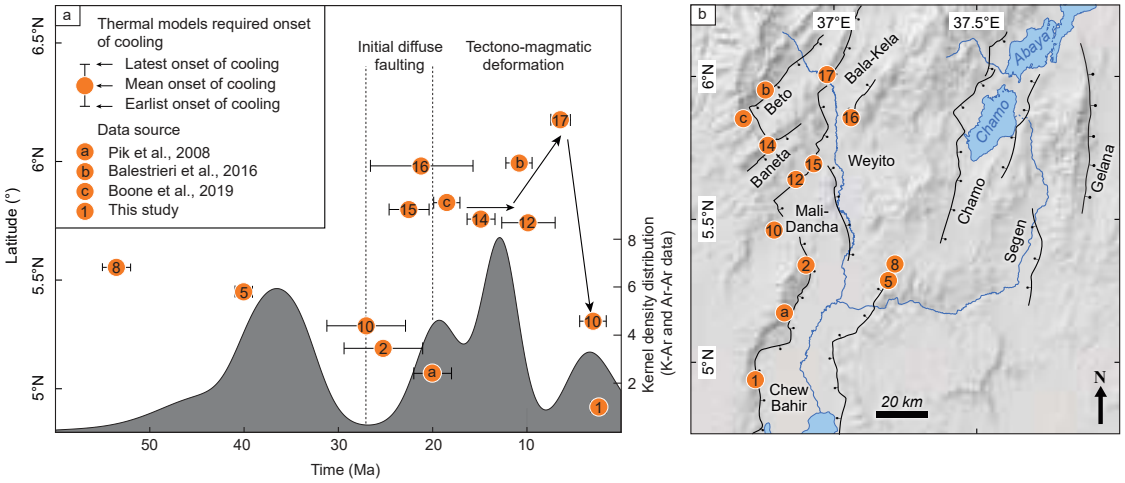

Figure 3.6: Thermal history models for individual samples, and kernel-density distribution of compiled regional K-Ar and Ar-Ar data from volcanic rocks (Davidson and Rex, 1980; Davidson, 1983; Ebinger *et al.*, 1993, 2000; George, 1998; George and Rogers, 2002; Haileab *et al.*, 2004; Rooney, 2010; Jicha and Brown, 2014; Franceschini *et al.*, 2020). (a) Onset of cooling estimated from a mean of the earliest and latest onset of cooling. Arrow indicates deformation migration. (b) Sample locations.

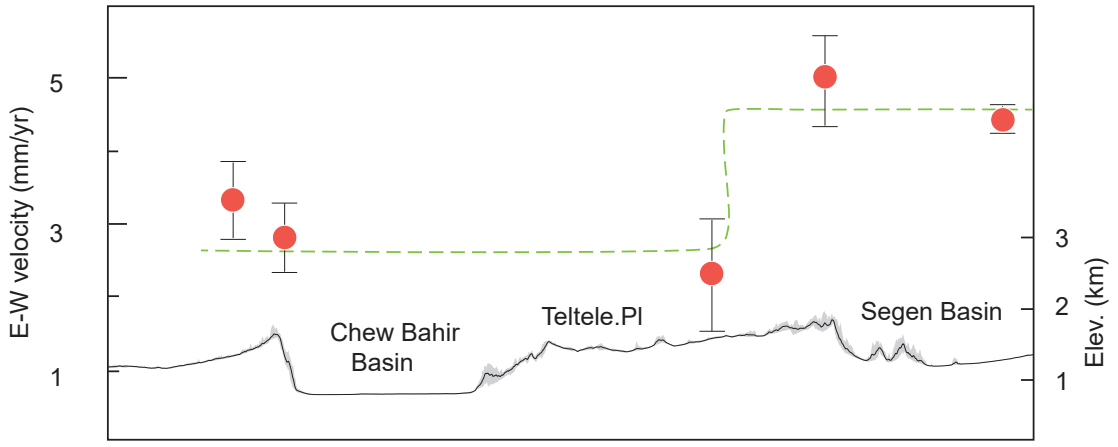

Figure 3.7: Velocity profile and 1 sigma uncertainty with topographic swath (10 km) profile across the Chew Bahir (CB) and Segen (Se) basins (modified from Knappe *et al.*, 2020).

3.5.3 Rifting and magmatism

Our new thermochronological results are striking in terms of the overall spatiotemporal characteristics of exhumation, rift-basin development, and the timing of magmatism during the evolution of the BRZ. The onset of widespread crustal cooling throughout the BRZ corresponds with the end of ubiquitous flood-basalt volcanism between 49 and 28 Ma (Davidson, 1983; Ebinger *et al.*, 2000; Rooney, 2020; Steiner *et al.*, 2022), suggesting that areally extensive faulting began shortly after emplacement of the basalt flows (Figs. 3.6, 3.8b and c). Subsequently, deformation progressively became more localized along the narrow zone of the Mali-Dancha and Bala-Kela basin margins in the Gofa Province and propagated northward during the late stages of rifting (Figs. 3.2b and 3.8d); this was accompanied by resumed regional volcanism (18–12 Ma; Davidson, 1983; Ebinger *et al.*, 2000), suggesting close tectono-magmatic relationships (Fig. 3.6).

The flood basalts in southwestern Ethiopia were emplaced in three phases, with a principal, spatially extensive eruptive phase that generated the Gamo-Mekonnen magmatic unit (Steiner *et al.*, 2022) during a ~10-Myr-long period between 38 and 27 Ma. Using geochemical characteristics, Steiner *et al* .(2022) showed that this phase of volcanism was particularly important due to the significant volumes of magma that must have moved through the magmatic plumbing system compared to prior magmatic phases. Such massive volcanism suggests lithospheric weakening through magmatic diking (*e.g.*, Buck, 2006), which thermally preconditioned the lithosphere for subsequent stretching (Steiner *et al.*, 2022). The mechanical strength of rocks in this region and farther south in Kenya may have been further reduced by the existence of NNE-SSW-striking Neoproterozoic basement fabrics that facilitated rift-parallel fracture propagation and normal faulting (*e.g.*, Morley, 1992; Bosworth and Morley, 1994; Hetzel and Strecker, 1994; Ebinger, 2000; Corti, 2013; Philippon *et al.*, 2014).

Overall, the thermal modeling results obtained from spatially distributed samples along and across the footwall blocks of the Chew Bahir Basin and Gofa Province suggest synchronous, tectonically driven crustal cooling. For example, time-temperature histories from samples located across the NW-SE-oriented flank of the Mali-Dancha (M1-2) and from along the Bala-Kela (K-6) basins appear to record the onset of cooling at rates of >2 °C/Myr between 27 and 21 Ma (Fig. 3.5b and d), supporting a previously inferred regional onset of faulting at ~20 ± 2 Ma (Pik *et al.*, 2008). Based on sample M-9, which was collected from the base of the rift flank at the transition zone between the Mali-Dancha and Bala-Kela basins (A.21), a consistent trend of protracted rapid cooling (~3.1 °C/Myr) that initiated at ~23 Ma was observed. Moreover, the synchronous onset of cooling across the BRZ following spatially extensive regional volcanism between 38 and 27 Ma (Steiner *et al.*, 2022) predates the onset of Nubia-Somalia plate motion at ~20 Ma (Iaffaldano *et al.*, 2014; DeMets and Merkouriev, 2016), suggesting that crustal weakening via magmatic diking (*e.g.*, Buck, 2006; Kendall and Bertelloni, 2016), possibly accompanied by the effects of mantle-drag forces (*e.g.*, Ebinger *et al.*, 2000, Brune *et al.*, 2023), may have triggered synchronous faulting across the BRZ at ~22 ± 3 Ma (Fig. 3.6). As shown above, following the spatially diffuse faulting in the BRZ, deformation progressively became more localized within a narrow zone

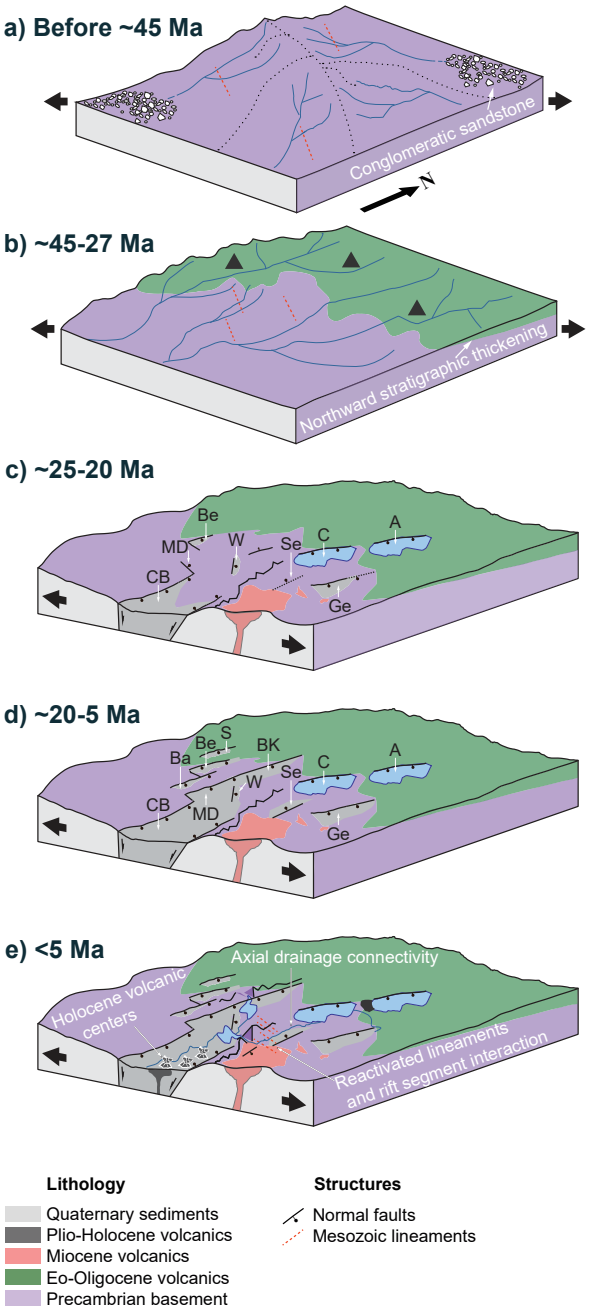

Figure 3.8: Evolutionary tectonic model for the BRZ: (a) spatially restricted, NW-SE-trending local relief developed during the late Cretaceous and prior to ~45 Ma; (b) prolonged massive volcanism (45–27 Ma; Steiner *et al.*, 2022); (c) diffuse faulting and isolated rift-basin development (CB: Chew Bahir, MD: Mali-Dancha, Be: Beto, W: Weyito, Ba: Baneta, BK: Bala-Kela, Se: Segen, C: Chamo, A: Abaya and Ge: Gelana) after the end of flood-basalt emplacement; (d) migration of deformation toward a narrow zone of the rift and northward fault propagation; (e) strain localization in the southern Gofa Province and Chew Bahir Basin, and tectonic interaction between the Chew Bahir Basin and the sMER. The red arrows indicate regional kinematic changes from the Cretaceous (~NW-SE) to the present (~E-W). The black arrow denotes extension direction.

and propagated toward the northern Gofa Province over time (Figs. 3.2b and 3.6). Modeling results obtained from samples B-2 and B-3 that were collected at different structural positions across the NE-SW-striking Baneta margin suggest rapid cooling to have started at ~15 Ma, with a rate of ~5 °C/Myr (Fig. 3.5a and b). Additionally, samples M-7 and M-8 from locations at the Mali-Dancha Basin escarpment (Baneta halfgraben) record the onset of rapid cooling at ~9 Ma, with rates of >~20 °C/Myr (Fig. 3.5b). These results may indicate that extensional faulting occurred in the Baneta halfgraben area during the middle Miocene. The geological cross sections constructed across the rift in the BRZ reveal a similar basinward migration of faulting over time (Fig. 3.3). The significant increase in tectonically related crustal cooling during the formation of the Baneta halfgraben between ~15 and 9 Ma thus suggests basinward strain localization during that interval (Fig. 3.2b), a phenomenon that has also been observed in other extensional regions during advanced rifting (*e.g.*, Morton *et al.*, 1979; Baker *et al.*, 1988; Agostini *et al.*, 2011; Melnick *et al.*, 2012). Similarly, in the Gelana and Chamo basins faulting has evolved from more diffuse spatial patterns toward locally focused extension in the center of the basins at ~13 Ma and during the Quaternary, respectively (Levitte *et al.*, 1974; Ebinger *et al.*, 1993; Balestraile *et al.*, 2016; Boone *et al.*, 2019).

The basinward migration of deformation in the southern Gofa Province propagated farther toward the Bala-Kela Basin in the late Miocene at ~6 Ma. To the west of the Bala-Kela Basin, consistent spatiotemporal patterns regarding the onset of faulting between the southwestern (20–17 Ma) and northwestern (8–6 Ma) Beto Basin margin have been reported by Boone *et al.*(2019) and demonstrate temporal variation in the onset of faulting between the southern and northern Gofa Province.

The discontinuous onset of faulting in the southern and northern parts of the Gofa Province may suggest that lateral fault propagation stalled during the growth of the rift basins. Fault-propagation patterns in such settings may be modified and influenced by many factors, including stratigraphic layer thickening (Benedicto *et al.*, 2003), rheological contrasts (Roche *et al.*, 2012), and the effects of inherited deformation fabrics (Camanni *et al.*, 2019; Corti, 2008; Molnar *et al.*, 2019). In particular, the presence of pre-existing deformation fabrics oriented at a high angle with respect to the developing rift may inhibit fault propagation (*e.g.*, Molnar *et al.*, 2019). Using the results of a seismic tomographic study, Kounoudis *et al.* (2021) imaged a NW-SE-trending pervasive band of high seismic-wave speeds below the southern Gofa Province and the northern Chew Bahir Basin. The authors conclude that the ~40-km-wide zone has a sharp, nearly vertical boundary that consistently follows the trend of structures inferred to be related to the Anza Rift. Interestingly, this region also coincides with an increase in surface topography (>1.5 km) attributed to northward thickening of the Eo-Oligocene flood basalts (Davidson, 1983), possibly suggesting a lithospheric strength contrast between the southern and northern sectors of the Gofa Province. The presence of these inherited heterogeneities between the basins might have significantly influenced the northward propagation of deformation and hence resulted in spatial disparity with regard to the onset of faulting. Thermal modeling results from the southern and northern Gofa Province exhibit this disparity in the onset of cooling. The southern Gofa

Province samples M7-8 record an onset of protracted rapid cooling at ~9 Ma, whereas sample K-1 from the northern Gofa Province documents a late Miocene (~6 Ma) onset of rapid cooling following a prior slow-cooling episode through the AHePRZ (Fig. 3.5a). The nature of crustal cooling in these areas is interpreted to reflect the Cenozoic extensional reactivation of these anisotropies. Therefore, we propose that the spatial disparity in the onset of rapid cooling between the southern and northern sectors of the Gofa Province may explain the current basin architecture, i.e., a wider and deeper basin in the south resulting from earlier rifting and a narrow basin in the north related to a later onset of rifting. A northward decrease in fault displacement (Fig. 3.3) and Quaternary fault-scarp characteristics that indicate ongoing tectonic activity along the Bala-Kela margin of the northern Gofa Province (Erbello *et al.*, 2022) is consistent with the recent onset of rapid cooling along the western margin of the Bala-Kela Basin.

The basinward shift in deformation and northward propagation of faulting during late-stage rifting temporally corresponds with a renewed pulse in volcanism. Phonolite eruptive centers aligned parallel to the orientation of the Mali-Dancha and Bala-Kela basins were active between 16 and 12 Ma (Davidson, 1980). Farther to the east, along the strike of the Gamo-Gidole margin, eruptive centers of the Getera-Kela basalts dated between 18 and 12 Ma (Ebinger *et al.*, 2000; George *et al.*, 2002) suggest that faulting may have been accompanied by magmatism during late-stage rifting; however, strain accommodation in that region was mainly through slip along the border faults during this period (Ebinger *et al.*, 2000). Pliocene-Holocene volcanic activity following the orientation of the Omo Valley (Jicha and Brown, 2014), the southeastern margin of the Chew Bahir Basin (Ebinger *et al.*, 2000), and the sMER (Corti *et al.*, 2013a; Philippon *et al.*, 2014) furthermore emphasize the importance of magmatism during rifting within the BRZ. For regions farther south, in the southern Turkana Rift, Rooney *et al* .(2022) suggested migration of deformation toward a narrow zone accompanied by spatially focused magmatism. Similarly, a recent structural and geochronological study in the nKR documented a significant influence of magmatism associated with Quaternary strain localization within the inner graben of the rift (Riedl *et al.*, 2022), similar to observations made in the central and southern sectors of the Kenya Rift (Baker *et al.*, 1986, 1988; Strecker *et al.*, 1990).

Taken together, our new thermochronological data and modeling results recording diffuse initial faulting at ~22 ± 3 Ma are consistent with earlier studies that inferred synchronous faulting within the BRZ (Boone *et al.*, 2019) at ~20 ± 2 Ma (Pik *et al.*, 2008), and the migration of deformation toward the northern Gofa Province over time (Bonini *et al.*, 2005; Philippon *et al.*, 2014; Balestraile *et al.*, 2016; Boone *et al.*, 2019). Furthermore, our high-resolution data suggests that initial diffuse faulting followed the end of massive volcanism between ~45 and 27 Ma (Fig. 3.6). Moreover, the documented crustal cooling associated with faulting in the Chew Bahir Basin and the Gofa Province reveals a close temporal relationship with regional pulses in magmatism (Fig. 3.6), and thus supports the notion of magma-assisted continental rifting suggested elsewhere in the EARs (*e.g.*, Kendall *et al.*, 2005; Rooney *et al.*, 2020c).

3.6 Conclusions

The combination of low-temperature thermochronological apatite and zircon (U-Th)/He data, thermal modeling results, structural information extracted from high-resolution TanDEM-X data in southern Ethiopia, as well as published regional $^{40}Ar/^{39}Ar$ data and seismicity data, provide insight into the tectono-geomorphic evolution of the Chew Bahir Basin and the Gofa Province from the Paleogene to the present (Fig. 3.8). Additionally, our study helps to characterize the nature of tectonic interaction between the sMER and nKR. The main outcomes of the study are summarized below.

1. The NW-SE-trending high topography in the BRZ may have been linked to the opening of the Anza Rift in northern Kenya, suggesting it was the source area for the spatially restricted Paleogene Turkana Grits in northern Kenya and compositionally similar conglomeratic sandstones in the sMER.
2. Spatially diffuse faulting associated with tectonically controlled rapid crustal cooling at ~22 ± 3 Ma corresponds with the end of ubiquitous flood-basalt volcanism, which was active between 45 and 27 Ma (Steiner *et al.*, 2022). This suggests that faulting initiated after the emplacement of flood basalts, supporting the notion of crustal weakening through volcanism during active rifting.
3. The migration of deformation along a narrow zone of the Gofa Province between ~15 and 9 Ma corresponds to a renewed pulse in volcanism (18–12 Ma), suggesting a progressive change in deformation mechanisms from tectonic faulting to magma-assisted rifting. The propagation of faulting toward the northern Gofa Province at ~6 Ma reflects a temporal north-to-south variation in rift-basin development, likely due to inherited crustal anisotropies and the northward increase in thickness of the Eo-Oligocene flood basalts.
4. Tectonic interaction between the sMER and nKR began during the early Pliocene and was facilitated by reactivation of the NW-SE-striking zones of weakness in the basement that are inferred to have formed during Cretaceous extensional processes associated with the Anza Rift.

3.7 References

Abbey, A.L., Wildman, M., Stevens Goddard, A.L., and Murray, K.E. (2023), Thermal history modeling techniques and interpretation strategies: Applications using QTQt. Geosphere, 19(2), 493-530. doi: 10.1130/GES02528.1

Aitken, A.R.A., Smithies, R.H., Dentith, M.C., Joly, A., Evans, S., and Howard, H.M. (2013), Magmatism-dominated intracontinental rifting in the Mesoproterozoic: The Ngaanyatjarra Rift, central Australia. Gondwana Research, 24(4), 886-901. doi: 10.1016/j.gr.2012.10.003

Agostini, A., Bonini, M., Corti, G., Sani, F., and Mazzarini, F. (2011), Fault architecture in the main Ethiopian rift and comparison with experimental models: implications for rift evolution and Nubia-Somalia kinematics. Earth and Planetary Science Letters, 301, 479-492. doi:10.1016/j.epsl.2010.11.024

Asfaw, L.M. (1990), Implication of shear deformation and earthquake distribution in the East African Rift between 4°N and 6°N. Journal of African Earth Sciences, 10(4), 745-751. doi: 10.1016/0899-5362(90)90041-C

Asrat, A., and Barbey, P. (2003), Petrology, geochronology and Sr-Nd isotopic geochemistry of the Konso pluton, south-western Ethiopia: Implications for transition from convergence to extension in the Mozambique Belt. International Journal of Earth Sciences, 92(6), 873-890. doi:10.1007/s00531-003-0360-9

Ayele, A., and Arvidsson, R. (1997), Fault mechanisms and tectonic implication of the 1985-1987 earthquake sequence in south-western Ethiopia. Journal of Seismology, 1(4), 383-394. doi:10.1023/A:1009774331917

Baker, B.H., Mitchell, J.G, and Williams, L.A. (1988), Stratigraphy, geochronology and volcano-tectonic evolution of the Kedong-Naivasha-Kinangop, Gregory Rift Valley, Kenya. Journal of the Geological Society, 145, 107-116. doi:10.1144/gs.jgs.145.1.0107

Baker, B.H. (1986), Tectonics and volcanism of the southern Kenya Rift Valley and its influence on rift sedimentation. Geological Society London, Special Publications. 25, 45–57. doi: 10.1144/gsl.sp.1986.025.01.05.

Baker, B.H., and Morgan, P. (1981), Continental rifting: Progress and outlook. Eos, Transactions American Geophysical Union, 62(29), 585-587. doi: 10.1029/e0062i029p00585-01

Balestrieri, M.L., Bonini, M., Corti, G., Sani, F., and Philippon, M. (2016), A refinement of the chronology of rift-related faulting in the Broadly Rifted Zone, southern Ethiopia, through apatite fission-track analysis. Tectonophysics, 671, 42–55. doi: 10.1016/j.tecto.2016.01.012

Benedicto, A., Schultz, R.A., and Soliva, R. (2003), Layer thickness and the shape of faults. Geophysical Research Letters, 30(20), 1-4. doi: 10.1029/2003GL018237

Bialas., R.W., Buck, R., and Qin, R. (2010), How much magma is required to rift a continent? Earth and Planetary Science Letters, 292, 68-78. doi: 10.1016/j.epsl.2010.01.021

Bonini, M., Corti, G., Innocenti, F., Manetti, P., Mazzarini, F., Abebe, T., and Pecskay, Z. (2005), Evolution of the Main Ethiopian Rift in the frame of Afar and Kenya rifts propagation. Tectonics, 24(1), 1-21. doi: 10.1029/2004TC001680

Boone, S.C., Balestrieri, M.L., Kohn, B.P., Corti, G., Gleadow, A.J.W., and Seiler, C. (2019), Tectonothermal evolution of the Broadly Rifted Zone, Ethiopian Rift. Tectonics, 38(3), 1070-1100. doi: 10.1029/2018TC005210

Bosworth, W., and Morley, C.K. (1994), Structural and stratigraphic evolution of the Anza rift, Kenya. Tectonophysics, 236(4), 93-115. doi:10.1016/0040-1951(94)90171-6

Bosworth, W., Huchon, P., and McClay, K. (2005), The Red Sea and Gulf of Aden Basins. In Phanerozoic Evolution of Africa. Edited by Catuneanu, R., Guiraud, P., Eriksson, B., Thomas, R., Shone., and R. Key. Journal of African Earth Sciences, 43, 334-378.

Bosworth, W., and Stockli, D.F. (2016), Early magmatism in the greater Red Sea rift: timing and significance. Canadian Journal of Earth Sciences, 53(11), 1158-1176. doi: 10.1139/cjes-2016-0019

Brown, R.W., Beucher, R., Roper, S., Stuart, F., and Persano, C. (2013), Natural age dispersion arising from the analysis of broken crystals: Part II. Practical application to apatite (U-Th)/He thermochronometry. Geochimica et Cosmochimica Acta, 120, 395-416. doi: 10.1016/j.gca.2013.05.042

Brune, S., Corti, G., and Ranalli, G. (2017), Controls of inherited lithospheric heterogeneity on rift linkage: Numerical and analog models of interaction between the Kenyan and Ethiopian rifts across the Turkana depression. Tectonics, 36, 1767–1786. doi: 10.1002/2017TC004739

Brune, S., Kolawole, F., Olive, J.A., Stamps, D.S., Buck, W.R., Buiter, S.J.H., Furman, T., and Shillington, D.J. (2023), Geodynamics of continental rift initiation and evolution. Nature Reviews Earth and Environment, 4, 235-253. doi: 10.1138/s43017-023-00391-3

Buck, W.R. (2006), The role of magma in the development of the Afro-Arabian Rift System. Geological Society London, Special Publications, 259(1), 43-54. doi: 10.1144/GSL.SP.2006.259.01.05

Buiter, S. J. H., Brune, S., Keir, D., and Peron-Pinvidic, G. (2022), Rifting continents. EGUsphere [preprint], doi: 10.5194/egusphere-2022-139, 2022

Camanni, G., Roche, V., Childs, C., Manzocchi, T., Walsh, J., Conneally, J., Saqab, M.M., and Delogkos, E. (2019), The three-dimensional geometry of relay zones within segmented normal faults. Journal of Structural Geology, 129, 1-45. doi: 10.1016/j.jsg.2019.103895

Chorowicz, J. (2005), The East African rift system. Journal of African Earth Sciences, 43(3), 379-410. doi:10.1016/j.jafrearsci.2005.07.019

Colleps, C. L., McKenzie, N. R., Guenthner, W. R., Sharma, M., Gibson, T. M., and Stockli, D. F., (2021), Apatite (U-Th)/He thermochronometric constraints on the northern extent of the Deccan large igneous province. Earth and Planetary Science Letters, 571, 1-13. doi: 10.1016/j.epsl.2021.117087

Corti, G. (2008), Control of rift obliquity on the evolution and segmentation of the main Ethiopian rift. Nature Geoscience, 1(4), 258-262. doi: 10.1038/ngeo160

Corti, G., Sani, F., Philippon, M., Sokoutis, D., Willingshofer, E., and Molin, P. (2013), Quaternary volcano-tectonic activity in the Soddo region, western margin of the southern Main Ethiopian Rift. Tectonics, 32, 861-879. doi: 10.1002/tect.20052, 2013

Corti, G., Cioni, R., Franceschini, Z., Sani, F., Scaillet, S., Molin, P., Isola, I., Mazzarini, F., Brune, S., Keir, D., Erbello, A., Muluneh, A., Illsley-Kemp, F., and Glerum, A. (2019), Aborted propagation of the Ethiopian rift caused by linkage with the Kenyan rift. Nature Communications, 10(1), 1-11. doi: 10.1038/s41467-019-09335-2

Courtillot, V., Jaupart, C., Manighetti, I., Tapponnier, P., and Besse, J. (1999), On causal links between flood basalts and continental breakup. Earth and Planetary Science Letters, 166, 177–195. doi: 10.1016/S0012-821X(98)00282-9

Courtillot, V.E., and Renne, P.R. (2003), On the ages of flood basalt events. Comptes Rendus Geoscience, 335 (1), 113-140, doi: 10.1016/S1631-0713(03)00006-3

Davidson, A. (1983), The Omo River Project, reconnaissance geology and geochemistry of parts of Ilubabor, Kefa, Gamu Gofa, and Sidamo. Ministry of Mines and Energy, Ethiopian Institute Geological Survey Bulletin, 2, 1-89

Davidson, A., and Rex, D.C. (1980), Age of volcanism and rifting in southwestern Ethiopia. Nature, 283, 657-658. doi: 10.1038/283657a0

deMenocal, P.B. (2004), African climate change and faunal evolution during the Pliocene-Pleistocene. Earth and Planetary Science Letters, 220(2), 3-24. doi: 10.1016/S0012-821X(04)00003-2

DeMets, C., and S. Merkouriev, S. (2016), High-resolution estimates of Nubia–Somalia plate motion since 20 Ma from reconstructions of the Southwest Indian Ridge, Red Sea and Gulf of Aden. Geophysical Journal International, 207(1), 317–332. doi: 10.1093/gji/ggw276

de Wit, M.J., and Chewaka, S. (1981), Plate tectonic evolution of Ethiopia and the origin of its mineral deposits: an overview. In Plate tectonics and metallogenesis: some guidelines to Ethiopian mineral deposits. Edited by Chewaka, S., and de Wit, M.J. Ethiopian Institute of Geological Survey Bulletin, 2, 115-129

Dodson, M.H. (1973), Closure temperature in cooling geochronological and petrological systems. Contributions to Mineralogy and Petrology, 40(3), 259-274. doi: 10.1007/BF00373790

Dommain, R., Riedl, S., Olaka, L.A., DeMenocal, P., Deino, A.L., Owen, R.B., Muiruri, V., Müller, J., Potts, R., and Strecker, M.R. (2022), Holocene bidirectional river system along the Kenya Rift and its influence on East African faunal exchange and diversity gradients. Proceedings of the National Academy of Sciences, 119(28). doi: 10.1073/pnas.2121388119

Ebinger, C., and Scholz, C.A. (2012), Continental rift basins: the East African perspective. In: Busby, C. and Azor, A. (eds): Tectonics of Sedimentary Basins: Recent Advances. Wiley, 185–208, doi: 10.1002/9781444347166.ch9

Ebinger, C.J., Yemane, T., Harding, D.J., Tesfaye, S., Kelley, S., and Rex, D.C. (2000), Rift deflection, migration, and propagation: Linkage of the Ethiopian and Eastern rifts, Africa. Geological Society of America Bulletin, 112(2), 163–176. doi: 10.1130/0016-7606(2000)112<163:RDMAPL>2.0.CO;2

Ebinger, C.J., Jackson, J.A., Foster, A.N., and Hayward, N.J. (1999), Extensional basin geometry and the elastic lithosphere: Philosophical Transactions Royal Society London, 357, 741–765. doi: 10.1098/rsta.1999.0351

Ebinger, C.J., Yemane, T., WoldeGabriel, G., Aronson, J.L., and Walter, R.C. (1993), Late Ecocene-Recent volcanism and faulting in the southern main Ethiopian rift. Journal of the Geological Society, 150(1), 99–108. doi: 10.1144/gsjgs.150.1.0099

Emishaw, L., and Abdelsalam, M.G. (2019), Development of Late Jurassic-Early Paleogene and Neogene-Quaternary rifts within the Turkana Depression, East Africa. Tectonics, 38, 2358–2377. doi: 10.1029/2018TC005389

Erbello, A., and Kidane, T. (2018), Timing of volcanism and initiation of rifting in the Omo-Turkana depression, southwest Ethiopia: Evidence from paleomagnetism. Journal of African Earth Sciences, 139, 319-329. doi: 10.1016/j.jafrearsci.2017.12.031

Erbello, A., Melnick, D., Zeilinger, G., Bookhagen, B., Pingel, H., and Strecker, M.R. (2022), Geomorphic expression of a tectonically active rift-transfer zone in southern Ethiopia. Geomorphology, 403, 1-20. doi: 10.1016/j.geomorph.2022.108162

Erbello, A., Colleps, C., Melnick, D., Sobel, E., Bookhagen, B., Pingel, H., Zeilinger, G., Van der Beek, P., and Strecker, M.R. (2022, October), Magma-assisted continental rifting: The broadly rifted zone in SW Ethiopia, East Africa [data set]. Zenodo. https://doi.org/10.5281/zenodo.7855434

Farley, K.A. (2002), (U-Th)/He dating: Techniques, calibrations, and applications. Reviews in Mineralogy and Geochemistry, 47(1), 819-844. doi: 10.2138/rmg.2002.47.18

Farley, K.A. (2000), Helium diffusion from apatite: General behavior as illustrated by Durango fluorapatite. Journal of Geophysical Research: Solid Earth, 105(2), 2903-2914. doi: 10.1029/1999jb900348

Farley, K.A., Wolf, R.A., and Silver, L.T. (1996), The effects of long alpha-stopping distances on (U-Th)/He ages. Geochimica et Cosmochimica Acta, 60(21), 4223-4229. doi: 10.1016/S0016-7037(96)00193-7

Flowers, R.M., Ketcham, R.A., Shuster, D.L., and Farley, K.A. (2009), Apatite (U-Th)/He thermochronometry using a radiation damage accumulation and annealing model. Geochimica et Cosmochimica Acta, 73(8), 2347-2365. doi: 10.1016/j.gca.2009.01.015

Foster, A., and Jackson, J. (1998), Source parameters of large African Earthquakes: Implications for rheology and kinematics. Geophysical Journal International, 134(2), 422–448. doi: 10.1046/j.1365-246x.1998.00568.x

Foster, D.A., and Gleadow, A.J.W. (1996), Structural framework and denudation history of the flanks of the Kenya and Anza Rifts, East Africa. Tectonics, 15(2), 258-271. doi: 10.1029/95TC02744

Fox, M., Dai, J.G., Carter, A., 2019. Badly behaved detrital (U-Th)/He ages: problems with He diffusion models or geological models? Geochemistry, Geophysics, Geosystems, 20(5), 2418–2432. doi: 10.1029/2018GC008102

Gallagher, K. (2012), Transdimensional inverse thermal history modeling for quantitative thermochronology. Journal of Geophysical Research: Solid Earth, 117, 1-16. doi: 10.1029/2011JB008825

Gallagher, K. (2018), Comment on ''Thermal history modelling: HeFTy vs. QTQt" by Vermeesch and Tian, Earth-Science Reviews (2014), 139, 279-290. Earth-Science Reviews, 176, 387-394. doi: 10.1016/j.earscirev.2017.11.001

Galetto, A., Georgieva, V., García, V.H., Zattin, M., Sobel, E.R., and Glodny, J. (2021), Cretaceous and Eocene rapid cooling phases in the southern Andes (36°–37°S): Insights from low-temperature thermochronology, U-Pb geochronology, and inverse thermal modelling from Domuyo area, Argentina. Tectonics, 40(6), 1-30. doi: 10.1029/2020TC006415

Guenthner, W. R., Reiners, P. W., Ketcham, R. A., Nasdala, L., and Giester, G. (2013), Helium diffusion in natural zircon: Radiation damage, anisotropy, and the interpretation of zircon (U-Th)/He thermochronology. American Journal of Science, 313, 145–198. doi: 10.2475/03.2013.01

Guenthner, W. R. (2021), Implementation of an alpha damage annealing model for zircon (U-Th)/He thermochronology with comparison to a zircon fission track annealing model. Geochemistry, Geophysics, Geosystems, 22 (2). doi: 10.1029/2019GC008757.

Gautheron, C., Tassan-Got, L., Ketcham, R.A., and Dobson, K.J. (2012), Accounting for long alpha-particle stopping distances in (U-Th-Sm)/He geochronology: 3D modeling of diffusion, zoning, implantation, and abrasion. Geochimica et Cosmochimica Acta, 96, 44-56. doi: 10.1016/j.gca.2012.08.016

George, R., Rogers, N., Kelley, S. (1998), Earliest magmatism in Ethiopia: Evidence for two mantle plumes in one flood basalt province. Geology, 26(10), 923-926. doi: 10.1130/0091-7613(1998)026<0923:EMIEEF>2.3.CO;2

George, R.M., and Rogers, N.W. (2002), Plume dynamics beneath the African plate inferred from the geochemistry of the Tertiary basalts of southern Ethiopia. Contributions to Mineralogy and Petrology, 144, 286–304. doi: 10.1007/s00410-002-0396-z

Gichile, S. (1992), Granulites in the Precambrian basement of southern Ethiopia: geochemistry, P-T conditions of metamorphism and tectonic setting. Journal of African Earth Sciences, 15(2), 251-263. doi: 10.1016/0899-5362(92)90072-K

Gouin, P. (1979), Earthquake history of Ethiopia and the Horn of Africa. Geophysical Observatory, University of Addis Ababa, Addis Ababa, 177-188.

Guenthner, W.R., Reiners, P.W., Ketcham, R.A., Nasdala, L., and Giester, G. (2013), Helium diffusion in natural zircon: Radiation damage, anisotropy, and the interpretation of zircon (U-Th)/He thermochronology. American Journal of Science, 313(3), 145-198. Geochimica et Cosmochimica Acta, 96, 44-56. doi: 10.2475/03.2013.01

Haileab, B., Brown, F.H., McDougall, I., and Gathogo, P.N. (2004), Gombe Group basalts and initiation of Pliocene deposition in the Turkana depression, northern Kenya and southern Ethiopia. Geological Magazine, 141(1), 41-53. doi: 10.1017/S001675680300815X

Hetzel, R., and Strecker, M.R. (1994), Late Mozambique Belt structures in western Kenya and their influence on the evolution of the Cenozoic Kenya Rift. Journal of Structural Geology, 16(2), 189-201. doi: 10.1016/0191-8141(94)90104-X

Hill, R.I. (1991), Starting plumes and continental break-up. Earth and Planetary Science Letters, 104, 398-416. doi: 10.1016/0012-821X(91)90218-7

Iaffaldano, G., Hawkins, R., and Sambridge, M. (2014), Bayesian noise-reduction in Arabia/ Somalia and Nubia/Arabia finite rotations since ~20 Ma: Implications for Nubia/Somalia relative motion. Geochemistry, Geophysics, Geosystems, 15(4), 845–854, doi: 10.1002/2013GC005089

Jicha, R.B., and Brown, H.F. (2014), An age for the Korath Range, Ethiopia and the viability of 40Ar/39Ar of kaersutite in Late Pleistocene volcanics. Quaternary Geochronology, 21, 53-57. doi: 10.1016/j.quageo.2013.03.007

Kazmin, V., Shifferaw, A., and Balcha, T. (1978), The Ethiopian basement: Stratigraphy and possible manner of evolution. Geologische Rundschau, 67(2), 531-546. doi: 10.1007/BF01802803

Knappe, E., Bendick, R., Ebinger, C., Birhanu, Y., Lewi, E., Floyd, M., King, R., Kianji, G., Mariita, N., Temtime, T., Waktola, B., Deresse, B., Musila, M., Kanoti, J., and Perry, M. (2020), Accommodation of East African rifting across the Turkana depression. Journal of Geophysical Research: Solid Earth, 125(2), 1-13. doi: 10.1029/2019JB018469

Kounoudis, R., Bastow, I.D., Ebinger, C.J., Ogden, C.S., Ayele, A., Bendick, R., Mariita, N., Kianji, G., Wigham, G., Musila, M., and Kibret, B. (2021), Body-wave tomographic imaging of the Turkana depression: Implications for rift development and plume-lithosphere interactions. Geochemistry, Geophysics, Geosystems, 22(8), 1-27. doi: 10.1029/2021GC009782

Kendall, J.M., and Bertelloni, C.L. (2016), Why is Africa rifting? Geological Society London, Special Publications, 420(1), 11-30. doi: 10.1144/SP420.17

Ketcham, R. A. (2005), Forward and inverse modeling of low-temperature thermochronometry data: Low-Temperature thermochronology: techniques, interpretations, and applications. Reviews in Mineralogy and Geochemstry, 58(1), 275-314. doi: 10.2138/rmg.2005.58.11

Levitte, D., Columba, J., and Mohr, P. (1974), Reconnaissance geology of the Amaro horst, southern Ethiopia Rift. Geological Society of America Bulletin, 85, 417-422

Mamo, T. (2012), Analysis of gravity field to reconstruct the structure of Omo basin in SW Ethiopia and implications for hydrocarbon potential. Marin and Petroleum Geology, 29, 104-114. doi: 10.1016/j.marpetgeo.2011.08.013

McCune, A.R., Thomson, K.S. and Olsen, P.E. (1984), Semiontid fishes from the Mesozoic great lakes of North America. Echelle, A. A. and Kornfield, I. (eds.), evolution of species flocks. University of Maine at Orono Press, Orono, p. 27-44

McKenzie, D. (1978), Some remarks on the formation of sedimentary basins. Earth Planetary Science Letters, 40, 25–32. doi: 10.1016/0012-821X(78)90071-7

Mége, D., Purcell, P., Pochat, S., and Guidat, T. (2015), The landscape and landforms of the Ogaden, south-east Ethiopia. In landscapes and landforms of Ethiopia. edited by Billi, P. World Geomorphological Landscapes, 323 – 348. doi: 10.1007/978-94-017-8026-1_19

Melnick, D., Garcin, Y., Quinteros, J., Strecker, M.R., Olago, D., Tiercelin, J.-J. (2012), Steady rifting in northern Kenya inferred from deformed Holocene lake shorelines of the Suguta and Turkana basins. Earth and Planetary Science Letters, 331–332, 335–346. doi.org/10.1016/j.epsl.2012.03.007

Molnar, N.E., Cruden, A.R., and Betts, P.G. (2019), Interactions between propagating rifts and linear weaknesses in the lower crust. Geosphere, 15(5), 1617-1640. doi:10.1130/GES02119.1

Morgan, P., and Baker, H.B. (1983), Processes of continental rifting. Developments in Geotectonics, 19, 1-10. doi: 10.1016/B978-0-444-42198-2.50007-9

Morley, C.K., Nelson, R.A., Patton, T.L., and Munn, S.G. (1990), Transfer zones in the East African rift system and their relevance to hydrocarbon exploration in rifts. American Association of Petroleum Geologists Bulletin, 74(8), 1234-1253. doi: 10.1306/0c9b2475-1710-11d7-8645000102c1865d

Morley, C.K., Wescott, W.A., Stone, D.M., Harper, R.M., Wigger, S.T., and Karanja, F.M. (1992), Tectonic evolution of the northern Kenyan Rift. Journal of the Geological Society, 149(3), 333-348. doi: 10.1144/gsjgs.149.3.0333

Mortimer, E., Kirstein, L.A., Stuart, F.M., and Strecker, M.R. (2016), Spatio-temporal trends in normal-fault segmentation recorded by low-temperature thermochronology: Livingstone fault scarp, Malawi Rift, East African Rift System. Earth and Planetary Science Letters, 455, 62-72. doi: 10.1016/j.epsl.2016.08.040

Morton, W.H, Rex, D.C, Mitchell, J.G., and Mohr, P. (1979), Riftward younging of volcanic units in the Addis Ababa region, Ethiopian rift valley. Nature, 280, 284-288. doi: 10.1038/280284a0

Muirhead, J.D., Scholz, C.A., and Rooney, T.O. (2022), Transition to magma-driven rifting in the south Turkana Basin, Kenya: Part I. Journal of the Geological Society, 176(6), 1-15. doi: 10.1144/jgs2021-159

Murray-Hughes, R. (1933), Notes on the geological succession, tectonics and economic geology of the Western half of the Kenya colony. Geological Survey of Kenya, 3

Murray, K.E., Stevens Goddard, A.L., Abbey, A.L., and Wildman, M. (2022), Thermal history modeling techniques and interpretation strategies: Applications using HeFTy. Geosphere, 18(5), 16622-1642. doi: 10.1130/GES02500.1

Musila, M., Ebinger, C., Sullivan, G., Bastow, I., Bendick, R., Ogden, C., Kounoudis, R. (2022), Strain accommodation during continental rifting: mantle lithosphere matters. In: AGU Fall Meeting Abstracts

Olsen, K.H. (1995), Continental rifts: evolution, structure, tectonics. Tectonophysics, 271(3-4), 333-334. doi. 10.1016/s0040-1951(97)88191-7

Owusu Agyemang, P.C., Roberts, E.M., Downie, B., and Sertich, J.J.W. (2019), Sedimentary provenance and maximum depositional age analysis of the Cretaceous? Lapur and Muruanachok sandstones (Turkana Grits), Turkana Basin, Kenya. Geological Magazine, 156(8), 1334-1356. doi: 10.1017/S0016756818000663

Philippon, M., Corti, G., Sani, F., Bonini, M., Balestrieri, M.L., Molin, P., Willingshofer, E., Sokoutis, D., and Cloetingh, S. (2014), Evolution, distribution, and characteristics of rifting in southern Ethiopia. Tectonics, 33, 485–508. doi: 10.1002/2013TC003430

Pik, R., Marty, B., Carignan, J., and Lavé, J. (2003), Stability of the Upper Nile drainage network (Ethiopia) deduced from (U-Th)/He thermochronometry: Implications for uplift and erosion of the Afar plume dome: Earth and Planetary Science Letters, doi: 10.1016/ S0012-821X(03)00457-6.

Pik, R., Marty, B., Carignan, J., Yirgu, G., and Ayalew, T. (2008), Timing of East African Rift development in southern Ethiopia: Implication for mantle plume activity and evolution of topography. Geology, 36, 167–170. doi: 10.1130/G24233A.1

Prömmel, K., Cubasch, U., and Kaspar, F. (2013), A regional climate model study of the impact of tectonic and orbital forcing on African precipitation and vegetation. Palaeogeography, Palaeoclimatology, Palaeoecology, 369, 154-162. doi: 10.1016/j.palaeo.2012.10.015

Reiners, P.W., Farley, K.A., and Hickes, H.J. (2002), He diffusion and (U-Th)/He thermochronometry of zircon: Initial results from Fish Canyon Tuff and Gold Butte. Tectonophysics, 349(4), 297-308. doi: 10.1016/S0040-1951(02)00058-6

Richter, M. J. E. A., Brune, S., Riedl, S., Glerum, A., Neuharth, D., and Strecker, M. R. (2021), Controls on asymmetric rift dynamics: Numerical modeling of strain localization and fault evolution in the Kenya Rift. Tectonics, 40(5), e2020TC006553. doi: 10.1029/2020tc006553

Riedl, S., Melnick, D., Njue, L., Sudo, M., and Strecker, M. R. (2022), Mid-Pleistocene to recent crustal extension in the inner graben of the northern Kenya Rift. Geochemistry, Geophysics, Geosystems, 23(3), 1-25. doi: 10.1029/2021GC010123

Roche, V., Homberg, C., and Rocher, M. (2012), Architecture and growth of normal fault zones in multilayer systems: A 3D field analysis in the South-Eastern Basin, France. Journal of Structural Geology, 37, 19-35. doi: 10.1016/j.jsg.2012.02.005

Rooney, T.O., Wallace, P.J., Muirhead, J.D., Chiasera, B., Alex Steiner, R., Girard, G., Karson, J.A. (2022), Transition to magma-driven rifting in the southern Turkana Basin, Kenya: Part II. Journal of the Geological Society, 179, 1-19. doi: 10.6084/m9.figshare.c.6026627

Rooney, T.O. (2020c), The Cenozoic magmatism of East Africa: Part III – Rifting of the craton. Lithos, 105390. doi: 10.1016/j.lithos.2020.105390

Rooney, T.O. (2017), The Cenozoic magmatism of East-Africa: Part I. Flood basalts and pulsed magmatism. Lithos, 286-287, 264-301. doi: 10.1016/j.lithos.2017.05.014

Savage, R.J., and Williamson, P.G. (1978), The early history of the Turkana Depression. In geological background to Fossil Man: Recent research in the Gregory Rift Valley, East Africa. Edited by Bishop, W.W. Geological Society London, Special Publication. 6, 375-394

Saunders, A.D., Fitton, J.G., Kerr, A.C., Norry, M.J., and Kent, R.W. (1997), The North Atlantic Igneous Province. In: Mahoney, J.J., Coffin, M.E. (Eds.), Large Igneous Provinces: Continental, Oceanic. Planetary Flood Volcanism. Geophysical Monograph Series, 45-93.doi: 10.1029/GM100p0045

Sengor, A.M.C., and Burke, K. (1978), Relative timing of rifting on earth and its tectonic implications. Geophysical Research Letters, 5, 419-421. doi: 10.1029/GL005i006p00419

Spiegel, C., Kohn, B.P., Belton, D.X., and Gleadow, A.J.W. (2007), Morphotectonic evolution of the central Kenya rift flanks: Implications for late Cenozoic environmental change in East Africa. Geology, 35(5), 427. doi: 10.1130/G23108A.1

Steiner, R.A., Rooney, T.O., Girard, G., Rogers, N., Ebinger, C.J., Peterson, L., and Phillips, R.K. (2022), Initial Cenozoic magmatic activity in East Africa: new geochemical constraints on magma distribution within the Eocene continental flood basalt province, in: Geological Society London, Special Publications, 26. doi: 10.1144/SP518-2020-262

Strecker, M.R., Blisniuk, P.M., Eisbacher, G.H. (1990), Rotation of extension direction in the central Kenya Rift. Geology 18, 299–302. doi.org/10.1130/0091-7613(1990)018<0299:roedit>2.3.CO;2

Teklay, M., Kröner, A., Mezger, K., and Oberhänsli, R. (1998), Geochemistry, Pb-Pb single zircon ages and Nd-Sr isotope composition of Precambrian rocks from southern and eastern Ethiopia: Implications for crustal evolution in East Africa. Journal of African Earth Sciences, 62(2), 207-227. doi: 10.1016/S0899-5362(98)00006-2

Torres Acosta, V., Bande, A., Sobel, E.R., Parra, M., Schildgen, T.F., Stuart, F., and Strecker, M.R. (2015), Cenozoic extension in the Kenya Rift from low-temperature thermochronology: Links to diachronous spatiotemporal evolution of rifting in East Africa. Tectonics, 34(12), 2367-2386. doi: 10.1002/2015TC003949

Torsvik, T.H., and Cocks, L.M.R. (2005), Norway in space and time: a centennial cavalcade. Norwegian Journal of Geology, 85, 73–86

Vauchez, A., Barruol, G., and Tommasi, A. (1997), Why do continents break-up parallel to ancient orogenic belts? Terra Nova, 9(2), 62-66. doi: 10.1111/j.1365-3121.1997.tb00003.x

Vetel, W., and Le Gall, B. (2006), Dynamics of prolonged continental extension in magmatic rifts: The Turkana Rift case study (North Kenya). Geological Society London, Special Publications, 259(1), 209-233. doi: 10.1144/GSL.SP.2006.259.01.17

Vermeesch, P., and Tian, Y. (2014), Thermal history modelling: HeFTy vs QTQt. Earth Science Reviews, 139, 279-290. doi: 10.1016/j.earscirev.2014.09.010

Vermeesch, P. (2018), IsoplotR: A free and open toolbox for geochronology. Geoscience Frontiers, 9(5), 1479-1493. doi: 10.1016/j.gsf.2018.04.001

Walsh, J., and Dodson, R.G. (1969), Geology of Northern Turkana. Geological Survey of Kenya, 82

Watkins, R.T. (1986), Volcano-tectonic control on sedimentation in the Koobi Fora sedimentary basin, Lake Turkana. Geological Society London, Special Publications, 25, 85-95. doi: 10.1144/GSL.SP.1986.025.01.08

White, R., and McKenzie, D. (1989), Magmatism at rift zones: the generation of volcanic continental margins and flood basalts. Journal of Geophysical Research, 94(6), 7685-7729. doi: 10.1029/JB094iB06p07685

WoldeGabriel, G., Aronson, J.L., and Walter, R.C. (1990), Geology, geochronology, and rift basin development in the central sector of the Main Ethiopia Rift. Geological Society of America, Bulletin, 102(4), 439-458. doi: 10.1130/0016-7606(1990)102<0439:GGARBD>2.3.CO;2

WoldeGabriel, G., Yemane, T., Suwa, G., White, T., and Asfaw, B. (1991), Age of volcanism and rifting in the Burji-Soyoma area, Amaro Horst, southern Main Ethiopian Rift: geo- and biochronologic data. Journal of African Earth Sciences, 13(3), 437-447. doi: 10.1016/0899-5362(91)90107-A

Wolfenden, E., Ebinger, C., Yirgu, G., Deino, A., and Ayale, D. (2004), Evolution of the northern main Ethiopian rift: birth of a triple junction. Earth and Planetary Science Letters, 224(2), 213-228. doi: 10.1016/j.epsl.2004.04.022

Worku, H., and Schandelmeier, H. (1996), Tectonic evolution of the Neoproterozoic Adola Belt of southern Ethiopia: Evidence for a Wilson Cycle process and implications for oblique plate collision. Precambrian Research, 77(4), 179-210. doi: 10.1016/0301-9268(95)00054-2

Yibas, B., Reimold, W.U., Armstrong, R., Koeberl, C., Anhaeusser, C.R., and Phillips, D. (2002), The tectonostratigraphy, granitoid geochronology and geological evolution of the Precambrian of southern Ethiopia. Journal of African Earth Sciences, 34(2), 57-84. doi: 10.1016/S0899-5362(01)00099-9

Zhou, R., Schoenbohm, L. M., Sobel, E. R., Davis, D. W., and Glodny, J. (2017), New constraints on orogenic models of the southern Central Andean Plateau: Cenozoic basin evolution and bedrock exhumation. Geological Society of America Bulletin, 129(2), 152-170. doi: 10.1130/B31384.1

Chapter 4

Geomorphic expression of a tectonically active rift-transfer zone in southern Ethiopia

Erbello, A., Melnick, D., Zeilinger, G., Bookhagen, B., Pingel, H., and Strecker, M.R., 2022, Geomorphic expression of a tectonically active rift-transfer zone in southern Ethiopia.
This chapter has been published in Geomorphology, v. 403, 108162, doi:10.1016/j.geomorph.2022.108162

Abstract

The Gofa Province and the Chew Bahir Basin of southern Ethiopia constitute tectonically active regions, where the Southern Main Ethiopian Rift converges with the Northern Kenya Rift through a wide zone of extensional deformation with several north to northeast-trending, left-stepping en-échelon basins. This sector of the Southern Main Ethiopian Rift is characterized by a semi-arid climate and a largely uniform lithology, and thus provides ideal conditions for studying the different parameters that define the tectonic and geomorphic features of this complex kinematic transfer zone. In this study, the degree of tectonic activity, spatiotemporal variations in extension, and the nature of kinematic linkage between different fault systems of the transfer zone are constrained by detailed quantitative geomorphic analysis of river catchments and focused field work. We analyzed fluvial and landscape morphometric characteristics in combination with structural, seismicity, and climatic data to better evaluate the tectono-geomorphic history of this transfer zone. Our data reveal significant north-south variations in the degree of extension from the Sawula Basin in the north (mature) to the Chew Bahir Basin in the south (juvenile). First, normalized channel-steepness indices and the spatial arrangement of knickpoints in footwall-draining streams suggest a gradual, southward shift in extensional deformation and recent tectonic activity. Second, based on 1-km radius local relief and mean-hillslope maximum values that are consistent with k_{sn} anomalies, we confirm strain localization within zones of fault interaction. Third, morphometric indices such as hypsometry, basin asymmetry factor, and valley floor width to valley height ratio also indicate a north to south gradient in tectonic activity, highlighting the importance of such a wide transfer zone with diffuse extension linking different rift segments during the break-up of continental crust.

4.1 Introduction

Continental rift basins typically evolve from spatially limited areas of tectonic subsidence into topographically well expressed, often linear zones of extension with major basin-bounding normal faults, which may interact and ultimately link together before continental break-up and plate separation (Buck, 1991; Nelson *et al.*, 1992; Gupta *et al.*, 1998; Ebinger and Scholz, 2012). In advanced stages of extensional deformation major rift-bounding normal faults and formerly isolated extensional basins that may have existed during early phases of rifting often interact kinematically via structurally complex areas known as transfer zones (Rosendahl, 1987; Morley *et al.*, 1990; Nelson *et al.*, 1992; Koehn *et al.*, 2010; Zwaan and Schreurs, 2017, Zwaan and Schreurs, 2020). The kinematic interaction between such formerly isolated basins and their bounding faults results in characteristic topographic and tectonogeomorphic features that have long been recognized to reflect the spatial and temporal trends of rift propagation (*e.g.*, Penck, 1924; Gawthorpe and Leeder, 2000; Densmore *et al.*, 2007; Ebinger and Scholz, 2012).

Specifically, arid extensional environments, due to their generally good preservation of fault scarps and other tectono-geomorphic features, lend themselves to an assessment of rifting processes and their influence on landscape evolution as well as the current degree of tectonic activity (*e.g.*, Davis, 1899; Bull and McFadden, 1977; Leeder and Jackson, 1993; Gawthorpe *et al.*, 2003). Therefore, in addition to tectonically controlled rift-sedimentation patterns through time, the analysis of morphologic indicators retrieved from topographic features and landscape metrics provide excellent archives to decipher spatiotemporal trends in extensional processes. These metric indicators may include topographic relief (*e.g.*, Cowie, 1998; Goldsworthy and Jackson, 2000; Densmore, 2004), mean elevation and local relief (*e.g.*, Kirby *et al.*, 2007; Burbank and Anderson, 2011), normalized channel steepness indices of footwall streams (*e.g.*, Kirby and Whipple, 2012; Whittaker and Boulton, 2012), the distribution patterns of knickpoints along faults crossing main channels (*e.g.*, Boulton and Whittaker, 2009; Miller *et al.*, 2013; Gallen and Wegmann, 2017), and the frequency of slope breaks in longitudinal stream profiles (*e.g.*, Ewiak *et al.*, 2015). Additionally, morphometric indices including hypsometric integral, valley floor width to valley height ratio, and the basin-asymmetry factor have been successfully used to deduce spatial variations in tectonic activity (*e.g.*, Bull and McFadden, 1977; Ramírez-Herrera, 1998; El Hamdouni *et al.*, 2008; Pérez-Peña 2009b; Kothyari *et al.*, 2018; Bull, 2007).

The Cenozoic East African Rift System (Fig. 4.1) is an ideal place to analyze the spatiotemporal characteristics of geomorphic features that reflect ongoing regional tectonics with different stages of rift development (Chorowicz, 2005; Ebinger and Scholz, 2012). The eastern branch of the East African Rift System extends from the region south of Afar to Malawi and comprises several structurally complex segments where deformation between offset extensional structures is accommodated within oblique transfer faults (Rosendahl, 1987; Morley *et al.*, 1990; Riedl *et al.*, 2020). A prominent transfer region in the northern sector of the East African Rift System exists between the Southern Main Ethiopian Rift and the Northern Kenya Rift and constitutes a 300-km-wide zone of extensional deformation, referred to as the broadly rifted zone (Wolde-Gabriel

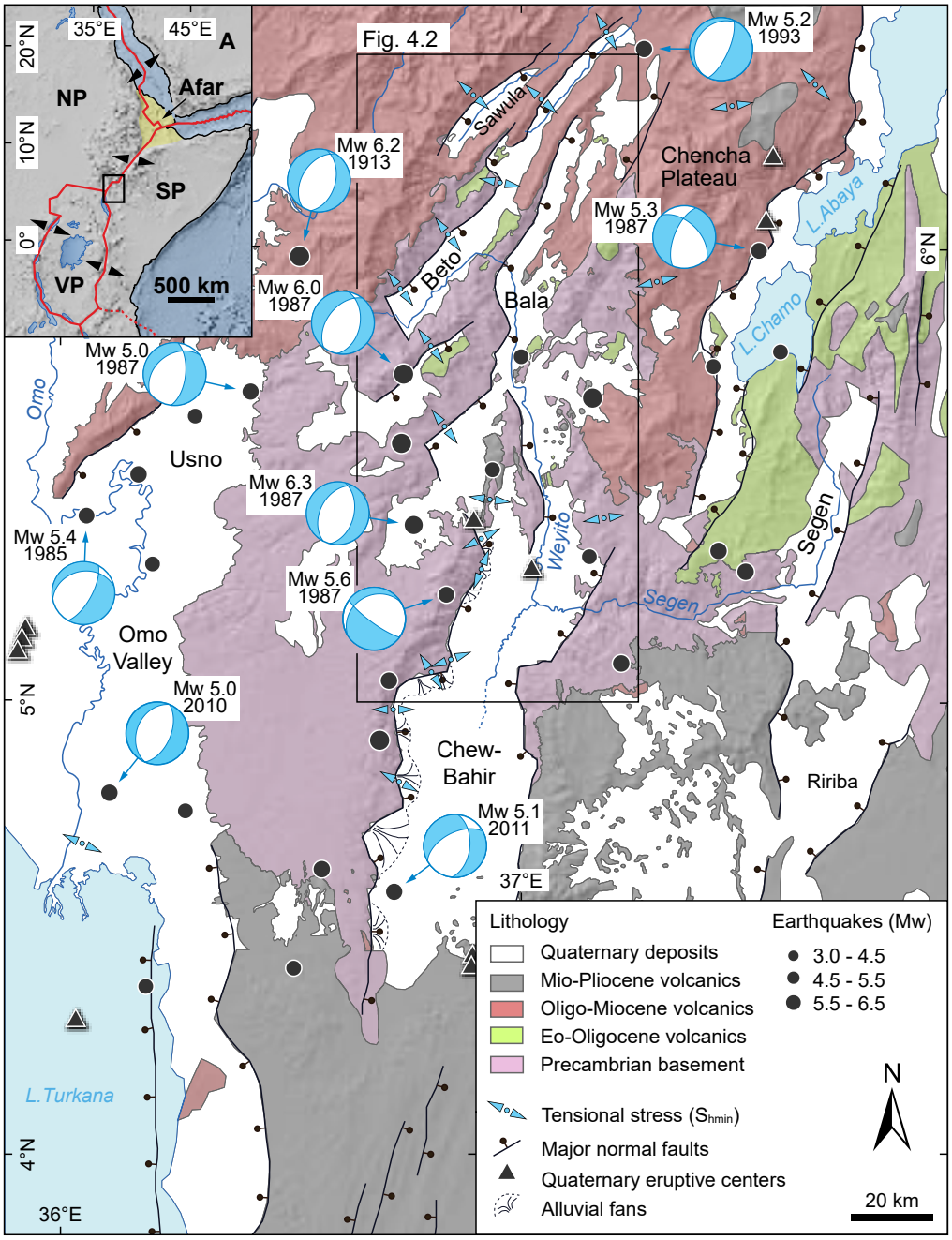

Figure 4.1: Tectonic setting of the Southern Main Ethiopian Rift and the Northern Kenya Rift, principal stratigraphic units, and Quaternary faults (Davidson, 1983; Vétel *et al.*, 2005); Quaternary eruptive centers (Davidson, 1983; Ebinger *et al.*, 2000; Franceschini *et al.*, 2020), local paleostress data (Boccaletti *et al.*, 1998; Bonini *et al.*, 2005; Heidbach *et al.*, 2018; Philippon *et al.*, 2014), earthquake focal mechanisms (Harvard CMT catalogue; Asfaw, 1990; Ayele and Arvidsson, 1997; Foster and Jackson, 1998), and seismic events (black dots) are from the International seismological center (ISC). Inset map at top left shows the East African and Red Sea Rift plate boundaries (A: Arabia plate; SP: Somalia plate; NP: Nubia plate; VP: Victoria plate) with the location of the study area (black box). The northeast-oriented Sawula, Beto, and Bala basins constitute the Gofa Province.

and Aronson, 1987; Ebinger *et al.*, 2000). This arid to semi-arid environment comprises numerous fault scarps, fault-bounded blocks, and intervening fault-controlled depressions. The broadly rifted zone is characterized by inherited Mesozoic-Paleogene crustal anisotropies (Ebinger *et al.*, 2000; Philippon *et al.*, 2014; Brune *et al.*, 2017; Emishaw *et al.*, 2017) that are oblique to the trend of the Southern Main Ethiopian Rift and the Northern Kenya Rift (Corti *et al.*, 2019). However, the presence of crustal anisotropies in the broadly rifted zone and superposed effects of changes in rift kinematics through time in East Africa (*e.g.*, Bosworth and Strecker, 1997; Boccaletti *et al.*, 1998) make it difficult to unambiguously identify and assess the evolution of Quaternary fault patterns.

The Chew Bahir Basin and the Gofa Province, within the broadly rifted zone, comprise discrete, north to northeast-oriented, fault-bounded en-échelon basins in the structural transfer zone between the Southern Main Ethiopian Rift, the Turkana depression, and the Northern Kenya Rift (Fig. 4.1). These basins include the Chew Bahir, Mali-Dancha, Beto, and Sawula basins. Low-temperature thermochronology studies indicate that extensional deformation started in the Chew Bahir Basin at about 20 Ma (Pik *et al.*, 2008), whereas in the north of the Gofa Province (Beto Basin), deformation began at ca. 12 Ma (Philippon *et al.*, 2014; Balestrieri *et al.*, 2016; Boone *et al.*, 2019). Based on geochronological and structural studies, the Gofa Province was classified by Wolde-Gabriel and Aronson (1987) as a failed rift-basin segment, while the Chew Bahir Basin in the south was thought to represent a young stage of extensional tectonism. In contrast, Ebinger *et al.* (2000) suggested that only in the north of the Gofa Province tectonic activity ceased during the Pliocene, unlike the seismically active Chew Bahir Basin. In another study, Philippon *et al.* (2014) used normalized channel-steepness index analyses and seismicity data to infer a decrease in recent faulting in the northern sector of the Gofa Province and a current strain localization in the Chew Bahir Basin.

Considering the previous analyses, this study aims to address two critical questions that have remained unanswered. First, what is the spatiotemporal distribution of deformation and its geomorphic signature in the broadly rifted zone between the Chew Bahir Basin and the northern Gofa Province? Second, how did the structures in the various fault-bounded basins and isolated fault segments in the Chew Bahir Basin and the Gofa Province interact during the young development of the broadly rifted zone? To evaluate spatial differences in the evolution of the Chew Bahir Basin and the Gofa Province, we combined morphometry, climatic information, and geological field data to identify, characterize, and extract geomorphic signatures related to tectonic processes.

4.2 Setting

4.2.1 Tectonic and geologic setting

The northeast-trending, active Main Ethiopian Rift, which separates the continental Nubia and Somalia plates, is an integral part of the East African Rift System, where present-day extension

rates may reach up to 5 mm/yr (Saria *et al.*, 2014). The kinematic mechanisms responsible for the development of the Main Ethiopian Rift and associated volcano-tectonic features have been the subject of ongoing debate about the neotectonic activity of this region. For example, Boccaletti *et al.* (1998) and Bonini *et al.* (2005) suggested a multiphase kinematic model of rift evolution, involving a Miocene border fault generated during oblique extension, and a Plio-Quaternary shift of tectono-magmatic processes toward the rift axis characterized by approximately orthogonal east-west-oriented extension. In contrast, several other studies (*e.g.*, George and Rogers, 2002; Corti, 2012; Muluneh *et al.*, 2014; DeMets and Merkouriev, 2016; Erbello *et al.*, 2016) have argued for a sustained constant extension direction with an orientation of 95° –100° (Fernandes *et al.*, 2004; Kogan *et al.*, 2012; Stamps *et al.*, 2008). Farther south, in the Northern Kenya Rift, Bosworth and Strecker (1997) suggested a change in the extension direction from an original east-west to a neotectonic northwest-southeast orientation during the Quaternary.

Seismic reflection and well data from southern Sudan and northern Kenya suggest episodic extension in the Southern Main Ethiopian Rift and the area of the present-day Northern Kenya Rift during the Cretaceous (Bosworth and Morley, 1994). The propagation of structures in the Southern Main Ethiopian Rift and in northern Kenya has been influenced by inherited pre-existing Neoproterozoic basement fabrics and Mesozoic and/or Paleogene rift structures, leading to a complex zone of deformation (Davidson and Rex, 1980; Morley *et al.*, 1992; Bosworth and Morley, 1994; Ebinger *et al.*, 2000; Brune *et al.*, 2017; Emishaw and Abdelsalam, 2019). Ebinger *et al.* (2000, and references therein) suggested that the unusual width of this extensional zone originated from the termination of fault splays of the Southern Main Ethiopian Rift and the Northern Kenya Rift, respectively. However, Corti *et al.* (2019) considered the prominent low-elevation broadly rifted zone as a nascent oblique transfer zone, where faults from the Southern Main Ethiopian Rift and the Northern Kenya Rift interact.

Within the broadly rifted zone, Neoproterozoic basement fabrics and/or lineaments with unknown kinematics are observed in the south and become progressively less evident to the north. The region comprises 10 to 50-km-wide, north to northeast trending en-échelon rift basins referred to as the Gofa Province (Davidson, 1983) and the Chew Bahir Basin. The Gofa Province and the Chew Bahir Basin are tectonically active and are bordered by uplifted tectonic flanks that are structurally linked with the northern extent of the Kenya Rift (Bonini *et al.*, 2005). The east-dipping and north-northeast striking faults bordering the Southern Main Ethiopian Rift are Miocene in age (Wolde-Gabriel *et al.*, 1991; Ebinger *et al.*, 1993, 2000; Philippon *et al.*, 2014; Boone *et al.*, 2019), and are kinematically linked by shorter northwest striking transfer faults (Ebinger *et al.*, 2000; Philippon *et al.*, 2014; Brune *et al.*, 2017). An approximately east-west oriented structural domain inferred from Bouguer gravity anomalies furthermore complicates the interpretation of the structural history of this region, as these anomalies appear to be associated with sediment-filled Mesozoic to Cenozoic paleo-rift basins in the subsurface (Emishaw and Abdelsalam, 2019). The steplike pattern of the present-day rift basins reveals a progressive decrease in basin width and the degree of extension (Philippon *et al.*, 2014).

Pre-rift volcanic uplands (Ebinger *et al.*, 1993; George and Rogers, 2002) in the north of the Gofa Province and the adjacent Kenyan and Ethiopian domes define the low relief of the Gofa Province and Chew Bahir Basin within the broadly rifted zone remarkably well. The en-échelon footwall blocks of the rift margin and scattered volcanic eruptive centers (Ebinger *et al.*, 2000) within the Gofa Province and south of the Chew Bahir basin further diversify the regional character of the topography and the landscape.

The oldest rocks in the study region comprise Pan-African gneisses, amphibolites, and granulites that are mainly exposed in the footwall margin of the Chew Bahir Basin and the southern Gofa Province (Davidson, 1983) (Fig. 4.2a). An up to 8-m-thick Tertiary sandstone layer unconformably covers these rocks (Ebinger *et al.*, 1993). Fractured basaltic lava flows, trachybasalts, and locally restricted phonolite plugs with subordinate tuff layers comprise the Miocene trap series (Davidson, 1983; Ebinger *et al.*, 2000) that covers the northwestern and northern plateau regions of the Gofa Province. Within the rift, the segmented, fault-bounded basins expose a sedimentary fill comprised of Quaternary fluvio-lacustrine strata, alluvial-fan deposits along the range fronts, and minor outcrops of lacustrine silty clay (Davidson, 1983; Ebinger *et al.*, 2000).

The high-grade metamorphic basement rocks along the margins of the Chew Bahir Basin and southern Gofa Province are pervasively fractured by undifferentiated lineaments that may have resulted from brittle deformation processes during the Pan-African orogeny (Levitte *et al.*, 1974; Yemane and Yohunie, 1987) and subsequent tectonic overprint during Mesozoic and Cenozoic extension (Morley *et al.*, 1990, 1992; Emishaw *et al.*, 2019). In contrast, the Cenozoic volcanics in the Gofa Province are less affected by such features and appear to be controlled primarily by north-northeast-striking Cenozoic normal fault systems (Davidson, 1983). This structural preconditioning in both bedrock areas may influence overall rock-mass strength and thus determine the resistance to weathering and erosional processes affecting the different fault blocks.

The high-elevation, western margins of the Chew-Bahir Basin and the Gofa Province are characterized by generally east-dipping normal faults and provide the source material for the basin-fill deposits in the adjacent depressions. Stream channels draining footwalls in the Chew Bahir region cut across obliquely oriented, undifferentiated lineaments, whereas channels in the Mali-Dancha Basin tend to be parallel to these structures (Fig. 4.2a and b). Catchments in the Gofa Province are less dissected by lineaments and drain toward the Weyito River (Fig. 4.2a and b), which transports sediments to the Chew Bahir Basin. However, some of the catchments feed rivers that flow to the north and form tributaries of the Omo River (Fig. 4.1). The Segen River in the Southern Main Ethiopian Rift flows south and southwest to the Chew Bahir Basin, following the regional topographic gradient.

4.2.2 Seismicity

Earthquakes with magnitudes between Mw = 3.0 and 6.5 have been recorded in the broadly rifted zone since 1913 (Gouin, 1979). These events cluster in a narrow zone between the Chew Bahir,

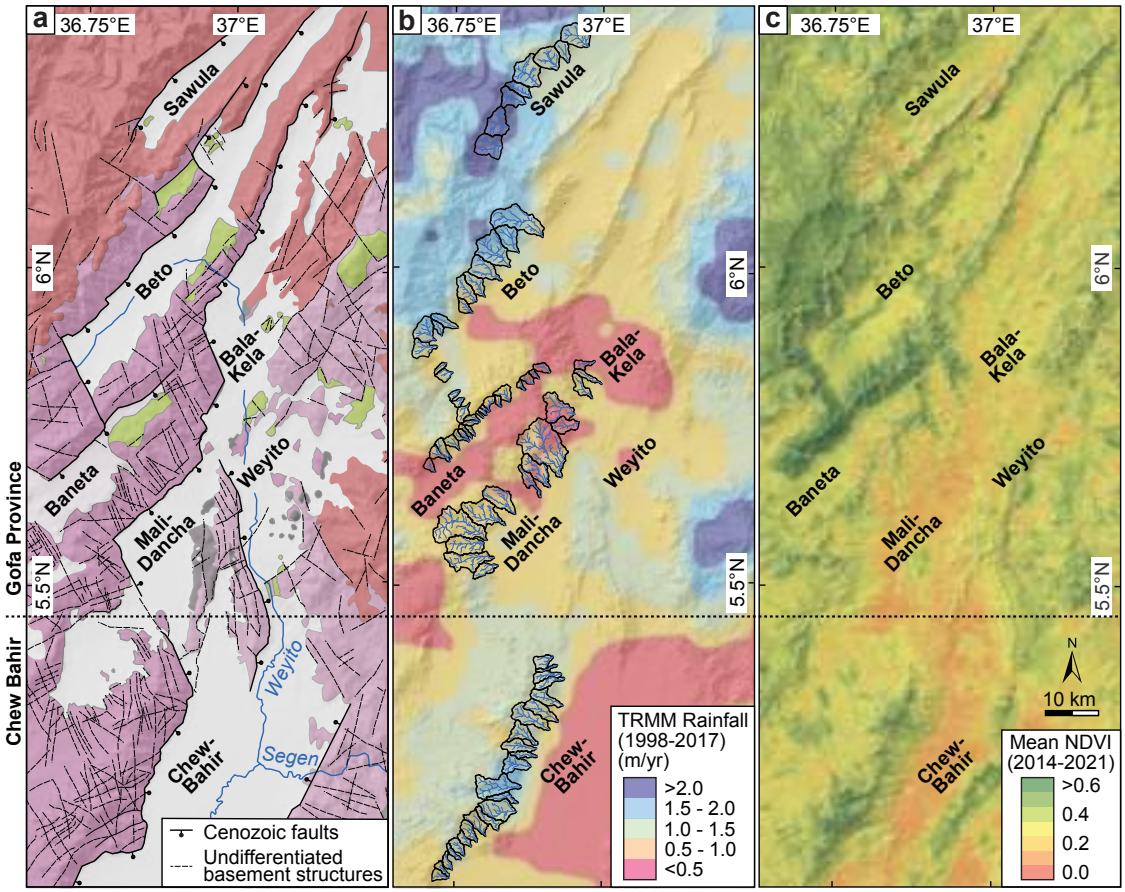

Figure 4.2: Lithologic units (a), annual rainfall distribution (b) and mean $NDVI$ (c) in the Chew Bahir Basin and the Gofa Province. Lithologic units and tectonic lineaments from Davidson (1983); details of the distribution of geological units are shown in Fig. 4.1. Averaged annual rainfall amounts are based on 10 years of TRMM data (Bookhagen, 2010) and mean $NDVI$ has been obtained from 2014 to 2021 Sentinel-2 satellite data (D'Odorico *et al.*, 2013).

Mali-Dancha, Baneta, and Segen basins and in the lower Omo Valley (Fig. 4.1). This northeast oriented cluster of seismicity and seismic-moment release patterns has been interpreted to reflect a narrow belt of extension connecting the Southern Main Ethiopian Rift and the Northern Kenya Rift (Corti *et al.*, 2019). Major earthquakes occurred in this region in 1913 (Mw = 6.2) and 1919 (Mw = 6.5). More recently, regional seismicity has been associated with earthquake swarms, such as in October 1987 (Mw = 5.1 to 6.3), for which focal mechanisms indicate normal faulting with a minor component of oblique slip and hypocenter depths of less than 15 km (Ayele and Arvidsson, 1997; Foster and Jackson, 1998). These events were associated with surface ruptures (Asfaw, 1990; Ayele and Arvidsson, 1997) and clearly attest to the ongoing extensional processes in the region. Additionally, few earthquakes have been recorded along the margins of Lake Abaya (*e.g.*, Mw = 5.3 in 1987) and in the north of the Beto Basin (Mw = 5.2 in 1993). During

the past 20 years, earthquakes at shallower depths (~10 km) have been recorded (Mw = 5 in 2010 and Mw = 5.1 in 2011) in the Chew Bahir Basin. The diffuse nature of seismicity (Gouin, 1979) and isolated emplacement of magmatic dikes in the Chew Bahir Basin and Gofa Province suggest that extensional strain is accommodated by slip along the range-bounding border faults as well as diking and normal faulting within the rift-basin interior (Ebinger *et al.*, 2000).

4.2.3 Climatic setting

Rainfall in the Chew Bahir Basin and the Gofa Province originates from moisture transported from the Indian Ocean and the Congo forest. Large-scale advection from the Indian Ocean (Levin *et al.*, 2009) generates a bimodal annual rainfall distribution in the region from March to May and October to November; an additional period of rainfall from July to September is generated by humid Congo air masses from the southwest (Nicholson, 1996). The cooler high-elevation sectors of the footwall blocks in the broadly rifted zone receive the largest amount of rainfall, and runoff from these areas is directed toward the semi-arid to arid interior of the intervening basins (Gasse, 2000; Seleshi and Zanke, 2004). High-resolution TRMM (Tropical Rainfall Measurement Mission) satellite measurements show that the distribution of annual rainfall largely follows the elevation gradient (Bookhagen and Burbank, 2010). While high-altitude regions such as the Chencha and Sawula mountains receive up to 3000 mm/yr, adjacent basin floors receive only about 400 mm/yr of rainfall (Fig. 4.2b). The average annual rainfall for the entire region is ca. 1250 mm/yr.

The rainfall patterns are also reflected by the regional vegetation cover, which provides a proxy for precipitation. The averaged Normalized Difference Vegetation Index ($NDVI$) was derived from 30 m Sentinel-2 satellite data for the period between 2015 and 2021. The data show an increasing trend in vegetation cover from the southern Chew Bahir Basin to the northern Baneta and Beto basins, and slightly decreases toward the Sawula Basin (Fig. 4.2c). While each catchment exhibits a range of $NDVI$ values indicated by their standard deviations, the observed gradients in the mean $NDVI$ values are robust (Fig. 4.3).

Although the present-day climate is arid to semi-arid in the Southern Main Ethiopian Rift and northern Kenya, environmental conditions have oscillated between wetter and drier periods during the Quaternary (Garcin *et al.*, 2012; Kaboth-Bahr *et al.*, 2021; Schaebitz *et al.*, 2021); during the transitions toward wetter periods erosional processes may have been more efficient in this environment (*e.g.*, Garcin *et al.*, 2017).

4.3 Methods

We analyzed morphometric indices from 89 catchments and their main stream channels from the margins of normal-fault bounded basins in the Chew Bahir and Gofa provinces using a subset of the 12 m TanDEM-X WorldDEM (Rizzoli *et al.*, 2017; Wessel *et al.*, 2018). The structural, and topographic continuity of the en-échelon basin margins, the distinct rock-type exposure

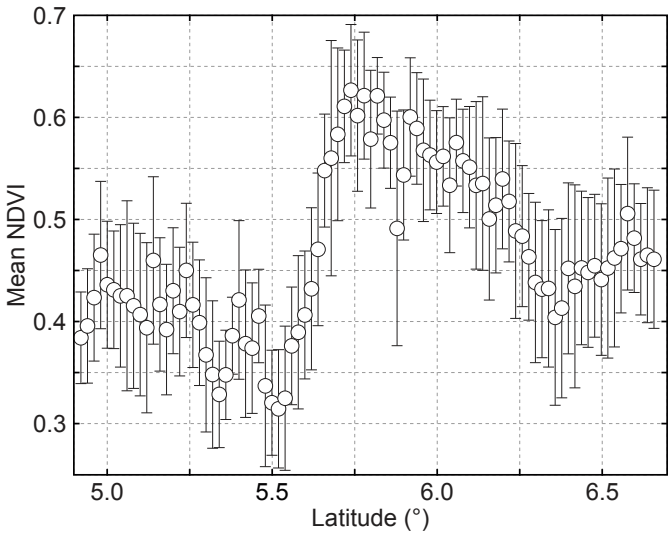

Figure 4.3: Catchment mean $NDVI$ and standard deviation (error bars) from the western basin margins of Chew Bahir and Gofa provinces plotted against latitude.

along the margins of the Chew-Bahir, the Mali-Dancha, Baneta, and Sawula basins, and limited lithologic variability (i.e., only between the high-grade basement rocks and Tertiary volcanic rocks) within the selected catchments of the Beto Basin affords an opportunity to analyze and compare morphometric indices and geomorphic markers in the region. Due to a lack of in-situ rock-strength measurements we investigated rock strength by analyzing hillslope angles and the distribution of steepness indices for each catchment. The geomorphic metrics mirror variations in the mechanical properties of rocks. For this purpose, we used DEM processing tools in ArcGIS, CalHypso (Pérez-Peña *et al.*, 2009a), TopoToolbox (Schwanghart and Kuhn, 2010; Schwanghart and Scherler, 2014), and the Topographic Analysis Kit (Forte and Whipple, 2019). Computed results were subsequently verified in the field. Furthermore, regional seismicity, rainfall, and vegetation cover were also considered to identify morphological anomalies and prominent regional geomorphic markers. The calculated values of morphometric indices (drainage-basin asymmetry factor, hypsometric integral, valley floor width to valley height ratio) and geomorphic markers (local relief, hillslope angle, channel-steepness index, and knickpoints) are summarized in Table 4.1. These measurements were integrated with field observations and seismicity data to characterize the regional fault evolution and the character of neotectonic activity.

4.3.1 Hypsometry

Hypsometry describes the distribution of surface area binned by elevations (Schumm, 1956; Strahler, 1952). To be able to compare individual catchments, the hypsometric curve of a catchment is constructed by plotting the areal ratio of elevations against the normalized elevation. Its shape represents either juvenile (convex), intermediate, or mature (concave) landscape evo-

lutionary stages of a catchment and was previously used to infer tectonically controlled spatial variation in landscape evolution (Strahler, 1952; Schumm, 1956; Pérez-Peña *et al.*, 2009b). The assumption is based on the notion that the hypsometry is convex, if the catchment is actively uplifting and becomes progressively concave once denudation exceeds uplift (*e.g.*, El Hamdouni *et al.*, 2008). A positive correlation established between hypsometric integral (HI, i.e., the area beneath the hypsometric curve) and rock uplift for a tectonically active environment (Lifton and Chase, 1992; Chen *et al.*, 2003; Pérez-Peña *et al.*, 2009a) may help to understand spatial variations in tectonic activity, such as along the basin margins within the Gofa Province and the Chew Bahir Basin.

4.3.2 Drainage-basin asymmetry factor (AF)

The drainage-basin asymmetry factor (AF) describes the pattern and geometry of stream networks within a catchment, both quantitatively and qualitatively (Cox, 1994). In the absence of lithological contrast within a catchment, AF detects tectonic tilting along the horizontal axis (Hare and Gardner, 1985) and is defined as:

$$AF = 100\frac{A_r}{A_t} \tag{4.1}$$

where A_r is the catchment area to the right in flow direction (i.e. facing downstream) of the main channel and A_t is total catchment area. AF values of 50, define stream networks that developed in a stable tectonic setting (Hare and Gardner, 1985), while AFs that significantly deviate from 50 suggest instability. The index is sensitive to changes in lithology or tectonic tilting perpendicular to the main channel (across a catchment) (*e.g.*, El Hamdouni *et al.*, 2008). Based on the degree of deviation from 50 ($\Delta AF = |AF - 50|$), our AF results may be grouped into three groups: $\Delta AF < 5$: symmetrical catchments, $\Delta AF = 5$ to 10: moderately tilted catchments, $\Delta AF > 15$: strongly tilted catchments (*e.g.*, El Hamdouni *et al.*, 2008). Laterally continuous exposure of gneissic rocks and trachy-basalts along the margins of the Gofa Province and on the margins of the Chew Bahir Basin suits this method to investigate spatially variable tectonic activity.

4.3.3 Valley floor width to valley height ratio (VF)

The valley floor width to valley height ratio (VF) defines the shape of a valley in cross-section as broad-floored (U-shaped) or narrow-floored (V-shaped), associated with low and high uplift rates, respectively (Bull and McFadden, 1977). It is expressed as:

$$VF = \frac{2Vfw}{(Eld - Esc) + (Erd - Esc)} \tag{4.2}$$

where Vfw is the width of the valley floor; and Eld and Erd are elevations of the left and right drainage divides, respectively; and Esc is the elevation of the valley floor. While $VF < 1$

signifies V-shaped valleys with a relatively high rock uplift rate, $VF > 1$, suggest U-shaped valleys developed under relatively low uplift rates (*e.g.*, Bagha *et al.*, 2014). Valley-floor width significantly differs along a stream channel and progressively narrows toward the channel head (Ramírez-Herrera, 1998). Therfore, a specified measurement distance from the range front between 0.5 km and 2.0 km facilitates comparison between different channels (*e.g.*, Silva *et al.*, 2003). Here, measured parameters (*e.g.*, elevation of the flanks and the valley floor and width of the valley) were recorded at a distance of 0.5 km from adjacent range fronts. In this study, results from the Gofa Province and the Chew Bahir Basin were combined with the spatial distribution of knickpoints to estimate the degree of regional tectonic activity along basin-bounding normal faults.

4.3.4 Stream-length gradients, channel-steepness indices, and identification of knickpoints

The stream-length gradient index is a proxy of stream power per unit length that is correlated with the total stream power available at a particular reach of a channel (*e.g.*, Pérez-Peña *et al.*, 2009a), and according to Hack (1957) it is expressed as:

$$Sl = \frac{\Delta h}{\Delta l} l \tag{4.3}$$

where $\delta h/\delta l$ is the local slope of the channel segment being evaluated, and l is the channel length. The stream length-gradient index can be influenced by changes in lithology, or tectonic activity (*e.g.*, Merritts and Ellis, 1994; Bishop *et al.*, 2005). Hence, variations in the regional stream length-gradient could result either from contrasts in rock resistance to incision between different lithologies or active faulting (*e.g.*, Seeber and Gornitz, 1983).

Channel length influences the stream-length gradient index and normalizing the local stream-length gradient by its slope defines the normalized stream-length gradient index that can depict the steeper segment of a channel (Chen *et al.*, 2003). The stream length-gradient index has been used to characterize tectonic activity of regions where variations in rock strength are negligible (de Araújo Monteiro *et al.*, 2010).

Channel concavity is an integral part of the stream-power model for bedrock rivers (*e.g.*, Whipple and Tucker, 1999; Whipple, 2004; Wobus *et al.*, 2006); it is a characteristic metric to reveal tectonic activity or resistance of channel lithology to erosion. We use a reference channel concavity ($\Theta_{ref} = 0.45$) to calculate channel steepness indices (k_{sn}) following:

$$S = k_{sn} A^{-\Theta} \tag{4.4}$$

where S is channel slope, A is drainage area, Θ and k_{sn} are the concavity and steepness indices, respectively. We solve this power-law relation for the steepness index (k_{sn}) for individual channel segments. Rapid changes and generally high values of k_{sn} have been associated with recent tectonic activity (*e.g.*, Snyder *et al.*, 2000; Wobus *et al.*, 2006; Pérez-Peña *et al.*, 2009a,

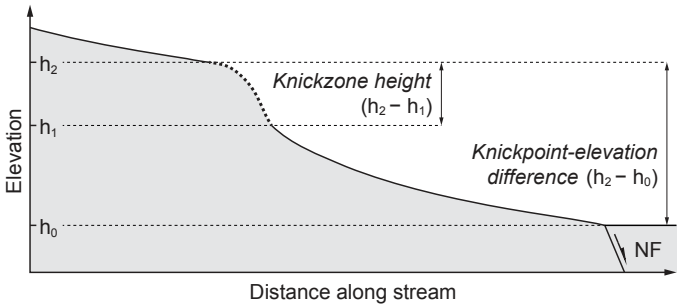

Figure 4.4: Schematic transient stream profile across a range-bounding normal fault (NF) showing a steepened section (knickzone) associated with normal faulting. In this study, we rely on two height-difference metrics: (1) knickzone height, i.e., the maximum vertical offset for the concave part of a stream (Schwanghart and Scherler, 2014; Neely *et al.*, 2017); and (2) knickpoint-elevation difference, i.e., the maximum vertical offset between the top of the knickzone and the bounding fault.

2009b). The normalized channel-steepness index has been used to characterize tectonic activity of regions with variations in rock strength (de Araújo Monteiro *et al.*, 2010; Bookhagen and Strecker, 2012; Olen *et al.*, 2015; Purinton and Bookhagen, 2017). For this study, k_{sn} values for the entire stream network were generated by comparing a strictly concave upward profile with the stream longitudinal profile extracted from the 12 m DEM; a knickzone is identified when an offset is obtained between the stream longitudinal profile and the steady-state, concave-upward profile (Schwanghart and Kuhn, 2010; Schwanghart and Scherler, 2014). The tectonically related knickzones or knickpoints can also be identified by the investigation of k_{sn} and longitudinal profiles via abrupt changes in channel slope (Neely *et al.*, 2017). We distinguish between two metrics of knickpoint-elevation differences in their vertical direction. We refer to the knickzone height as the maximum vertical offset for the concave part of the stream (*e.g.*, Schwanghart and Scherler, 2014; Neely *et al.*, 2017), and we refer to the knickpoint-elevation difference as the maximum vertical offset between the top concave section of the knickzone and the bounding fault of the footwall (Fig. 4.4). In the Gofa Province and the Chew Bahir Basin the scales of these two different metrics may help to decipher fault-evolution characteristics as shown in other extensional terrains (*e.g.*, Boulton and Whittaker, 2009; Whittaker and Boulton, 2012; Kent *et al.*, 2017).

4.3.5 Topographic relief and hillslope analysis

In previous studies of tectonically active regions systematic topographic analysis of local relief and hillslope angles has been widely used to extract spatiotemporal tectonic trends (*e.g.*, Cowie, 1998; Goldsworthy and Jackson, 2000; Montgomery and Brandon, 2002; Densmore, 2004; Kirby *et al.*, 2007; DiBiase *et al.*, 2010; Burbank and Anderson, 2011). Local relief is a scale-dependent measurement of the height difference between the highest and the lowest point in a circular neighborhood (Ahnert, 1970). The choice of the scaling window is sensitive to hillslope length

and catchment size (DiBiase *et al.*, 2010). In this study, we measured local relief within 1 km of each pixel (1-km radius relief). The availability of high-resolution TanDEM-X data (Rizzoli *et al.*, 2017; Wessel *et al.*, 2018), the characteristics of the substrate materials of the catchments, and the spatially variable fault-scarp morphology within the transfer zone between the Southern Main Ethiopian Rift and the Northern Kenyan Rift provide a unique opportunity to extract spatial trends in surface-deformation signals. To extract these signals, we relied on morphometric indices, geomorphic markers, and computed catchment mean hillslope angle, as well as topographic relief. Hillslope angles were calculated using a 3 × 3 pixel window (ca. 36 × 36 m; Schwanghart and Kuhn, 2010; Schwanghart and Scherler, 2014).

In addition to average hillslope values (median, mean), we calculated several percentiles from the full hillslope-angle distributions of each catchment to better quantify the variations between individual catchments. We used the width of the distribution as a proxy for slope variability within a catchment (DiBiase *et al.*, 2018). Specifically, we used the ratio of the 90th and 50th percentile (median) to characterize their variability and analyze these values between catchments along the basin margin. A ratio of 2 indicates that the 90th percentile is twice as high as the median value; smaller ratios indicate a narrower distribution. This metric is often used in climatology to identify extreme weather events (*e.g.*, Boers *et al.*, 2015; Ramezani-Ziarani *et al.*, 2019; Smith and Bookhagen, 2020). Accordingly, we used this technique in our study and combined similar percentile ratios of channel-steepness indices from each catchment as proxies for channel variability along the margins of the Chew Bahir Basin and the Gofa Province.

4.4 Results

4.4.1 Hypsometry

Hypsometric integral (HI) values from the Gofa Province and the Chew Bahir Basin exhibit a distinct southward-increasing pattern, from $HI = 0.29$ in the Sawula Basin to $HI = 0.68$ in the Chew Bahir Basin (Fig. 4.5a). This pattern is mimicked by the southward-shifting shapes of the normalized hypsometries of the studied catchments, from concave to convex, i.e., from mature to juvenile landscape development stages (Fig. 4.6). Approximately an equal percentage of catchments in the Sawula Basin exhibits concave and intermediate hypsometric curves. Intermediate and subordinate convex hypsometric curves characterize the Beto and Baneta basins. Similarly, the Mali-Dancha Basin is characterized by intermediate to convex hypsometries. Most catchments from the Chew Bahir region exhibit a convex shape with subordinate intermediate hypsometric curves.

4.4.2 Drainage-basin asymmetry factor (AF)

The calculated AF values from the Gofa Province and the Chew Bahir Basin vary from 17 (tectonic tilting to the southern side of the catchment) to 78 (tectonic tilting to the northern side)

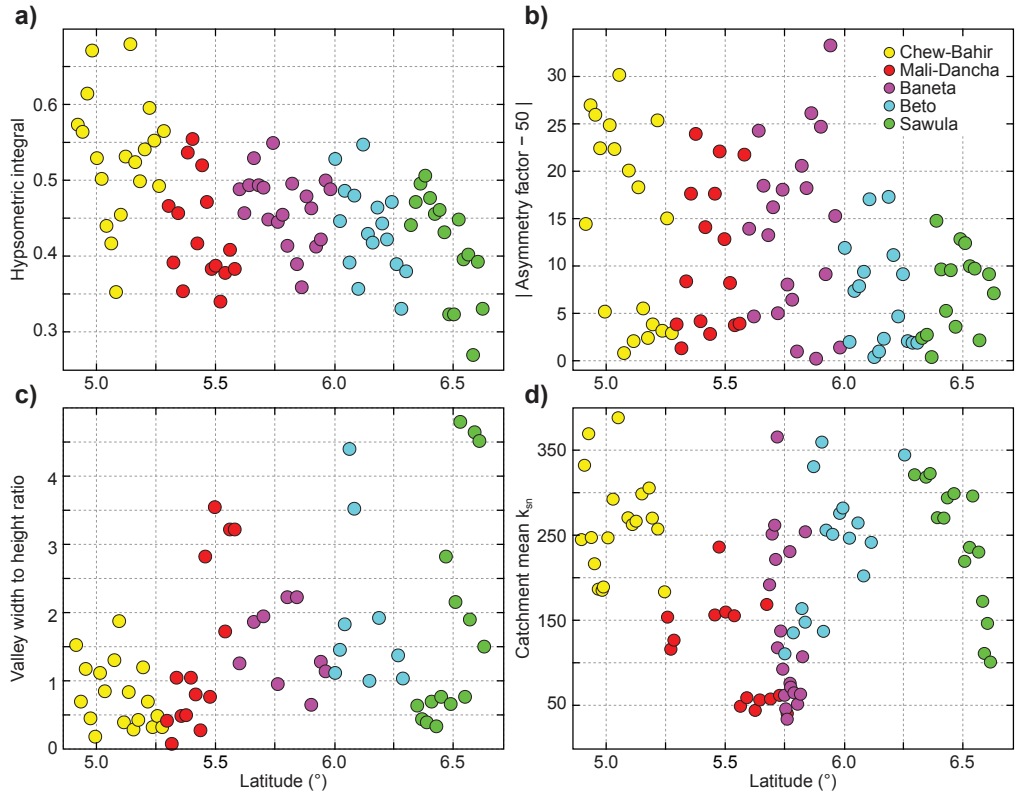

Figure 4.5: Morphometric indices vs. latitude calculated from footwall catchments of the Chew Bahir Basin and the Gofa Province. (a) Hypsometric integral, showing a northward decrease reflecting northward basin maturation; (b) absolute value of asymmetry factor minus 50, showing stable catchments in the north and tectonically tilted, unstable catchments in the south; (c) valley floor width to valley height ratio, showing deeply incised narrow valleys in the south and wider valleys in the north; (d) catchment mean channel-steepness index, showing spatially distributed peak values (>300) related to fault-link zones (see text for further discussion).

(Fig. 4.5b). The tilt changes between a southward direction ($AF < 45$) and a northward direction ($AF > 55$) around a horizontal axis. In addition, the AF index values from a few northward-directed catchments in the Mali-Dancha and Beto areas reflect alternating tilt directions between east and west, whereas only a few of the catchments tend to be symmetric or show no preferred tectonic tilt direction. About an equal percentage of the analyzed catchments from Mali-Dancha reflects tectonic tilting and the existence of symmetric catchments. More than 60% of the catchments in the Chew Bahir Basin document the effects of tectonic tilting. The overall intensity of recorded tectonic tilts $|AF - 50| > 5$) exhibits a gentle increase between the Gofa Province and the Chew Bahir Basin (Fig. 4.5b).

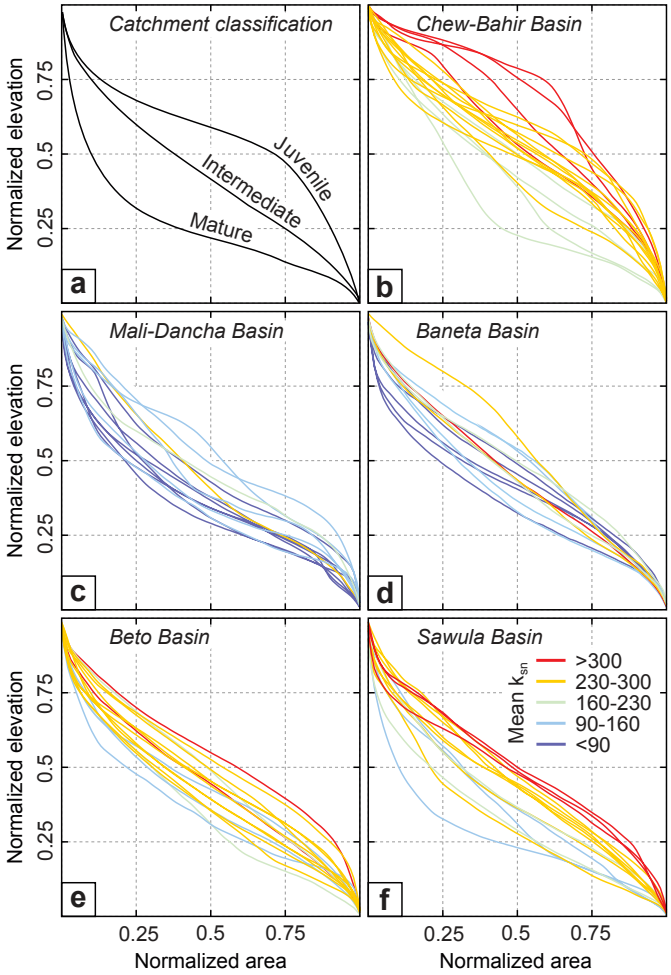

Figure 4.6: Normalized hypsometries of analyzed catchments (see Figs. 4.1 and 4.2 for location). (a) Expected hypsometric curves of different basin evolution stages (Strahler, 1952). (b–f) Hypsometric curves of analyzed catchments from Chew Bahir, Mali-Dancha, Baneta, Beto, and Sawula basins color-coded according to their catchment mean k_{sn}. Convex channels of the Chew Bahir Basin record high k_{sn} values (>300–160 $m^{0.9}$) and characterize a juvenile catchment whereas intermediate to concave channels of Baneta, Beto and Sawula catchments mainly record intermediate to low k_{sn} values (300–<90 $m^{0.9}$) that reflect intermediate to mature catchments. Channels parallel to lineaments in the Mali- Dancha area record intermediate to concave profiles with low k_{sn} values (160–<90 $m^{0.9}$).

4.4.3 Valley floor width to valley height ratio (VF)

VF values determined for 65 catchments range from 4.7 (Sawula Basin) to 0.2 (Mali-Dancha Basin) and show a scattered, but weak southward-decreasing trend (Fig. 4.5c). Broader U-shaped valleys ($VF > 3.5$) were identified only in the Beto and Sawula areas (Gofa Province), while the catchments along the Chew Bahir Basin form mainly V-shaped valleys ($VF < 1$). Thus, it can be asserted that although there are Vshaped valleys in all the regions studied, the proportion of U-shaped valleys decreases southward.

4.4.4 Longitudinal stream profile, channel-steepness index, and knickpoint analyses

Representative catchments (>3 km²) across the active fault margins of each basin and fault-linked zones were selected to conduct longitudinal stream-profile analyses. Most stream profiles show a characteristic concave-downward shape (Fig. 4.7). Slope-area analyses indicate two or more prominent slope-break type knickpoints along main channels draining into the Chew-Bahir (Catchment 12), Mali-Dancha (Catchments 25 and 26) and Sawula (Catchment 78) basins, while Catchment 72 along the Beto Basin exhibits a vertical step in the upstream channel (Fig. 4.8). The amount of slope breaks tends to be higher at locations where orthogonally to obliquely striking marginal faults are linked. Longitudinal profiles from the footwall margin of the Beto and Sawula basins reveal steady-state, concave-upward profiles without prominent breaks in slope (Fig. 4.7j–k). The distance between the range front and the first identified slope-break knickpoint along the longitudinal profile ranges between ca. 0.2 km and >4 km (Fig. 4.7a, e, g, k).

The k_{sn} values obtained from the analyzed catchments show a range between 20 and 600 $m^{0.9}$. While low k_{sn} values (<100 $m^{0.9}$) are observed along channels parallel to lineaments with unknown kinematic history and channels across fault terminations (Fig. 4.9a), high k_{sn} values (>100 $m^{0.9}$) are limited to the main channels of the Chew Bahir Basin and are laterally scattered along the basin-bounding range front.

Similarly, a range of knickzone heights (20–280 m) was recorded from the analyzed catchments. Low-value ($\leq$ 30 m) knickzones are distributed throughout all catchments of the Gofa Province and the Chew Bahir Basin. Channels parallel to inherited lineaments (*e.g.*, Mali- Dancha Basin) and across fault terminations (*e.g.*, north of the Sawula Basin) record few knickpoints, and these occur only at the channel head (Fig. 4.9b). This characteristic consistently corresponds with low k_{sn} values (<100 $m^{0.9}$), and concave stream profiles. The spatial distribution of knickzone heights of >50 m documents an increasing trend from north (Sawula Basin) to south (Chew Bahir Basin). The notably greater values ($\leq$ 70 m) cluster in the Chew Bahir Basin and the southern Gofa Province (Figs. 4.7, 4.10a). The spatial distribution pattern of greater knickzone heights consistently follows an increasing trend in the number of prominent breaks in slope along the channel profiles toward the south. Channels across fault-linked sectors of the basins record a

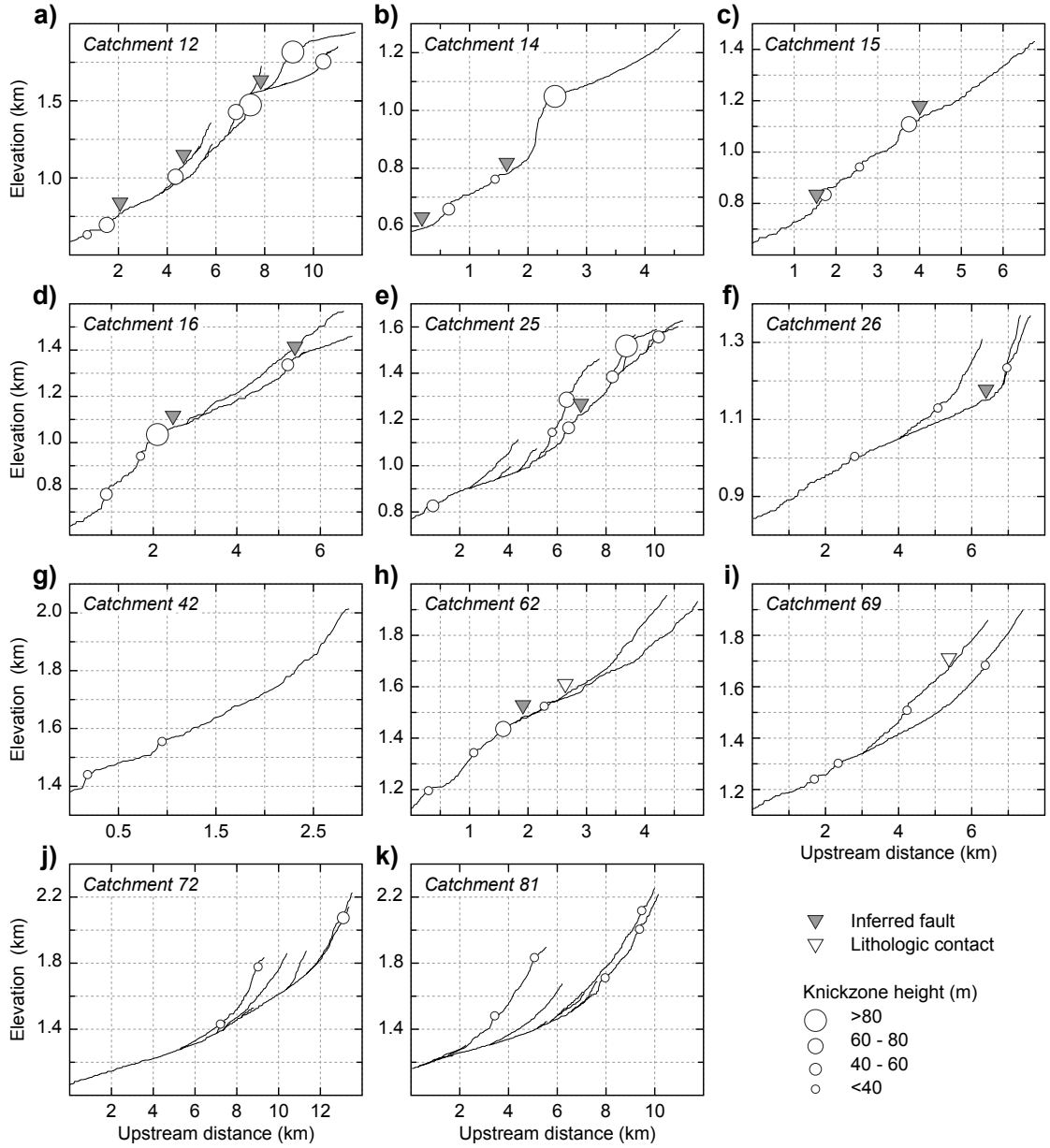

Figure 4.7: Representative stream profiles with projected locations of knickpoints (circles), inferred faults (gray triangle), and lithological contacts (white triangle) from the Chew Bahir Basin and the Gofa Province. For catchment locations, see Figs. 4.2 and 4.9.

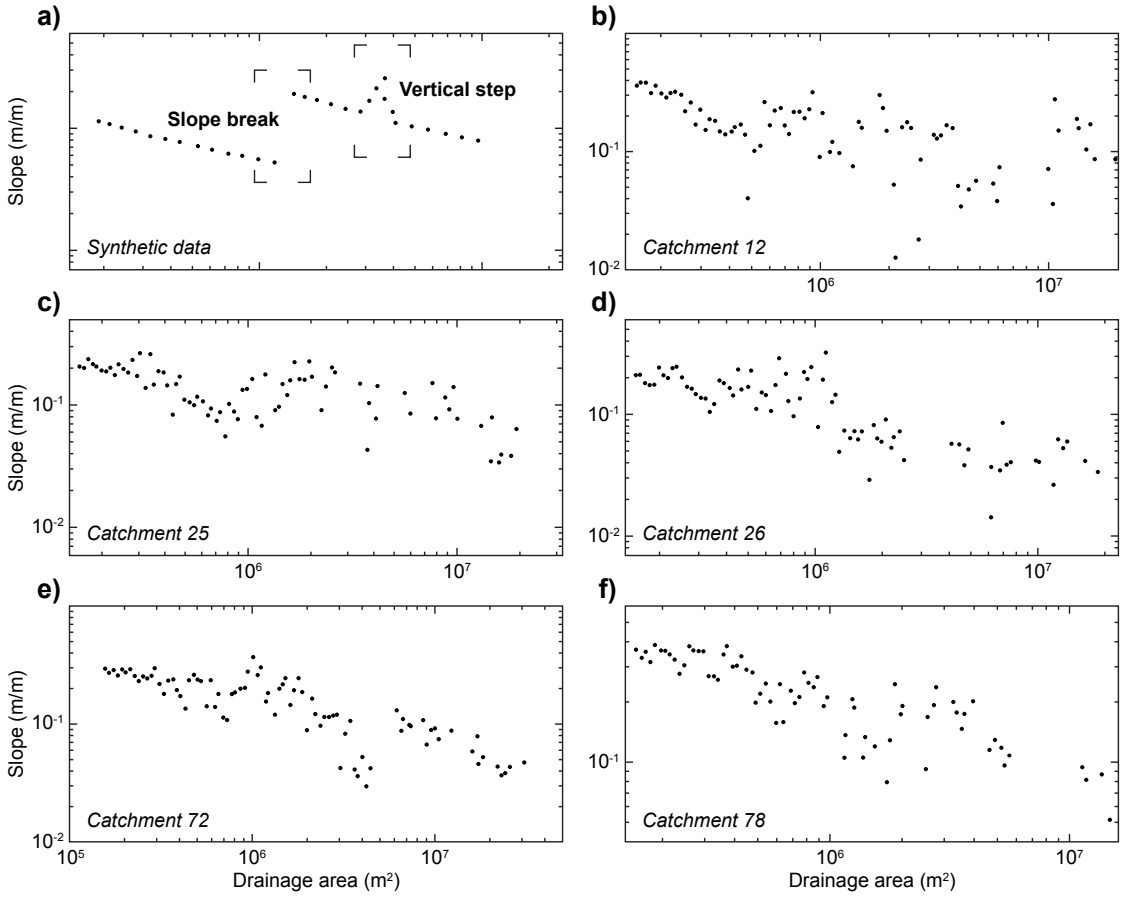

Figure 4.8: Slope-area plots (logS vs. logA) to highlight step changes associated with river knickpoints. (a) Expected vertical step and slope-break characteristics of knickpoints using synthetic data (modified from Kirby and Whipple, 2012). Note slope-break characteristics in the Chew Bahir (b), Mali-Dancha (c-d), and Sawula (f) catchments, and characteristics of an upstream limited vertical step in catchment 78 from the Beto Basin (e).

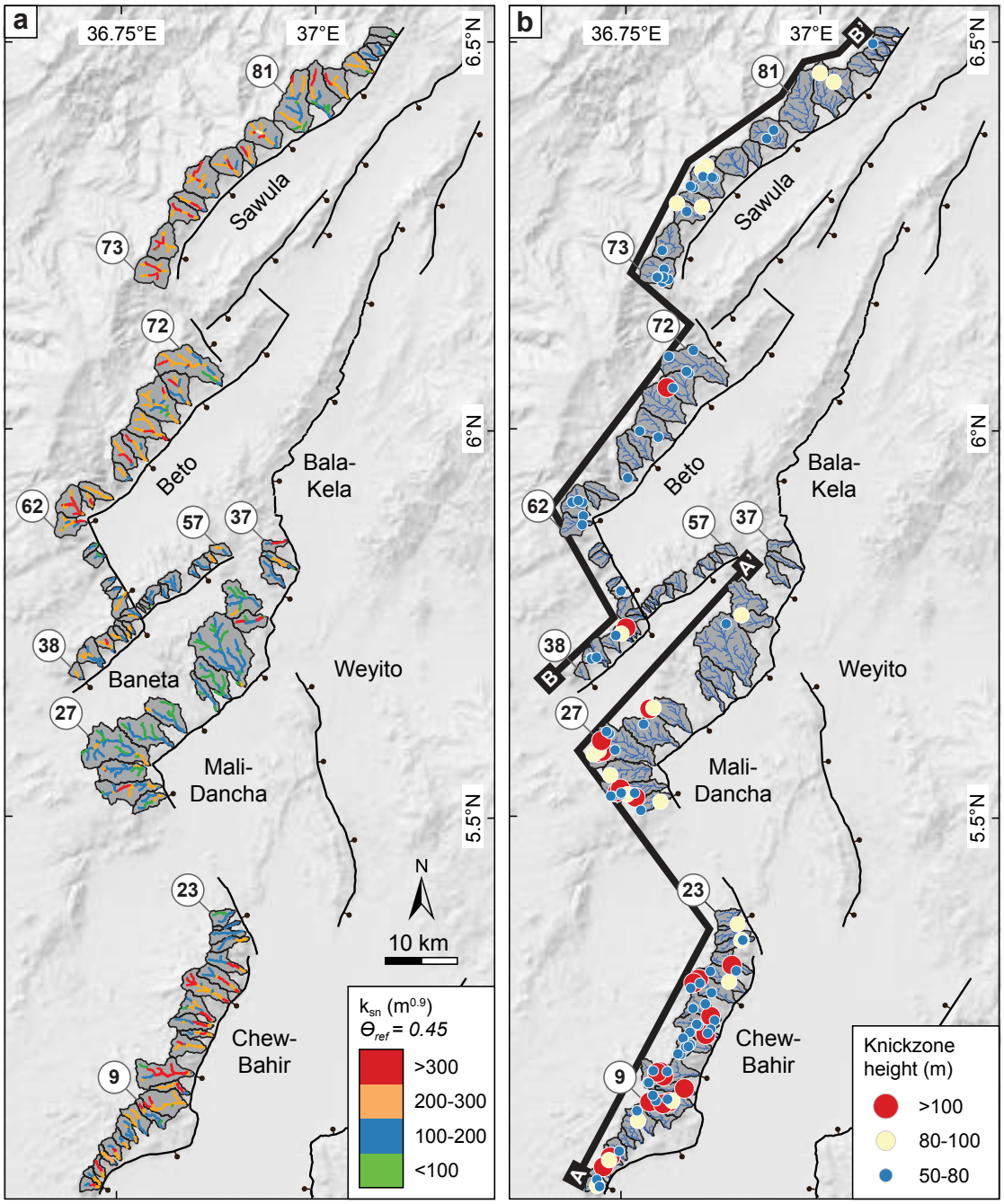

Figure 4.9: Shaded relief maps of the Chew Bahir Basin and the Gofa Province showing the drainage divides and stream networks of each studied catchment (labeled from south to north). Basin-bounding normal faults are denoted in black lines with extended filled circles. (a) Stream network color-coded according to k_{sn} values. (b) Circles mark the location of extracted knickpoints, with color and size corresponding to their knickzone height (>50 m). Bold black lines indicate the position and orientation of topographic swath profiles A-A′ and B-B′ illustrated in Fig. 4.11.

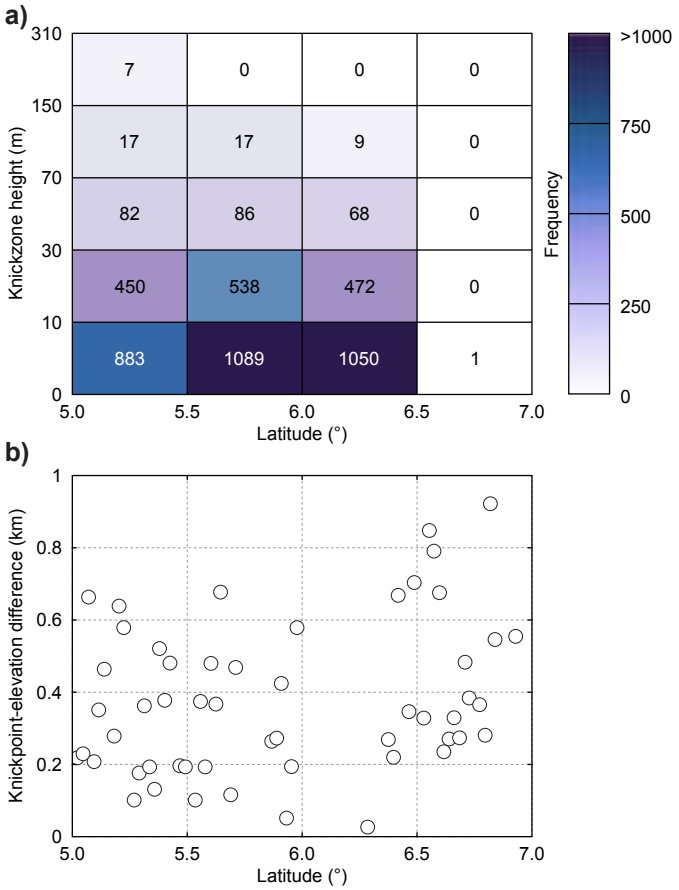

Figure 4.10: (a) 2-D histogram of knickpoints from the Chew Bahir Basin and the Gofa Province showing the frequency of identified knickpoints by latitude (binned by 0.5°). (b) Knickpoint-elevation difference by latitude. Note the frequency of larger knickzone heights (>70 m) and increase in knickpointelevation differences with latitude, reflecting higher uplift rate and Quaternary tectonism toward the south.

higher magnitude of knickzone heights compared to adjacent channels (Fig. 4.9b; catchment numbers: 4, 12, 18, 26, 27, and 44, Fig. 4.11a and b). Furthermore, knickpoints at fault-linked zones of the Chew Bahir Basin exhibit a closely spaced distribution along the main channel; this distribution becomes less prominent in the Gofa Province (Fig. 4.9b). The knickpoint-elevation difference from the range front varies along the margins of the Chew Bahir Basin and the Gofa Province. In the Chew Bahir Basin, of knickpoint clusters close to the range front are observed; conversely, knickpoints in the Gofa Province tend to be in upstream sectors, farther away from the range front (Fig. 4.10b).

4.4.5 Local topographic relief and hillslope analysis

Local relief computed with a 1-km-radius using the TanDEM-X data reveals a consistent trend that is aligned with other morphometric indices and geomorphic markers. The left-stepping,

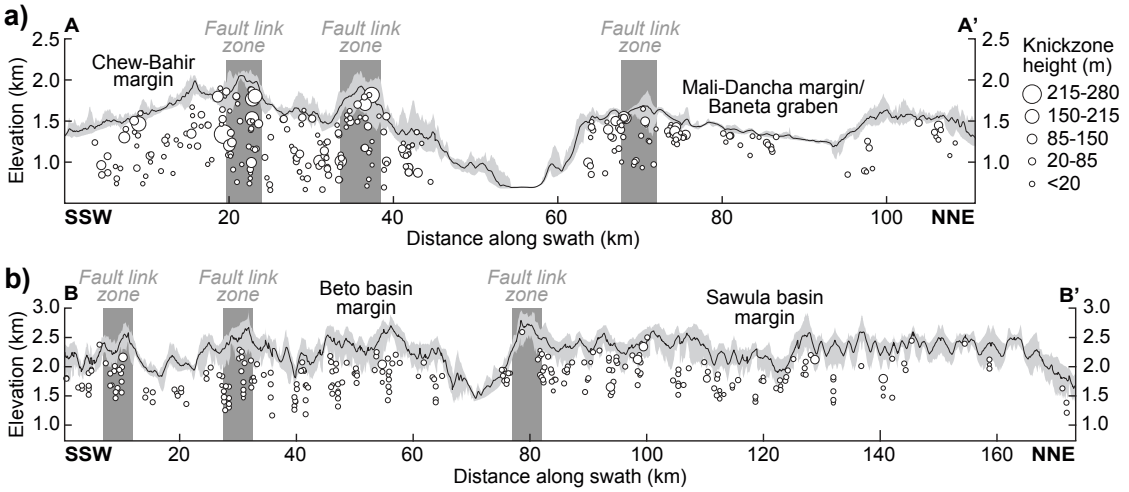

Figure 4.11: Topographic swath profiles (2-km-wide) along (a) the Chew Bahir and Mali-Dancha basin margins (A-A′) and (b) the Baneta-Beto-Sawula basin margins (B-B′) with projected knickpoint elevation (circles) and knickzone height (circle diameter). Note the clustering of high-magnitude knickzone heights at fault-linked zones associated with local topographic peaks along the Chew Bahir and Mali-Dancha basin margins. In contrast, the Baneta-Beto-Sawula profile reveals rather low-magnitude knickzone heights and less pronounced topographic variability along the northwestern margin of the Sawula Basin. For location and orientation of the swath profiles see Fig. 4.9b.

en-échelon-arranged footwall margins of the Chew Bahir Basin and the Gofa Province reflect higher local relief values compared to the surrounding depressions. Particularly in areas with interacting faults, local relief increases to peak values of >150 m. The local base level of the discrete basins drops by about 5–10 m from the north (Sawula Basin) to the south (Chew Bahir Basin). Consistent with the low morphometric signatures and geomorphic markers, the local relief along the footwall margin of the Mali-Dancha Basin is significantly lower compared to the adjacent basins. Additionally, local-relief values progressively decrease toward the north of the Bala-Kela, Beto, and Sawula basin fault scarps where basin widths decrease (Fig. 4.12a). Field inspection of representative high local-relief locations confirmed that many of these areas coincide with fresh fault scarps, emphasizing the role of active Quaternary extension (Fig. 4.12b–e).

Catchment mean hillslope angles range from 35° (Beto Basin) to 20° (Mali-Dancha Basin) (Fig. 4.13a). The basin-averaged hillslope angles in the Beto Basin (32°) are slightly steeper compared to the Chew Bahir (31°), Baneta (30°), and Sawula (27°) basins (Fig. 4.13b). The Mali- Dancha Basin displays gentler hillslope angles (21°) than any other basin in the study area. A statistical analysis of the ratio of the 90th and 50th percentiles of hillslope angles results in similar values (<1.5) for the areas along the margins; however, the Mali-Dancha Basin displays exceptionally high values. The high ratios indicate a broad distribution of hillslope angles, including some very steep values. The 90th/50th percentile ratios of k_{sn} exhibit a gently increasing trend from

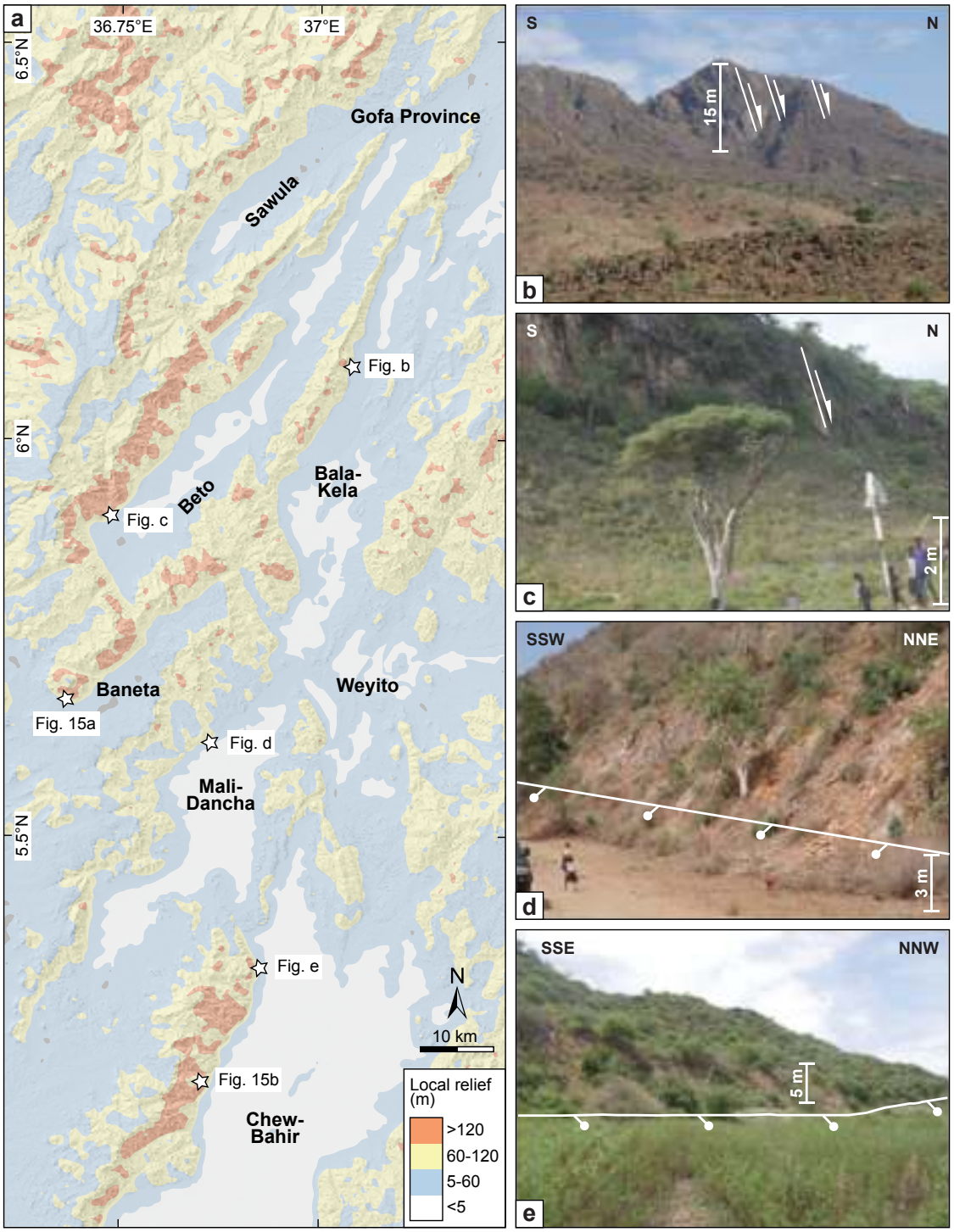

Figure 4.12: (a) Local relief within a 1-km-radius for the Chew Bahir Basin and the Gofa Province and location of photos from Bala-Kela (b), Beto (c), Mali-Dancha (d), and Chew Bahir (e). Topographic relief is well pronounced along the margins of the Chew Bahir, Baneta, and Beto basins. This topographic feature slowly vanishes toward the north.

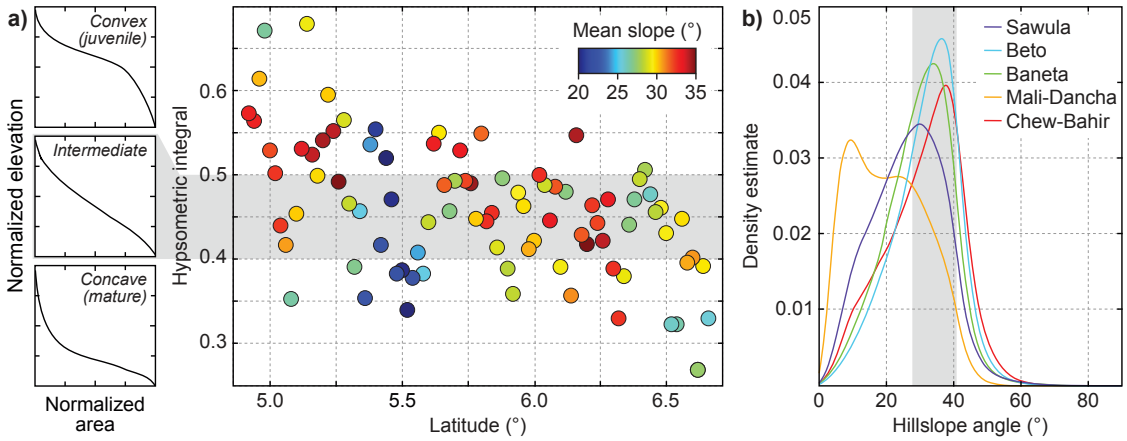

Figure 4.13: (a) Catchment hypsometric integral (color-coded according to catchment mean hillslope angle) vs. latitude and drainage-basin classification (normalized hypsometric curves, modified from El Hamdouni *et al.*, 2008). The close correspondence between the high hypsometric integral values (>0.5) and mean slope (>25°) in the lower latitudes characterize actively downcutting juvenile basins whereas the progressive decrease in hypsometric integral values (<0.5) along with mean slope in the higher latitudes reflects an increase in basin maturity toward the north. (b) Kernel density distribution of hillslope angles estimated from each pixel in the DEM from the Chew-Bahir (red), Mali-Dancha (yellow), Baneta (green), Beto (blue) and Sawula (purple) basins. The shaded area highlights statistically clustered peak (mode) values of hillslope angles.

the Sawula Basin to the Chew Bahir Basin (Fig. 4.14), indicating that the range of steepness indices becomes larger.

Table 4.1: Mean catchment-specific morphometric indices and geomorphological markers.

Catchment number	$NDVI$	AF	HI	VF	1-km-radius relief (m)	Slope (°)	k_{sn} ($m^{0.9}$)	Number of knick-points*
1	0.38	35.56	0.57	0.65	133.81	32.75	268.70	2
2	0.40	76.98	0.56	0.24	132.50	32.68	246.04	1
3	0.42	75.96	0.61	0.28	98.28	29.86	332.95	1
4	0.47	72.46	0.67	0.19	93.81	25.82	369.83	2
5	0.44	55.14	0.53	0.11	122.66	31.74	248.48	1
6	0.43	74.85	0.50	0.28	138.94	32.15	217.83	0
7	0.43	72.34	0.44	0.41	148.14	32.11	188.12	0
8	0.43	19.80	0.35	0.72	132.71	30.29	186.76	2
9	0.42	50.82	0.42	1.31	115.57	25.64	190.66	0
10	0.40	29.91	0.45	1.32	134.68	29.60	248.11	7
11	0.39	47.96	0.53	0.30	137.93	29.53	293.33	1
12	0.46	31.72	0.68	2.54	118.72	29.53	388.51	7
13	0.56	55.56	0.52	0.72	152.42	33.87	271.58	6

Table 4.1 continued from previous page

Catchment number	$NDVI$	AF	HI	VF	1-km-radius relief (m)	Slope (°)	k_{sn} ($m^{0.9}$)	Number of knick-points*
14	0.39	52.44	0.50	0.36	108.85	29.33	263.62	3
15	0.43	53.84	0.54	0.68	158.39	34.26	267.57	3
16	0.40	24.60	0.60	0.66	115.32	29.59	299.46	4
17	0.45	46.81	0.55	0.39	164.41	33.93	306.37	5
18	0.42	64.99	0.49	1.48	158.98	34.92	271.18	2
19	0.40	47.12	0.57	0.20	126.46	28.16	258.41	2
20	0.87	53.86	0.47	0.38	110.61	27.80	185.02	0
21	0.35	51.30	0.39	0.11	105.93	26.09	155.43	2
22	0.33	41.62	0.46	0.63	142.14	24.28	117.92	3
23	0.35	32.33	0.35	0.46	73.92	21.15	128.50	2
24	0.39	26.05	0.54	0.35	86.05	23.05	157.96	9
25	0.42	54.19	0.55	1.19	81.25	19.36	237.33	1
26	0.39	64.12	0.42	0.89	83.01	21.05	161.37	8
27	0.37	52.79	0.52	0.22	68.70	18.35	157.03	1
28	0.40	32.34	0.47	1.22	69.57	18.85	51.21	0
29	0.34	27.90	0.38	2.72	83.17	20.45	61.20	1
30	0.32	62.82	0.39	2.73	96.04	18.71	46.39	1
31	0.31	58.17	0.34	5.82	74.52	18.47	58.64	1
32	0.32	53.76	0.38	2.03	86.09	20.85	59.74	1
33	0.38	46.07	0.41	1.98	101.29	23.25	63.99	0
34	0.39	71.78	0.38	0.92	105.62	24.31	42.68	1
35	0.40	61.80	0.44	0.98	126.60	27.81	–	0
36	0.43	47.40	0.54	–	160.12	32.79	–	0
37	0.47	48.72	0.55	2.22	127.86	29.10	–	0
38	0.55	63.92	0.49	0.99	158.40	31.35	–	0
39	0.56	45.33	0.46	5.73	110.56	26.26	170.23	2
40	0.58	25.60	0.49	–	141.09	27.16	193.25	1
41	0.61	68.49	0.53	1.43	149.41	33.13	252.50	0
42	0.63	63.25	0.49	–	175.97	31.84	262.90	1
43	0.60	33.82	0.49	2.20	164.99	34.50	222.90	1
44	0.62	54.98	0.45	–	143.17	29.57	366.00	1
45	0.58	68.05	0.55	–	147.45	31.20	119.57	0
46	0.62	58.03	0.45	0.30	148.70	32.38	139.20	0
47	0.59	56.42	0.46	–	128.14	32.37	94.59	0
48	0.58	51.02	0.41	1.24	64.07	28.25	131.20	0
49	0.49	70.57	0.50	–	48.20	26.44	118.01	0
50	0.54	31.77	0.39	1.54	36.12	27.52	160.02	0
51	0.60	76.16	0.36	1.49	78.15	27.67	110.50	0

Table 4.1 continued from previous page

Catchment number	$NDVI$	AF	HI	VF	1-km-radius relief (m)	Slope (°)	k_{sn} ($m^{0.9}$)	Number of knick-points*
52	0.59	50.18	0.48	–	73.56	28.89	132	0
53	0.57	25.27	0.46	0.76	66.95	29.26	136.35	0
54	0.56	59.11	0.41	–	53.62	30.05	145.49	0
55	0.56	16.76	0.42	2.59	65.34	29.61	148.90	0
56	0.56	65.26	0.50	0.84	109.11	32.37	139.81	0
57	0.53	48.61	0.49	2.94	255.19	27.96	131.06	0
58	0.58	43.49	0.46	–	112.55	33.42	153.51	1
59	0.58	51.98	0.45	4.74	231.99	33.24	132.32	0
60	0.55	42.60	0.49	1.33	137.06	31.53	113.99	0
61	0.53	57.88	0.39	10.27	165.42	28.66	123.66	0
62	0.54	59.41	0.48	3.74	149.54	26.33	95.15	1
63	0.50	67.04	0.36	–	331.31	30.52	137.28	4
64	0.51	50.35	0.55	2.46	360.02	34.21	157.42	0
65	0.54	50.95	0.43	1.57	138.80	31.45	158.59	0
66	0.66	47.66	0.42	–	257.14	35.01	172.91	1
67	0.49	67.26	0.46	–	252.23	32.13	144.44	0
68	0.48	61.15	0.44	–	276.69	31.85	152.38	0
69	0.46	54.71	0.42	–	282.96	33.92	157.19	2
70	0.44	40.89	0.47	2.04	247.73	33.19	146.82	1
71	0.43	47.96	0.39	1.16	265.52	32.28	146.36	1
72	0.43	51.90	0.33	1.44	203.60	32.23	146.23	4
73	0.40	51.93	0.38	–	242.79	28.50	127.23	6
74	0.41	52.43	0.44	0.97	344.98	26.38	129.67	1
75	0.45	52.77	0.47	0.90	321.88	25.90	117.42	2
76	0.43	50.37	0.50	1.12	319.04	27.76	117.69	1
77	0.45	64.81	0.51	0.71	323.29	27.10	131.73	7
78	0.45	40.32	0.48	1.49	271.67	25.04	116.02	0
79	0.45	55.23	0.46	1.71	271.21	27.52	131.81	0
80	0.44	40.41	0.46	1.39	294.81	28.81	123.01	2
81	0.45	46.44	0.43	1.22	299.80	28.73	136.38	0
82	0.46	62.83	0.32	1.61	220.66	25.01	115.87	1
83	0.47	37.55	0.32	2.22	237.00	25.56	112.74	1
84	0.50	59.99	0.45	2.95	297.00	29.28	140.10	0
85	0.48	59.75	0.40	–	231.45	30.12	144.16	0
86	0.46	52.19	0.40	1.64	173.87	30.41	158.07	0
87	0.46	78.21	0.27	2.22	112.97	26.70	94.72	1
88	0.46	40.85	0.39	–	148.09	29.14	130.42	0
89	0.46	42.85	0.33	–	102.89	24.70	88.60	0

Table 4.1 continued from previous page

Catchment number	$NDVI$	AF	HI	VF	1-km-radius relief (m)	Slope (°)	k_{sn} ($m^{0.9}$)	Number of knick-points*

$NDVI$–Normalized difference vegetation index; AF-Asymmetry factor; HI–Hypsometric integral; VF–Valley floor to valley height ratio; k_{sn}–Normalized steepness index; *Number of knickpoints in a catchment with a knickzone height >50 m.

4.5 Discussion

4.5.1 Origin of morphometric characteristics

Based on our DEM analyses, we argue that the morphometric and geomorphic characteristics along the flanks of the Chew Bahir Basin and basin-bounding highs within the Gofa Province reflect the degree of neotectonic activity in the context of the structural overlap and kinematic linkage between the Southern Main Ethiopian Rift and the Northern Kenya Rift. The analyzed catchments from the elevated footwalls of the basin-bounding normal faults are covered by either talus from the pervasively fractured gneissic basement rocks or the less fractured Oligo-Miocene volcanics (Fig. 4.2a). Although we do not have direct measurements on variations in rock strength at different locations, the pervasive fracturing of the mechanically strong, high-grade metamorphic rocks may have ultimately resulted in similar geomorphic signatures that characterize the less fractured volcanic rocks (*e.g.*, Molnar *et al.*, 2007). Furthermore, the clustered hillslope-angle mode (peak) values from the Chew Bahir (37.5°), Baneta (33.9°), Beto (36.4°), and Sawula (30.2°) basins and the consistently similar hillslope-percentile ratios from these areas (Figs. 4.13 and 4.14) reflect similar stability thresholds along the footwalls. Such a relationship in stability threshold suggests similar rock-mass strengths of the compositionally very different rock units (*e.g.*, DiBiase *et al.*, 2018). Consequently, despite the differences in the composition and inherent mechanical strength of the rocks in the different footwall catchments and range-front areas, the crystalline basement and volcanic lithologies both constitute sectors of low lithological variability and relatively consistent substrate strength, resulting in uniform erodibility characteristics.

The TRMM-derived mean annual rainfall data indicate that there is a weak rainfall gradient from north (>1.5 m/yr) to south (>0.5 m/yr) (Fig. 4.2b). This is also reflected in the vegetation cover data ($NDVI$), with denser vegetation in the north than in the south (Figs. 4.2c, 4.3). But there is virtually no variability in rainfall, nor is there a significant variability in protective vegetation cover along the fault scarps of the Chew Bahir Basin or in the northern part of the study area. There is a step-change in between these areas as shown by the $NDVI$ vegetation cover profile (Fig. 4.3). We therefore suggest that regional rainfall variability along the first-order tectonic structures is not strong enough to exert a significant control on the observed

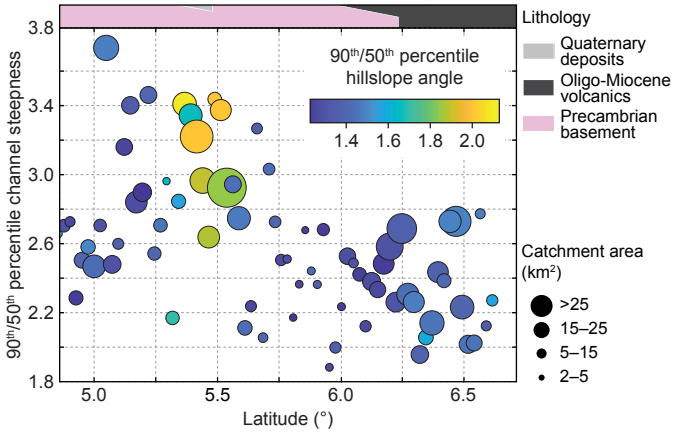

Figure 4.14: 90th/50th percentile ratio of channel steepness along the basin margins (color-coded according to the 90th/50th percentile ratio of hillslope angles) plotted against latitude. Circle size relates to catchment area. The colored bar at the top shows the distribution of lithologic units with latitude. The distribution of hillslope-angle percentile ratios, particularly ratios <1.5 suggests no significant variability in stability thresholds (a proxy for rock-mass strength; *e.g.*, DiBiase *et al.*, 2018) and a gradient in channel-steepness percentile ratios (a proxy for differences in recent tectonic activity; *e.g.*, Snyder *et al.*, 2000; Wobus *et al.*, 2006; Pérez-Peña *et al.*, 2009a, 2009b).

morphometric and geomorphic patterns in these environments. Instead, the overall arid to semi-arid conditions suggest a primarily tectonic control on the observed morphometric and geomorphic characteristics, with a possibly subordinate climatic contribution in areas of higher precipitation gradients, such as in the Sawula Basin.

In general, the formation of knickpoints might be related to baselevel change due to tectonic or erosional downstream processes (Begin *et al.*, 1981; Gardner, 1983; Hassan and Klein, 2002; Tucker and Whipple, 2002; Yanites *et al.*, 2010), lithological variations (Holland and Pickup, 1976; Neely *et al.*, 2017), or pre-existing structures (Weissel and Seidl, 1997). We note in our study area that knickpoints in footwall blocks are spatially strongly correlated with the location of nearby Quaternary faults, as inferred from the analysis of knickpoint, fault, and lithological contact locations (Fig. 4.7). The knickpoints in the Chew Bahir Basin are mostly located between ~0.2 and 1 km upstream from the normal faults that bound the footwall blocks. As lithologic differences do not exist within the analyzed catchments, except for a few catchments in the Beto Basin, the correspondence between knickpoints near the range fronts (Fig. 4.7a–d) consequently suggests that the principal knickpoints are controlled by repeated fault motion. This structural interpretation is consistent with the overall level of seismogenic normal faulting within the Chew Bahir and southern Gofa regions (Asfaw, 1990; Ayele and Arvidsson, 1997; Foster and Jackson, 1998; Fig. 4.1). Thus, repeated neotectonic fault slip at the border faults of the different fault blocks appears to be a viable mechanism for having caused base-level changes that influence channel steepness and knickpoint formation in both areas. In addition, our field observations from the Chew Bahir Basin and the southern Gofa Province have revealed co-linear knickpoints in adjacent, parallel-flowing streams (~0.5 to 1 km apart) that appear to be aligned with minor

normal faults (Fig. 4.15a and b). Furthermore, observations of active tectonic features (Figs. 4.12b–e, 4.16b and c) and the associated high-relief morphology (local relief >120 m; Fig. 4.12a) strongly suggest tectonic control of topographic growth in the region. Taken together, we emphasize that many of the aligned knickpoints are unrelated to lithologic contrasts and must have been formed by multiple, potentially seismogenic offsets and subsequent headward erosion into the footwall blocks.

4.5.2 Spatial variation in tectonic activity

Overall, deformation in the Gofa Province and the Chew Bahir Basin is spatially disparate and appears to be localized within specific areas, as suggested by the spatial variation in HI, hypsometry, VF, and k_{sn} of the studied catchments along the major basin-bounding normal faults. HI values progressively increase from the Sawula Basin (0.28) to the Chew Bahir Basin (0.68). This increase correlates with the overall change in the form of the hypsometric curves from concave shapes in the north (mature) to convex in the south (juvenile) (Fig. 4.6). Catchments with high HI (>0.5) and convex hypsometries define basins of juvenile morphology, whereas low HI (<0.5) and intermediate to concave hypsometries represent more mature, erosionally overprinted catchments (Strahler, 1952; Schumm, 1956; El Hamdouni *et al.*, 2008; Pérez-Peña *et al.*, 2009b). Thus, both the observed southward increase in HI and the change in catchment hypsometries indicate increasingly juvenile, tectonically controlled landscapes. In addition, the proportion of analyzed basins with a mature signature ($HI < 0.5$) decreases from north to south: Sawula (94%), Beto (88%), Baneta (85%), Mali-Dancha (80%), and Chew Bahir (32%). By using morphometric criteria developed by Font *et al.* (2010), we interpret the basins with $HI > 0.5$ and mean hillslope angles of >25° as actively incising catchments (mainly in the Chew Bahir Basin), whereas lower HI and mean hillslope angles correspond to much more mature, subdued catchments (mainly in the northern Gofa Province) (Fig. 4.13a). This southward increase in incision corresponds with the proposed progressive change in basin maturity and is compatible with our knickpoint analysis.

The morphometric analysis of basin asymmetry reveals a moderate increase in both the number of tilted catchments and the degree of tectonic tilting along a horizontal axis of catchments in the southern Gofa Province and the Chew Bahir Basin, which indicates an increase in fault-slip rate along the basin margin in the south.

The analysis of the valley floor width to valley height ratio (VF) documents V-shaped narrow valleys ($VF < 1$) and U-shaped wider valleys ($VF > 1$). Given the regional tectonic characteristics, the narrow valleys must have developed in response to active tectonic uplift of the footwalls, whereas the wider valleys experienced more pronounced lateral erosion during protracted tectonic quiescence (*e.g.*, El Hamdouni *et al.*, 2008). In fact, our VF analysis shows that V-shaped valleys are predominantly found in the Chew Bahir Basin, suggesting relatively high tectonic activity in this region, while the Gofa Province seems to be less active, as the catchments show

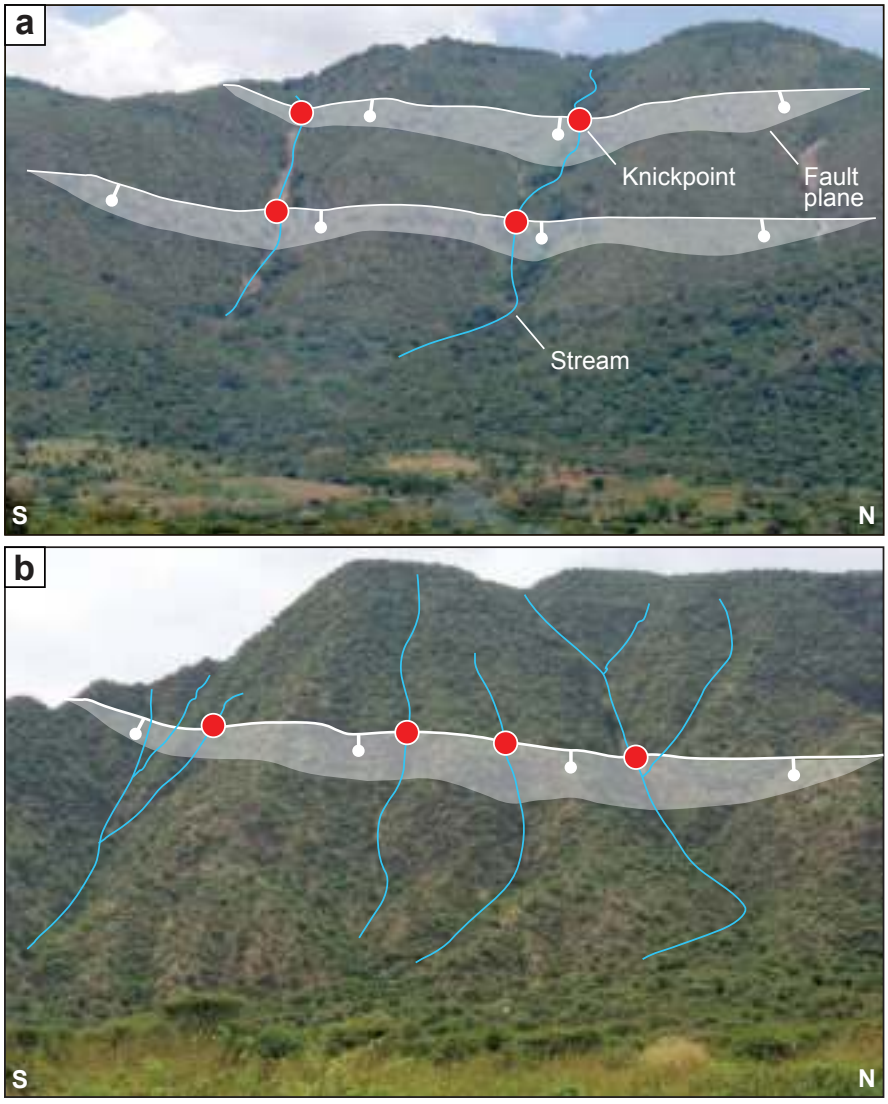

Figure 4.15: Representative field photos showing fault-crossing streams (blue), laterally distributed knickpoints (red circles), and fresh fault scarp morphology (white transparent envelope). The co-linear arrangement of knickpoints along the fresh fault scarps suggests synchronous development of knickpoints during Quaternary surface ruptures. For locations see Fig. 4.12a.

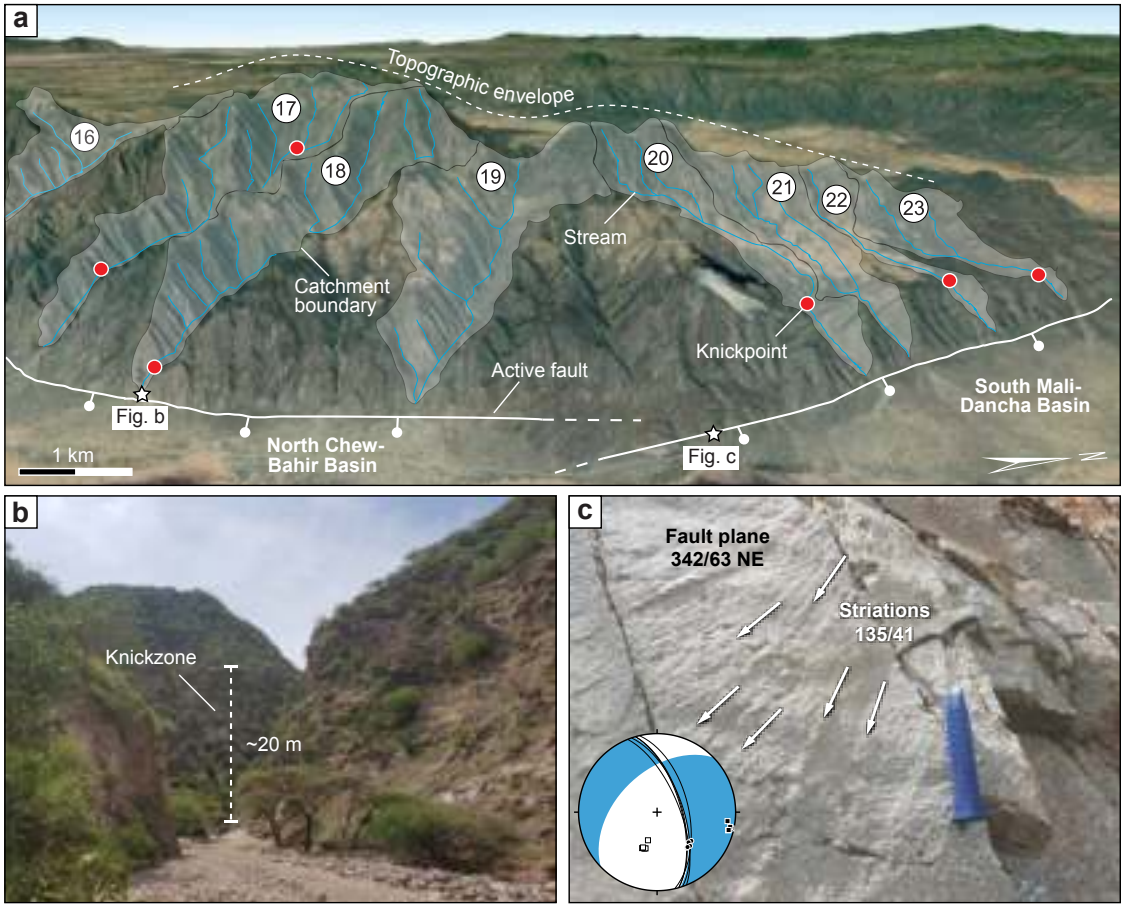

Figure 4.16: (a) Oblique view of a fault-link zone between the north-striking Chew Bahir fault and the northwest-striking Mali-Dancha Basin border fault showing catchments 16 to 23 and major knickpoints along the drainage network, local topographic envelope, and location of photos shown in panels b–c (Google Earth). (b) Knickzone close to the active mountain front. (c) Surface of an oblique-slip fault near a fault-link zone highlighted by slickenlines/striations (white arrows) and pseudo focal-plane solution from structural field data.

a wider range of VFs, with a higher proportion of U-shaped valleys, some of which may have reached a steady state.

Whereas the V-shaped valleys of the Chew Bahir Basin have knickpoints that are generally within a distance of less than 1 km from the range fronts, the more U-shaped valleys along the northern basins are characterized by knickpoints that occur exclusively in upstream areas close to the channel heads within the footwall blocks (Figs. 4.5c, 4.9b, 4.11). In combination, the spatial clustering of high k_{sn} values (>300 $m^{0.9}$) and knickzone heights of >100 m (Fig. 4.9) thus reflects an elevated level of tectonic activity in the Chew Bahir Basin and the southern Gofa Province. In contrast, low values of k_{sn}, local relief, and mean hillslope angles at the Mali-Dancha Basin appear to be controlled by inherited linear basement structures aligned with the channels (Fig. 4.2a).

Finally, the distribution of regional seismicity suggests a spatial variation in tectonic activity along the strike of the structures of the Gofa Province and the Chew Bahir Basin, consistent with the systematic north (mature) to south (juvenile) changes in catchment characteristics and an overall gradient in tectonic activity in the same direction. Importantly, this is also indicated by the southward increase in the amount of extension (*e.g.*, Philippon *et al.*, 2014; Zwaan and Schreurs, 2020), which may result from ongoing tectonic interaction of extensional structures between the Southern Main Ethiopian Rift and the Northern Kenya Rift (Ebinger *et al.*, 2000; Corti *et al.*, 2019).

4.5.3 Implications for fault growth, fault interaction, and structural influence on environmental conditions in the Southern Main Ethiopian Rift

The fault evolution along the rift margins of the Chew Bahir Basin and the Gofa Province can be distinguished in terms of two phases: first, the formation of isolated fault segments during initial rifting; and second, a convergence and termination of a few fault tips within the fault segments through protracted tectonic interaction. Mean local relief, normalized channel-steepness indices, knickpoints, and longitudinal stream profiles support this interpretation. For example, local relief progressively decreases toward the north of the Sawula, Beto, and Bala-Kela basins (Fig. 4.12). This phenomenon of topographic minima is likely due to a long-term slip deficit of the faults (*e.g.*, Cartwright *et al.*, 1995) and is indicative of fault terminations, consistent with basin narrowing.

In contrast, mean local relief varies along strike of the basin-bounding faults and increases in areas of fault linkage. Similarly, catchment mean k_{sn} values vary along strike of the bounding faults and follow the trend of the local relief (Fig. 4.17). This increase in both morphometric indicators suggests enhanced tectonic uplift and current strain localization at fault-link zones of formerly isolated fault segments. This interpretation is supported by empirical studies that demonstrate a positive correlation between topographic relief, k_{sn}, and rock-uplift rate (*e.g.*, Kirby *et al.*, 2007; Miller *et al.*, 2013). The peaks in local relief and k_{sn} also correspond with the maximum topographic envelope (Figs. 4.11a–b, 4.16a), which is consistent with the expected

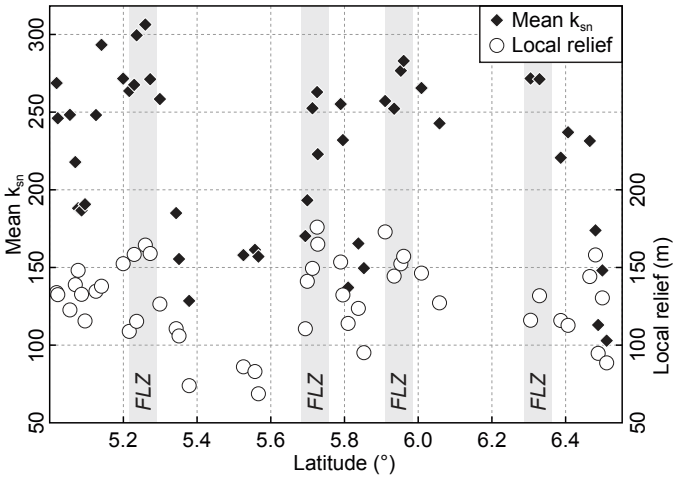

Figure 4.17: Catchment average local relief (1-km-radius) and mean k_{sn} plotted against latitude. Shaded regions highlight fault-link zones (FLZ). The parallel increase in local relief and mean k_{sn} values toward fault-linked zones reflects ongoing fault interaction in the region.

displacement at fault-link zones between two formerly independent fault systems (*e.g.*, Scholz *et al.*, 1993; Cartwright *et al.*, 1995; Dawers and Anders, 1995).

Multiple slope breaks along the stream profiles indicate episodic rupturing (Ewiak *et al.*, 2015) at fault-link zones of the en-échelon basins and suggest progressive deformation at these locations. The spatial distribution of knickpoint-elevation differences near the range fronts (Fig. 4.10b) indicates a north-to-south increase in recent tectonic activity within the Gofa Province and the Chew Bahir Basin. Moreover, the systematic decrease in knickzone height and a shift of knickpoints toward the channel head in areas of fault linkage in the Gofa Province indicates that current uplift rates in the north must be rather low. The higher rainfall rate at the channel head in the Sawula Basin might additionally contribute to the more pronounced upstream migration of knickpoints in this basin. In contrast, southward-increasing knickzone heights (Figs. 4.7a-k, 4.10a) and other geomorphic indicators, such as HI, and AF (Fig. 4.5a–b) suggest a higher level of tectonic activity in this region.

In general, our spatiotemporal morphotectonic assessments are consistent with earlier studies that inferred decreased recent fault activity in the northern Gofa Province and strain localization in the Chew Bahir Basin (Philippon *et al.*, 2014), as well as fault termination in the northern Beto Basin (Boone *et al.*, 2019). By using a broad spectrum of morphometric indicators in addition to the concept of knickzones applied by Philippon *et al.* (2014) we were able to increase the resolution of geomorphic observations that allow us to evaluate the complex Quaternary regional tectonic activity of the broadly rifted zone in greater detail. In addition, we were able to decipher the nature of tectonic interactions between adjacent en-échelon basins that had previously not been recognized. Importantly, field evidence and well-developed morphometric indices (*e.g.*, local relief and k_{sn}) in the northern part of the Gofa Province have furthermore

revealed signatures of local tectonic activity, whereas these areas were originally characterized as being tectonically inactive (*e.g.*, Wolde-Gabriel and Aronson, 1987; Ebinger *et al.*, 2000; Philippon *et al.*, 2014; Zwaan and Schreurs, 2020).

From a paleoenvironmental perspective the ongoing extension and tectonic subsidence in the broadly rifted zone has generated favorable conditions for hydrological connectivity within this extensional province; Quaternary tectonic activity is responsible for a structural and geomorphic framework of transiently connected hydrologic basins along the rift axis that are currently isolated, but that were hydrologically linked during times of greater moisture availability and precipitation in the recent geological past (Butzer *et al.*, 1972). The Chew Bahir Basin is the southernmost fault-bounded basin of the Southern Main Ethiopian Rift that has been hydrologically connected with different sub-basins of the Ethiopian Rift to the north and Lake Turkana to the southwest, such as during the Holocene African Humid Period (Butzer *et al.*, 1972; Garcin *et al.*, 2012; Fischer *et al.*, 2020). During this period of increased moisture availability, the Chew Bahir Basin constituted an important pathway between the basins of the Ethiopian Rift, Lake Turkana, and the White Nile, which helped sustain hydrologic connectivity and fostered the dispersal of species (Nyamweru, 1989; van der Lubbe *et al.*, 2017). Similar observations regarding tectonically disconnected catchments and transiently connected basins were reported from rifted areas farther south (Dommain *et al.*, 2018; Olivotos *et al.*, 2021). For example, dating the highstands of the Mweru paleolake at the Zambia-DR Congo border, suggest strong tectonic control of lake-basin formation and superposed enhanced episodic rainfall and runoff that allowed basin linkage (Olivotos *et al.*, 2021).

With respect to the overall level of tectonic activity in the transition between the Northern Kenya Rift and the Southern Main Ethiopian Rift, field observations and satellite image analysis reveal that Holocene alluvial-fan deposits overlie lacustrine shorelines in the Chew Bahir Basin that formed during the African Humid Period (Foerster *et al.*, 2012). Interestingly, these alluvial fans do not display normal-fault scarps or other deformation features. This is in stark contrast to the Lake Turkana and Suguta basins farther south (Fig. 4.18), where normal faults affecting deposits and landforms of the African Humid Period are common (Melnick *et al.*, 2012). This implies that fault-slip rates must be lower in the Chew Bahir Basin. This difference in the degree of Holocene tectonic activity supports our geomorphic results and suggests that the regional extension rate of ~4 mm/yr (i.e., Stamps *et al.*, 2008; Saria *et al.*, 2014) results from low slip rates along many, but widely distributed faults across the ~25-km-wide Chew Bahir Basin. In contrast, in the structurally more developed Northern Kenya Rift, deformation is restricted to the ~30-km-wide inner graben (Dunkley *et al.*, 1993; Melnick *et al.*, 2012).

Taken together, our observations contribute toward a growing body of evidence that the Southern Main Ethiopian Rift is a complex kinematic transfer zone within a nascent extensional plate boundary, where young tectonic activity and seismicity document ongoing southward rift propagation and linkage with the northern sectors of the Kenya Rift. In addition, our study shows the versatility of combined morphometric and field-based structural observations in assessing the degree of tectonic activity in extensional geological provinces.

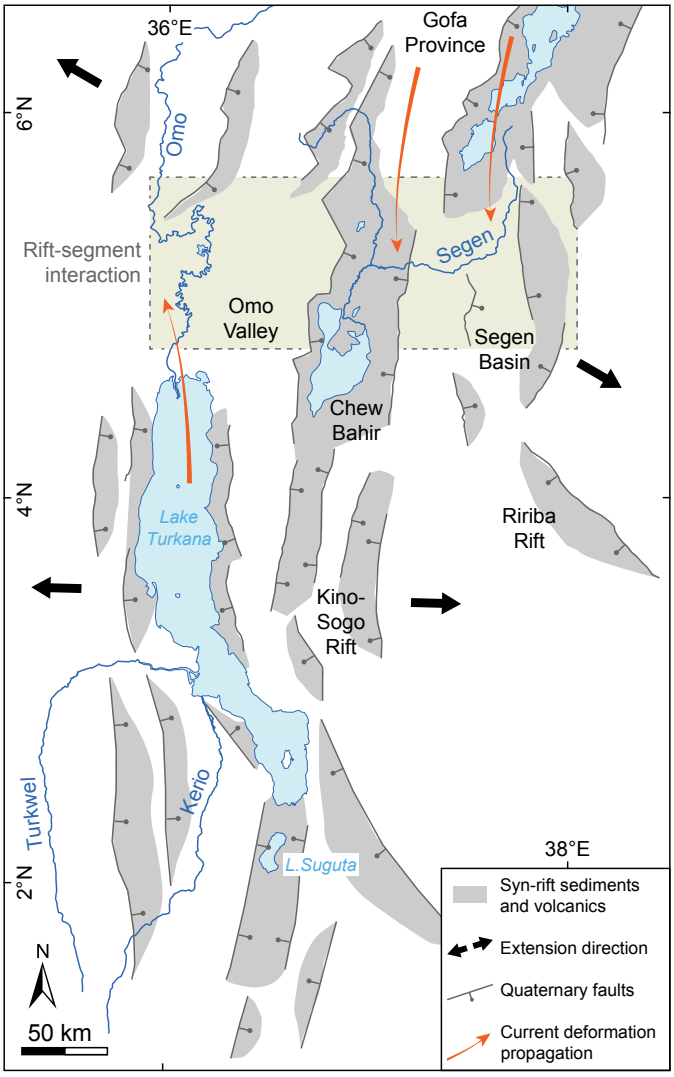

Figure 4.18: Simplified structural map showing the main neotectonic structures within the transfer zone between the Southern Main Ethiopian Rift and the Northern Kenya Rift; thin, orange arrows denote current direction of fault propagation.

4.6 Conclusion

Morphometric indices and geomorphic markers extracted from 12 m TanDEM-X data combined with information from geologic, seismic, climatic, and field observation have been used to investigate the spatiotemporal landscape evolution and to characterize fault activity in the Chew Bahir Basin and the Gofa Province. Our results show that morphometric indices, topographic signatures, and geomorphic markers vary systematically along strike of the left-stepping en-échelon Chew Bahir Basin and the Gofa Province. The detected morphometric and geomorphic anomalies allowed us to reconstruct the Quaternary tectonic activity and its impact on the landscape evolution of this tectonically complex region. Our principal findings are:

1. The morphometric and geomorphic anomalies in the Chew Bahir Basin and the Gofa Province are mainly of tectonic origin as suggested by our analysis of TanDEM-X data, geologic and seismicity data, remote sensing imagery, and field observations.
2. The parallel to sub-parallel orientation of inherited basement fabrics controls the pattern of channels in the Mali-Dancha Basin. These areas are associated with anomalously low values of local relief, hillslope angles, and normalized channel steepness indices.
3. Tectonic activity progressively increases from north to south in the investigated area, and current deformation is localized in the Chew Bahir Basin and southern Gofa Province, as indicated by an along-strike, southward increase in the values of different morphometric indices and frequent geomorphic features typical of active tectonism. This pattern of deformation is consistent with the previously suggested tectonic interaction between the Southern Main Ethiopian Rift and the Northern Kenya Rift.
4. The strain localization in areas of fault interaction and within relay zones indicates that initially isolated fault segments have been linked over time.

4.7 References

Ahnert, F., 1970. Functional relationships between denudation, relief, and uplift in large, mid-latitude drainage basins. Am. J. Sci. 268, 243–263.

Asfaw, L.M., 1990. Implication of shear deformation and earthquake distribution in the East African Rift between 4°N and 6°N. J. Afr. Earth Sci. 10, 745–751.

Ayele, A., Arvidsson, R., 1997. Fault mechanisms and tectonic implication of the 1985–1987 earthquake sequence in south-western Ethiopia. J. Seismol. 1, 383–394.

Bagha, N., Arian, M., Ghorashi, M., Pourkermani, M., Hamdouni, R.E., Solgi, A., 2014. Evaluation of relative tectonic activity in the Tehran basin, central Alborz, northern Iran. Geomorphology 213, 66–87.

Balestrieri, M.L., Bonini, M., Corti, G., Sani, F., Philippon, M., 2016. A refinement of the chronology of rift-related faulting in the Broadly Rifted Zone, southern Ethiopia, through apatite fission-track analysis. Tectonophysics 671, 42–55.

Begin, Z.B., Meyer, D.F., Schumm, S.A., 1981. Development of longitudinal profiles of alluvial channels in response to base-level lowering. Earth Surf. Process. 6, 49–68.

Bishop, P., Hoey, T.B., Jansen, J.D., Artza, I.L., 2005. Knickpoint recession rate and catchment area: the case of uplifted rivers in Eastern Scotland. Earth Surf. Process. 30, 767–778.

Boccaletti, M., Bonini, M., Mazzuoli, R., Abebe, B., Piccardi, L., Tortorici, L., 1998. Quaternary oblique extensional tectonics in the Ethiopian Rift (Horn of Africa). Tectonophysics 287, 97–116.

Boers, N., Bookhagen, B., Marengo, J., Marwan, N., von Storch, J.S., Kurths, J., 2015. Extreme rainfall of the South American Monsoon System: a dataset comparison using complex networks. J. Clim. 28, 1031–1056.

Bonini, M., Corti, G., Innocenti, F., Manetti, P., Mazzarini, F., Abebe, T., Pecskay, Z., 2005. Evolution of the Main Ethiopian Rift in the frame of Afar and Kenya rifts propagation. Tectonics 24, TC1007.

Bookhagen, B., 2010. Appearance of extreme monsoonal rainfall events and their impact on erosion in the Himalaya. Geomat. Nat. Haz. Risk 1, 37–50.

Bookhagen, B., Burbank, D.W., 2010. Toward a complete Himalayan hydrological budget: spatiotemporal distribution of snowmelt and rainfall and their impact on river discharge. J. Geophys. Res. Earth Surf. 115, F03019.

Bookhagen, B., Strecker, M.R., 2012. Spatiotemporal trends in erosion rates across a pronounced rainfall gradient: examples from the southern Central Andes. Earth Planet. Sci. Lett. 327–328, 97–110.

Boone, S.C., Balestrieri, M.-L., Kohn, B.P., Corti, G., Gleadow, A.J.W., Seiler, C., 2019. Tectonothermal evolution of the broadly rifted zone, Ethiopian Rift. Tectonics 38, 1070–1100.

Bosworth, W., Morley, C.K., 1994. Structural and stratigraphic evolution of the Anza rift, Kenya. Tectonophysics 236, 93–115.

Bosworth, W., Strecker, M.R., 1997. Stress field changes in the Afro-Arabian rift system during the Miocene to Recent period. Tectonophysics 278, 47–62.

Boulton, S.J., Whittaker, A.C., 2009. Quantifying the slip rates, spatial distribution and evolution of active normal faults from geomorphic analysis: field examples from an oblique-extensional graben, southern Turkey. Geomorphology 104, 299–316.

Brune, S., Corti, G., Ranalli, G., 2017. Controls of inherited lithospheric heterogeneity on rift linkage: numerical and analog models of interaction between the Kenyan and Ethiopian rifts across the Turkana depression. Tectonics 36, 1767–1786.

Buck, W.R., 1991. Modes of continental lithospheric extension. J. Geophys. Res. Solid Earth 96, 20161–20178.

Bull, W.B., McFadden, L.D., 1977. Tectonic geomorphology north and south of the Garlock Fault, California. In: Doehring, D.O. (Ed.), Geomorphology in Arid Regions: A Proceedings Volume of the 8th Annual Geomorphology Symposium. State University of New York, Binghamton, pp. 115–138.

Bull, W.B., 2007. Tectonic Geomorphology of Mountains: A New Approach to Paleoseismology. John Wiley & Sons, Ltd.

Burbank, D.W., Anderson, R.S., 2011. Tectonic Geomorphology. John Wiley & Sons, Ltd.

Butzer, K.W., Isaac, G.L., Richardson, J.L., Washbourn-Kamau, C., 1972. Radiocarbon dating of East African lake levels. Science 175, 1069–1076.

Cartwright, J.A., Trudgill, B.D., Mansfield, C.S., 1995. Fault growth by segment linkage: an explanation for scatter in maximum displacement and trace length data from the Canyonlands Grabens of SE Utah. J. Struct. Geol. 17, 1319–1326.

Chen, Y.-C., Sung, Q., Cheng, K.-Y., 2003. Along-strike variations of morphotectonic features in the Western Foothills of Taiwan: tectonic implications based on streamgradient and hypsometric analysis. Geomorphology 56, 109–137.

Chorowicz, J., 2005. The East African rift system. J. Afr. Earth Sci. 43, 379–410.

Corti, G., 2012. Evolution and characteristics of continental rifting: analog modelinginspired view and comparison with examples from the East African Rift System. Tectonophysics 522–523, 1–33.

Corti, G., Cioni, R., Franceschini, Z., Sani, F., Scaillet, S., Molin, P., Isola, I., Mazzarini, F., Brune, S., Keir, D., Erbello, A., Muluneh, A., Illsley-Kemp, F., Glerum, A., 2019. Aborted propagation of the Ethiopian rift caused by linkage with the Kenyan rift. Nat. Commun. 10, 1309.

Cowie, P.A., 1998. A healing–reloading feedback control on the growth rate of seismogenic faults. J. Struct. Geol. 20, 1075–1087.

Cox, R.T., 1994. Analysis of drainage-basin symmetry as a rapid technique to identify areas of possible quaternary tilt-block tectonics: an example from the Mississippi Embayment. Geol. Soc. Am. Bull. 106, 571–581.

Davidson, A., 1983. The Omo river project, reconnaissance geology and geochemistry of parts of Ilubabor, Kefa, Gemu Gofa and Sidamo, Ethiopia. In: Ethiopian Institute Geological Surveys Bulletin, 2, pp. 1–89.

Davidson, A., Rex, D.C., 1980. Age of volcanism and rifting in southwestern Ethiopia. Nature 283, 657–658. https://doi.org/10.1038/283657a0. Davis, W.M., 1899. The geographical cycle. Geogr. J. 14, 481–504.

Dawers, N.H., Anders, M.H., 1995. Displacement-length scaling and fault linkage. J. Struct. Geol. 17, 607–614.

de Araújo Monteiro, K., Missura, R., de Barros Correa, A.C., 2010. Application of the Hack index–or stream length-gradient index (SL index)–to the Tracunhaém river watershed, Pernambuco, Brazil. Geociências 29, 533–539.

DeMets, C., Merkouriev, S., 2016. High-resolution estimates of Nubia-Somalia plate motion since 20 Ma from reconstructions of the Southwest Indian Ridge, Red Sea and Gulf of Aden. Geophys. J. Int. 207, 317–332.

Densmore, A.L., 2004. Footwall topographic development during continental extension. J. Geophys. Res. Earth Surf. 109, F03001.

Densmore, A.L., Gupta, S., Allen, P.A., Dawers, N.H., 2007. Transient landscapes at fault tips. J. Geophys. Res. Earth Surf. 112, F03S08.

DiBiase, R.A., Rossi, M.W., Neely, A.B., 2018. Fracture density and grain size controls on the relief structure of bedrock landscapes. Geology 46, 399–402.

DiBiase, R.A., Whipple, K.X., Heimsath, A.M., Ouimet, W.B., 2010. Landscape form and millennial erosion rates in the San Gabriel Mountains, CA. Earth Planet. Sci. Lett. 289, 134–144.

Dommain, R., Garcin, Y., Potts, R., Riedl, S., Strecker, M.R., 2018. Rift-basin compartmentalization, fluvial connectivity and changing environments: tectonic and climatic forcing of environmental conditions during hominin evolution in the East African Rift System. In: Pardee Symposium; Human Evolution and Environmental History in Africa: 25 Years of Transformative Research. Geol. Soc. America Annual Meeting, Indianapolis, Abstract Vol., 223-2. https://gsa.confex.com/gsa/2018A M/webprogram/Paper320056.html.

D'Odorico, P., Gonsamo, A., Damm, A., Schaepman, M.E., 2013. Experimental evaluation of Sentinel-2 spectral response functions for NDVI time-series continuity. IEEE Trans. Geosci. Remote 51, 1336–1348.

Dunkley, P., Smith, M., Allen, D.J., Darling, W.G., 1993. The geothermal activity and geology of the northern sector of the Kenya Rift Valley. In: British Geological Survey Research Report SC/93/1, p. 202. https://nora.nerc.ac.uk/id/eprint/507920/.

Ebinger, C., Scholz, C.A., 2012. Continental rift basins: the East African perspective. In: Busby, C., Azor, A. (Eds.), Tectonics of Sedimentary Basins: Recent Advances. Wiley- Blackwell, pp. 183–208.

Ebinger, C.J., Yemane, T., Harding, D.J., Tesfaye, S., Kelley, S., Rex, D.C., 2000. Rift deflection, migration, and propagation: linkage of the Ethiopian and Eastern rifts, Africa. Geol. Soc. Am. Bull. 112, 163–176.

Ebinger, C.J., Yemane, T., Wolde-Gabriel, G., Aronson, J.L., Walter, R.C., 1993. Late Eocene-Recent volcanism and faulting in the southern main Ethiopian rift. J. Geol. Soc. Lond. 150, 99–108.

El Hamdouni, R., Irigaray, C., Fernández, T., Chacón, J., Keller, E.A., 2008. Assessment of relative active tectonics, southwest border of the Sierra Nevada (southern Spain). Geomorphology 96, 150–173.

Emishaw, L., Abdelsalam, M.G., 2019. Development of Late Jurassic-Early Paleogene and Neogene-Quaternary rifts within the Turkana Depression, East Africa from satellite gravity data. Tectonics 38, 2358–2377.

Emishaw, L., Laó-Dávila, D.A., Abdelsalam, M.G., Atekwana, E.A., Gao, S.S., 2017. Evolution of the broadly rifted zone in southern Ethiopia through gravitational collapse and extension of dynamic topography. Tectonophysics 699, 213–226.

Erbello, A., Corti, G., Agostini, A., Sani, F., Kidane, T., Buccianti, A., 2016. Modeling along-axis variations in fault architecture in the Main Ethiopian Rift: implications for Nubia-Somalia kinematics. J. Geodyn. 102, 24–38.

Ewiak, O., Victor, P., Oncken, O., 2015. Investigating multiple fault rupture at the Salar del Carmen segment of the Atacama Fault System (northern Chile): fault scarp morphology and knickpoint analysis. Tectonics 34, 187–212.

Fernandes, R.M.S., Ambrosius, B.A.C., Noomen, R., Bastos, L., Combrinck, L., Miranda, J. M., Spakman, W., 2004. Angular velocities of Nubia and Somalia from continuous GPS data: implications on present-day relative kinematics. Earth Planet. Sci. Lett. 222, 197–208.

Fischer, M.L., Markowska, M., Bachofer, F., Foerster, V.E., Asrat, A., Zielhofer, C., Trauth, M.H., Junginger, A., 2020. Determining the pace and magnitude of lake level changes in Southern Ethiopia over the last 20,000 years using lake balance modeling and SEBAL. Front. Earth Sci. 8, 197.

Foerster, V., Junginger, A., Langkamp, O., Gebru, T., Asrat, A., Umer, M., Lamb, H.F., Wennrich, V., Rethemeyer, J., Nowaczyk, N., Trauth, M.H., Schaebitz, F., 2012. Climatic change recorded in the

sediments of the Chew Bahir basin, southern Ethiopia, during the last 45,000 years. Quat. Int. 274, 25–37.

Font, M., Amorese, D., Lagarde, J.-L., 2010. DEM and GIS analysis of the stream gradient index to evaluate effects of tectonics: the Normandy intraplate area (NW France). Geomorphology 119, 172–180.

Forte, A.M., Whipple, K.X., 2019. Short communication: the topographic analysis kit (TAK) for TopoToolbox. Earth Surf. Dyn. 7, 87–95.

Foster, A.N., Jackson, J.A., 1998. Source parameters of large African earthquakes: implications for crustal rheology and regional kinematics. Geophys. J. Int. 134, 422–448.

Franceschini, Z., Cioni, R., Scaillet, S., Corti, G., Sani, F., Isola, I., Mazzarini, F., Duval, F., Erbello, A., Muluneh, A., Brune, S., 2020. Recent volcano-tectonic activity of the Ririba Rift and the evolution of rifting in South Ethiopia. J. Volcanol. Geotherm. Res. 403, 106989.

Gallen, S.F., Wegmann, K.W., 2017. River profile response to normal fault growth and linkage: an example from the Hellenic forearc of south-central Crete,Greece. Earth Surf. Dyn. 5, 161–186.

Garcin, Y., Melnick, D., Strecker, M.R., Olago, D., Tiercelin, J.-J., 2012. East African mid- Holocene wet–dry transition recorded in palaeo-shorelines of Lake Turkana, northern Kenya Rift. Earth Planet. Sci. Lett. 331–332, 322–334.

Garcin, Y., Schildgen, T.F., Acosta, V.T., Melnick, D., Guillemoteau, J., Willenbring, J., Strecker, M.R., 2017. Short-lived increase in erosion during the African Humid Period: evidence from the northern Kenya Rift. Earth Planet. Sci. Lett. 459, 58–69.

Gardner, T.W., 1983. Experimental study of knickpoint and longitudinal profile evolution in cohesive, homogeneous material. Geol. Soc. Am. Bull. 94, 664.

Gasse, F., 2000. Hydrological changes in the African tropics since the Last Glacial Maximum. Quat. Sci. Rev. 19, 189–211.

Gawthorpe, R.L., Jackson, C.A.-L., Young, M.J., Sharp, I.R., Moustafa, A.R., Leppard, C. W., 2003. Normal fault growth, displacement localisation and the evolution of normal fault populations: the Hammam Faraun fault block, Suez Rift,Egypt. J. Struct. Geol. 25, 883–895.

Gawthorpe, R.L., Leeder, M.R., 2000. Tectono-sedimentary evolution of active extensional basins. Basin Res. 12, 195–218.

George, R., Rogers, N., 2002. Plume dynamics beneath the African Plate inferred from the geochemistry of the Tertiary basalts of southern Ethiopia. Contrib. Mineral. Petrol. 144, 286–304.

Goldsworthy, M., Jackson, J., 2000. Active normal fault evolution in Greece revealed by geomorphology and drainage patterns. J. Geol. Soc. Lond. 157, 967–981.

Gouin, P., 1979. In: Earthquake History of Ethiopia and the Horn of Africa. International Development Research Centre, Ottawa, ON, CA, p. 259.

Gupta, S., Cowie, P.A., Dawers, N.H., Underhill, J.R., 1998. A mechanism to explain riftbasin subsidence and stratigraphic patterns through fault-array evolution. Geology 26, 595.

Hack, J.T., 1957. Studies of longitudinal stream profiles in Virginia and Maryland. Geol. Surv. Prof. Pap. 294, 45–94.

Hare, P.W., Gardner, T.W., 1985. Geomorphic indicators of vertical Neotectonism along converging plate margins, Nicoya Peninsula, Costa Rica. In: Morisawa, M., Hack, J.T. (Eds.), Tectonic Geomorphology: Proceedings of the 15th Annual Binghamton Geomorphology Symposium. Allen & Unwin, Boston, pp. 123–134.

Hassan, M.A., Klein, M., 2002. Fluvial adjustment of the Lower Jordan River to a drop in the Dead Sea level. Geomorphology 45, 21–33.

Heidbach, O., Rajabi, M., Cui, X., Fuchs, K., Müller, B., Reinecker, J., Reiter, K., Tingay, M., Wenzel, F., Xie, F., Ziegler, M.O., Zoback, M.-L., Zoback, M., 2018. The World Stress Map database release 2016: crustal stress pattern across scales. Tectonophysics 744, 484–498.

Holland, W.N., Pickup, G., 1976. Flume study of knickpoint development in stratified sediment. Geol. Soc. Am. Bull. 87, 76–82.

Kaboth-Bahr, S., Gosling, W.D., Vogelsang, R., Bahr, A., Scerri, E.M.L., Asrat, A., Cohen, A.S., Düsing, W., Foerster, V., Lamb, H.F., Maslin, M.A., Roberts, H.M., Sch¨abitz, F., Trauth, M.H., 2021. Paleo-ENSO influence on African environments and early modern humans. Proc. Natl. Acad. Sci. 118, e2018277118.

Kent, E., Boulton, S.J., Whittaker, A.C., Stewart, I.S., Alçiçek, M.C., 2017. Normal fault growth and linkage in the Gediz (Alas¸ehir) Graben, Western Turkey, revealed by transient river long-profiles and slope-break knickpoints. Earth Surf. Process. 42, 836–852.

Kirby, E., Johnson, C., Furlong, K., Heimsath, A., 2007. Transient channel incision along Bolinas Ridge, California: evidence for differential rock uplift adjacent to the San Andreas Fault. J. Geophys. Res. Earth Surf. 112, F03S07.

Kirby, E., Whipple, K.X., 2012. Expression of active tectonics in erosional landscapes. J. Struct. Geol. 44, 54–75.

Koehn, D., Lindenfeld, M., Rümpker, G., Aanyu, K., Haines, S., Passchier, C.W., Sachau, T., 2010. Active transsection faults in rift transfer zones: evidence for complex stress fields and implications for crustal fragmentation processes in the western branch of the East African Rift. Int. J. Earth Sci. 99, 1633–1642.

Kogan, L., Fisseha, S., Bendick, R., Reilinger, R., McClusky, S., King, R., Solomon, T., 2012. Lithospheric strength and strain localization in continental extension from observations of the East African Rift. J. Geophys. Res. Solid Earth 117.

Kothyari, G.C., Singh, A.P., Mishra, S., Kandregula, R.S., Chaudhary, I., Chauhan, G., 2018. Evolution of drainage in response to brittle - ductile dynamics and surface processes in Kachchh Rift Basin, Western India. In: Sharkov, E.V. (Ed.), Tectonics - Problems of Regional Settings. IntechOpen. https://doi.org/10.5772/ intechopen.73653.

Leeder, M.R., Jackson, J.A., 1993. The interaction between normal faulting and drainage in active extensional basins, with examples from the western United States and central Greece. Basin Res. 5, 79–102.

Levin, N.E., Zipser, E.J., Cerling, T.E., 2009. Isotopic composition of waters from Ethiopia and Kenya: insights into moisture sources for eastern Africa. J. Geophys. Res. Atmos. 114, D23306.

Levitte, D., Columba, J., Mohr, P.A., 1974. Reconnaissance geology of the Amaro horst, southern Ethiopia. Geol. Soc. Am. Bull. 85, 417–422.

Lifton, N.A., Chase, C.G., 1992. Tectonic, climatic and lithologic influences on landscape fractal dimension and hypsometry: implications for landscape evolution in the San Gabriel Mountains, California. Geomorphology 5, 77–114.

Melnick, D., Garcin, Y., Quinteros, J., Strecker, M.R., Olago, D., Tiercelin, J.-J., 2012. Steady rifting in northern Kenya inferred from deformed Holocene lake shorelines of the Suguta and Turkana basins. Earth Planet. Sci. Lett. 331–332, 335–346.

Merritts, D., Ellis, M., 1994. Introduction to special section on tectonics and topography. J. Geophys. Res. Solid Earth 99, 12135–12141.

Miller, S.R., Sak, P.B., Kirby, E., Bierman, P.R., 2013. Neogene rejuvenation of central Appalachian topography: evidence for differential rock uplift from stream profiles and erosion rates. Earth Planet. Sci. Lett. 369–370, 1–12.

Molnar, P., Anderson, R.S., Anderson, S.P., 2007. Tectonics, fracturing of rocks, and erosion. J. Geophys. Res. 112, F03014.

Montgomery, D.R., Brandon, M.T., 2002. Topographic controls on erosion rates in tectonically active mountain ranges. Earth Planet. Sci. Lett. 201, 481–489.

Morley, C.K., Nelson, R.A., Patton, T.L., Munn, S.G., 1990. Transfer zones in the East African Rift System and their relevance to hydrocarbon exploration in rifts. Am. Assoc. Pet. Geol. Bull. 74, 1234–1253.

Morley, C.K., Wescott, W.A., Stone, D.M., Harper, R.M., Wigger, S.T., Karanja, F.M., 1992. Tectonic evolution of the northern Kenyan Rift. J. Geol. Soc. Lond. 149, 333–348.

Muluneh, A.A., Cuffaro, M., Doglioni, C., 2014. Left-lateral transtension along the Ethiopian Rift and constrains on the mantle-reference plate motions. Tectonophysics 632, 21–31.

Neely, A.B., Bookhagen, B., Burbank, D.W., 2017. An automated knickzone selection algorithm (KZ-Picker) to analyze transient landscapes: calibration and validation. J. Geophys. Res. Earth Surf. 122, 1236–1261.

Nelson, R.A., Patton, T.L., Morley, C.K., 1992. Rift-segment interaction and its relation to hydrocarbon exploration in continental rift systems. Am. Assoc. Pet. Geol. Bull. 76, 1153–1169.

Nicholson, S.E., 1996. A review of climate dynamics and climate variability in eastern Africa. In: Johnson, T.C., Odada, E.O. (Eds.), Limnology, Climatology and Paleoclimatology of the East African Lakes. CRC Press, London, pp. 25–56.

Nyamweru, C., 1989. New evidence for the former extent of the Nile drainage system. Geogr. J. 155, 179.

Olen, S.M., Bookhagen, B., Hoffmann, B., Sachse, D., Adhikari, D.P., Strecker, M.R., 2015. Understanding erosion rates in the Himalayan orogen: a case study from the Arun Valley. J. Geophys. Res. Earth Surf. 120, 2080–2102.

Olivotos, S., Niedermann, S., Flügel, T., Mouslopoulou, V., Merchel, S., Cotterill, F., Bookhagen, B., G¨artner, A., Rugel, G., Scharf, A., Nadeau, M.-J., Braucher, R., Seiler, M., 2021. Quaternary landscape evolution in a tectonically active rift basin (paleo-lake Mweru, south-central Africa). Geomorphology 381, 107669.

Penck, W., 1924. Die morphologische Analyse: ein Kapitel der physikalischen Geologie. In: Geographische Abhandlungen, 2, p. 283.

Pérez-Peña, J.V., Azañón, J.M., Azor, A., 2009. CalHypso: an ArcGIS extension to calculate hypsometric curves and their statistical moments. Applications to drainage basin analysis in SE Spain. Comput. Geosci. 35, 1214–1223.

Pérez-Peña, J.V., Azañón, J.M., Azor, A., Delgado, J., González-Lodeiro, F., 2009. Spatial analysis of stream power using GIS: SLk anomaly maps. Earth Surf. Process. 34, 16–25.

Philippon, M., Corti, G., Sani, F., Bonini, M., Balestrieri, M.-L., Molin, P., Willingshofer, E., Sokoutis, D., Cloetingh, S., 2014. Evolution, distribution, and characteristics of rifting in southern Ethiopia. Tectonics 33, 485–508.

Pik, R., Marty, B., Carignan, J., Yirgu, G., Ayalew, T., 2008. Timing of East African Rift development in southern Ethiopia: Implication for mantle plume activity and evolution of topography. Geology 36, 167–170.

Purinton, B., Bookhagen, B., 2017. Validation of digital elevation models (DEMs) and comparison of geomorphic metrics on the southern Central Andean Plateau. Earth Surf. Dyn. 5, 211–237.

Ramezani-Ziarani, M., Bookhagen, B., Schmidt, T., Wickert, J., de la Torre, A., Hierro, R., 2019. Using convective available potential energy (CAPE) and dew-point temperature to characterize rainfall-extreme events in the South-Central Andes. Atmosphere 10, 379.

Ramírez-Herrera, M.T., 1998. Geomorphic assessment of active tectonics in the Acambay Graben,Mexican Volcanic Belt. Earth Surf. Process. 23, 317–332.

Riedl, S., Melnick, D., Mibei, G.K., Njue, L., Strecker, M.R., 2020. Continental rifting at magmatic centres: structural implications from the Late Quaternary Menengai Caldera, central Kenya Rift. J. Geol. Soc. Lond. 177, 153–169.

Rizzoli, P., Martone, M., Gonzalez, C., Wecklich, C., Borla Tridon, D., Br¨autigam, 2017. Generation and performance assessment of the global Tandem-X digital elevation model. J. Photogramm. Remote Sens. 132, 119–139.

Rosendahl, B.R., 1987. Architecture of continental rifts with special reference to East Africa. Annu. Rev. Earth Planet. Sci. 15, 445–503.

Saria, E., Calais, E., Stamps, D.S., Delvaux, D., Hartnady, C.J.H., 2014. Present-day kinematics of the East African Rift. J. Geophys. Res. Solid Earth 119, 3584–3600.

Schaebitz, F., Asrat, A., Lamb, H.F., Cohen, A.S., Foerster, V., Duesing, W., Kaboth- Bahr, S., Opitz, S., Viehberg, F.A., Vogelsang, R., Dean, J., Leng, M.J., Junginger, A., Ramsey, C.B., Chapot, M.S., Deino, A., Lane, C.S., Roberts, H.M., Vidal, C., Tiedemann, R., Trauth, M.H., 2021. Hydroclimate changes in eastern Africa over the past 200,000 years may have influenced early human dispersal. Commun. Earth Environ. 2, 123.

Scholz, C.H., Dawers, N.H., Yu, J.-Z., Anders, M.H., Cowie, P.A., 1993. Fault growth and fault scaling laws: preliminary results. J. Geophys. Res. Solid Earth 98, 21951–21961.

Schumm, S.A., 1956. Evolution of drainage systems and slopes in badlands at Perth Amboy, New Jersey. Geol. Soc. Am. Bull. 67, 597–646.

Schwanghart, W., Kuhn, N.J., 2010. TopoToolbox: a set of Matlab functions for topographic analysis. Environ. Model. Softw. 25, 770–781.

Schwanghart, W., Scherler, D., 2014. Short Communication: TopoToolbox 2 – MATLABbased software for topographic analysis and modeling in Earth surface sciences. Earth Surf. Dyn. 2, 1–7.

Seeber, L., Gornitz, V., 1983. River profiles along the Himalayan arc as indicators of active tectonics. Tectonophysics 92, 335–367.

Seleshi, Y., Zanke, U., 2004. Recent changes in rainfall and rainy days in Ethiopia. Int. J. Climatol. 24, 973–983.

Silva, P.G., Goy, J.L., Zazo, C., Bardají, T., 2003. Fault-generated mountain fronts in southeast Spain: geomorphologic assessment of tectonic and seismic activity. Geomorphology 50, 203–225.

Smith, T., Bookhagen, B., 2020. Assessing multi-temporal snow-volume trends in high mountain Asia from 1987 to 2016 using high-resolution passive microwave data. Front. Earth Sci. 8, 559175.

Snyder, N.P., Whipple, K.X., Tucker, G.E., Merritts, D.J., 2000. Landscape response to tectonic forcing: digital elevation model analysis of stream profiles in the Mendocino triple junction region, northern California. Geol. Soc. Am. Bull. 112, 1250–1263.

Stamps, D.S., Calais, E., Saria, E., Hartnady, C., Nocquet, J.-M., Ebinger, C.J., Fernandes, R.M., 2008. A kinematic model for the East African Rift. Geophys. Res. Lett. 35, L05304.

Strahler, A.N., 1952. Dynamic basis of geomorphology. Geol. Soc. Am. Bull. 63, 923–938.

Tucker, G.E., Whipple, K.X., 2002. Topographic outcomes predicted by stream erosion models: sensitivity analysis and intermodel comparison. J. Geophys. Res. Solid Earth 107(B9), 2179.

van der Lubbe, H.J.L., Krause-Nehring, J., Junginger, A., Garcin, Y., Joordens, J.C.A., Davies, G.R., Beck, C., Feibel, C.S., Johnson, T.C., Vonhof, H.B., 2017. Gradual or abrupt? Changes in water source of Lake Turkana (Kenya) during the African Humid Period inferred from Sr isotope ratios. Quat. Sci. Rev. 174, 1–12.

Vétel, W., Gall, B.L., Walsh, J.J., 2005. Geometry and growth of an inner rift fault pattern: the Kino Sogo Fault Belt, Turkana Rift (North Kenya). J. Struct. Geol. 27, 2204–2222.

Weissel, J.K., Seidl, M.A., 1997. Influence of rock strength properties on escarpment retreat across passive continental margins. Geology 25, 631–634.

Wessel, B., Huber, M., Wohlfart, C., Marschalk, U., Kosmann, D., Roth, A., 2018. Accuracy assessment of the global TanDEM-X Digital Elevation Model with GPS data. ISPRS J. Photogramm. Remote Sens. 139, 171–182.

Whipple, K.X., 2004. Bedrock rivers and the geomorphology of active orogens. Annu. Rev. Earth Planet. Sci. 32, 151–185.

Whipple, K.X., Tucker, G.E., 1999. Dynamics of the stream-power river incision model: implications for height limits of mountain ranges, landscape response timescales, and research needs. J. Geophys. Res. Solid Earth 104, 17661–17674.

Whittaker, A.C., Boulton, S.J., 2012. Tectonic and climatic controls on knickpoint retreat rates and landscape response times. J. Geophys. Res. Earth Surf. 117, F02024.

Wobus, C., Whipple, K.X., Kirby, E., Snyder, N., Johnson, J., Spyropolou, K., Crosby, B., Sheehan, D., 2006. Tectonics from topography: procedures, promise, and pitfalls. In: Willett, S.D., Hovius, N., Brandon, M.T., Fisher, D.M. (Eds.), Tectonics, Climate, and Landscape Evolution. Geological Society of America Special Paper, Penrose Conference Series, 398, pp. 55–74.

Wolde-Gabriel, G., Aronson, J.L., 1987. Chow Bahir rift: a "failed" rift in southern Ethiopia. Geology 15, 430–433.

Wolde-Gabriel, G., Yemane, T., Suwa, G., White, T., Asfaw, B., 1991. Age of volcanism and rifting in the Burji-Soyoma area, Amaro Horst, southern Main Ethiopian Rift: geo- and biochronologic data. J. Afr. Earth Sci. 13, 437–447.

Yanites, B.J., Tucker, G.E., Mueller, K.J., Chen, Y.-G., 2010. How rivers react to large earthquakes: evidence from central Taiwan. Geology 38, 639–642.

Yemane, T., Yohunie, T., 1987. Geological Report on Teritiary and Quaternary Rocks of Agere-Mariam Sheet (NG-37.10). Ethiopian Institute of Geological Survey, Addis Ababa.

Zwaan, F., Schreurs, G., 2020. Rift segment interaction in orthogonal and rotational extension experiments: implications for the large-scale development of rift systems. J. Struct. Geol. 140, 104119.

Zwaan, F., Schreurs, G., 2017. How oblique extension and structural inheritance influence rift segment interaction: insights from 4D analog models. Interpretation 5, SD119–SD138.

Chapter 5

Temporal variation in counterclockwise vertical-axis block rotations across a rift overlap zone, southwestern Ethiopia, East Africa

Erbello, A., Dupont-Nivet, G., Kidane, T., Nowaczyk, N., Sudo, M., Melnick, D., Bookhagen, B., Brune, S., Corti, G., Gecho, G., and Strecker, M.R.

This chapter is almost finished and ready to submit to Geochemistry, Geophysics, Geosystems

---

Abstract

In the East African Rift System, the southward propagation of the Main Ethiopian rifts and northward propagation of the Kenya rifts has resulted in the Broadly Rifted Zone (BRZ), a ~40-km-wide zone of overlap between the Chew Bahir Basin-Gofa Province and the southern Main Ethiopian Rift. The tectonic interaction between the propagating rifts and deformation mechanisms across the BRZ are still not well understood. This study presents paleomagnetic and geochronologic data from samples collected in Eo-Oligocene (45–35 Ma) and Miocene (18–11 Ma) volcanic and sedimentary rocks within the BRZ. Rock magnetic properties indicate simple titano-magnetite mineralogies carrying a primary remnant magnetization from which straightforward Characteristic Remanent Magnetization directions were obtained. Site-mean paleomagnetic directions obtained from samples subjected to the progressively increased alternative field and thermal demagnetizations reflect stable normal and reversed polarity directions. A comparison of the mean directions obtained for the Eo-Oligocene (Ds=352.6°, Is=-17.0°, N=18, α_{95}=5.5°) and Miocene (Ds=2.9°, Is=0.9°, N=9, α_{95}=12.4°) volcanics relative to the pole for stable South Africa and with respect to corresponding ages, record a significant counterclockwise (CCW) rotation of ~11.1°± 6.4° and insignificant CCW rotation of ~3.2° ± 11.5°, respectively, reflecting a decrease in the amount of block rotations over time. The post-Eocene rotations are pervasive and systematic across the BRZ, suggesting a common mechanism. The decrease in the extent of block rotations is compatible with progressive, regional

rotations accrued until the present day, and too small to be statistically detected by the Miocene data. In the context of the regional tectonic evolution with a trend toward a narrow zone of focused extension in the rift centers during late-stage rifting, much of the deformation associated with block rotations probably occurred before the final emplacement of the Miocene volcanics. Given the inherited fabrics in the basement rocks exposed in southern Ethiopia the observed counterclockwise block rotations were likely accompanied and aided by the reactivation of NW-SE-striking inherited basement lineaments, supporting the notion that inherited crustal structures in the transition between the southern Main Ethiopian Rift and the northern Kenya Rift played a significant role during rifting.

5.1 Introduction

Continental rifts are nascent extensional plate boundaries and commonly evolve from the growth of normal-fault bounded, initially isolated basins to linked graben systems, and ultimately ocean basins (*e.g.*, Ebinger *et al.*, 1999; Ebinger and Scholz, 2012 and references therein). In map view, these fault-bounded basins are often laterally separated. A lateral transfer of extensional strain between these basins is thus required over time to kinematically link these different sites of tectonic subsidence and to maintain crustal extension between spatially disparate rift segments (*e.g.*, Rosendahl, 1987; Childs *et al.*, 1993, 1995). Consequently, as adjacent rift segments propagate, overlap, and finally interact with one another to form larger, connected basins, either closely spaced, obliquely slipping normal faults (*e.g.*, Morley, 1990; Ebinger *et al.*, 1999; Peacock *et al.*, 2002; Bellahsen *et al.*, 2013) or discrete transfer faults with strike-slip kinematics (*e.g.*, Peacock *et al.*, 2002; Acocella *et al.*, 2005) may develop at a variety of scales (*e.g.*, Macdonald and Fox, 1983; Dawers and Anders, 1995; Koukouvelas *et al.*, 1999). The structural character of these complex zones of extension may be further complicated either when the transfer of strain is associated with the reactivation of inherited crustal-scale heterogeneities or if crustal block rotations are involved to accommodate the differential motion of blocks (*e.g.*, Bosworth 1985; Rosendahl *et al.*, 1987; Morley *et al.*, 1990, 1992; Hetzel and Strecker, 1994; Corti, 2008). Over time, therefore, it can be expected that the linking of disparate extensional basins will result in a patchwork of different deformation styles and basin architectures, varying patterns of volcanism and seismicity, and pronounced variations in topography (*e.g.*, Bosworth, 1985; Rosendahl *et al.*, 1987; Morley, 1994). The topographic relief patterns of such transfer zones may exert a crucial influence not only on the dispersal patterns of biota and thus on biodiversity (*e.g.*, Dommain *et al.*, 2022), but also on the evolution of the hydrological network and sediment transport as well as on the permeability and fluid flow along individual structures (*e.g.*, Morley *et al.*, 1990; Nelson *et al.*, 1992; Morley *et al.*, 1994; Olaka *et al.*, 2022).

Therefore, characterizing and understanding the kinematics of faults in transfer zones, also known as accommodation zones (*e.g.*, Rosendahl *et al.*, 1987), is an important step in identifying the individual stages of rift evolution and the environmental impact of fault systems, especially at the termination of rift segments. One of the key tectonically active extensional regions where

different types and spatial scales of rift-transfer zones can be observed at various evolutionary stages is the Cenozoic East African Rift System (EARS). Along strike, the EARS comprises several propagating rift segments that interact via complex transfer faults, often characterized by wide zones of diffuse deformation (*e.g.*, Rosendahl *et al.*, 1987; Morley, 1992; Ebinger *et al.*, 1999; Koehn *et al.*, 2008; Brune *et al.*, 2017; Corti *et al.*, 2019; Kolawole *et al.*, 2021).

With a length of ~2000 km, the EARS extends from the Afar depression in the north to Malawi and Mozambique in the south; in the Turkana depression it bifurcates into an eastern and a western branch. The eastern branch, comprising the southern Afar, Main Ethiopian, and Kenya rifts is characterized by pronounced volcano-tectonic processes, whereas the western branch is volcanically less active (Fig. 5.1a). Geological and geophysical data from the western and eastern branches indicate that many of the adjacent rift segments are linked by transfer faults (*e.g.*, Kolawole *et al.*, 2021); often, fault motion within these transfer zones is influenced by inherited structures related to earlier deformation processes (*e.g.*, Delvaux, 1989; Brune *et al.*, 2017; Corti *et al.*, 2019). In contrast, other transfer zones in the EARS are characterized by a wide area of overlap between propagating strands of normal faults (*e.g.*, Morley, 1994, Ebinger *et al.*, 1999; Acocella, 2005).

Based on paleomagnetic, geodetic, seismic, and mechanical modeling results, microplate rotations between overlapping rift segments have been inferred from different sectors in the EARS and the Afar Rift (*e.g.*, Acton *et al.*, 1991; Kidane *et al.*, 2003, 2009; Koehn *et al.*, 2008; Saria *et al.*, 2013, 2014; Muluneh *et al.*, 2014; Nugsse *et al.*, 2018; Philippon *et al.*, 2014; Brune *et al.*, 2017; Glerum *et al.*, 2020). While in the northern Main Ethiopian and southern Afar rifts, Kidane *et al.* (2003) and Nugsse *et al.* (2018) inferred a counterclockwise block rotation of a rift zone located between right-stepping Quaternary magmatic segments, such paleomagnetic studies from the southern Main Ethiopian Rift (sMER), the Broadly Rifted Zone (BRZ), and farther south in the Kenya Rift and western branch of the EARS, are not available. Continuous geodetic measurements along and across the EARS indicate that the Ufipa Horst located between the left-stepping Rukwa and Tanganyika rifts (Fig. 5.1b) is rotating in a clockwise direction (Calais *et al.*, 2006; Stamps *et al.*, 2008, 2018, 2021; Fernandes *et al.*, 2013; Deprez *et al.*, 2013; Saria *et al.*, 2013, 2014). Farther north in the western branch, numerical and analog modeling of extensional structures (*e.g.*, Koehn *et al.*, 2008; Ayue and Koehn; 2010) has also indicated a clockwise rotation of the Rwenzori microplate, which is located between the left-stepping structures that delimit the Edward and Albert rifts (Fig. 5.1c). Similarly, counterclockwise rotation involving reactivated Mesozoic crustal anisotropies affects an uplifted crustal block between right-stepping rift segments of the Chew-Bahir-Gofa Province and the sMER (*e.g.*, Philippon *et al.*, 2014; Brune *et al.*, 2017). Finally, and at a much larger spatial scale, a counterclockwise rotation of a mechanically strong, undeformed layer of the Victoria microplate located between the right-stepping eastern and western branches of the EARS was inferred by Glerum et al. (2020) (Fig. 5.1d). These findings show that the type of rift overlap (right- or left-stepping) controls the direction of microplate rotation across all relevant scales because the geometric relationship between stepover and rotation is scale-invariant (Koehn *et al.*, 2010; Glerum *et al.*, 2020). Taken together, the inferred

microplate rotations between the propagating structures of the Rukwa and Tanganyika rifts (Ufipa Horst), the Edward and Albert rifts (Rwenzori microplate), the eastern and western branches of the EARS (Victoria microplate), and between the sMER and the Chew Bahir-Gofa Province (Gidole-Chencha Horst) are mainly based on analog and numerical modeling as well as short-term geodetic observations. However, the structural history of many of these transfer zones has remained ambiguous because detailed geological or paleomagnetic data do not exist to further constrain their spatiotemporal evolution and the kinematic history on long timescales.

Addressing this gap in knowledge, our study combines structural, geochronological, and paleomagnetic data to investigate temporally constrained deformation mechanisms during the structural linkage of rift basins. To achieve this, we chose a ~75 to 125-km-long and ~20 to 40-km-wide zone of overlap between the sMER and the Chew-Bahir-Gofa Province in the eastern branch of the EARS for two principal reasons: First, the geochronologic constraints are excellent, and this part of the EARS is characterized by Eocene–Miocene volcanic successions (Davidson and Rex, 1980; Davidson, 1983; WoldeGabriel *et al.*, 1991; Ebinger *et al.*, 1993, 2000; George, 1998; George and Rogers, 2002; Bonini *et al.*, 2005; Rooney *et al.*, 2010) that are well-suited for additional radiometric age determination and paleomagnetic analysis of potentially rotated crustal blocks within the transfer zone. Second, extensional processes in this region have been sustained for more than 15 Ma until the present day (*e.g.*, Ebinger *et al.*, 2000; Bonini *et al.*, 2005; Pik *et al.*, 2008; Philippon *et al.*, 2014; Balestrieri *et al.*, 2016; Boone *et al.*, 2019; Corti *et al.*, 2019; Knappe *et al.*, 2020; Erbello *et al.*, 2022), and the available regional structural and stratigraphic framework allows an assessment of long-term aspects of rift-segment interaction and linkage.

5.2 Tectonic and geologic setting

5.2.1 Tectonic setting

The propagating rift segments of the sMER and northern Kenya Rift (nKR) interact across a wide area located in southern Ethiopia, resulting in a structurally complex extensional deformation zone with imprints of multiple tectonic events. NW-SE-striking tectonic lineaments related to Cretaceous-Paleogene paleo-rifts cut obliquely NNE-SSW-striking Neoproterozoic basement fabrics (Morley *et al.*, 1992; Bosworth and Morley, 1994; Brune *et al.*, 2017; Emishaw and Abdelsalam, 2019), which are sub-parallel to the N-S to NE-SW-striking Cenozoic rift structures (Corti, 2009; Kendall and Lithgow-Bertelloni, 2016). The Cretaceous-Paleogene lineaments are associated with the Melut and Muglade rift basins in Sudan and South Sudan, and the Anza Rift in northern Kenya (*e.g.*, Bosworth and Morley, 1994). Satellite gravity data from the BRZ reveals prominent, E-W-striking lineaments that link the Cretaceous-Paleogene rift basins in South Sudan and northern Kenya (*e.g.*, Mamo, 2012; Emishaw *et al.*, 2019), but the structures and deposits of the N-S to NE-SW-trending Cenozoic rift basins of the active EARS mostly obscure these relationships (*e.g.*, Ebinger *et al.*, 1993). Regionally, extensional deformation related to the Nubia-Somalia plate motion appears to have originated in the northern Turkana region between

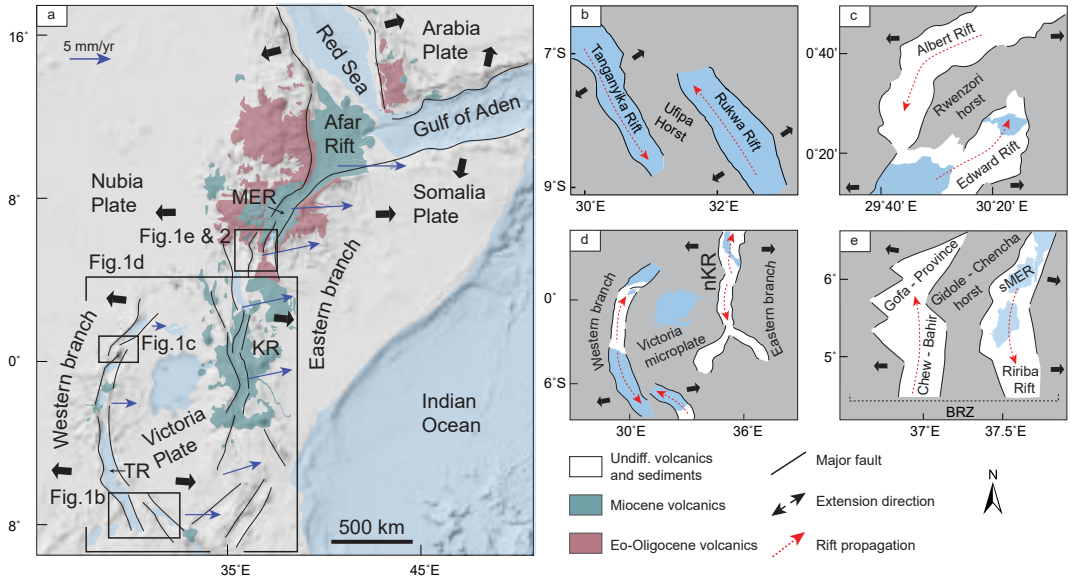

Figure 5.1: Tectonic setting and overlapping rift segments of the East African Rift System (EARS). (a) Plate kinematics and velocity vectors (Stamps *et al.*, 2020), major faults, and volcano-stratigraphic units (Rooney *et al.*, 2017a and references therein) outcropping in the EARS (Kenya Rift, KR; Main Ethiopian Rift, MER; and Afar Rift) superimposed on hill-shaded relief. (b–e) show propagating (red arrow) and overlapping rift segments between the Tanganyika and Rukwa rifts (b), Albert and Edward rifts (c), eastern and western branches of the east African Rift System (d), and southern MER (sMER) and the Chew Bahir-Gofa Province across the Broadly Rifted Zone (BRZ) (e).

35 and 25 Ma (Boone *et al.*, 2019; Ragon *et al.*, 2019) and migrated toward the north in the Chew Bahir Basin (*e.g.*, Bonini *et al.*, 2005 and references therein) by ~20 Ma (Pik *et al.*, 2008). By approximately 10 Ma, rifting had propagated farther north into the Gofa Province but stalled where the extensional faults intersected pre-existing NW-SE-oriented Mesozoic lineaments (WoldeGabriel and Aronson, 1987; Kounoudis *et al.*, 2021; Erbello *et al.*, manuscript in review). This suggests that strain was accommodated along these reactivated structures that strike at high angles with respect to the overall direction of rift propagation (*e.g.*, Molnar *et al.*, 2019).

In the study area, extensional deformation that formed the Gidole-Chencha Horst has been associated with a 20 Ma N-S-striking dikes whose emplacement may have followed the reactivation of the NW-SE-oriented lineaments (Bonini *et al.*, 2005). This is in contrast to the suggestion by Ebinger *et al* .(2000) that the main phase of faulting along the western margin of the Chamo Basin on the eastern side of the Gidole-Chencha Horst began later, at ~15 Ma. Following the development of the western margin of the Chamo Basin, faulting migrated toward the north and south of the sMER during the middle Miocene (*e.g.*, Levitte, 1974; WoldeGabriel *et al.*, 1991; Bonini *et al.*, 2005; Boone *et al.*, 2019). The southward migration of deformation terminated in the Ririba Rift during the late Pliocene (*e.g.*, WoldeGabriel *et al.*, 1991; Levitte, 1974; Ebinger *et al.*, 2000; Bonini *et al.*, 2005; Corti *et al.*, 2019; Franceschini *et al.*, 2020). During the Quaternary, volcanism associated with extensional faulting migrated toward the present-day narrow axial zone of the sMER (*e.g.*, Ebinger *et al.*, 2000), along the strike of the Turkana Rift and the lower Omo Valley (Jicha and Brown, 2014). Currently, deformation is localized in the southern Gofa Province, the Chew Bahir Basin (*e.g.*, Ebinger *et al.*, 2000; Philippon *et al.*, 2014; Erbello *et al.*, 2022), and the Segen Basin (Levitte, 1974). The strain localization in these zones of overlap has been interpreted as reflecting ongoing tectonic interaction between the sMER and the nKR (*e.g.*, Ebinger *et al.*, 2000; Philippon *et al.*, 2014; Corti *et al.*, 2019; Knappe *et al.*, 2020; Erbello *et al.*, 2022).

In addition to concentrated volcano-tectonic activity across the BRZ, normal-faulting earthquakes recorded at shallow crustal depths in the region since 1913 have clustered along a narrow zone between the lower Omo Valley, the southern Gofa Province, and the Chew Bahir and Segen basins (Gouin, 1979; Asfaw, 1990; Ayele and Arvidsson, 1997; Foster and Jackson, 1998). The few earthquakes recorded document a strike-slip component (Ayele, 2000; Bonini *et al.*, 2005 and references therein; Musila *et al.*, 2020), supporting the notion that the current tectonic interaction between the sMER and the nKR benefits from inherited structures striking at high angle to the trend of the rift (Knappe *et al.*, 2019).

5.2.2 Geologic setting

5.2.2.1 Neoproterozoic basement rocks

In the study area, Neoproterozoic basement rocks comprising NNE-SSW-striking foliations have been interpreted to control the site of Cenozoic rifting in the region (Vauchez *et al.*, 1997).

High-grade amphibolites and layered granulites (Gichile, 1992), which are characterized by NNE-SSW-striking foliations (Davidson, 1983), reflect important tectono-thermal events during the collisional pan-African orogeny between 750 Ma and 550 Ma (Asrat and Barbey, 2003). Structurally and temporally related basement fabrics have been mapped in central-northern Kenya (*e.g.*, Key *et al.*, 1989; Hetzel and Strecker, 1994), suggesting a structural continuity between the two areas (Gichile, 1992), as expressed by regional lineaments oriented sub-parallel to the Quaternary faults (*e.g.*, Kendall and Lithgow-Bertelloni, 2016). However, local E-W-striking foliations associated with layered granulites are also known to occur along the southwest margin of the Chamo Basin, across the Konso Plateau, and in the Segen Basin (Davidson, 1983; Gichile, 1992; Asrat and Barbey, 2003). De Wit and Chewaka (1981) considered these local foliations to be related to post-Pan-African tectonic events associated with the emplacement of the Konso pluton at ~449 ± 2 Ma (Asrat, and Barbey, 2003). Compositionally related plutonic rocks from the west of the Konso Plateau (Davidson, 1983) and the Segen Basin margin have provided radiometric ages between 526 ± 5 Ma and 554 ± 23 Ma (Gichile, 1992; Worku and Schandelmeier, 1996; Teklay *et al.*, 1998; Yibas *et al.*, 2002).

5.2.2.2 Cretaceous sedimentary rocks

The volcanic units studied are underlain by a thin, yet prominent and silicified basal conglomeratic sandstone that unconformably covers the crystalline basement rocks (Davidson and Rex, 1980; Ebinger *et al.*, 1993). This unit is exposed mainly along the flanks of the Amaro Horst (WoldeGabriel, 1991; Ebinger *et al.*, 1993), where its thickness varies along strike (Ebinger *et al.*, 1993); it is absent to the west of the BRZ (Moore and Davidson, 1978; Davidson, 1983; Philippon *et al.*, 2014). Based on the sharpness of the conformable contact with overlying Eo-Oligocene volcanic rocks and the proximal sediment-clast composition, Davidson (1983) inferred an early Paleogene depositional age for this sandstone. Conversely, Levitte et al. (1974) suggested, on the basis of petrographic characteristics, that the unit may correspond to the late Cretaceous lower unit of the Turkana grits of northern Kenya (Arambourg and Wolff, 1969).

5.2.2.3 Cenozoic rocks

The sampled Eo-Oligocene volcanic successions are well exposed along the margins of the sMER, the Gofa Province, and the nKR, with thicknesses ranging from several hundred meters to about one kilometer (Fig. 5.2) (Davidson, 1983; Ebinger *et al.*, 1993, 2000; George, 1998). Across the BRZ in southern Ethiopia, these volcanic sequences reflect prolonged magmatism between 45 and 28 Ma (Davidson and Rex, 1980; Davidson, 1983; Ebinger *et al.*, 2000; George and Rogers, 2002, Rooney, 2017; Steiner *et al.*, 2021). The study area covers the Gidole-Chencha Horst between the Chew Bahir Basin-Gofa Province and the sMER, where volcanic eruptive centers distributed along the margin of the Chamo and Abaya basins reflect a NW-SE-oriented extension direction (Ebinger *et al.*, 2000). The Eocene-Oligocene volcanic successions are characterized successively by Amaro basalts, Arba-Minch tuffs, Gamo basalts, and Amaro tuffs (Ebinger *et al.*,

1998; Rooney, 2017). The ~250-m-thick tholeiitic Amaro basalt is exposed along the Amaro Horst and overlies the ubiquitous Cretaceous conglomeratic sandstone layer; it constitutes the lower section of the exposed volcanic sequences and yielded a K-Ar age of 44.9 ± 0.7 Ma (Ebinger *et al.*, 1993). Compositionally similar basalt flows overlie the crystalline basement rocks along the southern Amaro Horst and were dated to 42.5 ± 0.7 Ma (*e.g.*, WoldeGabriel *et al.*, 1991). The cataclastically deformed silicic Arba-Minch tuff unit, dated at ~37 and 39 Ma, is exposed along the southwestern margin of the Chamo Basin and is overlain by the 35–37 Ma Gamo basalts and the widespread Amaro tuff unit dated at 33 Ma (Ebinger *et al.*, 1993, 2000).

The second main phase of magmatism in southern Ethiopia is documented by a sequence of early Miocene Getera-Kela basalts (Levitte *et al.*, 1974; Zanettin *et al.*, 1978) and N-S-striking dike swarms (Bonini *et al.*, 2005). The Oligocene Amaro tuff is generally overlain by the ~500-m-thick Getera-Kela basalt unit sampled in this study, which has an age range between 18 and 11 Ma (Davidson, 1983; Ebinger *et al.*, 1993). Phonolitic eruptive centers in the Segen, Mali-Dancha, and Bala-Kela basins are distributed along the strike of the Quaternary faults and were dated between 16 and 12 Ma (Davidson and Rex, 1980; Ebinger *et al.*, 2000). The Getera-Kela volcanics are capped by a basalt dated ~11 Ma (WoldeGabriel *et al.*, 1991).

After a period of volcano-tectonic quiescence during the late Miocene (*e.g.*, Bonini *et al.*, 2005), early Pliocene lava flows of the Gombe Group were emplaced along the Omo-Turkana Depression (Watkins, 1983; Brown *et al.*, 1985). Although these basaltic flows were not sampled for our paleomagnetism study, they provide key markers of deformation and rift evolution. A ~5-m-thick, ~4-m.y.-old basalt is exposed in the western Usno Basin (Ebinger *et al.*, 2000), extending ~150 km farther north along the Omo Valley (Davidson, 1983). The Mursi basalts of an equivalent age outcrop in the northern Omo Valley (Brown and Nasha, 1976). In addition, outliers of petrographically similar thin basaltic flows exist along the western margin of the Chew Bahir Basin (*e.g.*, Davidson, 1983; Haileab *et al.*, 2004). Conventional K-Ar dating of the basaltic units across the Omo-Turkana region indicates a protracted eruptive period between ~6 and 3 Ma (*e.g.*, Brown, 1969, Brown *et al.*, 1985; McDougall and Watkins, 1988; McDougall, 1985). More recently, Haileab *et al* .(2004) suggested that these basaltic units were emplaced at ~4 Ma and collectively called them Gombe Group basalts (Watkins, 1983), and Erbello and Kidane (2018) further specified that these thin lava flows erupted between ~4.05 and 4.18 Ma. During the late to middle Pliocene, basaltic volcanism and faulting shifted eastward in the Ririba Rift (WoldeGabriel *et al.*, 1991; Levitte, 1974; Ebinger *et al.*, 2000; Bonini *et al.*, 2005; Corti *et al.*, 2019; Franceschini *et al.*, 2020), before magmatism became focused in a narrow zone along the Chamo Basin (*e.g.*, Ebinger *et al.*, 1993) and the Omo Valley (Jich and Brown, 2014) during the Quaternary.

5.3 Sampling and methods

Volcanic and sedimentary rocks are commonly characterized as archives of the Earth's magnetic field, acquired during the emplacement and/or deposition of the rock units. The well-exposed Eo-Oligocene and Miocene volcanics and sedimentary rocks from the Gidole-Chencha Horst in southern Ethiopia are ideally suited to yield paleomagnetic information related to tectonic deformation across the region (Fig. 5.2). A total of 40 paleomagnetic sites were selected from Eo-Oligocene and Miocene volcanics and sediments, respectively (Table B.1). Four to eight standard core samples were collected from each site using a gasoline powered motor drill. Samples were oriented using a standard device with a magnetic compass and sun orientations to assess local declinations. Bedding orientations were carefully measured from the top of flows and sedimentary layers for tilt corrections. Additionally, ten block samples (~1–1.5 kg) from representative sites were collected for $^{40}Ar/^{39}Ar$ dating to complement the age constraints of the sampled volcanic units (Table B.1).

The paleomagnetic core samples were cut into standard specimens in sample preparation laboratories at the University of Potsdam, Germany and Addis Ababa University, Ethiopia. Natural remnant magnetization (NRM) of each specimen was measured before subjecting the specimens to incrementally increased Alternative Field (AF) and thermal (TH) demagnetization experiments at the paleomagnetic laboratory of the GFZ German Research Centre for Geosciences in Potsdam. A few samples were processed thermally in the paleomagnetic laboratory of the Addis Ababa University. To define the most effective demagnetization scheme for the separation of components and determination of characteristic remnant magnetizations (ChRM) to be applied in the rest of the samples, pilot specimens were first processed in AF, TH, and a combination of AF and TH, with detailed demagnetization steps (5 to 120 mT for AF and 20 °C to 700 °C for TH). Ultimately, AF demagnetizations on most of the pilot specimens resulted in a well-separated linear component with simple progressive decay. Based on these results, the bulk of the specimens were processed by 12 AF demagnetization steps (NRM, 5, 10, 15, 20, 30, 35, 40, 60, 80, 100, 120 mT). ChRM directions were obtained using a principal component analysis (Kirschvink, 1980) on a minimum of four consecutive steps following a procedure outlined in PaleoMac 6.5 (Cogné, 2003) that was also used to determine a Fisher means of the ChRM directions for each site (Fisher, 1953; McFadden and McElhinny, 1988).

To characterize rock magnetic properties, high-temperature (20–700°C) thermomagnetic experiments were performed on representative samples using a multifunction kappabridge (MFK-1A) at GFZ to determine bulk magnetic susceptibility of the sampled lava flows and sediments. A powdered sample of ~100 mg was placed in a glass tube and subjected to incremental heating to 700°C and cooling back to 40°C during the experiment. The bulk magnetic susceptibility was measured at a 5°C interval.

To provide a temporal constraint of the sampled volcanic units, $^{40}Ar/^{39}Ar$ dating was performed on representative samples at the University of Potsdam. A groundmass sample (~100 gram) was prepared from fresh rock samples collected at 10 representative sites following proce-

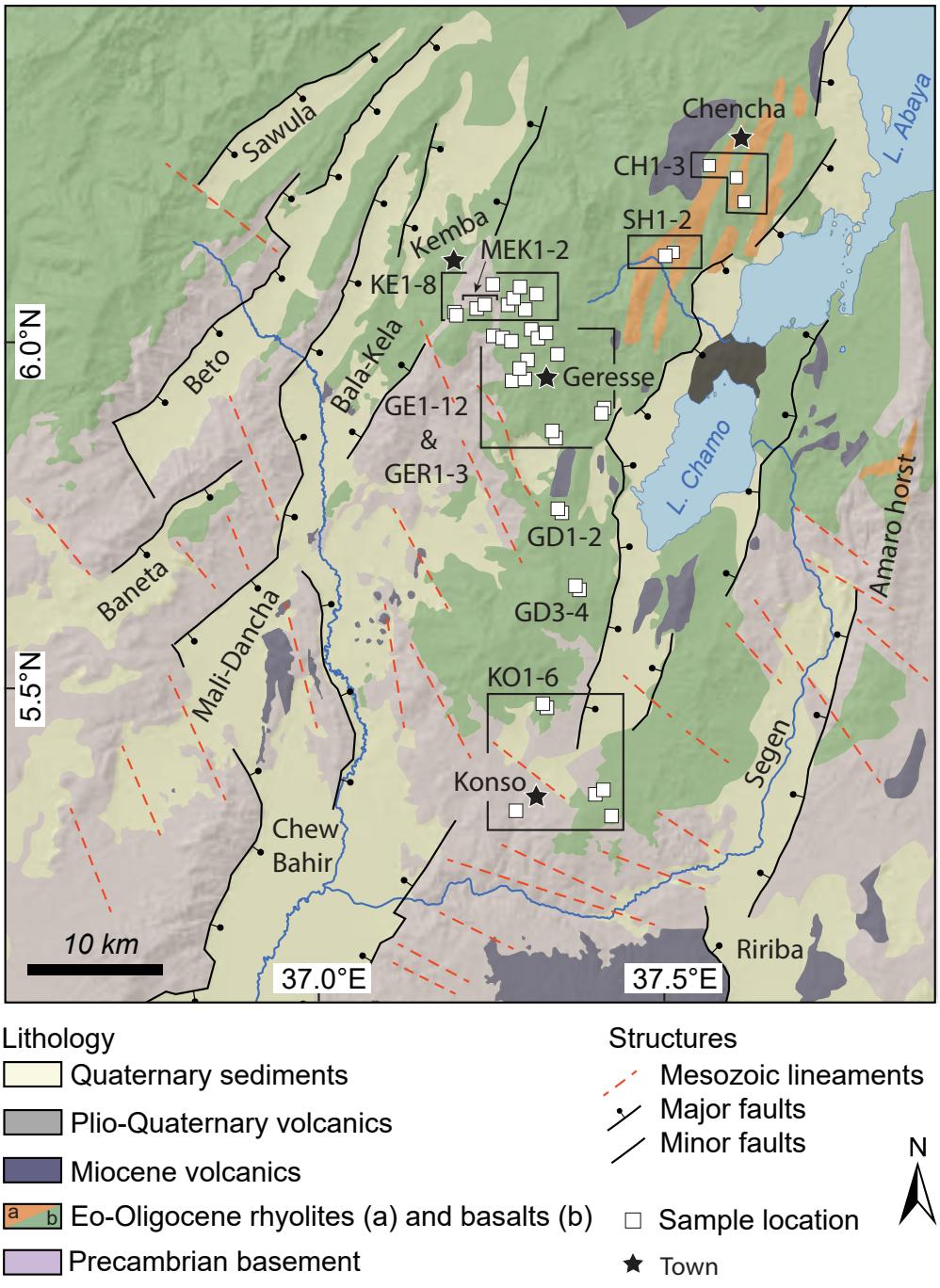

Figure 5.2: Geologic setting of the sMER and the Chew Bahir-Gofa Province (Mali-Dancha, Baneta, Beto, Bala-Kela, and Sawula basins), stratigraphic units (Davidson, 1983; and Bonini *et al.*, 2005), Mesozoic lineaments, and Quaternary faults (Davidson, 1983) are superimposed on a hill-shaded relief. Open squares indicate sampling sites grouped by locality (black boxes).

dures outlined by Wilke *et al.* (2010) and Halama *et al.* (2012). All samples were irradiated for approximately four hours at Oregon State TRIGA Reactor facility, USA prior to isotopic measurement at the University of Potsdam. The irradiated samples were subjected to an experiment involving ten to twelve steps of incremental heating using a mass spectrometer. Between three consecutive step-heating experiments, blank analysis was measured for all the samples. Using the age-spectrum displayed by measured apparent ages from each heating steps, a plateau age was determined based on a minimum of three contiguous steps with apparent age overlapping within 22σ, and together comprising >50% of the total ^{39}Ar released (*e.g.*, Fleck *et al.*, 1977; Uto *et al.*, 1997). In some cases, a forced plateau age was estimated from a minimum of three concordant steps (with apparent age overlapping within 2σ) containing >50% of the ^{39}Ar release in total. For the plateau and forced plateau ages of the initial ^{40}Ar/^{36}Ar ratios obtained from the normal and inverse isochrons comprising only the plateau steps was compared relative to the atmospheric value (Lee *et al.*, 2006) in order to validate the selection of the plateau steps at the 95% confidence level. The validated plateau or forced plateau ages were farther compared relative to the isochron ages obtained from the plateau steps. The details about the age results are provided in Supplementary Information (Table B.4–7 and Figure B. 1).

5.4 Results

5.4.1 ^{40}Ar/^{39}Ar

The ^{40}Ar/^{39}Ar dating results of samples from the Gidole-Chencha Horst exhibit plateau ages ranging between 43 and 33 Ma for the Gamo-Amaro basalts and between 20 and 17 Ma for the Getera-Kela basalts.

Sample MEK-2 collected from west of the Gidole-Chencha Horst was dated at 42.61 ± 0.27 Ma, similar to a basaltic flow overlying crystalline basement in the southern Amaro Horst that was dated at 42.53 ± 0.70 Ma (WoldeGabriel *et al.*, 1991). Similar plateau ages of 39.37 ± 0.16 Ma, 38.97 ± 0.17 Ma, and 37.20 ± 0.12 Ma were obtained at sites GD-3, GE-7, and CH-3, respectively. A basalt exposure at site KO-3 located in the south of the Gidole-Chencha Horst was dated at 34.01 ± 0.20 Ma. Sample GER-2 dated at 33.62 ± 0.10 Ma collected from the highly fractured welded tuff unit located at a higher elevation to the west of GE-7 provided the youngest age of all the dated Eo-Oligocene volcanics (Fig. 3b). This welded tuff unit correlates with the widely distributed Amaro tuff (~33 Ma), both of which cover Eo-Oligocene rock units from a ~500m thick Miocene volcanics (Davidson, 1983; Ebinger *et al.*, 1993; Bonini *et al.*, 2005). A pervasively fractured basalt flow exposed at site GE-1 yielded an early Miocene plateau age of 19.55 ± 0.10 Ma (Fig. 3c). Farther to the west across the Gidole-Chencha Horst, a similar plateau age of 19.80 ± 0.10 Ma was obtained from a basalt at site GE-12, where it overlies other, sub-horizontal basalt flows (GE-10 and GE-11). These units are characterized by well-developed flow structures and no intervening paleosol horizons; possibly, these basalt sheets represent laccoliths that are closely linked with the N-S-striking dikes emplaced at about 20 Ma (*e.g.*, Bonini *et al.*, 2005).

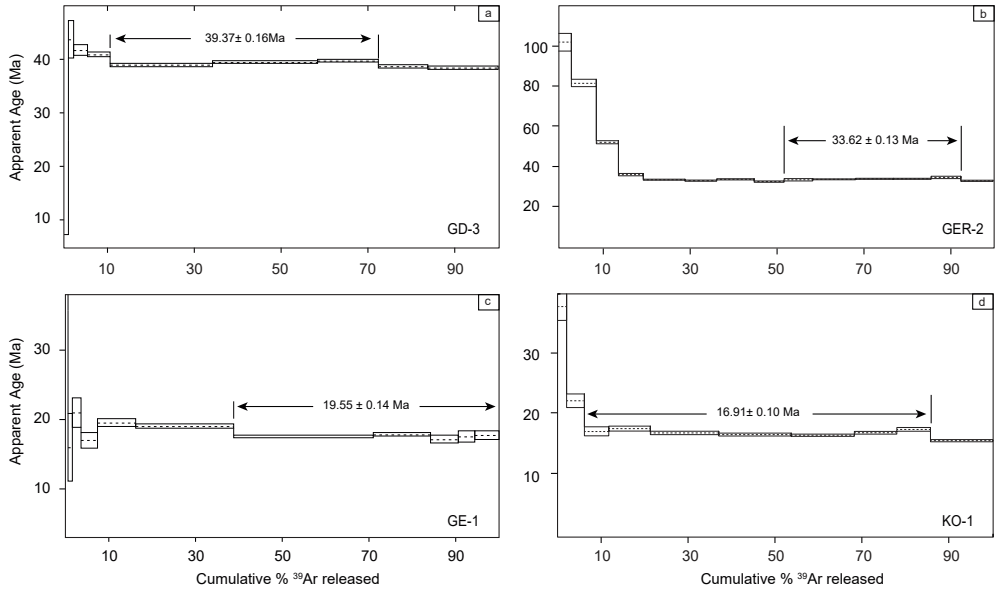

Figure 5.3: Representative $^{40}Ar/^{39}Ar$ dating results from basaltic flows sampled for paleomagnetic investigation across the Gidole-Chencha Horst. Plateau ages were calculated from individual apparent ages (broken lines) obtained from consecutive heating experiments, overlapping in a 2σ uncertainty (solid lines).

Sample KO-1 collected from a columnar-jointed basalt located to the west of the Segen basin yielded a well constrained Miocene age of 16.91 ± 0.10 Ma (Fig. 3d). Our age spectra of the Miocene volcanics are compatible with the age range between 18 and 11 Ma of the Getera-Kela basalts (Ebinger *et al.*, 2000). Interestingly, our data suggest that Miocene volcanism across the region might have been initiated at ~20 Ma and be closely linked with diking processes (Bonini *et al.*, 2005) and synchronous with faulting across the BRZ (Pik *et al.*, 2008).

5.4.2 Paleomagnetic results

The NRM intensities measured prior to the demagnetization experiments gave an average value of 1.1 and 7.1 A/m for the Eo-Oligocene and Miocene volcanics and sediments, respectively. Most of the basaltic samples from Eocene, Oligocene, and Miocene rocks display characteristic titanomagnetite behaviors. In these samples, thermal demagnetizations show most of the decay between 500°C and 600°C. This decay behavior is also reflected by a sharp decrease in this temperature range in thermomagnetic runs (Fig. 5.4). AF demagnetizations of these samples show that most of the decay generally occurs between 10 and 100 mT. In some samples, a residual stronger coercivity remanence is preserved above 100 mT (Figs. 5.5a, c, and e, and 5.6c and e). Thermal demagnetizations of such samples show a final decay between 600 and 680°C, suggesting the presence of hematite (Fig. 5.3f). The presence of goethite is not indicated by thermal demagnetization, and thermomagnetic runs both show no significant decay between 0

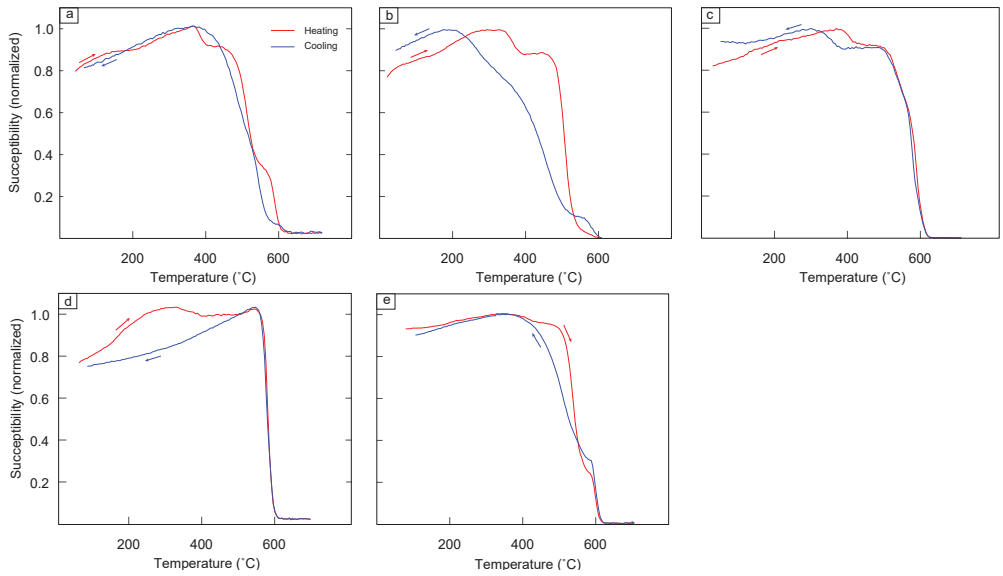

Figure 5.4: High-temperature thermomagnetic experiment results for the Eo-Oligocene and Miocene volcanics and sediments. Curves (a–e) show the heating (red line) and cooling (blue line) experiment for Eo-Oligocene (a–c) and Miocene (d and e) volcanics and sediments.

and 150°C in most of the samples. Together, these observations suggest a ChRM carried mainly by titanomagnetite. Most samples were thus demagnetized using AF, yielding linear decay towards the origin defining a ChRM between 10 and 100 mT. In a few samples, a secondary overprint was removed before 20 mT; in the samples from sites CH-3, GD-2, GER-1, GER-2, and KO-3, however, most of the NRM was demagnetized before 20 mT. The latter are characterized by a low Mean Destructive Field (MDF; Table B.1). Because they tended to display outlying directions, which was interpreted as resulting from remagnetization by lightning strike and/or from highly viscous mineralogies, they were rejected from further analyses when the MDF was below 10 mT.

The AF and TH demagnetization experiments were successful in progressively decaying the total NRM. The MDF for most of the analyzed samples is removed in a range of applied fields and thermal heating. For example, site means of MDF for the Eo-Oligocene volcanics varies between 4 and 61 mT , and between 5 and 42 mT for the Miocene volcanics and sediments. In 85 percent of the cases, the MDF for the Eo-Oligocene volcanics is higher than 10 mT, whereas for the Miocene volcanics and sediments it is lower than 10 mT in 10 percent of the cases (Table. 1). Representative TH experimental results reveal a range of demagnetization behavior between 380°C and 600°C.

High-field thermomagnetic experiment results from representative specimens exhibit the coexistence of two or three (ChRM) components in most cases. The curie temperature marking the ChRM range between 320°C and 590°C for the Eo-Oligocene basalts (Fig. 5.4a), and between 280°C and 570°C for the Miocene volcanics (Fig. 5.4b). The wide range of the Curie temperatures

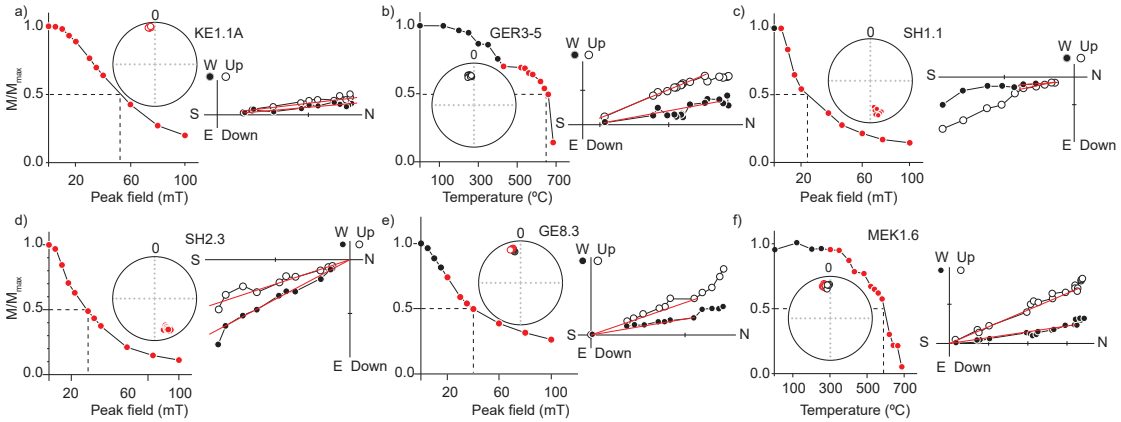

Figure 5.5: The specimens were treated by AF (a, c, d, and e), and TH (f) demagnetization experiments. Most of the results exhibit a single component of magnetization (a and d); however, in a few cases two components of magnetizations were identified (b, c, and e). The secondary component was removed between 5 and 15 mT AF (c and e) or TH demagnetization up to 420°C (b and f). Demagnetization steps used for a principal component analysis (red solid line) for each specimen are marked as red circles in the corresponding stereonet plot and decay curve.

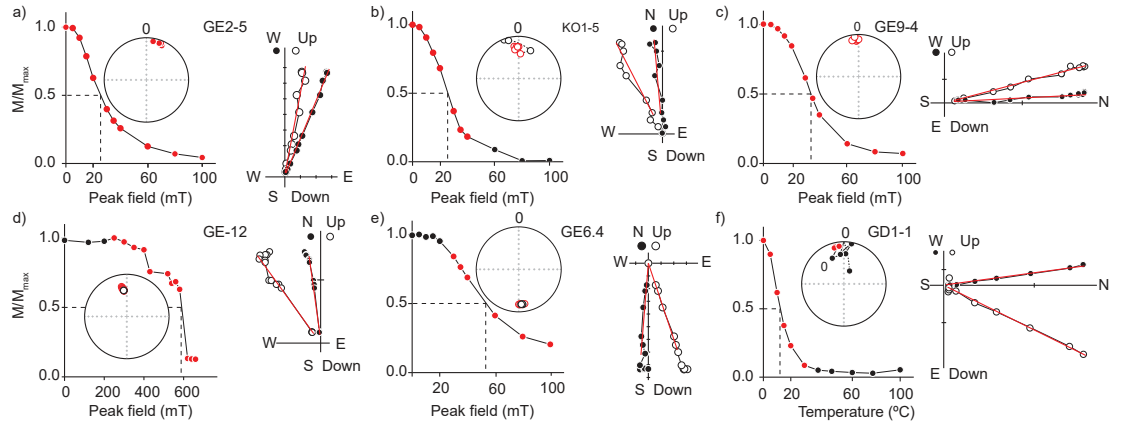

Figure 5.6: Typical behavior of AF and TH demagnetization results for representative specimens obtained from the Miocene rocks. Panels (a–f) indicate orthogonal vector diagrams with a corresponding stereonet plot and decay curve for each specimen treated by AF (a–e) and TH (f) demagnetization experiments. Measured demagnetization steps used for a principal component analysis (red solid line) for each specimen are marked as red circles.

is consistent with the broad distribution of the MDF values (Table B.1). Specimens KE6-1 and KE7-4 collected from two successive Eo-Oligocene basalt flows exhibit a single ChRM component marked by a Curie temperature between 530°C and 590°C, reflecting titanomagnetite and magnetite as the dominant magnetic mineralogy, respectively. In most cases, the final ChRM demagnetized Curie temperature range of 570°C to 600°C suggest the absence of hematite-bearing samples and supports our preferred AF demagnetization method for analyzing the bulk of the samples. The progressively increased AF and TH demagnetization experiments successfully extracted the high-stable components (ChRM) from low-stable components (secondary components). The low-stable components were isolated between 5 and 20 mT applied fields, whereas the ChRM acquired during cooling of a lava flow identified from 20 to 40 mT with vector end points progressively directed toward the origin (Figs. 5.5 and 5.6). Sites CH-4, GD-2, GD-3, and KO-4 recording MDF <10 mT were excluded from further analysis (Table B.1). Most of the sites record stable normal and reversed polarity directions with declinations ranging between ~346° and 014° for the normal polarities, and ~160° and 183° for the reversed directions.

5.4.2.1 Paleomagnetic directions

Based on existing regional geochronologic information (*e.g.*, Davidson and Rex, 1980; Davidson, 1983; Ebinger *et al.*, 1993, 2000; George, 1998; George and Rogers, 2002; Bonini *et al.*, 2005; Rooney *et al.*, 2010), detailed petrographic studies (Steiner *et al.*, 2021), and our new $^{40}Ar/^{39}Ar$ data, we grouped the mean directions of the analyzed sites into Eo-Oligocene rocks (45–27 Ma; *e.g.*, Steiner *et al.*, 2021) and Miocene rocks (20–11 Ma).

The overall mean direction for each classified group was estimated from each site recording a 95% confidence interval of <15° per site. A summary of the results is provided in B.2 and B.3 and Figure 7.

The Eo-Oligocene volcanics record normal (Ds=353.6°, Is=-16.5°, N=16, α_{95}=6.0°) and reverse (Ds=162.6°, Is=27.3°, N=3, α_{95}=18.5°) polarity directions. Despite, the declination and inclination directions of the normal and reversed polarities are differ by ~11° and ~14°, respectively, the normal and reverse polarity directions overlap within the 95% confidence interval. After excluding site KE-4, recording larger uncertainty (α_{95} > 15°) the declination and inclination directions differences decreased to ~9° and ~8°, respectively, and the directions remain antipodal, indicating a positive reversal test. An overall mean direction obtained for the Eo-Oligocene rocks is Ds=348.0°, Is=-17.2°, N=21, α_{95}=9.8°

The Miocene rocks record mainly stable normal polarity (Ds=4.1°, Is=0.7°, N=8, α_{95}=14.1°), except for two samples from site GE-6, which were obtained from a thin layer of sediment and records reverse geomagnetic polarity (Dg=175.5°, Ig=32.2°, α_{95}=11.0°). However, the formal reversal test between the mean for the normal polarity and the reverse direction is negative.

Considering the age range of the sediment of between 15 and 17 Ma and its stratigraphic relationship with respect to the Miocene volcanics (WoldeGabriel *et al.*, 1991; Ebinger *et al.*, 1998), an overall mean direction including the sediment site was obtained (Ds=0.1°, Is=-4.6°,

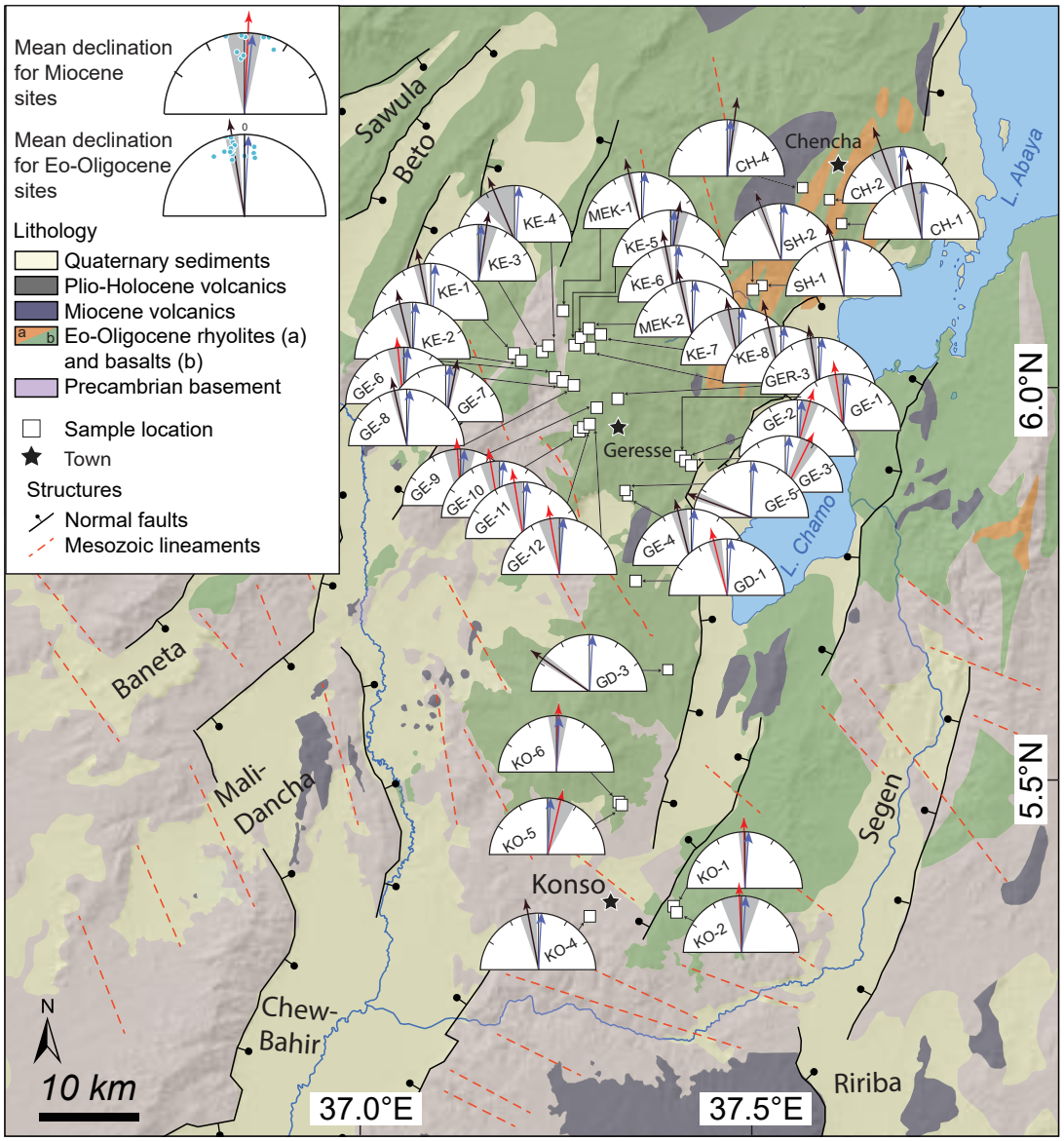

Figure 5.7: Mean paleomagnetic directions (declination) for each site distributed along and across the Gidole-Chencha Horst superimposed on the sampled stratigraphic units (Davidson, 1983; Bonini *et al.*, 2005) and hillshade relief map. Open square indicates sampling site location. In each site, observed mean declination direction (arrow) is indicated with the corresponding 95% confidence interval (gray shaded cone) for the Eo-Oligocene (dark blue) and Miocene (red) volcanics and sediments. The blue arrow indicates the expected direction relative to the pole for Africa at 40 Ma. Inset map at the top left shows overall mean direction (half-circle diagram) obtained from each site (light blue circles) for the Eo-Oligocene and Miocene volcanics.

N=11, α_{95}=12.5°). However, successive basaltic flows of GE-10, 11 and GE-12 dated at 19.8 ± 0.1 Ma, separated by well-developed flow structures and with no intervening paleosol horizon in between, exhibit indistinguishable magnetization directions, suggesting that the flows are likely the same or that they were emplaced within a short time interval relative to the rate of geomagnetic secular variation. For this reason, these flows were combined; and site GE-9 and KO-2, recording a larger uncertainty (α_{95}>15°) were excluded before an overall mean for the Miocene volcanics and sediments was recalculated (Ds=2.9°, Is=0.9°, N=9, α_{95}=12.4°).

The estimated directions from the Getera-Kela basalts and sediments were transformed into a Virtual Geomagnetic Pole (VGP) to obtain an average pole (ϕ_s =189.7°, λ_s =83.9°, S=18.4, N=9, α_{95}=9.7°) for the Miocene rocks. The observed higher scatter (S) in the distribution of the VGPs is likely related to the fewer number of sites (N<10; Butler *et al.*, 1992); however, our results are comparable to the expected VGP distribution for the Miocene rocks at lower latitudes, which ranges between 13.8 and 16.5 (Lhuillier and Gilder, 2019). Based on these considerations, we transformed the directions obtained from the classified groups of the Eo-Oligocene and Miocene volcanics into virtual geomagnetic poles for further analysis.

The VGP for the Eo-Oligocene basalts is ϕ_s=255.9°, λ_s=70.4°, α_{95}=8.3°, N=21. However, the three sites CH-2 (Ds=342.5°, Is=-62.9°, α_{95}=13.6°), GD-4 (Ds=304.7°, Is=8.8°, α_{95}=3.7°) and GE-5 (Ds=291.4°, Is=-39.3°, α_{95}=8.3°) were identified as transitional directions, recording VGPs located at >30° far away from the overall mean VGP (*e.g.*, McFadden *et al.*, 1991). As a result, a new overall mean direction (Ds=352.7°, Is=-14.6°, N=18, α_{95}=7.0°) and VGP (ϕ_s=243.5°, λ_s=73.5°, α_{95}=4.4°, N=18,) was recalculated from stable polarity directions after exclusion of the three sites.

5.5 Discussion

5.5.1 Vertical-axis tectonic rotations

The paleomagnetic data obtained from the Eo-Oligocene and Miocene rocks may be interpreted in terms of two process: (1) time-dependent vertical axis rotations of fault blocks, and (2) latitudinal motion relative to the reference plate (South Africa). The VGPs obtained for the Eo-Oligocene (ϕ_s =243.5°, λ_s =73.5°, N=18, α_{95}=4.4°) and Miocene (ϕ_s =189.8°, λ_s =83.9°, N=9, α_{95}=9.7°) basalts and sediments (Fig. 8a and b) were compared relative to the pole for stable South Africa during the corresponding ages using the procedure provided in Vaes *et al* .(2022) available from www.APWPonline.org. The VGP comparison for the Eocene volcanics (35–45 Ma) relative to the paleopoles for stable South Africa in the 35–45 Ma age range, resulted in a significant counterclockwise rotation of R= 11.1°± 6.4° and no significant flattening or Latitudinal Displacement of L = 4.2° ± 6.2° (Fig. 5.8c and d). For the Miocene volcanics and sediments, the observed VGPs in the 11–20 Ma age range relative to the pole for South Africa in the 11–20 Ma age range yield statistically insignificant counterclockwise block rotation of R = 3.2° ± 11.5°, and insignificant Latitudinal Displacement of L = 2.8° ± 11.5°. Careful inspection of the results in map view (Fig. 5.7) indicate the rotations are not concentrated at a single location

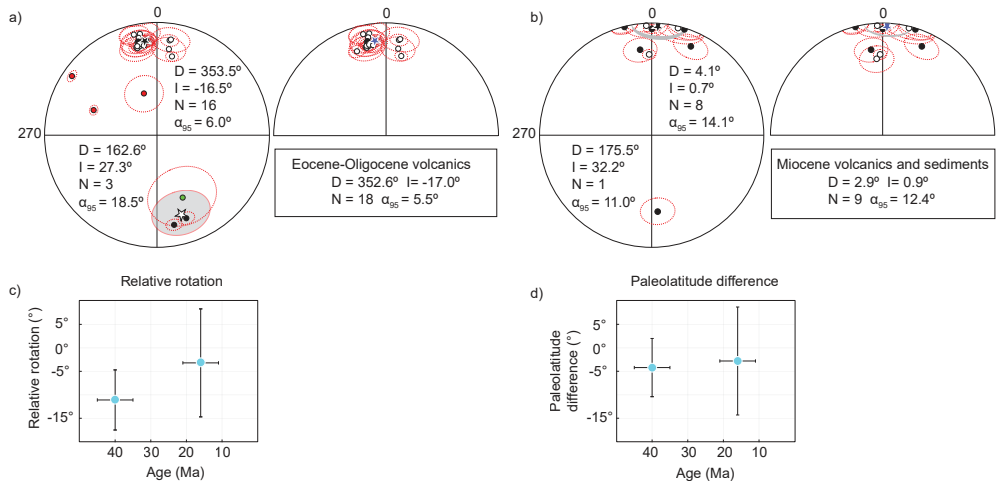

Figure 5.8: Stereographic projection of individual site means direction (circle) and for the Eo-Oligocene and Miocene volcanics. The black, white, and blue stars in the stereographic projections indicate the mean for normal, reversed, and overall mean directions, respectively for the Eo-Oligocene (a) and Miocene (b) volcanics and sediments within the corresponding 95% confidence interval (gray circle or envelope). The red circle with a broken line and envelope indicates the 95% confidence interval for individual site mean directions. The red solid circles indicate transitional directions. The overall mean direction was calculated after excluding site mean with 95% confidence interval >15 (green solid circle). The lower panels show relative rotation (c) and flattening or latitudinal displacement (d) obtained from a reference pole for stable South Africa at a corresponding age range between 35 and 45 Ma, and 11 and 20 Ma (Vaes *et al.*, 2022).

but suggest a small, but significant post-Eocene counterclockwise vertical-axis block rotation that systematically affected the zone of structural overlap between the Chew Bahir Basin-Gofa Province and the sMER. Although the age of the rotations clearly postdates the emplacement of the Eocene volcanics (35–45 Ma), constraining the age further is not straightforward. The similarity and regional distribution of the rotation suggest a common underlying mechanism although we cannot exclude the possibility that the rotations may have occurred in several phases at a different time and location. The smaller and statistically insignificant rotation documented in the Miocene dataset (11–20 Ma), indicates that at least part of the rotations recorded by the Eocene data, had occurred before the emplacement of the Miocene rocks. Either most of the rotation had occurred by the Miocene, or the rotations may have continued progressively until recently. We discuss below the potential implication of the vertical-axis rotations with regard to the regional structural background and proposed models of rift evolution.

5.5.2 Implications for deformation mechanisms

The detected counterclockwise block rotations are consistent with proposed models for the evolution of the sMER. Our results support the expected vertical-axis block rotations that have been proposed in relation to rift overlap between the Chew Bahir Basin-Gofa Province and the

sMER (*e.g.*, Philippon *et al.*, 2014; Brune *et al.*, 2017). Furthermore, the counterclockwise block rotations quantified by our analysis support the predicted block-deformation patterns obtained in analog and numerical modeling studies (Brune *et al.*, 2017; Glaume *et al.*, 2020; Neuharth *et al.*, 2021). Further insight into the deformation mechanisms can be obtained by considering the spatial and temporal characteristics of the extent of the vertical-axis block rotations across the overlap zone.

By combining our findings with published geologic information from the BRZ, we can explain the temporal variation in the amount of block rotation by at least two different end-member scenarios. In the first scenario, deformation accompanied by counterclockwise block rotation started at ~20 Ma, synchronous with faulting (*e.g.*, Pik *et al.*, 2008), and continued until the present day. During this period, the Eo-Oligocene and Miocene volcanic sequences would have been subjected to deformation associated with vertical-axis block rotation. Consequently, in this model of sustained rotation and deformation, the Eo-Oligocene volcanics would record a larger amount of tectonic overprint than the Miocene volcanic and sedimentary sequences. In the second scenario, much of the vertical-axis block rotation would occur during initial rifting affecting the Eo-Oligocene volcanics, but the region would have experienced limited block rotations since the late Miocene.

The documented temporal variation in the extent of the vertical axis block rotation is compatible with the spatial change in tectonic activity across the region during Mio-Pliocene time (*e.g.*, Davidson, 1983, Ebinger *et al.*, 2000; Chorowicz, 2005; WoldeGabriel *et al.*, 1991; Ebinger *et al.*, 1993, 2000; Bonini *et al.*, 2005; Pik *et al.*, 2008; Philippon *et al.*, 2014, Brune *et al.*, 2017; Boone *et al.*, 2019; Corti *et al.*, 2019). Geochronologic, structural, and field data from the sMER indicate that major faulting along the eastern margin of the Gidole-Chencha Horst occurred between 18 and 14 Ma. Following the development of the marginal fault, deformation migrated toward the Segen Basin and a narrow zone of the sMER during the middle Miocene and Pliocene, respectively (Levitte, 1974; WoldeGabriel *et al.*, 1991; Ebinger *et al.*, 2000; Bonini *et al.*, 2005). West of the Gidole-Chencha Horst along the Gofa Province, a concurrent shift in deformation toward the southern Gofa Province and the Chew Bahir Basin has been suggested by WoldeGabriel *et al.*, (1991) and Ebinger *et al.*, (2000). However, recent geomorphic investigation on river catchments verified by field observation reveal Quaternary active normal faults, and young tectonic landforms along the western margin of Mali-Dancha and Bala-Kela basin in the Gofa Province. The documented spatiotemporal variation in tectonic activity across the BRZ (Philippon *et al.*, 2014; Erbello *et al.*, 2022), would be compatible with the second scenario discussed above. Accordingly, a significant amount of counterclockwise block rotation must have occurred during the early Miocene, either prior to or during the deposition of the Miocene volcanics and sediments, which was superseded by a decrease in block rotation and accompanied by a migration of deformation and strain localization in the current rift sectors.

Importantly, from a more regional perspective our results suggest that extending this data set in future studies would help to better constrain the reference pole of Africa and pinpoint its slowdown during northward convergence associated with the Africa-Eurasia collision and

its implication for East African plume dynamics (*e.g.*, Faccenna *et al.*, 2019). Our study also emphasizes that caution is necessary for the definition of the reference pole for Africa based on volcanic rocks from rifts or regions close to the rift flanks that may have recorded small local, but systematic rotations such as those observed in southern Ethiopia (*e.g.*, Besse and Courtillot, 1999; 2002).

5.5.3 The role of inherited lineaments in rifting

With respect to the spatiotemporal changes of the locations of volcanism and extension in southern Ethiopia (*e.g.*, Ebinger *et al.*, 2000, Philippon *et al.*, 2014, Corti *et al.*, 2019, Knappe *et al.*, 2020), the degree to which tectonic processes reactivated inherited crustal-scale lineaments during the Cenozoic is also expected to have changed over time. In such a scenario, where vertical-axis rotations involve structural blocks with pre-existing fabrics inherited from previous geodynamic processes, it may be inferred that the NW-SE-striking inherited zones of weakness parallel to the rotating blocks may have facilitated lateral motion and efficient kinematic transfer between different rift sectors. For example, the amount of ~11 ± 6.4° counterclockwise block rotation recorded by the Eo-Oligocene volcanic rocks appears to have significantly decreased over time, as is documented from the Miocene volcanics. The large extent of vertical axis block rotation might have been facilitated by NW-SE-oriented lineaments achieved during early rifting. However, due to the overall block motion, this process would have later slowed down as the overlapping rift segments would have connected with each other to develop larger, through-going extensional structures (Neuharth *et al.*, 2021). In this context it is noteworthy that low-temperature thermochronologic data from the Gofa Province record rapid exhumation across the NW-SE-oriented margin of the Beto Basin in the early Miocene (Boone *et al.*, 2019). The reactivation of the NW-SE-striking lineaments during the early Miocene, thus likely reflects the role of inherited zones of weakness in facilitating fracture propagation during early rifting processes. Interestingly, recent seismic tomographic imaging from the BRZ exhibited a nearly vertical, NW-SE-trending pervasive band of lineaments below the southern Gofa Province and the northern Chew Bahir Basin (Kounoudis *et al.*, 2021). Additionally, thermochronological data from this region obtained at the margin of the Gofa Province show spatial variation regarding the onset of faulting and tectonic exhumation (*e.g.*, Balestrieri *et al.*, 2016). Lineaments striking at high angles with respect to the orientation of the rift, such as the NW-SE-striking reactivated Mesozoic rift-related structures in the BRZ, may have inhibited meridionally oriented fault propagation and accommodated extensional processes by shearing along these inherited anisotropies (*e.g.*, Molnar *et al.*, 2019). In line with these observations are earthquake focal mechanism solutions that partly indicate a component of horizontal shearing and oblique normal faulting within this Ethiopian extensional province. For example, Asfaw (1990) suggested oblique-slip faulting along the basin-bounding Chew Bahir and southern Gofa Province faults during the Quaternary. Furthermore, earthquakes recorded from the Chew Bahir Basin, the Segen Basin, and regions farther away in the northwestern sector of South Sudan, suggest strike-slip faulting along the

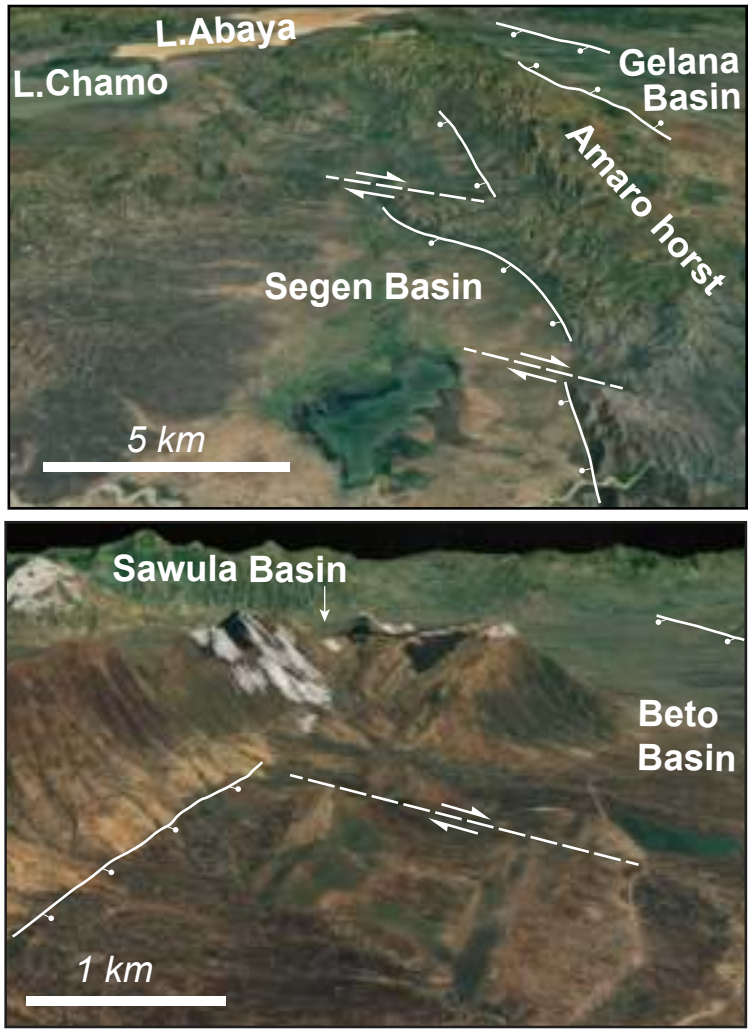

Figure 5.9: Northwest view of the sMER (Segen, Chamo, Gelana, and Abaya basins) and the Gofa Province (Beto and Sawula basins) with basin-bounding faults (white extended lines with ball and bar symbol). The white broken lines indicate NW-SE-striking lineaments with an inferred strike-slip component

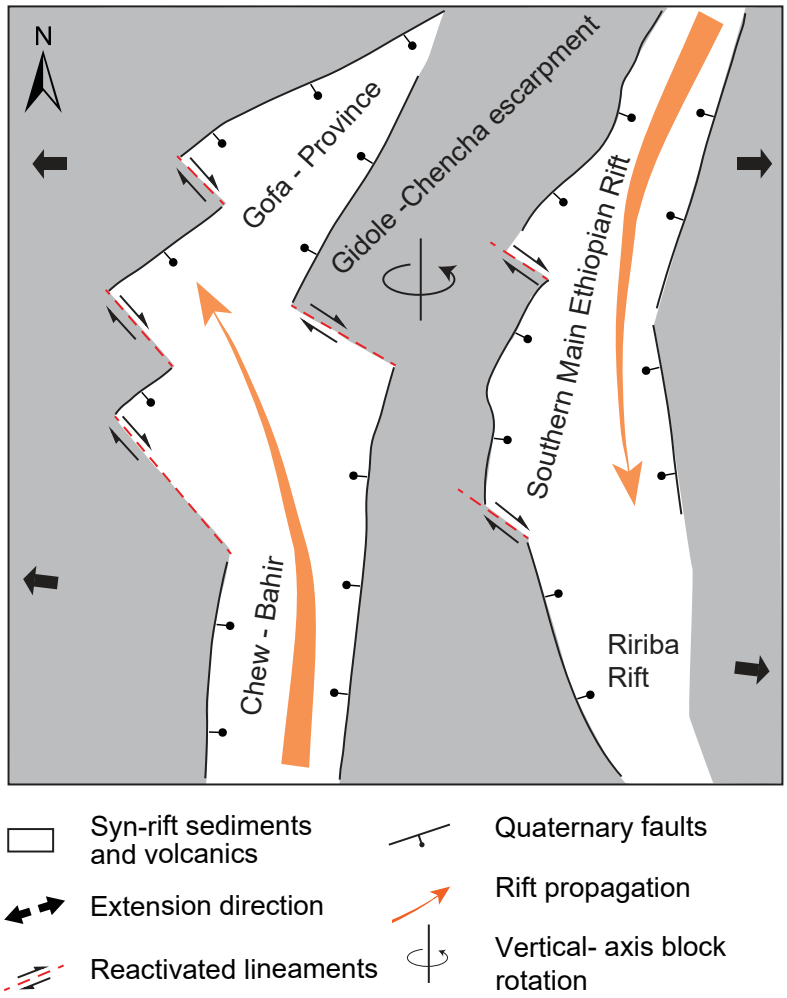

Figure 5.10: Oppositely propagating, parallel rift segments and associated vertical axis block rotation across the overlap zone between the sMER and the Chew Bahir Basin-Gofa Province. The black and orange arrows indicate local plate kinematics (Philippon *et al.*, 2014) and direction of propagating rift segments, respectively. Inferred NW-SE-striking inherited lineaments shown as red broken lines.

NW-SE- and N-S-striking lineaments (Ayele, 2000). Finally, a seismicity study in the BRZ and nKR (Musila *et al.*, 2020; Sullivan *et al.*, 2021) revealed right-lateral strike-slip faulting in the transition between the sMER and nKR. This possibly reflects the reactivation of NW-SE-striking lineaments similar to structures such as shown in (Figs. 5.9 and 5.10). Such structures may have facilitated the counterclockwise block rotation between both rift sectors, although lateral displacement along the lineaments appears to be limited (Ebinger *et al.*, 2000).

5.6 Conclusion

Paleomagnetic data combined with published and new $^{40}Ar/^{39}Ar$ data from across the ~40-km-wide zone of overlap between the bi-directionally propagating sMER and the Chew Bahir Basin-Gofa Province reveal a temporal evolution of deformation associated with post-Eocene, approximately 10 to 15° counterclockwise vertical-axis block rotations across the region.

The data suggests a decrease in the amount of vertical axis block rotation over time that corresponds well with the migration of deformation toward the axial zone of the sMER and the Chew Bahir Basin-Gofa Province. In light of regional structural and low-temperature thermochronology data our observations suggest that much of the deformation related to the vertical axis block rotations likely occurred in the early Miocene between about 18 and 22 Ma and progressively decreased following a migration of the locus of deformation to the rift axis during the Pliocene.

The pattern of regional counterclockwise block rotations that most likely occurred during early Miocene initial rifting, is closely associated with the reactivation of NW-SE-striking Mesozoic lineaments, reflecting the influence of inherited structures during extension. However, further paleomagnetic studies are necessary to ascertain the timing of rotations. The rich volcanic record of southern Ethiopia would provide the opportunity to do this in rare detail. Our study demonstrates the potential of paleomagnetic analysis to constrain tectonic models and quantitatively limit the extent of deformation of southern Ethiopia and other rift systems. Extending the dataset would also enable to better constrain the reference pole of Africa and pinpoint its slowdown during northward convergence associated with the Africa-Eurasia collision and its implication for plume migration. In this context, our study emphasizes that care should be taken when defining the reference pole for Africa from rifts or a proximal region to the rift margin that may have recorded small local, but systematic rotations as seen in the plateau volcanics of southern Ethiopia.

5.7 References

Aanyu, K., and Koehn, D. (2011), Influence of pre-existing fabrics on fault kinematics and rift geometry of interacting segments: Analogue models based on the Albertine Rift (Uganda), Western Branch-East African Rift System. Journal of African Earth Sciences. doi:10.1016/j.jafrearsci.2010.10.003

Acocella, V., Morvillo, P., and Funiciello, R. (2005), What controls relay ramps and transfer faults within rift zones? Insights from analogue models. Journal of Structural Geology. doi:10.1016/j.jsg.2004.11.006

Acton, G.D., Stein, S., and Engeln, J.F. (1991), Block rotation and continental extension in Afar: A comparison to oceanic microplate systems. Tectonics, doi:10.1029/90TC01792 Asfaw, L.M. (1990), Implication of shear deformation and earthquake distribution in the East African Rift between 4°N and 6°N. Journal of African Earth Sciences. doi:10.1016/0899-5362(90)90041-C

Ayele, A., and Arvidsson, R. (1997), Fault mechanisms and tectonic implication of the 1985-1987 earthquake sequence in south-western Ethiopia. Journal of Seismology. doi:10.1023/A:1009774331917

Balestrieri, M.L., Bonini, M., Corti, G., Sani, F., and Philippon, M. (2016), A refinement of the chronology of rift-related faulting in the Broadly Rifted Zone, southern Ethiopia, through apatite fission-track analysis. Tectonophysics, 671, 42–55. doi:10.1016/j.tecto.2016.01.012

Bellahsen, N., Leroy, S., Autin, J., Razin, P., d'Acremont, E., Sloan, H., Pik, R., Ahmed, A., and Khanbari, K. (2013), Pre-existing oblique transfer zones and transfer/transform relationships in continental margins: New insights from the southeastern Gulf of Aden, Socotra Island, Yemen. Tectonophysics. doi:10.1016/j.tecto.2013.07.036

Besse, J., and Courtillot, V. (2002), Apparent and true polar wander and the geometry of the geomagnetic field over the last 200 Myr. Journal of Geophysical Research: Solid Earth. doi:10.1029/2000jb000050

Besse, J., and Courtillot, V. (1991), Revised and synthetic apparent polar wander paths of the African, Eurasian, North American and Indian plates, and true polar wander since 200 Ma. Journal of Geophysical Research. doi:10.1029/90JB01916

Bonini, M., Corti, G., Innocenti, F., Manetti, P., Mazzarini, F., Abebe, T., and Pecskay, Z. (2005), Evolution of the Main Ethiopian Rift in the frame of Afar and Kenya rifts propagation. Tectonics. doi:10.1029/2004TC001680

Boone, S. C., Balestrieri, M.L., Kohn, B.P., Corti, G., Gleadow, A.J.W., and Seiler, C. (2019), Tectonothermal Evolution of the Broadly Rifted Zone, Ethiopian Rift. Tectonics. doi:10.1029/2018TC005210

Boone, Samuel C., Kohn, B.P., Gleadow, A.J.W., Morley, C.K., Seiler, C., Foster, D.A. (2019), Birth of the East African Rift System: Nucleation of magmatism and strain in the Turkana Depression. Geology. doi:10.1130/G46468.1

Bosworth, W. (1992), Mesozoic and early Tertiary rift tectonics in East Africa. Tectonophysics. doi:10.1016/0040-1951(92)90014-W

Bosworth, W. (1985), Geometry of propagating continental rifts. Nature. doi:10.1038/316625a0 Bosworth, W., and Morley, C.K. (1994), Structural and stratigraphic evolution of the Anza rift, Kenya. Tectonophysics. doi:10.1016/0040-1951(94)90171-6

Brune, S., Corti, G., and Ranalli, G. (2017), Controls of inherited lithospheric heterogeneity on rift linkage: Numerical and analog models of interaction between the Kenyan and Ethiopian rifts across the Turkana depression. Tectonics, 36, 1767–1786. doi:10.1002/2017TC004739

Childs, C., Easton, S.J., Vendeville, B.C., Jackson, M.P.A., Lin, S.T., Walsh, J.J., and Watterson, J. (1993), Kinematic analysis of faults in a physical model of growth faulting above a viscous salt analogue. Tectonophysics. doi:10.1016/0040-1951(93)90346-L

Childs, C., Watterson, J., and Walsh, J.J. (1995), Fault overlap zones within developing normal fault systems. Journal - Geological Society (London). doi:10.1144/gsjgs.152.3.0535

Chorowicz, J. (2005), The East African rift system. Journal of African Earth Sciences. doi:10.1016/j.jafrearsci.2005.07.019

Chu, D., and Gordon, R.G. (1999), Evidence for motion between Nubia and Somalia along the Southwest Indian ridge. Nature. doi:10.1038/18014

Cogne, J.P. (2003), PaleoMac: A MacintoshTM application for treating paleomagnetic data and making plate reconstructions. Geochemstry, Geophysics, Geoszstems, 4(1), 1-8. doi:10.1029/2001GC000227, 2003.

Corti, G. (2008), Control of rift obliquity on the evolution and segmentation of the main Ethiopian rift. Nature Geoscience. doi:10.1038/ngeo160

Corti, G., Cioni, R., Franceschini, Z., Sani, F., Scaillet, S., Molin, P., Isola, I., Mazzarini, F., Brune, S., Keir, D., Erbello, A., Muluneh, A., Illsley-Kemp, F., and Glerum, A. (2019), Aborted propagation of the Ethiopian rift caused by linkage with the Kenyan rift. Nature Communications, 10. doi:10.1038/s41467-019-09335-2

Dawers, N.H., and Anders, M.H. (1995), Displacement-length scaling and fault linkage. Journal of Structural Geology. doi:10.1016/0191-8141(94)00091-D

DeMets, C., Merkouriev, S., and Sauter, D. (2015), High-resolution estimates of Southwest Indian Ridge plate motions, 20 Ma to present. Geophysical Journal International. doi:10.1093/gji/ggv366

Dommain, R., Riedl, S., Olaka, L.A., DeMenocal, P., Deino, A.L., Owen, R.B., Muiruri, V., Müller, J., Potts, R., and Strecker, M.R. (2022), Holocene bidirectional river system along the Kenya Rift and its influence on East African faunal exchange and diversity gradients. Proceedings of the National Academy of Sciences 119. doi:10.1073/pnas.2121388119

Ebinger, C., and Scholz, C.A. (2012), Continental Rift Basins: The East African Perspective, in: Tectonics of Sedimentary Basins: Recent Advances. doi:10.1002/9781444347166.ch9

Ebinger, C.J., Jackson, J.A., Foster, A.N., and Hayward, N.J. (1999), Extensional basin geometry and the elastic lithosphere. Philosophical Transactions of the Royal Society A: Mathematical, Physical and Engineering Sciences. doi:10.1098/rsta.1999.0351

Ebinger, C.J., Yemane, T., Harding, D.J., Tesfaye, S., Kelley, S., and Rex, D.C. (2000), Rift deflection, migration, and propagation: Linkage of the Ethiopian and Eastern rifts, Africa. Bulletin of the Geological Society of America 112, 163–176. doi:10.1130/0016-7606(2000)112<163:RDMAPL>2.0.CO;2

Ebinger, C.J., Yemane, T., Woldegabriel, G., Aronson, J.L., and Walter, R.C. (1993), Late Ecocene-Recent volcanism and faulting in the southern main Ethiopian rift. Journal - Geological Society (London) 150, 99–108. doi:10.1144/gsjgs.150.1.0099

Emishaw, L., and Abdelsalam, M.G. (2019), Development of Late Jurassic-Early Paleogene and Neogene-Quaternary Rifts Within the Turkana Depression, East Africa From Satellite Gravity Data. Tectonics, 38, 2358–2377. doi:10.1029/2018TC005389

Erbello, A., and Kidane, T. (2018), Timing of volcanism and initiation of rifting in the Omo-Turkana depression, southwest Ethiopia: Evidence from paleomagnetism. Journal of African Earth Sciences. doi:10.1016/j.jafrearsci.2017.12.031

Erbello, A., Melnick, D., Zeilinger, G., Bookhagen, B., Pingel, H., and Strecker, M.R. (2022), Geomorphic expression of a tectonically active rift-transfer zone in southern Ethiopia. Geomorphology. doi:10.1016/j.geomorph.2022.108162

Fernandes, R.M.S., Miranda, J.M., Delvaux, D., Stamps, D.S., and Saria, E. (2013), Re-evaluation of the kinematics of victoria block using continuous GNSS data. Geophysical Journal International. doi:10.1093/gji/ggs071

Fisher, R. (1953), Dispersion on a Sphere. Proceedings of the Royal Society A: Mathematical, Physical and Engineering Sciences. doi:10.1098/rspa.1953.0064

Faccenna, C., Glišović, P., Forte, A., Becker, T.W., Garzanti, E., Sembroni, A., and Gvirtzman, Z. (2019), Role of dynamic topography in sustaining the Nile River over 30 million years. Nature Geoscience. doi:10.1038/s41561-019-0472-x

Franceschini, Z., Cioni, R., Scaillet, S., Corti, G., Sani, F., Isola, I., Mazzarini, F., Duval, F., Erbello, A., Muluneh, A., and Brune, S. (2020), Recent volcano-tectonic activity of the Ririba rift and the evolution of rifting in South Ethiopia. Journal of Volcanology and Geothermal Research. doi:10.1016/j.jvolgeores.2020.106989

Glerum, A., Brune, S., Stamps, D.S., and Strecker, M.R. (2020), Victoria continental microplate dynamics controlled by the lithospheric strength distribution of the East African Rift. Nature Communications. doi:10.1038/s41467-020-16176-x

Gouin, P. (1979), Earthquake History of Ethiopia and the Horn Of Africa. Geophysical Observatory,University of Addis Ababa, Addis Ababa.

Hetzel, R., and Strecker, M.R. (1994), Late Mozambique Belt structures in western Kenya and their influence on the evolution of the Cenozoic Kenya Rift. Journal of Structural Geology. doi:10.1016/0191-8141(94)90104-X

Katz, R.F., Ragnarsson, R., and Bodenschatz, E. (2005), Tectonic microplates in a wax model of sea-floor spreading. New Journal of Physics. doi:10.1088/1367-2630/7/1/037

Kendall, J.M., and Lithgow-Bertelloni, C. (2016), Why is Africa rifting?, in: Geological Society Special Publication. doi:10.1144/SP420.17

Kidane, T., Courtillot, V., Manighetti, I., Audin, L., Lahitte, P., Quidelleur, X., Gillot, P.-Y., Gallet, Y., Carlut, J., and Haile, T. (2003), New paleomagnetic and geochronologic results from Ethiopian Afar: Block rotations linked to rift overlap and propagation and determination of a ~2 Ma reference pole for stable Africa. Journal of Geophysical Research: Solid Earth. doi:10.1029/2001jb000645

Kidane, T., Otofuji, Y.I., Komatsu, Y., Shibasaki, H., and Rowland, J. (2009), Paleomagnetism of the Fentale-magmatic segment, main Ethiopian Rift: New evidence for counterclockwise block rotation linked to transtensional deformation. Physics of the Earth and Planetary Interiors. doi:10.1016/j.pepi.2009.04.006

Kirschvink, J.L. (1980), The least-squares line and plane and the analysis of palaeomagnetic data. Geophysical Journal of the Royal Astronomical Society. doi:10.1111/j.1365-246X.1980.tb02601.x

Knappe, E., Bendick, R., Ebinger, C., Birhanu, Y., Lewi, E., Floyd, M., King, R., Kianji, G., Mariita, N., Temtime, T., Waktola, B., Deresse, B., Musila, M., Kanoti, J., and Perry, M. (2020), Accommodation of East African Rifting Across the Turkana Depression. Journal of Geophysical Research: Solid Earth. doi:10.1029/2019JB018469

Koehn, D., Aanyu, K., Haines, S., and Sachau, T. (2008), Rift nucleation, rift propagation and the creation of basement micro-plates within active rifts. Tectonophysics. doi:10.1016/j.tecto.2007.10.003

Kolawole, F., Firkins, M.C., Al Wahaibi, T.S., Atekwana, E.A., and Soreghan, M.J. (2021), Rift interaction zones and the stages of rift linkage in active segmented continental rift systems. Basin Research 33, 2984–3020. doi:10.1111/bre.12592

Koukouvelas, I.K., Asimakopoulos, M., and Doutsos, T.T. (1999), Fractal characteristics of active normal faults: An example of the eastern Gulf of Corinth, Greece. Tectonophysics. doi:10.1016/S0040-1951(99)00087-6

Kounoudis, R., Bastow, I.D., Ebinger, C.J., Ogden, C.S., Ayele, A., Bendick, R., Mariita, N., Kianji, G., Wigham, G., Musila, M., and Kibret, B. (2021), Body-Wave Tomographic Imaging of the Turkana Depression: Implications for Rift Development and Plume-Lithosphere Interactions. Geochemistry, Geophysics, Geosystems. doi:10.1029/2021GC009782

Lee, J-Y., Marti, K., Severinghaus, J.P., Kawamura, K., Yoo, H-S., Lee, J.B., and Kim, J.S. (2006), A redetermination of the isotopic abundances of atmospheric Ar. Geochimica et Cosmochimica Acta, 70, 4507-4512. doi:10.1016/j.gca.2006.06.1563

Levitte, D., Columba, J., and Mohr, P. (1974), Reconnaissance geology of the Amaro Horest, southern Ethiopian Rift. Geological Society of America. doi:10.1130/0016-7606(1974)85<417:RGOTAH>2.0.CO;2

Lhuillier, F., and Gilder, S.A. (2019), Paleomagnetism and geochronology of Oligocene and Miocene volcanic sections from Ethiopia: geomagnetic variability in the Afro-Arabian region over the past 30 Ma. Geophysical Journal International, 216, 1466-1481. doi:10.1093/gji/ggy517

MacDonald, K.C., and Fox, P.J. (1983), Overlapping spreading centres: New accretion geometry on the East Pacific Rise. Nature. doi:10.1038/302055a0

McFadden, P.L., and McElhinny, M.W. (1988), The combined analysis of remagnetization circles and direct observations in palaeomagnetism. Earth and Planetary Science Letters. doi:10.1016/0012-821X(88)90072-6

McKenzie, D., and Jackson, J. (1986), A block model of distributed deformation by faulting. Journal of the Geological Society. doi:10.1144/gsjgs.143.2.0349

Molnar, N.E., Cruden, A.R., and Betts, P.G. (2019), Interactions between propagating rifts and linear weaknesses in the lower crust. Geosphere. doi:10.1130/GES02119.1

Moore, J.M., and Davidson, A. (1978), Rift structure in southern Ethiopia. Tectonophysics. doi:10.1016/0040-1951(78)90111-7

Morley, C.K., Nelson, R.A., Patton, T.L., and Munn, S.G. (1990), Transfer zones in the East African rift system and their relevance to hydrocarbon exploration in rifts. American Association of Petroleum Geologists Bulletin. doi:10.1306/0c9b2475-1710-11d7-8645000102c1865d

Morley, C.K., Wescott, W.A., Stone, D.M., Harper, R.M., Wigger, S.T., and Karanja, F.M. (1992), Tectonic evolution of the northern Kenyan Rift. Journal - Geological Society (London). doi:10.1144/gsjgs.149.3.0333

Muluneh, A.A., Kidane, T., Rowland, J., and Bachtadse, V. (2013), Counterclockwise block rotation linked to southward propagation and overlap of sub-aerial Red Sea Rift segments, Afar Depression: Insight from paleomagnetism. Tectonophysics. doi:10.1016/j.tecto.2013.02.030

Musila, M., Ebinger, C.J., Mwangi, S., Kianji, G., Ayele, A., Mariita, N., Bastow, I.D., and Bendick, R.O. (2020). Kinematics of linkage between the Main Ethiopian and Eastern rifts in the Turkana Depression. American Geophysical Union, Fall meeting. 2020AGUFMT024.0004M

Nelson, R.A., Patton, T.L., and Morley, C.K. (1992), Rift-segment interaction and its relation to hydrocarbon exploration in continental rift systems. American Association of Petroleum Geologists Bulletin. doi:10.1306/bdff898e-1718-11d7-8645000102c1865d

Neuharth, D., Brune, S., Glerum, A., Helne, C., and Welford, J.K. (2021), Formation of continental microplate through rift linkage: numerical modeling and its application to the Flemish Cap and Sao Paulo Plateau. Geochemistry, Geophysics, Geosystem. doi:10.1029/2020GC009615

Nugsse, K., Muluneh, A.A., and Kidane, T. (2018), Paleomagnetic evidence for counterclockwise rotation of the Dofan magmatic segment, Main Ethiopian Rift. Tectonophysics. doi10.1016/j.tecto.2018.03.013

Olaka, L.A., Kasemann, S.A., Sültenfuß, J., Wilke, F.D.H., Olago, D.O., Mulch, A., and Musolff, A. (2022), Tectonic control of groundwater recharge and flow in faulted volcanic aquifers. Water Resources Research, 58, 1-20. doi:10.1029/2022WR032016

Peacock, D.C.P. (2002), Propagation, interaction and linkage in normal fault systems. Earth-Science Reviews. doi:10.1016/S0012-8252(01)00085-X

Philippon, M., Corti, G., Sani, F., Bonini, M., Balestrieri, M.L., Molin, P., Willingshofer, E., Sokoutis, D., and Cloetingh, S. (2014), Evolution, distribution, and characteristics of rifting in southern Ethiopia. Tectonics, 33, 485–508. doi:10.1002/2013TC003430

Pik, R., Marty, B., Carignan, J., Yirgu, G., and Ayalew, T. (2008), Timing of East African Rift development in southern Ethiopia: Implication for mantle plume activity and evolution of topography. Geology 36, 167–170. doi:10.1130/G24233A.1

Ragon, T., Nutz, A., Schuster, M., Ghienne, J.F., Ruffet, G., and Rubino, J.L. (2019), Evolution of the northern Turkana Depression (East African Rift System, Kenya) during the Cenozoic rifting: New insights from the Ekitale Basin (28-25.5 Ma). Geological Journal. doi:10.1002/gj.3339

Rosendahl, B.R. (1987), Architecture of continental rifts with special reference to East Africa. Annual review of earth and planetary sciences. doi:10.1146/annurev.earth.15.1.445

Saria, E., Calais, E., Altamimi, Z., Willis, P., and Farah, H. (2013), A new velocity field for Africa from combined GPS and DORIS space geodetic Solutions: Contribution to the definition of the African reference frame (AFREF). Journal of Geophysical Research: Solid Earth. doi:10.1002/jgrb.50137

Saria, E., Calais, E., Stamps, D.S., Delvaux, D., and Hartnady, C.J.H. (2014), Present-day kinematics of the East African Rift. Journal of Geophysical Research: Solid Earth. doi:10.1002/2013JB010901

Schouten, H., Klitgord, K.D., and Gallo, D.G. (1993), Edge-driven microplate kinematics. Journal of Geophysical Research: Solid Earth. doi:10.1029/92jb02749

Stamps, D.S., Calais, E., Saria, E., Hartnady, C., Nocquet, J.M., Ebinger, C.J., and Fernandes, R.M. (2008). A kinematic model for the East African Rift. Geophysical Research Letters. doi:10.1029/2007GL032781

Stamps, D.S., Saria, E., and Kreemer, C. (2018), A Geodetic Strain Rate Model for the East African Rift System. Scientific Reports. doi:10.1038/s41598-017-19097-w

Steiner, R.A., Rooney, T.O., Girard, G., Rogers, N., Ebinger, C.J., Peterson, L., and Phillips, R.K. (2021), Initial Cenozoic magmatic activity in East Africa: new geochemical constraints on magma distribution within the Eocene continental flood basalt province, in: Geological Society Special Publication. doi:10.1144/SP518-2020-262

Sulivan, G., Musila, M., Kaus, E., Ebinger, C.J., Bastow, I., Kounoudis, R., Nderitu, S., Mariita, N. (2021). Structures and seismicity: showing shifting rift axis across the Turkana Depression. American Geophysical Union, Fall meeting. 2021AGUFM.T55F.23S

Tauxe, L. (2005), Inclination flattening and the geocentric axial dipole hypothesis. Earth and Planetary Science Letters. doi:10.1016/j.epsl.2005.01.027

Vaes, B., Gallo, L.C., and van Hinsbergen, D.J. J. (2022), On Pole Position: Causes of Dispersion of the Paleomagnetic Poles behind Apparent Polar Wander Paths. Journal of Geophysical Research, Solid Earth. doi: 10.1029/2022JB023953

Woldegabriel, G., Aronson, J.L., and Walter, R.C. (1990), Geology, geochronology, and rift basin development in the central sector of the Main Ethiopia Rift. Bulletin of the Geological Society of America. doi:10.1130/0016-7606(1990)102<0439:GGARBD>2.3.CO;2

WoldeGabriel, G., Yemane, T., Suwa, G., White, T., and Asfaw, B. (1991), Age of volcanism and rifting in the Burji-Soyoma area, Amaro Horst, southern Main Ethiopian Rift: geo- and biochronologic data. Journal of African Earth Sciences. doi:10.1016/0899-5362(91)90107-A

Chapter 6

Discussion

In this chapter, I synthesize my contribution toward a better understanding of the structural and geomorphic evolution of initially isolated rift basins in the BRZ of southern Ethiopia and their interaction and linkage over time. In my study thermochronologic, geochronologic, paleomagnetic, and morphometric data were combined with regionally distributed, well-dated volcanic sequences to investigate a hypothesis that links continental rifting and regional pulses in magmatic processes. Furthermore, I identified, characterized, and quantified crustal block deformation within the BRZ overlap zone between the sMER and the Chew Bahir Basin-Gofa Province to characterize the interaction of adjacent rift segments with an opposite direction of structural propagation.

6.1 Initial diffuse faulting across the Broadly Rifted Zone

The thermochronological part of my study revealed that time-temperature history paths obtained from thermal modeling of representative samples exhibit little or no significant uplift or crustal cooling across the BRZ prior to or during extensive magmatism in the interval between 45 and 27 Ma (*e.g.*, Davidson, 1983; Ebinger *et al.*, 2000; Bonini *et al.*, 2005; Steiner *et al.*, 2021). However, spatially offset samples from elevation transects that were collected at locations across the northeastern margin of the Chew Bahir Basin and one sample obtained from the bottom of the exposed footwall of the Weyito Basin flank record protracted, slow cooling that initiated during the Paleogene (Chapter 3; Fig. 3.2). A consistent onset of slow cooling during the early Paleogene has been reported from the Beto and Segen basins in the BRZ (Philippon *et al.*, 2014; Balestrieri *et al.*, 2016; Boone *et al.*, 2019), and farther south in the nKR (*e.g.*, Torres *et al.*, 2015), suggesting a regional, tectonically controlled cooling event related to the opening of the Anza Rift in northern Kenya (Morley *et al.*, 1990, 1992; Bosworth and Morley, 1994).

Based on gravity data, Mamo (2012) inferred NW-SE-striking lineaments masked by the basin-fill sediments and N-S-striking Quaternary structures. Farther to the southeast in the Kino-Sogo Rift, Emishaw and Abdelsalam (2019) extracted E-W-trending gravity anomalies, thought to reflect E-W-striking faults that may link the Anza paleorift of northern Kenya and the Melut and

Muglad basins in southern Sudan via the Chew Bahir and the Omo-Turkana depression (*e.g.*, Mamo, 2012).

The thermal modeling results obtained in my study, documenting slow cooling beginning during the Paleogene, and the temporally consistent uplift history reported from the Segen and Beto basins in the BRZ (*e.g.*, Philippon *et al.*, 2014; Balestrieri *et al.*, 2016; Boone *et al.*, 2019), fit this overall tectonic setting of extension and likely reflect an attainment of a NW-SE-trending local relief, assuming that the adjacent regions were characterized by low-elevation surfaces during this period (*e.g.*, Davidson and Rex, 1980). I suggest that the inferred local relief may have generated a source rock for the deposition of Cretaceous-early Paleogene (?) conglomeratic sandstones in southern Ethiopia and the strata of the lower unit of the Turkana Grits in northern Kenya (*e.g.*, Murray-Hughes, 1933; Arambourg and Wolff, 1969; Walsh and Dodson, 1969; Savage and Williamson, 1974; Levitte *et al.*, 1974; Woldegabriel, 1991; Owusu Agyemang *et al.*, 2019); these units were deposited prior to the emplacement of Eo-Oligocene volcanic strata between 45 and 27 Ma (*e.g.*, Steiner *et al.*, 2022).

Following widespread Eo-Oligocene volcanism, the onset of tectonically related rapid crustal cooling is recorded by samples from the BRZ and reflects initial diffuse regional faulting soon after the termination of magmatism between 27 and 20 Ma (Chapter 3; Fig. 3.6). Time-temperature histories obtained from samples collected from different structural positions across the southern margin of the Mali-Dancha Basin exhibit an onset of rapid cooling at ~27 Ma. Furthermore, thermal modeling results obtained for samples located at the lower footwalls of the Mali-Dancha (C-5) and Bala-Kela (K-6) basin margins record an onset of rapid cooling at 26 and 21 Ma, respectively. A consistent early Miocene onset of exhumation along the Chew Bahir Basin margin and the Gofa Province between ~20 and 17 Ma has been reported by Pik *et al.* (2008) and Boone *et al.* (2019), respectively. Taken together, it can be concluded that initial deformation in the BRZ associated with Cenozoic rifting initiated at ~23 Ma, following the end of massive volcanism between 45 and 27 Ma.

6.2 Late-stage rifting and rift-segment interaction

The low-temperature thermochronologic data and geomorphic evidence from the Chew Bahir Basin and the Gofa Province show that the diffuse faulting that still characterized the region at ~23 Ma shifted subsequently toward a narrow zone of extension in the Mali-Dancha-Bala-Kela basins (Chapter 3; Fig. 3.6), prior to the current strain localization in the southern Gofa Province and the Chew Bahir Basin. For example, thermal-modeling results obtained from samples located at different structural positions across the Baneta margin exhibit an onset of rapid cooling at ~15 Ma; however, samples from structurally lower positions obtained across the Baneta halfgraben (Mali-Dancha margin) record a later onset of cooling at ~9 Ma, suggesting tectonic subsidence of the halfgraben and faulting toward a narrow zone of the Gofa Province. Geological cross-sections constructed across the trend of the rift via the Baneta, Mali-Dancha,

Weyito and Segen basins, and from the Beto to the Gelana basins via the Bala-Kela and Chamo basins, exhibit a characteristic change in topographic gradient in proximity to the basin-bounding normal faults. A similar character of deformation involving step-faulting toward the narrow zone of the sMER (Ebinger *et al.*, 2000; Bonini *et al.*, 2005; Corti, 2013; Boone *et al.*, 2019) and the cMER and nMER (Morton, 1974; Agostini *et al.*, 2011) has been observed, suggesting the migration of extensional deformation toward a narrow axial zone.

Faulting activity had farther propagated toward the north of the Gofa Province much later at ~6 Ma. A similar south (20–17 Ma) to north-oriented (8–6 Ma) variation in the onset of crustal cooling has been reported from the Beto Basin farther to the west (Balestrieri *et al.*, 2016; Boone *et al.*, 2019), reflecting significant temporal disparity in the onset of faulting between the southern and northern Gofa provinces. A prominent NW-SE-trending high seismic-wave speed zone defined by a sharp vertical boundary passing through the northern Chew Bahir Basin and the southern Gofa Province and probably related to high-density lithologies (Kounoudis *et al.*, 2021), and a northward increase in topography due to stratigraphic thickening of the Eo-Oligocene basalts (Davidson, 1983) may have introduced lithospheric strength contrasts between the southern and northern Gofa provinces. The presence of such a crustal strength contrast at a high-angle to the trend of the rift trend possibly stalls fault propagation (Molnar *et al.*, 2019) and my refract extensional structures, resulting in spatial disparity with respect to the onset of faulting between the southern and northern Gofa provinces during the middle to late Miocene.

The northward-propagating faulting may have been redirected toward the current active zone of deformation in the southern Gofa Province and the Chew Bahir Basin between the late Miocene and early Pliocene. Resumed, rapid early Pliocene crustal cooling is well documented by my thermal modeling results. For example, jointly modeled samples collected from different structural positions across the NW-SE-striking Mali-Dancha Basin flank exhibit renewed rapid crustal cooling starting at ~5 Ma. Farther south, a sample (C-2) collected from the western low-elevation footwall margin of the Chew Bahir Basin records the onset of rapid cooling at ~3 Ma.

Based on geochronologic and seismicity data, WoldeGabriel and Aronson (1987) and Ebinger *et al.* (2000) proposed that faulting in the northern Gofa Province has shifted toward the currently active southern Gofa Province and the Chew Bahir Basin during the late Miocene and early Pliocene; however, active normal faults, and young tectonic landforms along the narrow zone of the Mali-Dancha and Bala-Kela basins in the Gofa Province were identified during field work in the context of this study. A set of elevation-transect samples (C10-12 and C7-9) that were collected across the northeastern margin of the Chew Bahir Basin, record a weighted mean age ranging between 77 and 33 Ma and exhibit slow cooling (<1.2°C/Myr) that started during the Paleogene. However, a samples (C-6) collected in the lower footwall of the margin farther south close to a regionally mapped NW-SE-striking undifferentiated lineament (Davidson and Rex, 1980) record a weighted mean age of ~3 Ma, likely suggesting an active deformation along the NW-SE striking inherited lineaments

Geomorphic markers extracted from river catchments in the footwalls of the left-stepping en-échelon basins using high-resolution TanDEM-X data, and verified by field observation are consistent with the thermochronologic results that record active Quaternary tectonism in the southern Gofa Province and the Chew Bahir Basin. Normalized channel-steepness index determinations and the computation of local relief with a radius of 1 km exhibit relative peak values at fault-linked sectors of the rift, with a general increase toward the south (Chapter 4; Figs. 4.12a and 4.17). Additionally, knickzone heights, hypsometric integrals and basin-asymmetry factors show a gradual increase toward the south, reflecting strain localization at fault-linked zones of the southern Gofa Province and the Chew Bahir Basin. Interestingly, geodetic observations (*e.g.*, Knappe *et al.*, 2020) showing a high strain rate of ~4.5 mm/yr between the southern Gofa Province-Chew Bahir Basin and the Segen Basin (Chapter 3. Fig. 3.7), and clustered seismicity along the Omo Valley, the southern Gofa Province, and the Chew Bahir and Segen basins, support the interpretation of current tectonic activity in the southern Gofa Province, the Chaw Bahir, and Segen basins.

Taken together, the thermochronologic, geomorphic, and field observations support the view of ongoing tectonic interaction between the rift segments in the BRZ, which may have started during the early Pliocene at ~5 Ma, following a basinward shift of deformation toward the Mali-Dancha and Bala-Kela basins and the propagation of faulting toward the northern Gofa Province between ~15 and 6 Ma.

The late-stage rifting that began during the Miocene and has lasted until the present-day coincides with a renewed pulse in magmatic activity within the BRZ. Phonolitic eruptive centers aligned parallel to the Mali-Dancha and Bala-Kela basins, and along strike of the Gidole-Chencha Horst were active between 18 and 12 Ma (Davidson, 1980; Ebinger *et al.*, 2000; George *et al.*, 2002). New $^{40}Ar/^{39}Ar$ geochronology carried out in this study indicates that the Miocene volcanic eruptions may have initiated at ~20 Ma, synchronous with the emplacement of dike swarms that have been dated along the Gidole-Chencha and Amaro horsts (Levitte, 1974; Bonini *et al.*, 2005). Based on geochemical evidence, Rooney (2010) inferred a shallow depth for melt-fractionation paths for the Miocene basalts in the area of the Gidole-Chencha Horst. The author interpreted the shallow melting column to be related to a lithospheric thinning during rifting.

6.3 Counterclockwise vertical axis block rotation between overlapping rift segments

The paleomagnetic investigation of samples collected from 40 sites from the Eo-Oligocene and Miocene volcanics and sediments exhibits a counterclockwise vertical-axis block rotation relative to the pole for stable South Africa. This rotation is likely related to the propagating rift segments, generating edge-driven forces along the microplate boundaries (*e.g.*, Schouten *et al.*, 1993; Neves *et al.*, 2003; Glerum *et al.*, 2020). Importantly, based on my paleomagnetism analysis and tectono-geomorphic observations the crustal block motion appears to have been accompanied

by shearing along reactivated NW-SE striking basement heterogeneities, thus emphasizing the pivotal role of inherited basement heterogeneities for tectonic reactivation during changing stress-field conditions.

The VGPs obtained for the Eo-Oligocene (ϕ_s =243.5°, λ_s =73.5°, N=18, α_{95}=4.4°) and Miocene (ϕ_s =189.7°, λ_s =83.9°, N=9, α_{95}=9.7°) basalts and sediments were compared relative to the pole for stable South Africa within the corresponding age range between 35 and 45 Ma and 11 and 20 Ma, respectively. A counterclockwise rotation of R= 11.1°± 6.4° and R= 3.2° ± 11.5° was estimated for Eo-Oligocene and Miocene volcanics and sediments with no significant latitudinal displacement for both rock units (Chapter 5; Fig. 5.8). The smaller, and statistically insignificant amount of counterclockwise block rotation recorded by the Miocene rock units may indicates that at least part of the rotation documented by the data obtained from Eocene rocks, had occurred before the final emplacement of the Miocene lava flows or, alternatively, the rotation may have been continuous until recently. I briefly discus below the potential mechanisms for the vertical axis block rotation with respect to the structural setting and previously proposed models for rift evolution in the study area.

Overall, the counterclockwise block rotation is consistent with the proposed rift-evolution models of the region (*e.g.*, Philippon *et al.*, 2014; Brune *et al.*, 2017) as well as deformation patterns recognized in analog and numerical modeling studies (Brune *et al.*, 2017; Glaume *et al.*, 2020; Neuharth *et al.*, 2021). The observation and interpretation provided in my study is therefore in line what would be expected from the long-term tectonic evolution of this complex tectonic region. Although no additional data has been collected, by combining published geologic information and my own observations from the BRZ, the observed temporal variation in the extent of the block rotation can be explained by at least two end-member scenarios. The first scenario is that the counterclockwise block rotation initiated at ~22 Ma, synchronous with faulting and that it has continued to the present day, and the Eo-Oligocene volcanics are old enough to reflect the full extent of deformation associated with the block rotation. Alternatively, it could be concluded that much of the vertical-axis block rotation occurred during initial rifting, affecting the Eo-Oligocene volcanics, but the region has been subjected to a decrease in the extent of block rotation overtime.

Geochronologic, structural, and field data indicate that major faulting that caused the western margin of the Abaya and Chamo basins occurred between 18 and 14 Ma, and had migrated toward the south in the Segen Basin and the axial zone of the sMER by Pliocene time (Levitte, 1974; WoldeGabriel *et al.*, 1991; Ebinger *et al.*, 2000; Bonini *et al.*, 2005). A contemporaneous middle Miocene to early Pliocene shift in deformation toward the western margin of the Bala-Kela Basin was documented from thermal modeling results (Chapter 3; Fig. 3.2b). From the Pliocene to the present, faulting was mainly focused on the southern Gofa Province and the Chew Bahir Basin (WoldeGabriel *et al.*, 1991; Ebinger *et al.*, 2000; Philippon *et al.*, 2014; Erbello *et al.*, 2022). Such a spatial change in tectonic activity during rifting may result in a decrease in the edge-driven forces along the boundaries of the deforming structural blocks (*e.g.*, Neuharth *et al.*, 2021). Accordingly, a significant amount of counterclockwise block rotation must have

occurred during the early Miocene, before the final emplacement of the Miocene volcanics and the deposition of sediments, followed by a subsequent decrease in the extent of block rotation.

Chapter 7

Additional references

Armitage, J.J., Petersen, K.D., Pérez-Gussinyé, M. (2018), The Role of Crustal Strength in Controlling Magmatism and Melt Chemistry During Rifting and Breakup. Geochemistry, Geophysics, Geosystems. doi:10.1002/2017GC007326

Arnous, A., Zeckra, M., Venerdini, A., Alvarado, P., Arrowsmith, R., Guillemoteau, J., Landgraf, A., Gutiérrez, A., Strecker, M.R. (2021), Corrigendum to "Neotectonic Activity in the Low-Strain Broken Foreland (Santa Bárbara System) of the North-Western Argentinean Andes (26°S)." Lithosphere. doi:10.2113/2021/3729035

Ayalew, D., Gibson, S.A. (2009), Head-to-tail transition of the Afar mantle plume: Geochemical evidence from a Miocene bimodal basalt-rhyolite succession in the Ethiopian Large Igneous Province. Lithos. doi:10.1016/j.lithos.2009.04.005

Bastow, I.D., Pilidou, S., Kendall, J.M., Stuart, G.W. (2010), Melt-induced seismic anisotropy and magma assisted rifting in Ethiopia: Evidence from surface waves. Geochemistry, Geophysics, Geosystems. doi:10.1029/2010GC003036

Balestrieri, M.L., Bonini, M., Corti, G., Sani, F., and Philippon, M. (2016), A refinement of the chronology of rift-related faulting in the Broadly Rifted Zone, southern Ethiopia, through apatite fission-track analysis. Tectonophysics, 671, 42–55. doi:10.1016/j.tecto.2016.01.012

Beniest, A., Koptev, A., Burov, E. (2017), Numerical models for continental break-up: Implications for the South Atlantic. Earth and Planetary Science Letters. doi:10.1016/j.epsl.2016.12.034

Birt, C.S., Maguire, P.K.H., Khan, M.A., Thybo, H., Keller, G.R., Patel, J. (1997), The influence of pre-existing structures on the evolution of the southern Kenya Rift Valley - Evidence from seismic and gravity studies. Tectonophysics. doi:10.1016/S0040-1951(97)00105-4

Bonini, M., Corti, G., Innocenti, F., Manetti, P., Mazzarini, F., Abebe, T., and Pecskay, Z. (2005), Evolution of the Main Ethiopian Rift in the frame of Afar and Kenya rifts propagation. Tectonics, 24(1), 1-21. doi: 10.1029/2004TC001680

Boone, S.C., Balestrieri, M.L., Kohn, B.P., Corti, G., Gleadow, A.J.W., and Seiler, C. (2019), Tectonothermal evolution of the Broadly Rifted Zone, Ethiopian Rift. Tectonics, 38(3), 1070-1100. doi: 10.1029/2018TC005210

Bosworth, W., and Morley, C.K. (1994), Structural and stratigraphic evolution of the Anza rift, Kenya. Tectonophysics, 236(4), 93-115. doi:10.1016/0040-1951(94)90171-6

Bosworth, W., Stockli, D.F., Helgeson, D.E. (2015), Integrated outcrop, 3D seismic, and geochronologic interpretation of Red Sea dike-related deformation in the Western Desert, Egypt - The role of the 23Ma Cairo "mini-plume." Journal of African Earth Sciences 109, 107–119. doi:10.1016/j.jafrearsci.2015.05.005

Bott, M.H.P., Kusznir, N.J. (1984), The origin of tectonic stress in the lithosphere. Tectonophysics. doi:10.1016/0040-1951(84)90190-2

Brune, S. (2014), Evolution of stress and fault patterns in oblique rift systems: 3-D numerical lithospheric-scale experiments from rift to breakup. Geochemistry, Geophysics, Geosystems. doi:10.1002/2014GC005446

Buck, W.R. (2006), The role of magma in the development of the Afro-Arabian Rift System. Geological Society Special Publication. doi:10.1144/GSL.SP.2006.259.01.05

Buck, W.R. (1991), Modes of continental lithospheric extension. Journal of Geophysical Research: Solid Earth. doi:10.1029/91JB01485

Buiter, S.J.H., Torsvik, T.H. (2014), A review of Wilson Cycle plate margins: A role for mantle plumes in continental break-up along sutures? Gondwana Research. doi:10.1016/j.gr.2014.02.007

Butler, R.F. (1998), Paleomagnetism: Magnetic domains to geologic terranes. pp (1-237).

Burke, K. (1996), The African Plate. South African Journal of Geology. https://hdl.handle.net/10520/EJC-942801f20

Brune, S., Corti, G., and Ranalli, G. (2017), Controls of inherited lithospheric heterogeneity on rift linkage: Numerical and analog models of interaction between the Kenyan and Ethiopian rifts across the Turkana depression. Tectonics, 36, 1767–1786. doi: 10.1002/2017TC004739

Calais, E., D'Oreye, N., Albaric, J., Deschamps, A., Delvaux, D., Déverchère, J., Ebinger, C., Ferdinand, R.W., Kervyn, F., Macheyeki, A.S., Oyen, A., Perrot, J., Saria, E., Smets, B., Stamps, D.S., Wauthier, C. (2008), Strain accommodation by slow slip and dyking in a youthful continental rift, East Africa. Nature. doi:10.1038/nature07478

Craig, T.J., and Jacjson, J.A. (2021), Variations in the seismogenic thickness of the east Africa. Journal of geophysical Research: Solid Earth. doi:10.1029/2020JB020754

Civiero, C., Hammond, J.O.S., Goes, S., Fishwick, S., Ahmed, A., Ayele, A., Doubre, C., Goitom, B., Keir, D., Kendall, J.M., Leroy, S., Ogubazghi, G., Rümpker, G., Stuart, G.W. (2015), Multiple mantle upwellings in the transition zone beneath the northern East-African Rift system from relative P-wave travel-time tomography. Geochemistry, Geophysics, Geosystems. doi:10.1002/2015GC005948

Clark, D., Leonard, M. (2003), Principal stress orientations from multiple focal-plane solutions: New insight into the Australian intraplate stress field, in: Special Paper of the Geological Society of America. doi:10.1130/0-8137-2372-8.91

Chorowicz, J. (2005), The East African rift system. Journal of African Earth Sciences, 43(3), 379-410. doi:10.1016/j.jafrearsci.2005.07.019

Corti, G. (2009), Continental rift evolution: From rift initiation to incipient break-up in the Main Ethiopian Rift, East Africa. Earth-Science Reviews. doi:10.1016/j.earscirev.2009.06.005

Corti, G., Bonini, M., Conticelli, S., Innocenti, F., Manetti, P., Sokoutis, D. (2003), Analogue modelling of continental extension: A review focused on the relations between the patterns of deformation and the presence of magma. Earth-Science Reviews. doi:10.1016/S0012-8252(03)00035-7

Courtillot, V. (1982). Propagating rifts and continental breakup. Tectonics. doi:10.1029/TC001i003p00239

Davidson, A. (1983), The Omo River Project, reconnaissance geology and geochemistry of parts of Ilubabor, Kefa, Gamu Gofa, and Sidamo. Ministry of Mines and Energy, Ethiopian Institute Geological Survey Bulletin, 2, 1-89

Davidson, A., and Rex, D.C. (1980), Age of volcanism and rifting in southwestern Ethiopia. Nature, 283, 657-658. doi: 10.1038/283657a0

deMenocal, P.B. (2004), African climate change and faunal evolution during the Pliocene-Pleistocene. Earth and Planetary Science Letters. doi:10.1016/S0012-821X(04)00003-2

Dewey, J.F. (1988), Extensional collapse of orogens. Tectonics. doi:10.1029/TC007i006p01123

Dèzes, P., Schmid, S.M., Ziegler, P.A. (2005), Reply to comments by L. Michon and O. Merle on "Evolution of the European Cenozoic Rift System: Interaction of the Alpine and Pyrenean orogens with their foreland lithosphere" by P. Dèzes, S.M. Schmid and P.A. Ziegler, Tectonophysics 389 (2004) 1-33. doi:10.1016/j.tecto.2005.02.002

Dommain, R., Riedl, S., Olaka, L.A., deMenocal, P., Deino, A.L., Owen, R.B., Muiruri, V., Müller, J., Potts, R., Strecker, M.R. (2022), Holocene bidirectional river system along the Kenya Rift and its influence on East African faunal exchange and diversity gradients. Proceedings of the National Academy of Sciences of the United States of America. doi10.1073/pnas.2121388119

Dugda, M.T., Nyblade, A.A., Julia, J., Langston, C.A., Ammon, C.J., Simiyu, S. (2005), Crustal structure in Ethiopia and Kenya from receiver function analysis: Implications for rift development in eastern Africa. Journal of Geophysical Research: Solid Earth. doi:10.1029/2004JB003065

Ebinger, C.J., Yemane, T., WoldeGabriel, G., Aronson, J.L., and Walter, R.C. (1993), Late Ecocene-Recent volcanism and faulting in the southern main Ethiopian rift. Journal of the Geological Society, 150(1), 99–108. doi: 10.1144/gsjgs.150.1.0099

Ebinger, C., Scholz, C.A. (2012), Continental Rift Basins: The East African Perspective, in: Tectonics of Sedimentary Basins: Recent Advances. doi:10.1002/9781444347166.ch9

Ebinger, C.J., Yemane, T., Harding, D.J., Tesfaye, S., Kelley, S., and Rex, D.C. (2000), Rift deflection, migration, and propagation: Linkage of the Ethiopian and Eastern rifts, Africa. Geological Society of America Bulletin, 112(2), 163–176. doi: 10.1130/0016-7606(2000)112<163:RDMAPL>2.0.CO;2

Ebinger, C.J., Sleep, N.H. (1998), Cenozoic magmatism throughout east Africa resulting from impact of a single plume. Nature. doi10.1038/27417

Emishaw, L., and Abdelsalam, M.G. (2019), Development of Late Jurassic-Early Paleogene and Neogene-Quaternary rifts within the Turkana Depression, East Africa. Tectonics, 38, 2358–2377. doi: 10.1029/2018TC005389

Estefanny Dávalos-Elizondo and Daniel A. Laó-Dávila. (2023), Structural analysis of fracture networks controlling geothermal activity in the northern part of the Malawi Rifted Zone from aeromagnetic and remote sensing data. Journal of Volcanology and Geothermal Research, 433. doi:10.1016/j.jvolgeores.2022.107713

Fairhead, J.D., Girdler, R.W. (1969), How far does the rift system extend through Africa? Nature. doi:10.1038/2211018a0 George, R. (1998), Earliest magmatism in Ethiopia: Evidence for two mantle plumes in one flood basalt province. Geology, 26(10), 923-926. doi: 10.1130/0091-7613(1998)026<0923:EMIEEF>2.3.CO;2

Göğüş, O.H., Psyklywec, R.N. (2008), Mantle lithosphere delamination driving plateau uplift and synconvergent extension in eastern Anatolia. Geology. doi10.1130/G24982A.1

Green, W.V., Achauer, U., Meyer, R.P. (1991), A three-dimensional seismic image of the crust and upper mantle beneath the Kenya rift. Nature. doi10.1038/354199a0

Gupta, S., Cowie, P.A., Dawers, N.H., Underhill, J.R. (1998), A mechanism to explain rift-basin subsidence and stratigraphic patterns through fault-array evolution. Geology. doi:10.1130/0091-7613(1998)026<0595:AMTERB>2.3.CO;2

Hassan, R., Williams, S.E., Gurnis, M., Müller, D. (2020), East African topography and volcanism explained by a single, migrating plume. Geoscience Frontiers. doi:10.1016/j.gsf.2020.01.003

Jadamec, M.A., Turcotte, D.L., Howell, P. (2007), Analytical models for orogenic collapse. Tectonophysics. doi: 10.1016/j.tecto.2007.01.007.

Ibs-von Seht, M., Blumenstein, S., Wagner, R., Hollnack, D., Wohlenberg, J. (2001), Seismicity, seismotectonics and crustal structure of the Southern Kenya Rift-new data from the Lake Magadi area. Geophysical Journal International. doi:10.1046/j.0956-540X.2001.01464.x

Kapp, P., Taylor, M., Stockli, D., Ding, L. (2008), Development of active low-angle normal fault systems during orogenic collapse: Insight from Tibet. Geology. doi:10.1130/G24054A.1

Keir, D., Ebinger, C.J., Stuart, G.W., Daly, E., Ayele, A. (2006), Strain accommodation by magmatism and faulting as rifting proceeds to breakup: Seismicity of the northern Ethiopian rift. Journal of Geophysical Research: Solid Earth. doi:10.1029/2005JB003748

Kendall, J.M., and Bertelloni, C.L. (2016), Why is Africa rifting? Geological Society London, Special Publications, 420(1), 11-30. doi: 10.1144/SP420.17

Kirby, S.H. (1980), Tectonic stresses in the lithosphere: constraints provided by the experimental deformation of rocks. Journal of Geophysical Research. doi:10.1029/JB085iB11p06353

Koptev, A., Calais, E., Burov, E., Leroy, S., Gerya, T. (2015), Dual continental rift systems generated by plume-lithosphere interaction. Nature Geoscience. doi:10.1038/ngeo2401

Landgraf, A., KüBler, S., Hintersberger, E., Stein, S. (2017), Active tectonics, earthquakes and palaeoseismicity in slowly deforming continents. Geological Society Special Publication. doi:10.1144/SP432.13

Levitte, D., Columba, J., and Mohr, P. (1974), Reconnaissance geology of the Amaro horst, southern Ethiopia Rift. Geological Society of America Bulletin, 85, 417-422

Latin, D., White, N. (1993), Magmatism in extensional sedimentary basins. Annali di Geofisica. Mamo, T. (2012), Analysis of gravity field to reconstruct the structure of Omo basin in SW Ethiopia and implications for hydrocarbon potential. Marin and Petroleum Geology, 29, 104-114. doi: 10.1016/j.marpetgeo.2011.08.013

KRISP working group. (1987), Structure of the Kenya rift from seismic refraction. Nature, 325, 1–23.

McCune, A.R., Thomson, K.S., Olsen, P.E. (1984), Semionotid fishes from the Mesozoic great lakes of North America. Evolution of Species Flocks 27–44.

McKenzie, D. (1978), Some remarks on the development of sedimentary basins. Earth and Planetary Science Letters. doi:10.1016/0012-821X(78)90071-7

Milanovsky, E.E. (1983), Major stages of rifting evolution in the earth's history. Tectonophysics. doi:10.1016/0040-1951(83)90036-7

Mora, A., Gaona, T., Kley, J., Montoya, D., Parra, M., Quiroz, L.I., Reyes, G., Strecker, M.R. (2009), The role of inherited extensional fault segmentation and linkage in contractional orogenesis: A reconstruction of lower cretaceous inverted rift basins in the Eastern Cordillera of Colombia. Basin Research. doi:10.1111/j.1365-2117.2008.00367.x

Morley, C.K. (1995), Developments in the structural geology of rifts over the last decade and their impact on hydrocarbon exploration. Geological Society Special Publication. doi:10.1144/GSL.SP.1995.080.01.01

Morley, C.K., Nelson, R.A., Patton, T.L., Munn, S.G. (1990), Transfer zones in the East African rift system and their relevance to hydrocarbon exploration in rifts. American Association of Petroleum Geologists Bulletin. doi:10.1306/0c9b2475-1710-11d7-8645000102c1865d

Morley, C.K., Wescott, W.A., Stone, D.M., Harper, R.M., Wigger, S.T., and Karanja, F.M. (1992), Tectonic evolution of the northern Kenyan Rift. Journal of the Geological Society, 149(3), 333-348. doi: 10.1144/gsjgs.149.3.0333

Moucha, R., Forte, A.M. (2011), Changes in African topography driven by mantle convection. Nature Geoscience. doi:10.1038/ngeo1235

Muirhead, J.D., Kattenhorn, S.A., Le Corvec, N. (2015), Varying styles of magmatic strain accommodation across the East African Rift. Geochemistry, Geophysics, Geosystems. doi:10.1002/2015GC005918

Muluneh, A.A., Brune, S., Illsley-Kemp, F., Corti, G., Keir, D., Glerum, A., Kidane, T., Mori, J. (2020). Mechanism for Deep Crustal Seismicity: Insight From Modeling of Deformation Processes at the Main Ethiopian Rift. Geochemistry, Geophysics, Geosystems. doi:10.1029/2020GC008935

Nelson, R.A., Patton, T.L., Morley, C.K. (1992), Rift-segment interaction and its relation to hydrocarbon exploration in continental rift systems. American Association of Petroleum Geologists Bulletin. doi:10.1306/bdff898e-1718-11d7-8645000102c1865d

Njinju, E.A., Atekwana, Estella A., Stamps, D.S., Abdelsalam, M.G., Atekwana, Eliot A., Mickus, K.L., Fishwick, S., Kolawole, F., Rajaonarison, T.A., Nyalugwe, V.N. (2019), Lithospheric Structure of the Malawi Rift: Implications for Magma-Poor Rifting Processes. Tectonics. doi:10.1029/2019TC005549

Nyblade, A.A., Sleep, N.H. (2003), Long lasting epeirogenic uplift from mantle plumes and the origin of the Southern African Plateau. Geochemistry, Geophysics, Geosystems. doi:/10.1029/2003GC000573

Oliva, S.J., Ebinger, C.J., Wauthier, C., Muirhead, J.D., Roecker, S.W., Rivalta, E., Heimann, S. (2019), Insights Into Fault-Magma Interactions in an Early-Stage Continental Rift From Source Mechanisms and Correlated Volcano-Tectonic Earthquakes. Geophysical Research Letters. doi:10.1029/2018GL080866

Olsen, K.H. (1995), Continental rifts: evolution, structure, tectonics. Continental rifts: evolution, structure, tectonics. doi:10.1016/s0040-1951(97)88191-7

Parra, M., Mora, A., Jaramillo, C., Torres, V., Zeilinger, G., Strecker, M.R. (2010), Tectonic controls on Cenozoic foreland basin development in the north-eastern Andes, Colombia. Basin Research. doi:10.1111/j.1365-2117.2009.00459.x

Parsons, T., Sleep, N.H., Thompson, G.A. (1992), and thickness I1 ,! 11, 1348–1356.

Petit, C., Déverchère, J. (2006), Structure and evolution of the Baikal rift: A synthesis. Geochemistry, Geophysics, Geosystems. doi:10.1029/2006GC001265

Pik, R., Marty, B., Carignan, J., Yirgu, G., and Ayalew, T. (2008), Timing of East African Rift development in southern Ethiopia: Implication for mantle plume activity and evolution of topography. Geology, 36, 167–170. doi: 10.1130/G24233A.1

Pik, R., Marty, B., Hilton, D.R. (2006), How many mantle plumes in Africa? The geochemical point of view. Chemical Geology. doi:10.1016/j.chemgeo.2005.09.016

Porth, R. (2000), A strain-rate-dependent force model of lithospheric strength. Geophysical Journal International. doi:10.1046/j.1365-246X.2000.00115.x

Prömmel, K., Cubasch, U., Kaspar, F. (2013), A regional climate model study of the impact of tectonic and orbital forcing on African precipitation and vegetation. Palaeogeography, Palaeoclimatology, Palaeoecology. doi:10.1016/j.palaeo.2012.10.015

Reilinger, R., McClusky, S. (2011), Nubia-Arabia-Eurasia plate motions and the dynamics of Mediterranean and Middle East tectonics. Geophysical Journal International. doi:10.1111/j.1365-246X.2011.05133.x

Reiners, P.W., and Ehlers, T.A. (2005), Low-temperature thermochronology: Techniques, interpretations and applications. Reviews in Mineralogy and Geochemistry. v. 58

Riedl, S., Melnick, D., Mibei, G.K., Njue, L., Strecker, M.R. (2019), Continental rifting at magmatic centres: Structural implications from the Late Quaternary Menengai Caldera, Central Kenya Rift. Journal of the Geological Society. doi:10.1144/jgs2019-021

Roecker, S., Ebinger, C., Tiberi, C., Mulibo, G., Ferdinand-Wambura, R., Mtelela, K., Kianji, G., Muzuka, A., Gautier, S., Albaric, J., Peyrat, S. (2017), Subsurface images of the Eastern Rift, Africa, from the joint inversion of body waves, surface waves and gravity: Investigating the role of fluids in early-stage continental rifting. Geophysical Journal International. doi:10.1093/gji/ggx220

Rooney, T.O. (2010), Geochemical evidence of lithospheric thinning in the southern Main Ethiopian Rift. Lithos. doi:10.1016/j.lithos.2010.02.002

Rooney, T.O. (2017), The Cenozoic magmatism of East-Africa: Part I. Flood basalts and pulsed magmatism. Lithos, 286-287, 264-301. doi: 10.1016/j.lithos.2017.05.014

Sengör, A.M.C., Burke, K. (1978), Relative timing of rifting and volcanism on Earth and its tectonic implications. Geophysical Research Letters. doi:10.1029/GL005i006p00419

Shackleton, R.M. (1993), Tectonics of the Mozambique Belt in East Africa. Geological Society Special Publication. doi:10.1144/GSL.SP.1993.076.01.17 Shackleton, R.M. (1976), A Discussion on global tectonics in Proterozoic times-Pan-African Structures. Philosophical Transactions of the Royal Society of London. Series A, Mathematical and Physical Sciences, 280(1298), 491–497. doi:10.1098/rsta.1976.0008

Shackleton, R.M. (1976), A Discussion on global tectonics in Proterozoic times-Pan-African Structures. Philosophical Transactions of the Royal Society of London. Series A, Mathematical and Physical Sciences, 280(1298), 491–497. https://doi.org/10.1098/rsta.1976.0008

Stamps, D.S., Flesch, L.M., Calais, E., Ghosh, A. (2014), Current kinematics and dynamics of Africa and the East African Rift System. Journal of Geophysical Research: Solid Earth. doi:10.1002/2013JB010717

Steiner, R.A., Rooney, T.O., Girard, G., Rogers, N., Ebinger, C.J., Peterson, L., and Phillips, R.K. (2022), Initial Cenozoic magmatic activity in East Africa: new geochemical constraints on magma distribution within the Eocene continental flood basalt province, in: Geological Society London, Special Publications, 26. doi: 10.1144/SP518-2020-262

Tiercelin, J.J. (1991), Natural resources in the lacustrine facies of the Cenozoic rift basins of East Africa. Lacustrine facies analysis. doi:10.1002/9781444303919.ch1

Tiercelin, J.J., and Lezzar,K.E. (2002), A 300 Million Years History of Rift Lakes in Central and East Africa: An Updated Broad Review In The East African great lakes: limnology, paleolimnology and biodiversity (pp. 3–60). Sptinger, Dordrecht. doi:10.1007/0–306–48201–0_1

William Hutchison, W., Ogilvie, Euan R. D., Birhane, Y.G., Barry, P.H., Fischer, T.P., Chris J. Ballentine, C. J., Hillegonds, D.J., Biggs, J., Albino, , F., Cervantes, C., and Guðbrandsson, S. (2023), Gas Emissions and Subsurface Architecture of Fault-Controlled Geothermal Systems: A Case Study of the North Abaya Geothermal Area. Geochemistry, Geophysics, Geosystems. doi: 10.1029/2022GC010822

Withjack, M.O., Scheiner, C., (1982), Fault patterns associated with domes-An experimental and analytical study. American Association of Petroleum Geologists Bulletin. doi:10.1306/03b59afd-16d1-11d7-8645000102c1865d

WoldeGabriel, G., Aronson, J.L., and Walter, R.C. (1990), Geology, geochronology, and rift basin development in the central sector of the Main Ethiopia Rift. Geological Society of America, Bulletin, 102(4), 439-458. doi: 10.1130/0016-7606(1990)102<0439:GGARBD>2.3.CO;2

Wright, T.J., Ebinger, C., Biggs, J., Ayele, A., Yirgu, G., Keir, D., Stork, A., (2006), Magma-maintained rift segmentation at continental rupture in the 2005 Afar dyking episode. Nature. doi:10.1038/nature04978

Zappettini, E.O., Rubinstein, N., Crosta, S., Segal, S.J. (2017), Intracontinental rift-related deposits: A review of key models. Ore Geology Reviews. doi:10.1016/j.oregeorev.2017.06.019

Zielke, O., and Strecker,M.R. (2009), Recurrence of Large Earthquakes in Magmatic Continental Rifts: Insights from a Paleoseismic Study along the Laikipia–Marmanet Fault, Subukia Valley, Kenya Rift. Bulletin of the Seismological Society of America. doi:10.1785/0120080015

Zoback, M.D. (2010), Earthquakes: Climate and intraplate shocks. Nature. doi:10.1038/466568a

Appendix A

Magma-assisted continental rifting: The Broadly Rifted Zone in SW Ethiopia, East Africa

Table A.1: AHe single grain age

Table 1: Apatite (U-Th)/He data summary

Sample code	Lat./Long. (°)	Elev. (m)	lab #	U (ppm)	Th (ppm)	^{147}Sm (ppm)	He (nmole/g)	eU (ppm)[a]	ESR (μm)[b]	Ft[c]	Uncc. age(Ma)[d]	2σ error(Ma)	Corr age(Ma)[e]	2σ error(Ma)	Termination[f]
			202998	1.59	2.5	17.5	0.03	2.2	100.9	0.9	2.5	0.3	2.9	0.3	2
			202999	1.21	5.2	16.3	0.03	2.4	86.47	0.8	1.9	0.3	2.3	0.3	2
C2	4.49/36.73	579	203000	5.11	19.4	22.7	0.20	9.7	78.47	0.8	3.7	0.3	4.6	0.2	2
			203001	2.96	6.5	17.6	0.04	4.5	89.98	0.8	1.7	0.2	2.1	0.2	2
			203002	1.26	5.1	21.9	0.46	2.5	95.14	0.8	32.3	2.2	38.3	1.2	2
Weighted mean ± 95% CI:													**3.1 ± 1.2**		
C3	36.85/5.08	546	203437	1.62	0.9	52.9	0.35	1.8	73.76	0.8	28.5	2.5	35.8	1.7	2
			203419	8.07	0.5	35.2	0.20	8.2	55.26	0.7	4.3	0.9	5.9	0.7	2
			203420	1.01	8.8	54.2	0.05	3.1	77.62	0.8	2.5	0.5	3.1	0.5	2
C4	5.27/36.91	631	203421	8.13	2.5	37.1	0.22	8.7	67.33	0.8	4.6	0.4	5.9	0.3	2
			203422	0.72	0.6	13.0	0.04	0.9	72.86	0.8	7.6	2.5	9.6	2.5	2
			203423	2.86	0.3	11.4	0.08	2.9	70.63	0.8	4.9	1.0	6.2	0.9	2
Weighted mean ± 95% CI:													**5.8 ± 0.3**		
			203084	1.35	2.1	15.6	0.14	1.8	79.52	0.8	13.0	1.1	16.0	0.7	2
			203085	3.35	3.2	23.1	0.18	4.1	85.07	0.8	7.7	0.6	9.3	0.2	2
C5	5.32/36.93	540	203086	1.07	4.2	18.8	0.18	2.0	70.69	0.8	15.2	1.8	19.3	1.4	2
			203087	2.20	2.0	24.7	0.20	2.7	67.16	0.8	12.8	1.4	16.5	0.9	2
			203088	0.84	1.3	8.5	0.13	1.1	45.31	0.7	19.6	6.4	29.3	5.4	2
Weighted mean ± 95% CI:													**10.3 ± 2.7**		
			203456	1.99	6.7	24.6	0.05	3.6	86.03	0.8	2.6	0.5	3.1	0.4	2
			203457	2.49	26.2	24.3	0.17	8.7	114.6	0.9	3.5	0.1	4.1	0.1	2
C6	5.13/37.13	590	203458	3.52	12.9	17.2	0.03	6.6	126.9	0.9	0.9	0.1	1.0	0.1	2
			203459	3.82	10.3	24.8	0.24	6.2	119.5	0.9	6.9	0.3	7.9	0.2	2
			203460	4.31	6.4	15.7	0.13	5.8	118.8	0.9	4.1	0.2	4.7	0.2	0
Weighted mean ± 95% CI:													**3.1 ± 2.2**		
			203431	1.35	2.6	4.0	0.31	2.0	98.94	0.8	28.7	1.4	33.8	1.1	2
			203432	0.36	1.2	2.1	0.12	0.6	94.81	0.8	33.6	3.5	39.9	2.2	2
			203433	0.16	0.5	1.6	0.04	0.3	60.58	0.8	22.4	15.2	29.8	14.8	2
			203434	0.59	1.1	0.5	0.09	0.9	72.27	0.8	19.0	2.8	24.0	2.5	0
C7	5.27/37.18	945	203435	1.44	1.6	3.1	0.25	1.8	58.62	0.7	24.7	4.2	33.2	2.3	0
			213994	0.33	1.2	2.3	0.17	0.6	92.52	0.8	49.1	2.6	58.5	2.0	2
			213995	0.27	0.4	1.5	0.04	0.4	110.7	0.9	21.3	1.6	24.6	1.2	2
			213996	0.05	0.3	1.6	0.05	0.1	111.3	0.9	72.5	5.9	83.8	3.9	2
			213997	0.24	0.9	1.6	0.08	0.5	110.9	0.9	31.7	2.0	36.7	1.2	2
Weighted mean ± 95% CI:													**31.9 ± 4.3**		
			203477	5.75	13.4	3.0	2.34	8.9	127.7	0.9	48.2	3.2	54.6	1.2	2
			203478	1.53	3.2	1.6	0.31	2.3	71.3	0.8	25.1	1.6	31.7	1.3	1
			203479	1.47	1.9	5.5	0.37	1.9	75.89	0.8	34.7	3.6	43.2	2.2	0
			203480	1.35	1.1	3.7	0.49	1.6	83.96	0.8	55.3	3.3	67.2	1.8	0
C8	5.27/37.19	1148	203481	2.50	4.7	1.9	0.89	3.6	74.12	0.8	45.6	2.1	57.1	1.6	2
			214002	8.84	11.4	0.6	2.40	11.5	68.81	0.8	38.4	2.6	49.1	0.9	2
			214003	0.94	0.2	4.6	0.15	1.0	92.2	0.8	27.1	1.5	32.4	1.0	2
			214004	2.42	4.3	2.5	0.56	3.4	73.32	0.8	30.2	1.9	38.0	1.1	2
			214005	4.30	5.9	5.8	0.40	5.7	80.11	0.8	13.0	0.7	16.0	0.3	1
Weighted mean ± 95% CI:													**32.8 ± 12.6**		
			203451	4.81	5.9	5.5	2.33	6.2	69.2	0.8	68.8	4.0	87.8	2.3	2
			203452	6.88	8.0	7.8	3.58	8.8	68.51	0.8	74.8	6.8	95.6	2.1	2
			203453	7.38	7.4	8.7	3.18	9.1	71.84	0.8	63.8	4.6	80.6	1.3	2
			203454	17.02	24.8	12.0	9.35	22.9	77.38	0.8	75.0	5.4	92.9	1.5	2
C9	5.28/37.23	1326	203455	14.24	20.4	14.9	9.95	19.0	79.33	0.8	95.5	3.4	117.5	1.5	2
			213952	3.12	3.6	4.4	1.25	4.0	112.4	0.9	57.4	2.2	66.2	1.6	2
			213953	3.46	4.3	4.9	2.18	4.5	126.7	0.9	88.8	2.9	100.7	1.3	2
			213954	3.14	3.4	5.5	1.24	3.9	102.9	0.9	57.6	2.0	67.3	1.4	2
			213955	4.00	5.6	6.5	1.48	5.3	102.5	0.9	50.7	3.8	59.4	1.2	2
			213956	5.73	5.3	6.8	1.67	7.0	108.3	0.9	43.9	3.6	51.0	0.9	1
Weighted mean ± 95% CI:													**77.3 ± 13.3**		

Table A.2: AHe single grain age

			203414	8.55	28.2	26.7	2.07	15.2	46.88	0.7	24.8	1.3	36.4	0.9	2
			203415	9.73	19.9	18.1	2.59	14.4	43.09	0.7	32.8	2.0	50.3	1.4	2
C10	5.34/37.22	1211	203416	6.88	16.5	15.0	2.05	10.7	54.21	0.7	34.8	3.9	48.1	1.9	1
			203417	10.61	22.4	25.7	2.78	15.9	63.57	0.8	31.9	2.7	41.7	1.1	2
			203418	7.41	21.9	21.1	1.82	12.6	53.47	0.7	26.3	1.4	36.6	0.9	2
Weighted mean ± 95% CI:													**39.8 ± 4.5**		
C12	5.33/37.24	1486	203476	11.56	1.6	4.4	4.63	11.9	85.98	0.8	71.5	1.2	86.3	0.9	2
			213968	5.17	9.6	17.6	1.18	7.4	84.27	0.8	29.0	1.5	35.2	0.8	2
			213969	7.82	11.0	23.9	1.20	10.4	80.56	0.8	20.9	1.5	25.7	0.6	1
			213970	5.35	7.9	18.4	0.34	7.2	61.22	0.8	8.5	0.7	11.3	0.6	2
			213971	7.63	14.2	21.9	0.80	11.0	56.04	0.7	13.3	1.2	18.2	0.7	2
M1	5.48/36.82	690	203089	9.41	18.4	30.5	1.16	13.7	95.41	0.8	15.2	0.8	18.2	0.4	1
			203090	14.10	14.2	24.2	0.66	17.4	42.19	0.6	6.9	0.8	10.7	0.7	1
			203091	4.26	6.9	17.8	0.42	5.9	49.52	0.7	12.9	2.0	18.5	1.3	2
			203092	1.85	5.3	23.0	0.08	3.1	52.24	0.7	4.6	1.1	6.4	1.0	2
			203093	8.47	6.3	26.8	1.03	10.0	38.42	0.6	18.7	2.0	30.7	1.3	0
Weighted mean ± 95% CI:													**18.7 ± 5.0**		
			203069	15.86	7.2	32.4	2.24	17.6	60.53	0.8	23.3	1.0	30.9	0.6	2
			203070	13.44	2.8	35.2	1.87	14.1	78.92	0.8	24.1	1.7	29.7	0.6	2
M2	5.47/36.78	881	203071	9.04	3.6	27.6	0.76	9.9	62.55	0.8	14.0	1.6	18.4	0.7	1
			203072	5.27	2.3	15.1	0.53	5.8	57.44	0.7	16.6	1.8	22.5	1.2	2
			203073	0.09	0.6	0.0	0.01	0.2	45.47	0.7	5.8	18.2	8.6	18.1	1
Weighted mean ± 95% CI:													**26.1 ± 6.2**		
			203050	15.05	21.1	3.2	2.82	20.0	71.94	0.8	26.0	1.6	32.8	0.5	1
M3	5.47/36.75	1088	203051	7.01	10.0	1.8	1.53	9.4	97.89	0.8	30.1	0.7	35.5	0.4	2
			203052	6.24	9.7	1.5	0.89	8.5	92.54	0.8	19.4	1.5	23.1	0.5	2
			203054	11.55	18.6	2.6	2.80	15.9	87.53	0.8	32.4	0.7	39.0	0.4	2
Weighted mean ± 95% CI:													**32.7 ± 6.9**		
			203064	3.10	3.0	11.6	0.32	3.8	48.33	0.7	15.2	1.8	22.1	1.5	0
			203065	2.23	5.2	13.2	0.17	3.5	52.1	0.7	9.0	2.0	12.6	1.8	2
M4	5.49/36.75	1286	203066	4.16	9.7	12.7	0.60	6.4	55.27	0.7	16.9	1.0	23.2	0.8	2
			203067	4.12	5.8	16.2	0.22	5.5	76.12	0.8	7.2	0.6	9.0	0.4	2
			203068	2.09	1.6	9.7	0.24	2.5	57.88	0.7	17.7	1.7	23.9	1.5	2
Weighted mean ± 95% CI													**22.9 ± 0.6**		
			203008	0.36	0.9	11.2	0.05	0.6	65.52	0.8	15.0	2.6	19.4	2.5	2
			203009	1.14	7.6	26.3	0.29	2.9	62.86	0.8	17.2	2.2	22.5	1.4	2
M5	5.50/36.73	1484	203010	0.35	0.4	0.4	0.01	0.4	64.62	0.8	5.5	2.7	7.1	2.7	2
			203011	0.60	0.6	1.6	0.08	0.7	66.89	0.8	20.3	3.3	26.2	2.4	2
			203012	0.74	3.4	15.1	0.19	1.5	61.28	0.8	20.9	3.8	27.7	2.4	2
Weighted mean ± 95% CI													**22.4 ±2.6**		
			203013	3.96	4.6	34.1	0.50	5.0	53.38	0.7	17.2	1.2	24.2	0.9	2
			203015	4.32	1.0	72.6	0.37	4.6	56.45	0.7	13.5	1.0	18.3	0.8	2
M6	5.60/36.84	717	203017	4.32	1.3	68.0	0.27	4.6	50.7	0.7	9.6	1.8	13.7	1.1	2
			213988	3.30	1.5	47.9	0.19	3.7	83.38	0.8	8.8	0.6	10.7	0.4	2
			213989	3.00	1.3	47.2	0.07	3.3	55.22	0.7	3.6	0.9	4.9	0.7	2
			213990	3.52	1.3	65.2	0.18	3.8	62.53	0.8	7.6	1.6	10.1	1.0	2
Weighted mean ± 95% CI:													**11.8 ±4.6**		
			202993	1.19	0.9	23.2	0.02	1.4	73.1	0.8	2.3	0.5	2.9	0.5	2
			202994	1.06	0.6	68.9	0.03	1.2	69.8	0.8	3.1	0.9	4.0	0.8	2
M7	5.63/36.86	714	202995	0.90	1.0	64.0	0.14	1.1	85.7	0.8	15.1	1.0	18.3	0.8	2
			202996	1.05	0.7	72.6	0.18	1.2	78.3	0.8	18.4	2.1	22.7	0.6	2
			202997	1.04	0.6	57.9	0.04	1.2	66.0	0.8	4.8	0.9	6.2	0.8	2
Weighted mean ± 95% CI:													**9.5 ±7.4**		
			203018	5.20	7.3	90.5	0.17	6.9	82.3	0.8	4.2	0.3	5.1	0.2	2
			203019	7.26	14.4	175.1	0.24	10.6	42.1	0.6	3.7	0.7	5.8	0.7	0
M8	5.63/36.85	898	203020	2.29	9.0	113.1	0.14	4.4	47.4	0.7	5.0	1.2	7.3	1.1	2
			203021	4.17	12.5	102.0	0.27	7.1	54.3	0.7	6.2	0.8	8.6	0.7	2
			203022	3.43	12.8	102.9	0.32	6.4	57.2	0.7	8.2	0.5	11.1	0.5	2
Weighted mean ± 95% CI:													**4.9 ± 0.5**		
			203079	1.74	3.0	44.0	0.13	2.4	81.79	0.8	8.6	0.7	10.5	0.4	2
			203080	3.44	8.1	39.2	0.32	5.4	96.07	0.8	10.5	0.5	12.5	0.4	2
M9	5.68/36.93	960	203081	4.59	8.3	37.9	0.95	6.5	71.37	0.8	25.5	1.4	32.3	0.7	2
			203082	2.39	3.9	10.3	0.53	3.3	75.81	0.8	29.1	2.7	36.2	1.1	2

Table A.3: AHe single grain age

			203083	5.20	8.2	27.3	0.52	7.1	81.53	0.8	13.0	0.6	15.9	0.4	2
Weighted mean ± 95% CI:													**15.5 ± 7.4**		
B1	5.66/36.69	1442	213973	0.55	0.8	51.3	0.10	0.7	55.48	0.7	15.1	4.2	20.7	2.58	2
			203003	1.75	0.8	8.1	0.23	1.9	68.89	0.8	21.0	1.8	26.8	1.1	2
			203004	1.47	1.4	17.6	0.17	1.8	69.96	0.8	16.6	1.5	21.1	1.2	2
			203005	1.79	1.1	6.0	0.05	2.0	66.47	0.8	4.5	0.9	5.9	0.7	2
			203006	0.40	1.0	0.1	0.01	0.6	39.82	0.6	2.6	10.1	4.1	10.1	2
B2	5.75/36.76	1390	213962	9.20	4.3	1.3	0.80	10.2	134.7	0.9	14.5	1.1	16.4	0.2	2
			213963	1.62	1.3	10.5	0.07	1.9	80.46	0.8	6.3	0.6	7.7	0.5	2
			213964	2.26	1.0	1.3	0.09	2.5	117.9	0.9	6.7	0.5	7.7	0.4	2
			213965	3.90	1.4	9.8	1.52	4.2	91	0.8	65.2	3.2	78.0	1.5	2
			213966	3.06	1.1	7.6	0.28	3.3	95	0.8	15.6	1.3	18.5	0.4	2
			213967	2.83	3.3	4.1	0.19	3.6	72.04	0.8	9.5	1.3	12.0	0.7	2
Weighted mean ± 95% CI:													**15.1 ±2.6**		
			203501	5.88	22.9	9.1	0.99	11.3	48.68	0.7	16.2	1.8	23.3	1.2	0
			203502	4.10	18.9	23.5	0.37	8.5	47.86	0.7	7.9	1.1	11.5	0.8	2
			203503	6.71	25.7	39.6	1.04	12.7	42.54	0.6	14.7	1.3	22.7	1.1	1
B3	5.75/36.75	1697	203504	4.76	17.6	22.1	0.48	8.9	44.81	0.7	9.8	1.7	14.7	1.2	1
			203505	9.12	27.0	30.5	2.88	15.5	40.36	0.6	33.8	3.8	53.7	2.1	0
			213986	5.30	16.1	28.9	0.60	9.1	51.2	0.7	11.3	1.5	16.0	0.8	1
			213987	2.50	13.6	23.4	0.30	5.7	58.1	0.7	9.3	1.0	12.5	0.8	2
Weighted mean ± 95% CI:													**15.6 ±3.7**		
B4	5.77/36.66	1425	203496	3.19	6.2	83.1	0.47	4.6	93.52	0.8	16.2	1.0	19.3	0.4	2
			203023	0.94	1.1	1.7	0.03	1.2	66.5	0.8	4.4	1.3	5.7	1.3	2
			203025	6.78	10.6	0.4	0.30	9.3	64.1	0.8	5.9	0.7	7.8	0.4	0
			203026	3.02	1.0	1.2	0.08	3.3	82.9	0.8	4.6	0.3	5.6	0.3	2
			203027	7.26	7.4	1.1	0.31	9.0	90.2	0.8	6.3	0.3	7.6	0.2	0
			213975	1.39	0.5	0.9	0.06	1.5	127	0.9	7.5	0.3	8.5	0.2	2
K1	5.98/36.97	895	213976	3.13	1.3	1.0	0.15	3.4	118	0.9	8.2	0.5	9.4	0.2	2
			213977	3.49	6.3	0.6	0.21	5.0	102	0.9	7.9	0.7	9.3	0.3	2
			213978	2.91	6.6	0.4	0.16	4.5	90.8	0.8	6.6	0.6	7.9	0.4	1
			213979	2.58	4.0	2.9	0.08	3.5	60.6	0.8	4.2	0.7	5.6	0.6	1
			213980	4.61	7.4	0.7	0.21	6.4	103	0.9	6.2	0.4	7.2	0.2	2
			213981	0.90	2.5	1.0	0.04	1.5	66.6	0.8	4.7	1.2	6.1	1.0	2
Weighted mean ± 95% CI:													**7.9 ± 0.7**		
			202988	1.52	5.2	4.8	0.10	2.7	68.2	0.8	6.6	0.9	8.5	0.84	0
			202989	1.64	3.8	4.2	0.09	2.5	62.9	0.8	6.8	1.1	8.9	0.95	0
			202990	1.85	5.9	4.4	0.19	3.2	60.5	0.8	10.8	1.4	14.4	1.21	0
			202992	1.35	4.0	3.6	0.07	2.3	53.9	0.7	5.8	1.6	8.0	1.57	2
K2	6.00/36.95	975	213957	1.53	3.9	3.5	0.21	2.5	114	0.9	16.0	0.6	18.4	0.42	2
			213958	0.59	1.1	1.7	0.03	0.9	79.4	0.8	6.4	1.2	7.9	1.07	1
			213959	0.87	2.1	1.6	0.07	1.4	82.5	0.8	9.8	1.4	12.0	1.14	1
			213960	2.25	5.8	6.3	0.16	3.6	90.5	0.8	8.0	0.6	9.6	0.38	2
			213961	1.56	4.5	3.5	0.15	2.6	93.4	0.8	10.5	1.2	12.5	0.60	1
Weighted mean ± 95% CI:													**10.2 ± 1.3**		
			203033	1.70	3.0	2.1	0.11	2.4	76.24	0.8	8.2	0.9	10.2	0.8	2
			203034	6.40	2.9	2.7	0.26	7.1	62.55	0.8	6.7	0.9	8.8	0.5	2
K3	6.04/37.01	1176	203035	3.77	8.0	20.6	0.13	5.7	79.01	0.8	4.2	0.5	5.1	0.3	2
			203036	4.58	8.3	1.7	0.18	6.5	107.6	0.9	4.9	0.3	5.8	0.2	1
			203037	5.35	5.6	0.9	0.46	6.7	64.69	0.8	12.6	1.2	16.4	0.6	2
Weighted mean ± 95% CI:													**5.9 ± 1.6**		
			203074	0.41	2.3	0.2	0.00	1.0	56.6	0.7	0.9	2.6	1.2	2.6	1
			203075	0.66	1.2	0.3	0.04	0.9	46.3	0.7	7.6	5.4	11.2	5.1	1
K4	6.01/37.04	1276	203076	1.00	2.0	2.9	0.06	1.5	42.1	0.6	7.9	4.9	12.3	4.5	2
			203077	0.33	0.6	0.7	0.01	0.5	54.1	0.7	2.2	5.7	3.0	5.7	2
			203078	0.19	0.3	0.4	0.01	0.3	60.7	0.8	8.0	7.8	10.6	7.8	2
Weighted mean ± 95% CI													**5.2 ± 4.9**		
			203408	2.37	8.9	0.9	0.31	4.5	94.06	0.8	12.8	0.5	15.3	0.3	2
			203409	3.13	8.2	1.2	0.24	5.0	61.81	0.8	8.9	1.3	11.8	1.0	0
			203411	2.01	9.0	3.9	0.23	4.1	71.55	0.8	10.0	1.0	12.7	0.9	2
			203412	3.09	9.7	1.1	0.26	5.4	68.44	0.8	8.8	0.8	11.3	0.6	2
K5	5.87/37.06	1055	203413	2.15	9.0	1.2	0.15	4.3	51.88	0.7	6.7	1.5	9.4	1.5	2

Table A.4: AHe single grain age

			213998	3.14	7.3	1.3	0.26	4.9	123.9	0.9	9.8	0.6	11.1	0.3	2
			213999	3.34	13.2	0.9	0.91	6.4	81.59	0.8	26.0	1.4	31.9	0.9	1
			214000	2.01	6.8	1.7	0.22	3.6	101.8	0.9	11.3	0.4	13.3	0.3	2
			214001	1.14	4.0	0.8	0.13	2.1	92.35	0.8	11.2	0.8	13.3	0.5	2
Weighted mean ± 95% CI:													**12.1 ±0.9**		
			203441	15.10	14.0	1.9	4.46	18.4	72.61	0.8	44.7	2.8	56.3	0.8	2
			203442	2.55	4.2	7.1	0.24	3.5	69.3	0.8	12.3	0.9	15.7	0.9	2
K6	5.85/37.05	998	203443	15.32	16.4	1.8	3.32	19.2	54.54	0.7	32.0	2.8	44.0	0.8	1
			203444	12.03	11.7	3.2	1.96	14.8	54.22	0.7	24.5	2.1	33.8	1.0	2
			203446	30.51	24.6	3.3	3.20	36.3	47.78	0.7	16.3	1.1	23.8	0.3	2
Weighted mean ± 95% CI													**29.8 ± 12.0**		
			203492	7.52	8.6	22.4	2.38	9.5	145	0.9	45.2	1.9	50.4	0.6	2
W1	5.87/37.06	1065	203493	4.41	7.0	21.7	1.43	6.1	122	0.9	42.3	3.0	48.2	0.9	2
			203495	6.47	7.4	21.9	1.79	8.2	97.56	0.8	39.5	3.3	46.6	0.8	1
Weighted mean ± 95% CI:													**47.8 ± 4.9**		
			213949	1.59	0.1	0.2	0.39	1.6	109.5	0.9	45.0	2.7	52.1	0.9	2
			213950	1.78	0.4	0.2	0.45	1.9	88.29	0.8	44.6	5.1	53.7	1.3	2
			213951	1.29	0.1	0.2	0.31	1.3	72.36	0.8	43.5	7.3	54.9	2.5	2
G1	5.55/37.41	1288	203471	2.28	0.8	4.1	0.55	2.5	69.65	0.8	41.1	3.3	52.4	1.9	2
			203472	0.71	0.8	0.3	0.08	0.9	48.68	0.7	15.5	6.8	22.4	5.6	2
			203473	0.93	1.3	0.4	0.12	1.2	51.28	0.7	18.1	4.8	25.5	3.8	0
			203474	0.73	0.3	0.2	0.08	0.8	61.44	0.8	18.7	3.9	24.8	3.3	2
			203475	2.52	0.4	0.2	0.12	2.6	64.77	0.8	8.6	1.1	11.2	1.0	2
Weighted mean ± 95% CI:													**50.3 ± 7.2**		
			203461	1.47	3.2	10.0	0.46	2.2	75.87	0.8	36.9	3.9	45.2	1.26	2
			203462	1.17	2.4	13.3	0.36	1.7	67.34	0.8	36.5	5.2	45.6	2.37	2
			203463	1.60	3.2	16.4	0.43	2.4	57.76	0.7	31.9	5.0	41.9	2.63	2
			203465	1.87	4.8	15.0	0.34	3.0	45.99	0.7	20.2	2.8	29.4	2.25	2
			213943	0.99	1.8	7.4	0.14	1.4	76.75	0.8	17.6	1.9	21.9	1.7	2
G2	5.43/37.37	1385	213944	1.05	2.0	11.4	0.13	1.5	71.62	0.8	14.5	1.1	18.4	0.9	2
			213945	0.95	2.4	10.0	0.12	1.5	65.71	0.8	14.1	1.6	18.3	1.2	2
			213946	0.78	1.8	11.0	0.17	1.2	73.98	0.8	23.9	2.2	30.0	1.6	2
			213947	1.04	1.9	5.1	0.91	1.5	74.24	0.8	109.4	7.6	136.8	3.5	2
			213948	1.35	3.0	7.6	0.33	2.1	58.04	0.7	28.7	2.5	38.2	1.9	2
Weighted mean ± 95% CI :													**26.8 ± 7,8**		

Note: Weighted mean ages were calculated using IsoplotR v.9 (Vermeesch, 2018). CI is confidence interval for the weighted mean age. Lat: Latitude, long: longitude and Elev: elevation. [a]eU is effective uranium concentration. [b]ESR is equivalent spherical radius. [c]Ft is the α-ejection correction after Farley et al (1996). [d]Uncorrected age. [e]Corrected age. [f]Termination (0T is no termination. 1T is one termination. 2T is two termination).

Table A.5: ZHe single grain age

Table 2: Zircon (U-Th)/He data summary

Sample code	Lat./Long (°)	Elev. (m)	lab #	U (ppm)	Th (ppm)	^{147}Sm (ppm)	He (nmole/g)	eU (ppm)[a]	ESR (μm)[b]	Ft[c]	Uncc. age(Ma)[d]	2σ error(Ma)	Corr age(Ma)[e]	2σ error(Ma)	Termination[f]
C1	4.84/36.73	632	203487	81.1	54.4	0.3	148.6	93.9	86.3	0.9	286.5	18.9	334.4	3.9	2
			203488	83.3	66.1	0.4	136.4	98.8	69.4	0.8	250.6	22.8	304.8	1.9	2
			203489	42.9	37.1	0.3	72.8	51.6	83.7	0.9	256	16.3	300.7	3.4	2
			203490	99.3	80.8	0.4	178.6	118.3	66.6	0.8	273.7	96.1	335.6	4.5	2
			203491	89.2	52.3	0.3	146.4	101.5	60.7	0.8	261.5	33.6	327.1	4.0	2
Mean ± s(t)													**320.5 ± 16.6**		
C11	5.33/37.23	1352	203428	559.6	157.9	3.4	426.14	596.7	56.0	0.8	131.0	4.7	167.2	1.41	2
			203429	275.5	97.8	2.1	331.64	298.5	54.2	0.8	202.4	13.1	260.6	3.04	2
			203430	574.3	150.5	3.3	380.18	609.7	62.9	0.8	114.5	10.1	142.2	1.94	2
Mean ± s(t)													**150.0 ± 62.4**		
W2	5.33/37.03	625	213984	125.3	24.5	0.1	144.2	131.1	62.7	0.8	200.5	43.2	248.5	3.9	2
			213985	183.7	45.4	1.1	254.8	194.4	52.0	0.8	238	46.1	309.2	6.2	1
Mean ± s(t)													**278.9 ± 42.9**		

Note: s(t) is standard deviation of the mean. Lat: Latitude, Long: Longitude and Elev: elevation. [a]eU is effective uranium concentration. [b]ESR is equivalent spherical radius. [c]Ft is the α-ejection correction after Farley et al (1996). [d]Uncorrected age. [e]Corrected age. [f]Termination (1T is one termination. 2T is two termination).

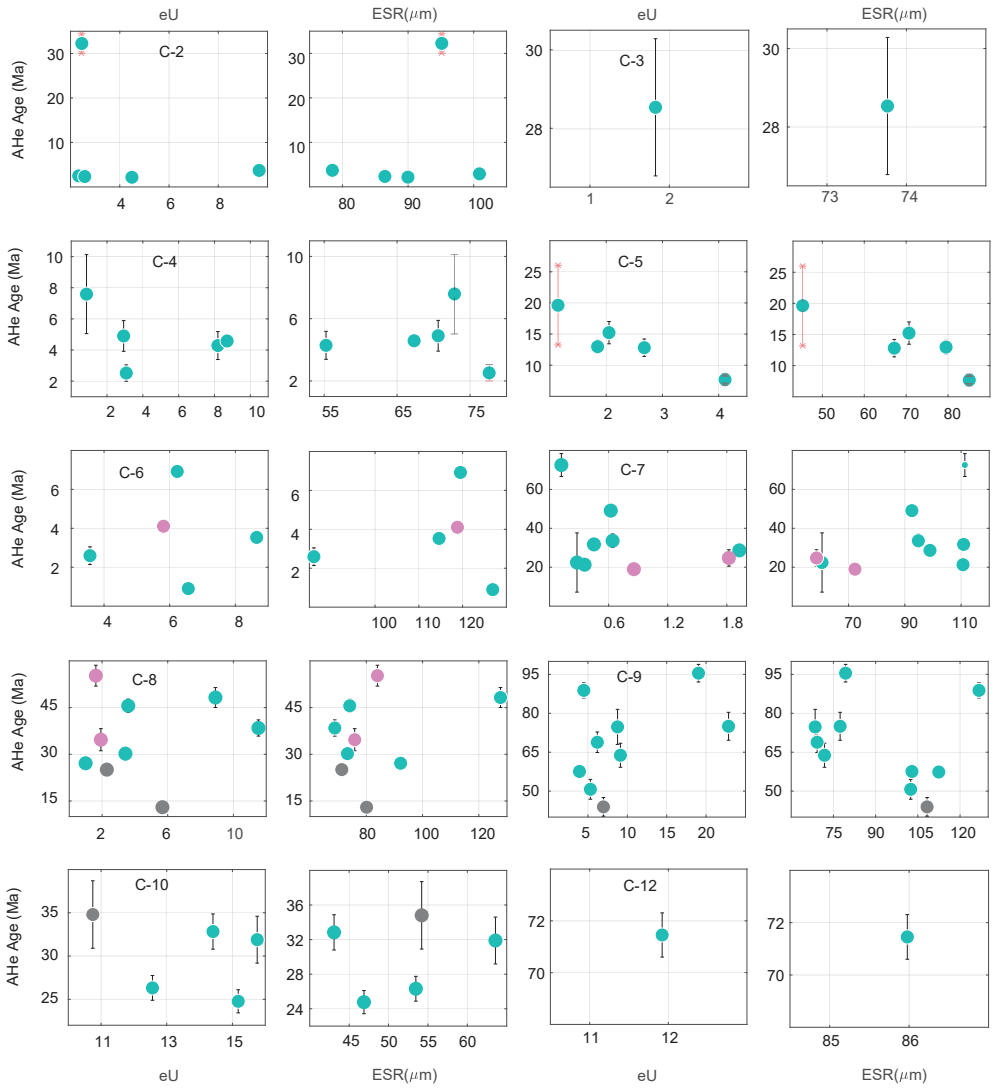

Figure A.1: Apparent age versus eU and ESR

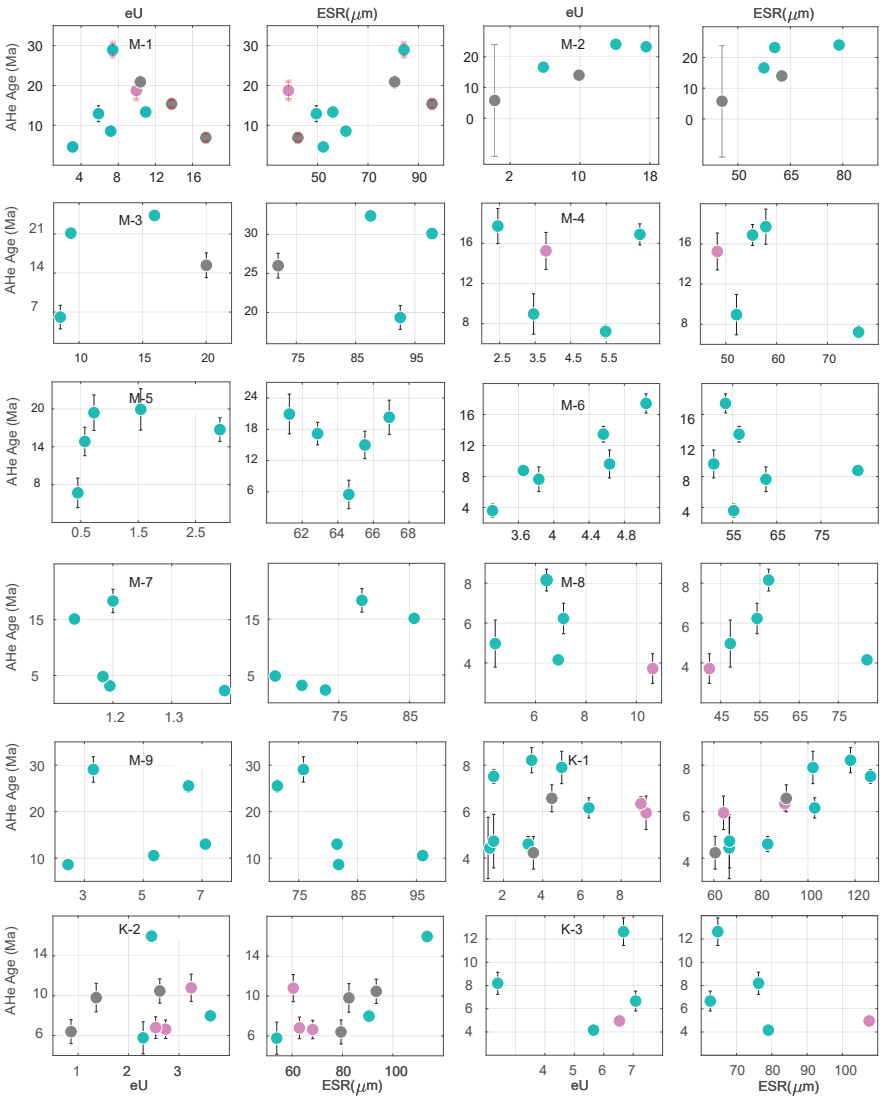

Figure A.2: Apparent age versus eU and ESR

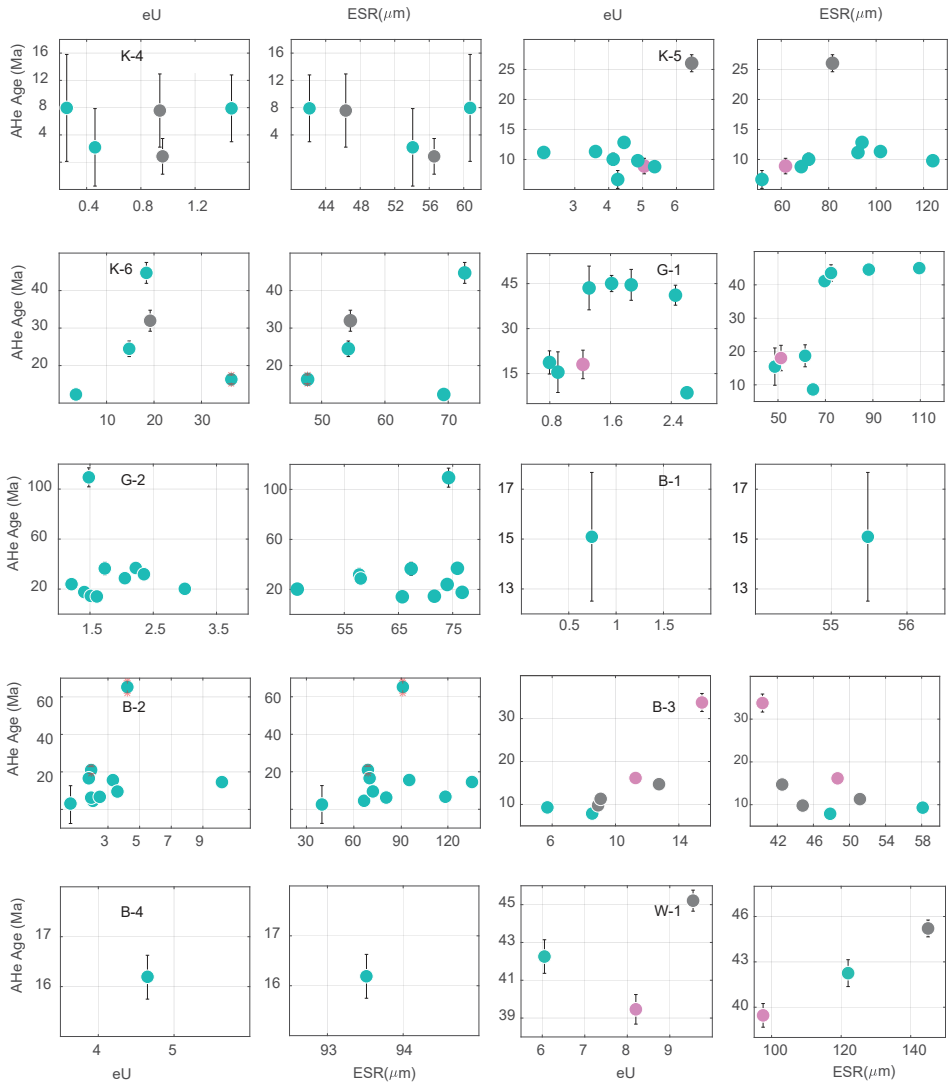

Figure A.3: Apparent age versus eU and ESR

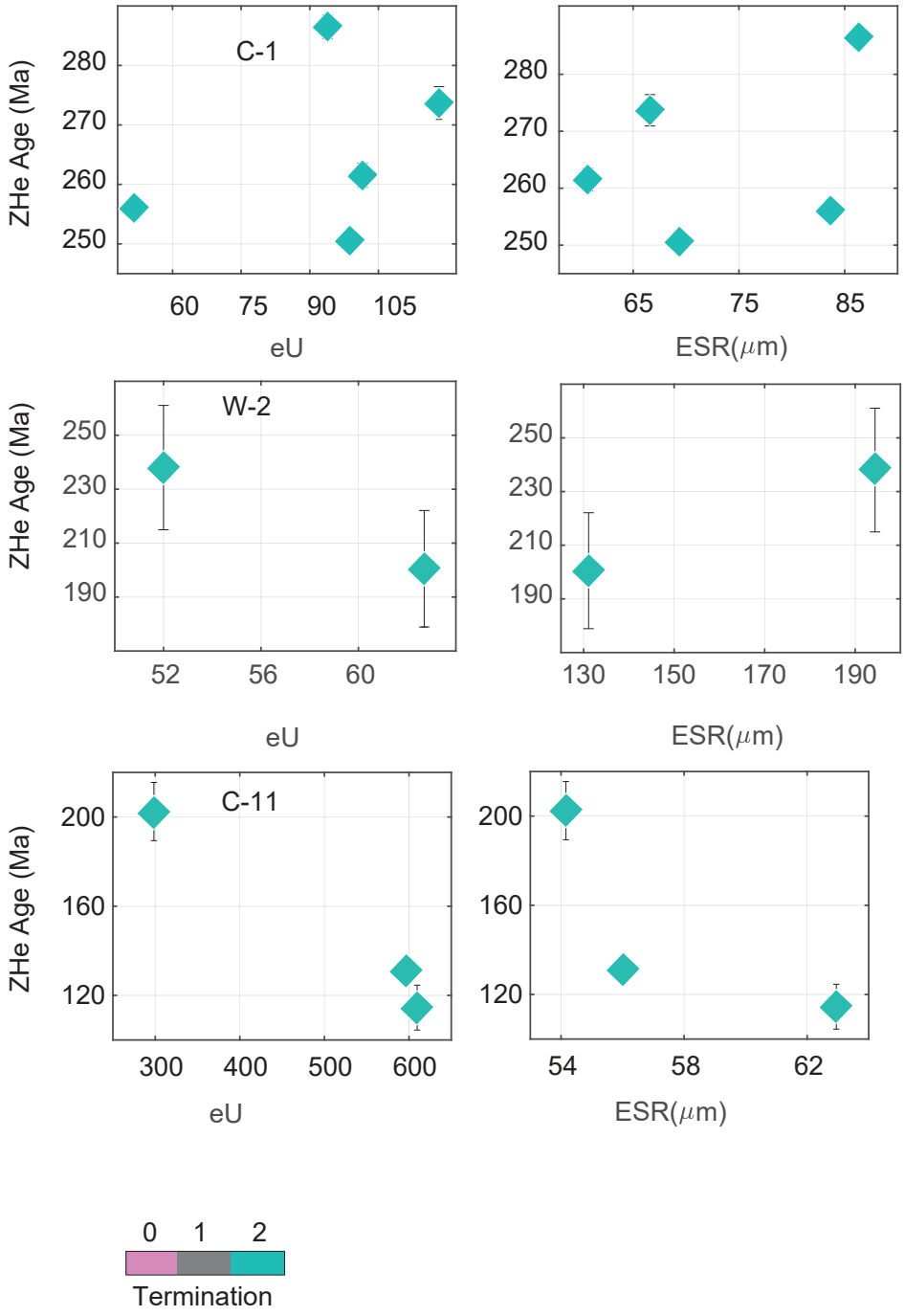

Figure A.4: Apparent age versus eU and ESR

Table A.6: Thermal modeling results for selected individual and set of elevation profile samples

Table 3: Thermal modeling results for individual and set of elevation profile samples

No	Sample code	Lat (°)	Long (°)	Elevation (m)	Earlist reqiured onset of cooling (Ma)	Latest reqiured onset of cooling (Ma)	Mean reqiured onset of cooling (Ma)	Stdv (Ma)	Cooling rate (°C/Myr), and time (Ma)	Comment
1	C-2	4.5	36.7	579.00	3	2	3	0.7	6.2, 3-15	
2	C-3	5.1	36.9	547					0.8, 30-20	Protracted cooling
3	C-5	5.3	36.9	560	29	23	26	4.2	1.9, 20-10	
4	[p]C7-9			1326-945	42	40	41	1.6	1.2, 20-10	middle sample
5	[p]C10-12			1486-1210	56	54	55	1.5	0.7, 40-10	middle sample
6	M-1	5.5	36.8	690	17	12	14	3.4	19.8,10-5	
7	M-2	5.5	36.9	881	32	20	26	8.4	2.3, 20-10	
8	[p]M1-2			881-690	30	24	27	4.2	5.4, 26-20	top sample
9	[p]M7-8			898-714	11	7	9	2.8	24.7, 8-6	bottom sample
10	M-9	5.7	36.9	960	24	21	23	2.1	3.1, 20-10	
11	B-2	5.8	36.8	1390	13	12	13	0.7	5.3, 10-4	
12	B-3	5.8	36.8	1697	18	12	15	4.2	2.9, 10-4	
13	[p]B2-3			1697-1390	16	14	15	1.4	4.8, 12-4	top sample
14	K-1	6.0	37.0	895	7	6	6	0.7	4.9, 5-2	
15	K-6	5.9	37.1	998	25	17	21	5.4	2.1, 14-4	
16	W-1	5.9	37.1	0.70					0.5, 30-10	Protracted cooling

[p]Jointly modeled elevation profile samples. Onset of cooling was determined based on the shape of the 95% credible interval (inflection point), marking change in cooling rate. The cooling rate was also calculated from the slope of the weighted mean expected thermal history between a specified time interval. [stdv]Standard deviation of the mean onset of cooling

Table A.7: Details on QTQt model for sample K1-6 and M1-2

QTQt model details														
1. Thermochronologic data:												4. Model outputs		
Sample	Grain ID	Mineral	U (ppm)	Th (ppm)	^{147}Sm (ppm)	eU (ppm)	ESR (µm)	Uncc. Age (Ma)	Corr age (Ma)	2σ error(Ma)	Termination	Model convergence		
K1	203023	ap	0.94	1.10	1.70	1.20	66.50	4.40	5.70	1.3	2	Birth	Death	outside
	213981	ap	0.90	2.50	1.00	1.50	66.60	4.70	6.10	1.2	2	0.1271	0.1261	0.006
	213975	ap	1.39	0.50	0.90	1.50	127.00	7.50	8.50	0.3	2			
	203026	ap	3.02	1.00	1.20	3.30	82.90	4.60	5.60	0.3	2			
	213976	ap	3.13	1.30	1.00	3.40	118.00	8.20	9.40	0.5	2			
	213979	ap	2.58	4.00	2.90	3.50	60.60	4.20	5.60	0.7	1			
	213978	ap	2.91	6.60	0.40	4.50	90.80	6.60	7.90	0.6	1			
	213977	ap	3.49	6.30	0.60	5.00	102.00	7.90	9.30	0.7	2			
	213980	ap	4.61	7.40	0.70	6.40	103.00	6.20	7.20	0.4	2			
	203027	ap	7.26	7.40	1.10	9.00	90.20	6.30	7.60	0.3	0			
	203025	ap	6.78	10.60	0.40	9.30	64.10	5.90	7.80	0.7	0			
K6	203442	ap	2.55	4.20	7.10	3.50	69.30	12.30	15.70	0.9	2	Model convergence		
	203444	ap	12.03	11.70	3.20	14.80	54.22	24.50	33.80	2.1	2	Birth	Death	outside
	203441	ap	15.10	14.00	1.90	18.40	72.61	44.70	56.30	2.8	2	0.0618	0.0613	0.007
	203443	ap	15.32	16.40	1.80	19.20	54.54	32.00	44.00	2.8	1			
	[a] 203446	*ap*	*30.51*	*24.60*	*3.30*	*36.30*	*47.78*	*16.30*	*23.80*	*1.1*	*2*			
M1	203092	ap	1.85	5.30	23.00	3.10	52.24	4.60	6.40	1.1	2	Model convergence		
	203091	ap	4.26	6.90	17.80	5.90	49.52	12.90	18.50	2.0	2	Birth	Death	outside
	213970	ap	5.35	7.90	18.40	7.20	61.22	8.50	11.30	0.7	2	0.0825	0.0820	0.005
	213969	ap	7.82	11.00	23.90	10.40	80.56	20.90	25.70	1.5	1			
	213971	ap	7.63	14.20	21.90	11.00	56.04	13.30	18.20	1.2	2			
	[a]213968	ap	5.17	9.60	17.60	7.40	84.27	29.00	35.20	1.5	2			
	[a]203093	ap	8.47	6.30	26.80	10.00	38.42	18.70	30.70	2.0	0			
	[a]203089	ap	9.41	18.40	30.50	13.70	95.41	15.20	18.20	0.8	1			
	[a]203090	ap	14.10	14.20	24.20	17.40	42.19	6.90	10.70	0.8	1			
	203072	ap	5.27	2.30	15.10	5.80	57.44	16.60	22.50	1.8	2			
	203071	ap	9.04	3.60	27.60	9.90	62.55	14.00	18.40	1.6	1			

Table A.8: Details on QTQt model for sample C2 and B2-3

M2	203070	ap	13.44	2.80	35.20	14.10	78.92	24.10	29.70	1.8	2	Model convergence		
	203069	ap	15.86	7.20	32.40	17.60	60.53	23.30	30.90	1.0	2	Birth	Death	outside
	[a] *203073*	*ap*	*0.09*	*0.60*	*0.00*	*0.20*	*45.47*	*5.80*	*8.60*	*18.2*	*1*	0.0825	0.0820	0.005
M1 and M2												0.0844	0.0842	0.163
	202998	ap	1.59	2.5	17.5	2.2	100.87	2.5	2.9	0.3	2	Model convergence		
	202999	ap	1.21	5.2	16.3	2.4	86.47	1.9	2.3	0.3	2	Birth	Death	outside
C2	203001	ap	2.96	6.5	17.6	4.5	89.98	1.7	2.1	0.2	2	0.0984	0.0978	0.015
	203000	ap	5.11	19.4	22.7	9.7	78.47	3.7	4.6	0.3	2			
	[a] *203002*	*ap*	*1.26*	*5.1*	*21.9*	*2.5*	*95.14*	*32.3*	*38.3*	*2.2*	2			
[b]C3	203437		1.62	0.9	52.9	0.35	1.8	73.76	28.5	2.5	2	0.2074	0.5603	0.007
	203006	ap	0.40	0.98	0.08	0.63	39.82	2.55	4.10	10.1	2	Model convergence		
	213963	ap	1.62	1.35	10.54	1.94	80.46	6.26	7.69	0.6	2	Birth	Death	outside
	203005	ap	1.79	1.10	6.03	2.05	66.47	4.54	5.86	0.9	2	0.1112	0.1111	0.006
	213964	ap	2.26	0.95	1.26	2.48	117.89	6.69	7.67	0.5	2			
B2	213967	ap	2.83	3.26	4.12	3.60	72.04	9.53	12.03	1.3	2			
	213962	ap	9.20	4.26	1.28	10.20	134.68	14.55	16.37	1.1	2			
	[a] *203004*	*ap*	*1.47*	*1.37*	*17.64*	*1.79*	*69.96*	*16.58*	*21.10*	*1.5*	2			
	[a] *203003*	*ap*	*1.75*	*0.80*	*8.13*	*1.93*	*68.89*	*20.99*	*26.81*	*1.8*	2			
	[a] *213966*	*ap*	*3.06*	*1.08*	*7.63*	*3.31*	*95.00*	*15.61*	*18.53*	*1.3*	2			
	[a] *213965*	*ap*	*3.90*	*1.40*	*9.80*	*4.22*	*91.00*	*65.25*	*78.04*	*3.2*	2			
	213987	ap	2.50	13.60	23.40	5.70	58.10	9.30	12.50	1.0	2	Model convergence		
	203502	ap	4.10	18.87	23.50	8.53	47.86	7.88	11.47	1.1	2	Birth	Death	outside
	203504	ap	4.76	17.62	22.13	8.90	44.81	9.80	14.72	1.7	1	0.1492	0.1494	0.030
B3	213986	ap	5.30	16.10	28.90	9.10	51.20	11.30	16.00	1.5	1			
	203501	ap	5.88	22.94	9.13	11.27	48.68	16.16	23.35	1.8	0			
	203503	ap	6.71	25.71	39.61	12.75	42.54	14.72	22.72	1.3	1			
	203505	ap	9.12	27.00	30.53	15.46	40.36	33.76	53.65	3.8	0			
B2 and B3												0.0891	0.0889	0.143
	213996	ap	0.05	0.3	1.6	0.1	111.33	72.5	83.8	5.9	2	Model convergence		
	203433	ap	0.16	0.5	1.6	0.3	60.58	22.4	29.8	15.2	2	Birth	Death	outside
	213995	ap	0.27	0.4	1.5	0.4	110.68	21.3	24.6	1.6	2	0.1253	0.1250	0.176

Table A.9: Details on QTQt model for samples C7-9

C-7	213997	ap	0.24	0.9	1.6	0.5	110.88	31.7	36.7	2.0	2			
	213994	ap	0.33	1.2	2.3	0.6	92.52	49.1	58.5	2.6	2			
	203432	ap	0.36	1.2	2.1	0.6	94.81	33.6	39.9	3.5	2			
	203434	ap	0.59	1.1	0.5	0.9	72.27	19.0	24.0	2.8	0			
	203435	ap	1.44	1.6	3.1	1.8	58.62	24.7	33.2	4.2	0			
	203431	ap	1.35	2.6	4.0	2.0	98.94	28.7	33.8	1.4	2			
C8	203477	ap	5.75	13.4	3.0	8.9	127.70	48.2	54.6	3.2	2			
	203478	ap	1.53	3.2	1.6	2.3	71.30	25.1	31.7	1.6	1			
	203479	ap	1.47	1.9	5.5	1.9	75.89	34.7	43.2	3.6	0			
	203480	ap	1.35	1.1	3.7	1.6	83.96	55.3	67.2	3.3	0			
	203481	ap	2.50	4.7	1.9	3.6	74.12	45.6	57.1	2.1	2			
	214002	ap	8.84	11.4	0.6	11.5	68.81	38.4	49.1	2.6	2			
	214003	ap	0.94	0.2	4.6	1.0	92.20	27.1	32.4	1.5	2			
	214004	ap	2.42	4.3	2.5	3.4	73.32	30.2	38.0	1.9	2			
	214005	ap	4.30	5.9	5.8	5.7	80.11	13.0	16.0	0.7	1			
C9	203451	ap	4.81	5.9	5.5	6.2	69.20	68.8	87.8	4.0	2			
	203452	ap	6.88	8.0	7.8	8.8	68.51	74.8	95.6	6.8	2			
	203453	ap	7.38	7.4	8.7	9.1	71.84	63.8	80.6	4.6	2			
	203454	ap	17.02	24.8	12.0	22.9	77.38	75.0	92.9	5.4	2			
	203455	ap	14.24	20.4	14.9	19.0	79.33	95.5	117.5	3.4	2			
	213952	ap	3.12	3.6	4.4	4.0	112.44	57.4	66.2	2.2	2			
	213953	ap	3.46	4.3	4.9	4.5	126.73	88.8	100.7	2.9	2			
	213954	ap	3.14	3.4	5.5	3.9	102.91	57.6	67.3	2.0	2			
	213955	ap	4.00	5.6	6.5	5.3	102.46	50.7	59.4	3.8	2			
	213956	ap	5.73	5.3	6.8	7.0	108.28	43.9	51.0	3.6	1			
C10	203414	ap	8.55	28.2	26.7	15.2	46.88	24.8	36.4	1.3	2	Model convergence		
	203415	ap	9.73	19.9	18.1	14.4	43.09	32.8	50.3	2.0	2	Birth	Death	outside
	203416	ap	6.88	16.5	15.0	10.7	54.21	34.8	48.1	3.9	1	0.1112	0.1111	0.006
	203417	ap	10.61	22.4	25.7	15.9	63.57	31.9	41.7	2.7	2			
	203418	ap	7.41	21.9	21.1	12.6	53.47	26.3	36.6	1.4	2			
	203428	zr	559.6	157.9	3.4	596.7	56.02	131.0	167.2	4.7	2			

Table A.10: Details on QTQt model for samples C5-10 and M7-9

C11	203429	zr	275.5	97.8	2.1	298.5	54.16	202.4	260.6	13.1	2			
	203430	zr	574.3	150.5	3.3	609.7	62.95	114.5	142.2	10.1	2			
C12	203476	ap	11.56	1.6	4.4	11.9	85.98	71.5	86.3	1.2	2			
M7	202993	ap	1.19	0.9	23.2	1.4	73.10	2.3	2.9	0.5	2	Model convergence		
	202994	ap	1.06	0.6	68.9	1.2	69.77	3.1	4.0	0.9	2	Birth	Death	outside
	202995	ap	0.90	1.0	64.0	1.1	85.67	15.1	18.3	1.0	2	0.0906	0.0900	0.170
	202996	ap	1.05	0.7	72.6	1.2	78.28	18.4	22.7	2.1	2			
	202997	ap	1.04	0.6	57.9	1.2	65.99	4.8	6.2	0.9	2			
M8	*203018*	ap	*5.20*	*7.3*	*90.5*	*6.9*	*82.31*	4.2	5.1	0.3	2			
	203019	ap	7.26	14.4	175.1	10.6	42.10	3.7	5.8	0.7	0			
	203020	ap	2.29	9.0	113.1	4.4	47.44	5.0	7.3	1.2	2			
	203021	ap	4.17	12.5	102.0	7.1	54.28	6.2	8.6	0.8	2			
	203022	ap	3.43	12.8	102.9	6.4	57.22	8.2	11.1	0.5	2			
[b]M9	203079	ap	1.74	3.0	44.0	2.4	81.79	8.6	10.5	0.7	2	Model convergence		
	203080	ap	3.44	8.1	39.2	5.4	96.07	10.5	12.5	0.5	2	Birth	Death	outside
	203081	ap	4.59	8.3	37.9	6.5	71.37	25.5	32.3	1.4	2	0.2032	0.2010	0.015
	203082	ap	2.39	3.9	10.3	3.3	75.81	29.1	36.2	2.7	2			
	203083	ap	5.20	8.2	27.3	7.1	81.53	13.0	15.9	0.6	2			
[b]W1	203492	ap	7.52	8.6	22.4	9.5	144.98	45.2	50.4	1.9	2	Model convergence		
	203493	ap	4.41	7.0	21.7	6.1	122.00	42.3	48.2	3.0	2	Birth	Death	outside
	203495	ap	6.47	7.4	21.9	8.2	97.56	39.5	46.6	3.3	1	0.0725	0.2803	0.008
[b]C-5	203084	ap	1.35	2.1	15.6	1.8	79.52	13.0	16.0	1.1	2	Model convergence		
	[c]203085	ap	3.35	3.2	23.1	4.1	85.07	7.7	9.3	0.6	2	Birth	Death	outside
	203086	ap	1.07	4.2	18.8	2.0	70.69	15.2	19.3	1.8	2	0.0446	0.3181	0.005
	203087	ap	2.20	2.0	24.7	2.7	67.16	12.8	16.5	1.4	2			
	[d]203088	ap	0.84	1.3	8.5	1.1	45.31	19.6	29.3	6.4	2			

[a]Excluded single grain ages from a sample coupled modeling by QTQt and HeFTy. Justification for the exclusion is provided in supplementary material 1B. ap: apatite, zr: zircon. [b]individual samples modeled only by QTQt. [c]excluded single grain age: anomalousely young date (youngest in sample) with bigger grain size in sample compared to the general date-eU trend. [d]excluded single grain age: anomalously old date (oldest in sample) having small grain size (smallest in sample) compared to general date-eU trend

Table A.11: Additional geologic information for thermal modeling by QTQt

2. Additional geologic information:							
Model initial		Iterations		Present day surface temperature	Geological constraint		Explanation
Time	Temperature	Burn-in	Post burn-in		Time	Temperature	
525 ± 25 Ma	450 ± 50°C	50000	200000	20 ± 10°C	80-30 Ma	120 -20°C	The Pan-African Orogenic event that occurred during the Neoproterozoic (525 ± 25 Ma; Davidson, 1983; Yibas et al., 2002; Asrat and Barbey, 2003) is considered as a rock formation age. Across the region, stratigraphic thicknesses for Paleogene sediments and Eo-Oligocene volcanics, underlaying the crystaline basement rocks are highly variable, and absent in some places (Levitte, 1974; WoldeGabriel et al., 1991, Davidson, 1983; Ebinger et al., 2000; Philippone et al., 2014). As a result, a broad time-temperature range was applied in order to give the model enough freedom of space to search for a solution. A geothermal gradient of 40 ± 3°C estimated from the region (Pik et al., 2003) was used for elevation profile samples modeling.
3. System- and model-specific parameters:							
He kinetic model: RDAAM (Flowers et al., 2009) and ZRDAAM (Guenthner et al., 2013)							
Modeling code: QTQt v5.8.0							
Model fitting criteria: Weighted mean posterior probablity distribution							
AHe and ZHe single grain ages with only one or two terminations were included.							
For elevation profile samples thermal modeling, a regionally estimated geothermal gradient of 40 ± 3°C (Pik et al., 2003) was used.							

Table A.12: Details on HeFTy model for samples K-1 and K-6

HeFTy Model details														
1. Thermochronologic data:													4. Output	
Sample	Grain ID	Mineral	U (ppm)	Th (ppm)	^{147}Sm (ppm)	eU (ppm)	ESR (µm)	Uncc. Age (Ma)	Percent error	Corr age (Ma)	Percent error	HeFTy Input?	Output	
K1	203023	ap	0.94	1.10	1.70	1.20	66.50	4.40	0.70	5.70	1.30	Yes; 15% Date error	ITERATIONS	35765
	213981	ap	0.90	2.50	1.00	1.50	66.60	4.70	0.70	6.10	1.00	Yes; 15% Date error	ACCEPTABLE	GOOD
	213975	ap	1.39	0.50	0.90	1.50	127.00	7.50	1.10	8.50	0.20	Yes; 15% Date error	1451	500
	203026	ap	3.02	1.00	1.20	3.30	82.90	4.60	0.70	5.60	0.30	Yes; 15% Date error		
	213976	ap	3.13	1.30	1.00	3.40	118.00	8.20	1.20	9.40	0.20	Yes; 15% Date error		
	213979	ap	2.58	4.00	2.90	3.50	60.60	4.20	0.60	5.60	0.60	Yes; 15% Date error		
	213978	ap	2.91	6.60	0.40	4.50	90.80	6.60	1.00	7.90	0.40	Yes; 15% Date error		
	213977	ap	3.49	6.30	0.60	5.00	102.00	7.90	1.20	9.30	0.30	Yes; 15% Date error		
	213980	ap	4.61	7.40	0.70	6.40	103.00	6.20	0.90	7.20	0.20	Yes; 15% Date error		
	203027	ap	7.26	7.40	1.10	9.00	90.20	6.30	1.00	7.60	0.20	Yes; 15% Date error		
	203025	ap	6.78	10.60	0.40	9.30	64.10	5.90	0.90	7.80	0.40	Yes; 15% Date error		
K6	203442	ap	2.55	4.20	7.10	3.50	69.30	12.30	2.50	15.70	0.90	Yes; 15% Date error	ITERATIONS	100425
	203444	ap	12.03	11.70	3.20	14.80	54.22	24.50	4.90	33.80	1.00	Yes; 15% Date error	ACCEPTABLE	GOOD
	203441	ap	15.10	14.00	1.90	18.40	72.61	44.70	8.90	56.30	0.80	Yes; 15% Date error	1251	500
	203443	ap	15.32	16.40	1.80	19.20	54.54	32.00	6.40	44.00	0.80	Yes; 15% Date error		
	[a] 203446	*ap*	*30.51*	*24.60*	*3.30*	*36.30*	*47.78*	*16.30*	*3.30*	*23.80*	*0.30*	No; Anomalously young grain with high eU compared to general date-eU relationship.		
	203092	ap	1.85	5.30	23.00	3.10	52.24	4.60	*0.92*	6.40	1.28	Yes; 20% Date error	ITERATIONS	9521201
	203091	ap	4.26	6.90	17.80	5.90	49.52	12.90	*2.58*	18.50	3.70	Yes; 20% Date error	ACCEPTABLE	GOOD
	213970	ap	5.35	7.90	18.40	7.20	61.22	8.50	*1.70*	11.30	2.26	Yes; 20% Date error	68250	92
	213969	ap	7.82	11.00	23.90	10.40	80.56	20.90	*4.18*	25.70	5.14	Yes; 20% Date error		

Table A.13: Details on HeFTy model for samples M1-2 and C-2

M1	213971	ap	7.63	14.20	21.90	11.00	56.04	13.30	*2.66*	18.20	3.64	Yes; 20% Date error		
	[a]213968	ap	5.17	9.60	17.60	7.40	84.27	29.00	*5.80*	35.20	7.04	No; Anomalously old date (oldest in sample) in respected eU range compared to general date-eU trend		
	[a]203093	ap	8.47	6.30	26.80	10.00	38.42	18.70	*3.74*	30.70	6.14	No; Anomalously small grain size with old date compared to general date-eU trend		
	[a]203089	ap	9.41	18.40	30.50	13.70	95.41	15.20	*3.04*	18.20	3.64	No; Anomalously large grain size with young date compared to general date-eU trend		
	[a]203090	ap	14.10	14.20	24.20	17.40	42.19	6.90	*1.38*	10.70	2.14	No; Comparivively young, high eU grain compared to general date-eU trend. No suitable tT paths when included		
M2	203072	ap	5.27	2.30	15.10	5.80	57.44	16.60	2.50	22.50	1.20	Yes; 15% Date error	ITERATIONS	390634
	203071	ap	9.04	3.60	27.60	9.90	62.55	14.00	2.10	18.40	0.70	Yes; 15% Date error	ACCEPTABLE	GOOD
	203070	ap	13.44	2.80	35.20	14.10	78.92	24.10	3.60	29.70	0.60	Yes; 15% Date error	28260	500
	203069	ap	15.86	7.20	32.40	17.60	60.53	23.30	3.50	30.90	0.\6	Yes; 15% Date error		
	[a] 203073	*ap*	*0.09*	*0.60*	*0.00*	*0.20*	*45.47*	*5.80*	*0.90*	*8.60*	*18.10*	No; Data quality uncertainty due to exceedingly low U concentration. However, grain follows general date-eU trend (overlaps that of M1). When included as input, improves model resolution with two distinct cooling events.		
C2	202998	ap	1.59	2.5	17.5	2.2	100.87	2.5	0.38	2.9	0.3	Yes; 15% Date error	ITERATIONS	3452403
	202999	ap	1.21	5.2	16.3	2.4	86.47	1.9	0.29	2.3	0.3	Yes; 15% Date error	ACCEPTABLE	GOOD
	203001	ap	2.96	6.5	17.6	4.5	89.98	1.7	0.26	2.1	0.2	Yes; 15% Date error	10934	293
	203000	ap	5.11	19.4	22.7	9.7	78.47	3.7	0.56	4.6	0.2	Yes; 15% Date error		

Table A.14: Details on HeFTy model for samples C-1 and B2-3

	[a] 203002	*ap*	*1.26*	*5.1*	*21.9*	*2.5*	*95.14*	*32.3*	*4.85*	*38.3*	*1.2*	No; Anomalously old grain with low eU compared to general date-eU relationship.		
C1	203487	zr	81.1	54.4	0.3	93.9	86.30	286.5	-	334.4	-	Included in synthetic grain average.		
	203488	zr	83.3	66.1	0.4	98.8	69.40	250.6	-	304.8	-	Included in synthetic grain average.		
	203489	zr	42.9	37.1	0.3	51.6	83.70	256	-	300.7	-	Included in synthetic grain average.		
	203490	zr	99.3	80.8	0.4	118.3	66.60	273.7	-	335.6	-	Included in synthetic grain average.		
	203491	zr	89.2	52.3	0.3	101.5	60.70	261.5	-	327.1	-	Included in synthetic grain average.		
	Synthetic Grain	*zr*	*79.16*	*58.14*	*0.34*	*92.82*	*73.34*	*265.66*	*39.85*	*320.52*	*48.1*	Yes; 15% Date error. Synthetic grain input from averaging all comparatively consistent single-grain zircon (U-Th)/He data.		
B2	203006	ap	0.40	0.98	0.08	0.63	39.82	2.55	0.51	4.10	10.10	Yes; 20% Date error	ITERATIONS	3944501
	213963	ap	1.62	1.35	10.54	1.94	80.46	6.26	1.25	7.69	0.46	Yes; 20% Date error	ACCEPTABLE	GOOD
	203005	ap	1.79	1.10	6.03	2.05	66.47	4.54	0.91	5.86	0.71	Yes; 20% Date error	99840	308
	213964	ap	2.26	0.95	1.26	2.48	117.89	6.69	1.34	7.67	0.35	Yes; 20% Date error		
	213967	ap	2.83	3.26	4.12	3.60	72.04	9.53	1.91	12.03	0.73	Yes; 20% Date error		
	213962	ap	9.20	4.26	1.28	10.20	134.68	14.55	2.91	16.37	0.16	Yes; 20% Date error		
	[a] 203004	*ap*	*1.47*	*1.37*	*17.64*	*1.79*	*69.96*	*16.58*	*3.32*	*21.10*	*1.24*	No; Anomalously old grain with low eU compared to general date-eU relationship.		
	[a] 203003	*ap*	*1.75*	*0.80*	*8.13*	*1.93*	*68.89*	*20.99*	*4.20*	*26.81*	*1.08*	No; Anomalously old grain with low eU compared to general date-eU relationship.		
	[a] 213966	*ap*	*3.06*	*1.08*	*7.63*	*3.31*	*95.00*	*15.61*	*3.12*	*18.53*	*0.36*	No; Comparitive old grain to those in similar eU range. Even with larger grain size, no suitable tT paths found when included.		

Table A.15: Additional geologic information for thermal modeling by HeFTy

	[a] 213965	*ap*	*3.90*	*1.40*	*9.80*	*4.22*	*91.00*	*65.25*	*13.05*	*78.04*	*1.49*	No; Anomalously old grain with moderate eU compared to general date-eU relationship.		
B3	213987	ap	2.50	13.60	23.40	5.70	58.10	9.30	1.40	12.50	0.80	Yes; 15% Date error	ITERATIONS	3561014
	203502	ap	4.10	18.87	23.50	8.53	47.86	7.88	1.18	11.47	0.85	Yes; 15% Date error	ACCEPTABLE	GOOD
	203504	ap	4.76	17.62	22.13	8.90	44.81	9.80	1.47	14.72	1.24	Yes; 15% Date error	10282	500
	213986	ap	5.30	16.10	28.90	9.10	51.20	11.30	1.70	16.00	0.80	Yes; 15% Date error		
	203501	ap	5.88	22.94	9.13	11.27	48.68	16.16	2.42	23.35	1.19	Yes; 15% Date error		
	203503	ap	6.71	25.71	39.61	12.75	42.54	14.72	2.21	22.72	1.07	Yes; 15% Date error		
	203505	ap	9.12	27.00	30.53	15.46	40.36	33.76	5.06	53.65	2.10	Yes; 15% Date error		

[a]Excluded single grain ages. ap:apatite, zr: zircon

2. Additional geologic information:						
Samples	Constraint	Time (Ma)		Temperature (°C)		Explanation
		Min	Max	Min	Max	
K1; K6; M1; M2; B2; B3	*1*	0	0	0	40	Present day surface temperature; 20 ± 20 °C
	2	1	70	20	125	Exploration constraint employed to permit potential reheating following constraint #3.
	3	30	80	20	120	Across the sampled region, stratigraphic thicknesses for Paleogene sediments and Eo-Oligocene volcanics, underlaying the crystaline basement rocks are highly variable, and absent in some places (Levitte, 1974; WoldeGabriel et al., 1991, Davidson, 1983; Ebinger et al., 2000; Philippone et al., 2014). As a result, a broad time-temperature range was applied in order to give the model enough freedom of space to search for a solution.
	4	70	300	20	200	Exploration constraint employed to allow model to explore various histories of radiation damage accumulation that may impac
C2 (ap) + C1 (zr)	*1*	0	0	0	40	Present day surface temperature; 20 ± 20 °C
	2	1	70	20	125	Exploration constraint employed to permit potential reheating following constraint #3.
	3	30	80	20	120	Across the sampled region, stratigraphic thicknesses for Paleogene sediments and Eo-Oligocene volcanics, underlaying the crystaline basement rocks are highly variable, and absent in some places (Levitte, 1974; WoldeGabriel et al., 1991, Davidson, 1983; Ebinger et al., 2000; Philippone et al., 2014). As a result, a broad time-temperature range was applied in order to give the model enough freedom of space to search for a solution.
	4	300	400	200	250	Constraint allowing model to explore cooling histories before 80 Ma that broadly agree with observed zircon (U-Th)/He data.

Table A.16: Additional geologic information for thermal modeling by HeFTy

3. System- and model-specific parameters:
He kinetic model: RDAAM (Flowers et al., 2009) and ZRDAAM (Guenthner et al., 2013)
Modeling code: HeFTy v2.1.4
Statistical fitting criteria: Default HeFTy values. Goodness of fit (GOF) values of >0.5 for "good" fits and >0.05 for "acceptable" fits
Numer of time-temperature paths attempted: Models set to stop once 500 good tT paths were found, and a minimum threshold of 75 good pathways was employed before manually termir
A total of 11 grains were input for sample K1 by using multi-sample-modelling in HeFTy due to the 7 grain input limit per sample. The data were split between "two" samples with the same tT path characteristics: Episodic history, with 8–14 randomly defined linear segments.

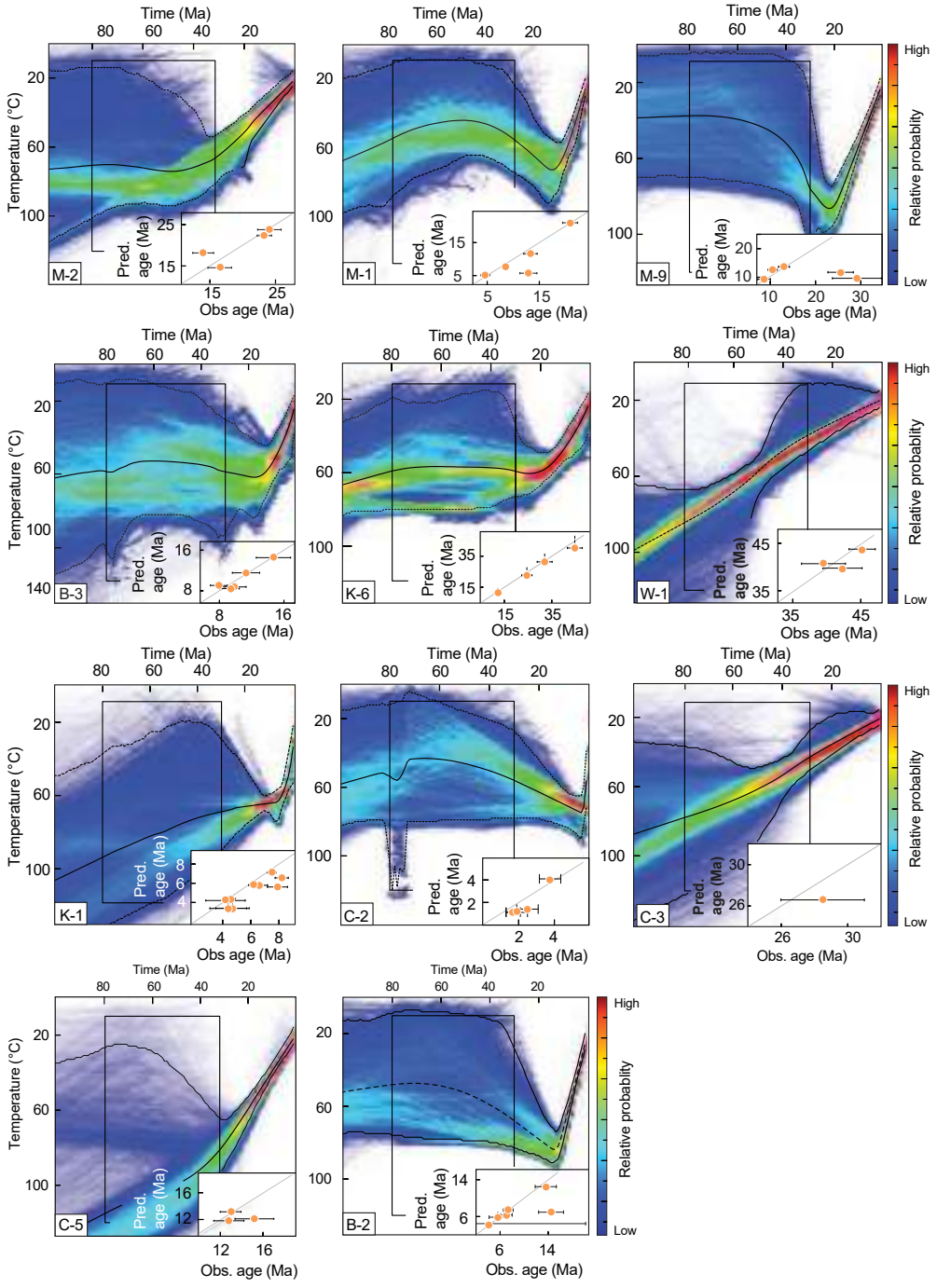

Figure A.5: QTQt modeling results for individual samples

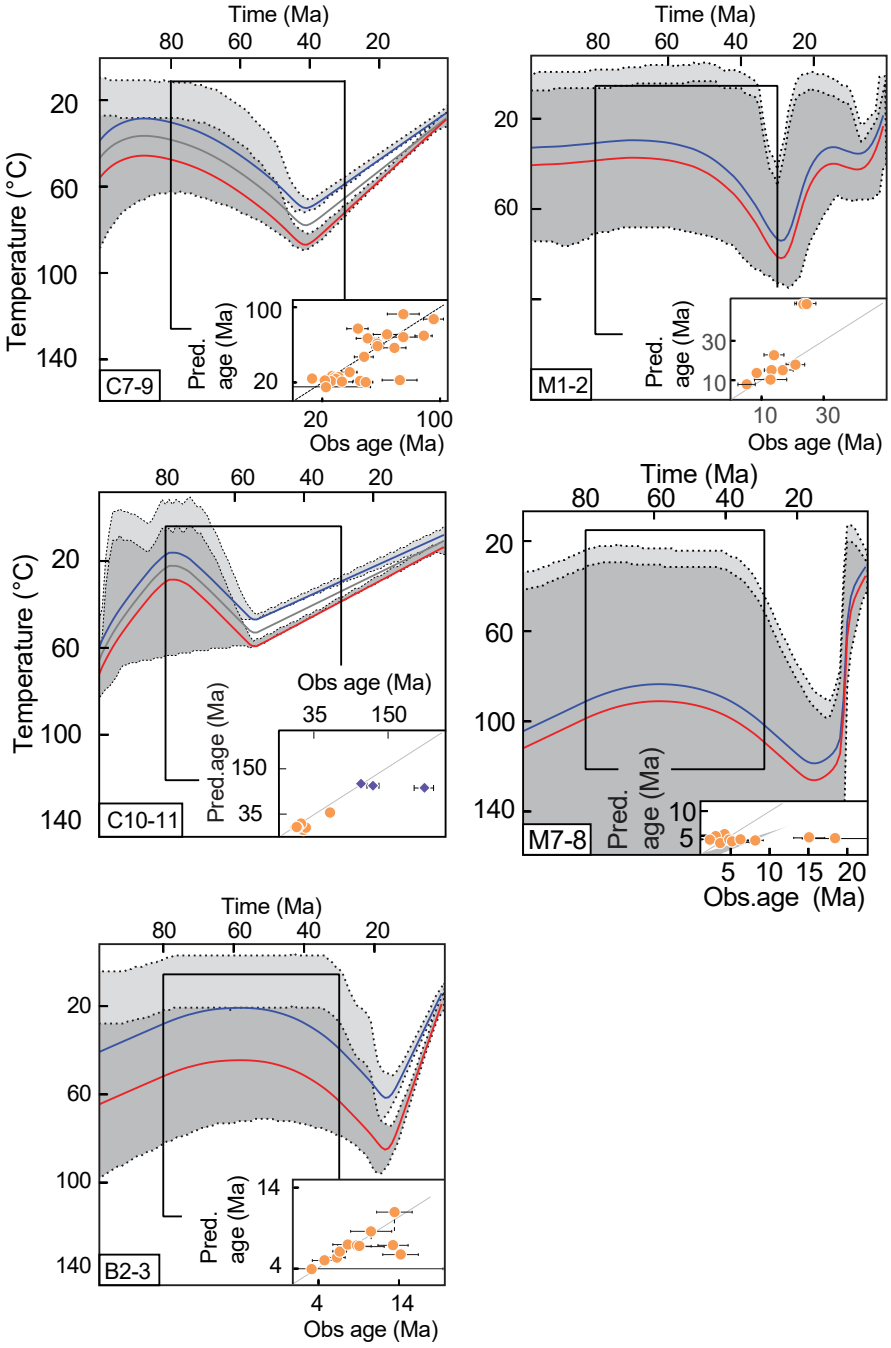

Figure A.6: QTQt modeling results for set of elevation profile samples

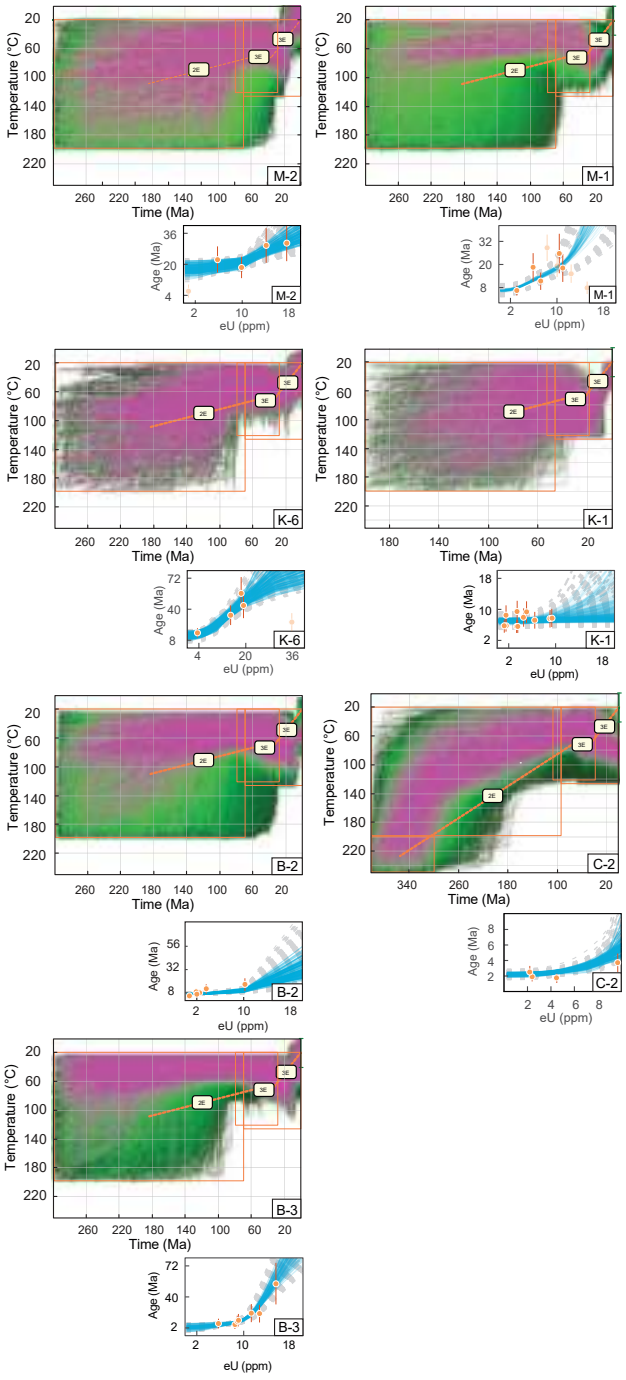

Figure A.7: HeFTy modeling results for individual samples

Appendix B

Temporal variation in counterclockwise vertical-axis block rotations across a rift overlap zone, southwestern Ethiopia, East Africa

---

Table B.1: Sample location and geologic information

Table 1: Sampling location, geologic information,dated rock units and site mean median destructive field (MDF)

Ref.no	ID	Sampling location			Bedding		N	MDF (mT)	Lithology	Age (Ma)	References
		Lat (°)	Lon (°)	Elev (m)	Strike	Dip					
1	CH-1	6.177	37.579	2289	200	5	10	39	Welded tuff	34.1 ± 1.3	Bonini et al., 2005
2	CH-2	6.177	37.579	2289	010	5	9	46	Welded tuff		
3	CH-3[a]	6.256	37.557	2762	010	5	8	7	Basaltic flow	*37.20 ± 0.12	This study
4	CH-4	6.255	37.541	2762	045	5	8	12	Basaltic flow		
5	SH-1	6.130	37.550	1321	000	0	6	29	Welded tuff		
6	SH-2	6.130	37.520	1325	192	7	4	25	Welded tuff		
7	GE-1	5.909	37.415	1396	000	0	8	13	Basaltic flow	19.55 ± 0.14	This study
8	GE-2	5.909	37.415	1396	000	20	8	15	Basaltic flow		
9	GE-3	5.909	37.416	1409	000	20	8	20	Sediment	15-17	WoldeGabriel et al., 1991
10	GE-4	5.873	37.349	1387	000	0	10	14	Basaltic flow		
11	GE-5	5.873	37.349	1387	000	0	7	46	Basaltic flow		
12	GE-6	6.015	37.270	2556	020	25	7	42	Sediment	15-17	WoldeGabriel et al., 1991
13	GE-7	6.020	37.260	2655	000	0	9	37	Basaltic flow	38.97 ± 0.17	This study
14	GE-8	6.020	37.260	2649	000	0	7	54	Basaltic flow		
15	GE-9	5.955	37.291	2176	000	0	8	37	Basaltic flow		
16	GE-10	5.949	37.288	2048	000	0	8	39	Basaltic flow		
17	GE-11	5.949	37.288	2054	000	0	8	32	Basaltic flow		
18	GE-12	5.949	37.288	2063	000	0	8	21	Basaltic flow	19.84 ± 0.06	This study
19	GER-1[a]	5.872	37.350	2730	000	0	9	7	Basaltic flow		
20	GER-2[a]	5.899	37.350	1920	000	0	8	4.2	Basaltic flow	*33.62 ± 0.13	This study
21	GER-3	6.015	37.269	2542	000	0	10	43	Basaltic flow		
22	KE-1	6.052	37.205	2557	000	0	9	46	Basaltic flow	41.96 ± 0.22	This study
23	KE-2	6.052	37.205	2557	000	0	7	13	Basaltic flow		
24	KE-3	6.046	37.210	2668	000	0	8	34	Basaltic flow		
25	KE-4	6.046	37.210	2668	000	0	5	42	Basaltic flow		
26	KE-5	6.055	37.241	2799	000	0	5	38	Basaltic flow		
27	KE-6	6.052	37.270	2705	000	0	8	30	Basaltic flow		
28	KE-7	6.052	37.270	2705	000	0	7	33	Basaltic flow		
29	KE-8	6.052	37.270	2705	000	0	7	36	Basaltic flow		
30	GD-1	5.643	37.383	1994	210	25	8	13	Sediment	15-17	WoldeGabriel et al., 1991
31	GD-2[a]	5.625	37.397	1695	000	0	8	4	Basaltic flow	39.37 ± 0.16	This study
32	GD-3	5.625	37.397	1695	000	0	8	16	Basaltic flow		
33	KO-1	5.327	37.458	1288	000	0	8	24	Basaltic flow	16.85 ± 0.2	This study
34	KO-2	5.327	37.458	1288	000	0	8	13	Basaltic flow		
35	KO-3[a]	5.315	37.463	1159	000	0	7	8	Basaltic flow		
36	KO-4	5.315	37.463	1159	000	0	5	26	Basaltic flow	34.01 ± 0.14	This study
37	KO-5	5.474	37.329	1785	000	0	7	27	Basaltic flow	12.7 ± 0.5	Ebinger et al., 2000
38	KO-6	5.474	37.329	1785	000	0	7	14	Basaltic flow		
39	MEK-1	6.051	37.270	2694	000	0	7	31	Basaltic flow	38.28 ± 0.07	This study
40	MEK-2	6.065	37.240	2712	000	0	7	12	Basaltic flow	42.61 ± 0.27	This study

Column headings: Ref.no: site reference number; ID, site name; Lat (°), Lon (°) and Elev (m) are locations in latitude, longitude and elevation, respectively. N, number of samples, MDF, site mean destructive field. [a]Sites excluded from further analysis (MDF<10mT). *Indicate forced plateau ages.

Table B.2: Paleomagnetic directions for the Eo-Oligocene volcanics

Table 2: Paleomagnetic directions and poles for the Eo-Oligocene volcanics sites

Ref.no	ID	N	In Situ		Tilt corrected				Pole			Lithology
			Dg	Ig	Ds	Is	α_{95}	k	ϕ_s	λ_s	α_{95}	
1	CH-1	5 (10)	350.8	-0.9	350.4	-9.7	11.3	27.0	258.7	75.4	11.4	Welded tuff
2	CH-2[b]	6 (9)	339.6	-62.9	342.5	-58.2	13.6	25.3	236.0	42.1	20.1	Welded tuff
4	CH-4	7 (8)	7.6	-16.2	7.6	-16.2	5.2	134.7	189.9	73.6	5.4	Basaltic flow
5	SH-1	6 (9)	169.2	19.4	169.2	19.4	4.9	184.0	251.1	70.5	5.1	Welded tuff
6	SH-2	4 (7)	154.2	23.9	152.1	19.4	3.9	291.0	264.8	63.7	5.5	Welded tuff
10	GE-4	4 (10)	347.0	-9.2	347.0	-9.2	8.3	123.5	268.6	73.3	8.4	Basaltic flow
11	GE-5[b]	8(8)	291.4	-39.3	291.4	-39.3	3.3	276.1	281.8	17.3	3.9	Basaltic flow
13	GE-7	8 (9)	10.8	-29.6	10.8	-29.6	4.0	232.1	191.3	65.7	4.4	Basaltic flow
14	GE-8	7 (7)	346.8	-21.1	346.8	-21.1	4.6	175.7	255.1	68.6	4.8	Basaltic flow
21	GER-3	4 (10)	351.6	-20.7	351.6	-20.7	6.4	204.3	357.8	80.0	13.1	Basaltic flow
22	KE-1	8(9)	349.4	-13.1	349.4	-13.1	7.1	73.6	257.2	73.5	7.2	Basaltic flow
23	KE-2	4(8)	347.3	-21.9	347.3	-21.9	10.9	52.9	253.2	68.5	11.5	Basaltic flow
24	KE-3	7(8)	8.3	-15.3	8.3	-15.3	11.1	30.6	186.2	73.9	11.4	Basaltic flow
25	KE-4[c]	4(5)	157.7	39.6	157.7	39.6	23.2	16.6				Basaltic flow
26	KE-5	5 (9)	7.9	-23.9	7.9	-23.9	10.3	57.0	194.3	69.9	11	Basaltic flow
27	KE-6	4 (8)	348.9	-20.7	348.9	-20.7	4.7	386.8	250.7	69.9	4.9	Basaltic flow
28	KE-7	5(7)	349.0	-18.2	349.0	-18.2	11.1	70.0	252.8	71.1	11.5	Basaltic flow
29	KE-8	7(7)	348.1	-17.0	348.1	-17.0	5.1	140.0	256.2	71.1	5.3	Basaltic flow
32	GD-3[b]	5 (8)	304.7	8.8	304.7	8.8	3.7	455.0	334.0	79.9	7.0	Basaltic flow
36	KO-4	5 (7)	348.6	16.3	348.6	16.3	10.3	80.6	323.0	78.3	10.6	Basaltic flow
39	MEK-1	7(10)	349.4	-18.9	349.4	-18.9	5.8	109.8	251.2	71.0	6	Basaltic flow
40	MEK-2	4(7)	347.5	-20.2	347.5	-20.2	9.0	119.1	254.3	69.3	9.4	Basaltic flow
	Mean_N	16	353.5	-16.5	353.6	-16.5	6.0	38.2				
	Mean_R	3	162.8	27.3	162.8	27.3	18.5	45.7				
	Overall mean	18	352.6	-17	352.6	-17.0	5.5	40.3	243.5	73.5	4.4	

Column headings: Ref.no: site reference number; ID, site name; N, number of samples (number of samples used to estimate site mean direction); Dg, Ig, Ds and Is, declination and inclination are in situ and directions corrected for tectonics; α_{95}, 95% confidence interval; K, precision parameter; ϕs and λs, VGP longitude and latitude, respectively; [b]Transitional directions; overall mean direction was calculated after [c]excluding site mean directions (α_{95}>15°).

Table B.3: Paleomagnetic directions for the Miocene basalts and sediments

Table 3: Paleomagnetic directions and poles for the Miocene volcanics and sediments

Ref.no	Site	N	In Situ		Tilt corrected				Pole			Lithology
			Dg	Ig	Ds	Is	α_{95}	k	ϕ_s	λ_s	α_{95}	
7	GE-1	7(8)	352.3	24.1	352.3	24.1	10.3	35.3	349.4	79.9	11.0	Basaltic flow
8	GE-2	4(5)	17.2	1.4	15.8	7.2	8.9	108.0	135.0	74.1	9.0	Basaltic flow
9	GE-3	4(5)	23.8	14.5	27.1	5.8	10.4	78.3	132.6	62.8	10.4	Sediment
12	GE-6	5(7)	175.5	32.2	353.9	2.3	11.0	50.0	268.9	82.2	11.0	Sediment
15	GE-9[d]	7(8)	357.0	-23.6	357.0	-23.6	16.4	12.4				Sediment
16	GE-10[e]	5(8)	350.3	-29.3	350.3	-29.3	10.5	65.0				
17	GE-11[e]	6(7)	350.2	-23.3	350.2	-23.3	8.4	54.0				Basaltic flow
18	GE-12[e]	5(8)	352.7	-33.0	352.7	-33.0	14.3	65.0				Basaltic flow
30	GD-1	8(8)	345.9	0.6	347.0	-5.1	6.8	67.6	275.4	74.6	6.8	Basaltic flow
33	KO-1	8(8)	0.1	5.7	0.1	5.7	4.5	153.4	215.1	87.5	4.5	Basaltic flow
34	KO-2[d]	4(7)	357.9	3.8	357.9	3.8	21.1	20.0				
37	KO-5	4(7)	13.8	-1.8	13.8	-1.8	14.0	43.8	151.7	74.8	14.0	Sediment
38	KO-6	2(7)	357.2	-2.5	357.2	-2.5	11.0	521.5	240.0	82.7	11.0	Basaltic flow
	GE-6-N[c]	2(2)	354.5	-21.5	354.0	13.0	17.2	213.0				Basaltic flow
	GE-6-R[c]	3(5)	176.4	39.4	173.8	4.9	113.0	173.8				Basaltic flow
	GE10-12		358.2	-28.7	358.2	-28.7	4.2	73.0	222.1	68.7	4.6	Basaltic flow
	Mean	12	0.1	-5.3	0.4	-6.1	11.7	14.7				
	Mean[f]	8			4.1	0.7	14.1	16.5				
	Overall Mean	9			2.9	0.9	12.4	18.3	189.7	83.9	9.7	

Column headings: Ref.no: site reference number; Mean, mean for normal polarity directions; [c]Combined antipodal polarity directions for sediment samples collected from GE-6; [f]A recalculated mean direction after excluding [d]sites with α_{95}>15°, and [e]a combined mean for sites recording closely similar directions was included. Further details on table column headings can be found in the caption of table 2

Table B.4: $^{40}Ar/^{39}Ar$ age data table-1

Table 4: $^{40}Ar/^{39}Ar$ age data

Laser output#	$^{40}Ar/^{39}Ar$		$^{37}Ar/^{39}Ar$		$^{36}Ar/^{39}Ar$ ($x10^{-3}$)		K/Ca	$^{40}Ar^*$ (%)	$^{39}Ar_K$ fraction (%)	$^{40}Ar^*/^{39}Ar_K$		Age(±1s) (Ma)	
Sample ID: CH-3 gm	*Laboratory ID: 1251*				*Irradiation ID: PO-9*								
J=	*(1.8713 ± 0.0024) x 10^{-3}*												
1.5%	671.86	± 16.59	2.26	± 0.94	2134.35	± 56.93	0.23	5.18	0.16	34.87	± 6.94	114.29	± 22.04
1.8%	282.95	± 5.19	1.72	± 0.48	927.67	± 17.46	0.31	2.17	0.34	6.14	± 1.90	20.65	± 6.36
2.1%	272.43	± 2.60	2.34	± 0.25	854.46	± 10.27	0.22	6.43	0.77	17.53	± 2.15	58.37	± 7.04
2.4%	39.92	± 0.01	1.49	± 0.02	83.88	± 0.06	0.35	37.57	5.59	15.02	± 0.02	50.11	± 0.09
2.7%	36.77	± 0.20	1.37	± 0.10	81.17	± 0.74	0.38	34.39	8.87	12.66	± 0.24	42.33	± 0.80
3.0%	21.62	± 0.11	1.21	± 0.04	31.82	± 0.31	0.44	56.51	14.79	12.23	± 0.12	40.90	± 0.40
3.2%	12.99	± 0.03	0.94	± 0.03	6.57	± 0.08	0.56	85.49	14.07	11.11	± 0.04	37.22	± 0.13
3.4%	12.58	± 0.05	1.27	± 0.01	5.29	± 0.07	0.41	88.27	10.54	11.11	± 0.05	37.21	± 0.17
3.6%	12.49	± 0.05	1.45	± 0.05	5.12	± 0.09	0.36	88.69	8.48	11.09	± 0.06	37.13	± 0.19
3.8%	11.35	± 0.04	2.12	± 0.04	2.72	± 0.04	0.25	94.36	8.50	10.73	± 0.04	35.93	± 0.15
4.0%	11.44	± 0.05	3.20	± 0.06	2.06	± 0.08	0.16	96.88	7.49	11.11	± 0.05	37.20	± 0.19
4.2%	11.19	± 0.04	2.39	± 0.04	1.63	± 0.06	0.22	97.37	8.73	10.92	± 0.05	36.56	± 0.16
4.4%	11.29	± 0.03	5.73	± 0.05	3.49	± 0.07	0.09	94.85	11.66	10.75	± 0.04	36.02	± 0.14

Plateau age (forced) (Ma):	37.20	± 0.12	Plateau steps:	7th to 9th	^{39}Ar %:	33.1	%	
Normal isochron age (Ma) from plateau:	36.95	± 0.67	Initial $^{40}Ar/^{36}Ar$ =	307.7	± 35.8	MSWD:	0.30	
Inverse isochron age (Ma) from plateau:	36.93	± 0.67	Initial $^{40}Ar/^{36}Ar$ =	308.9	± 35.8	MSWD:	0.29	
Total gas age (Ma):	38.77	± 0.12						

Laser output#	$^{40}Ar/^{39}Ar$		$^{37}Ar/^{39}Ar$		$^{36}Ar/^{39}Ar$ ($x10^{-3}$)		K/Ca	$^{40}Ar^*$ (%)	$^{39}Ar_K$ fraction (%)	$^{40}Ar^*/^{39}Ar_K$		Age(±1s) (Ma)	
Sample ID: MEK-2 gm	*Laboratory ID: 1252*				*Irradiation ID: PO-9*								
J=(1.9054 ± 0.0025) x 10-3													
1.5%	4712.84	± 57.85	2.63	± 0.81	15018.17	± 184.28	0.20	4.86	0.79	229.63	± 8.79	656.23	± 21.09
1.7%	578.11	± 4.91	4.39	± 0.24	1764.19	± 16.41	0.12	8.95	2.41	51.90	± 2.26	170.52	± 7.08
1.9%	100.13	± 0.70	5.21	± 0.22	282.02	± 2.21	0.10	16.33	3.89	16.41	± 0.36	55.68	± 1.21
2.2%	38.71	± 0.25	5.71	± 0.12	83.47	± 0.79	0.09	36.82	5.18	14.31	± 0.23	48.64	± 0.79
2.5%	34.71	± 0.14	2.66	± 0.08	70.92	± 0.71	0.20	39.62	11.35	13.77	± 0.22	46.85	± 0.74
2.8%	57.23	± 0.25	1.66	± 0.06	149.13	± 0.96	0.32	22.44	18.36	12.85	± 0.27	43.75	± 0.90
3.0%	28.31	± 0.20	1.66	± 0.07	52.65	± 0.53	0.32	44.95	15.98	12.74	± 0.15	43.37	± 0.50
3.2%	27.99	± 0.08	1.58	± 0.07	51.62	± 0.63	0.33	45.39	12.05	12.72	± 0.19	43.29	± 0.65
3.5%	27.08	± 0.08	1.79	± 0.05	50.28	± 0.36	0.29	45.09	10.58	12.22	± 0.12	41.63	± 0.40
3.8%	24.53	± 0.20	4.48	± 0.14	43.05	± 0.45	0.12	49.09	6.66	12.08	± 0.19	41.14	± 0.66
4.2%	18.16	± 0.17	8.61	± 0.18	23.56	± 0.72	0.06	65.09	4.58	11.89	± 0.25	40.51	± 0.83
4.4%	23.53	± 0.27	12.54	± 0.33	42.58	± 1.15	0.04	50.28	3.23	11.93	± 0.38	40.65	± 1.26
4.9%	38.76	± 0.30	13.19	± 0.32	84.00	± 0.89	0.04	38.04	4.93	14.88	± 0.25	50.54	± 0.85

Plateau age (Ma):	42.61	± 0.27	Plateau steps:	6th to 9th	^{39}Ar %:	57.0	%	
Normal isochron age (Ma) from plateau:	41.63	± 0.64	Initial $^{40}Ar/^{36}Ar$ =	302.9	± 2.9	MSWD:	2.11	
Inverse isochron age (Ma) from plateau:	41.68	± 0.64	Initial $^{40}Ar/^{36}Ar$ =	302.8	± 2.9	MSWD:	2.11	
Total gas age (Ma):	53.20	± 0.38						

Laser output#	$^{40}Ar/^{39}Ar$		$^{37}Ar/^{39}Ar$		$^{36}Ar/^{39}Ar$ ($x10^{-3}$)		K/Ca	$^{40}Ar^*$ (%)	$^{39}Ar_K$ fraction (%)	$^{40}Ar^*/^{39}Ar_K$		Age(±1s) (Ma)	
Sample ID: KE-1 gm	*Laboratory ID: 1253*				*Irradiation ID: PO-9*								
J=	*(1.8991 ± 0.0024) x 10^{-3}*												
1.5%	92.91	± 0.76	1.34	± 0.26	264.88	± 2.52	0.39	15.00	0.97	13.95	± 0.46	47.26	± 1.53
1.8%	28.41	± 0.12	1.80	± 0.08	56.60	± 0.4	0.29	41.02	3.92	11.67	± 0.12	39.6	± 0.4
2.0%	39.56	± 0.12	2.18	± 0.06	88.08	± 0.4	0.24	33.98	5.39	13.46	± 0.12	45.6	± 0.4
2.4%	34.79	± 0.09	2.06	± 0.05	68.51	± 0.3	0.26	41.68	9.60	14.52	± 0.09	49.2	± 0.3
2.6%	30.63	± 0.07	1.72	± 0.04	56.47	± 0.2	0.30	45.42	12.29	13.93	± 0.07	47.2	± 0.2
2.8%	25.70	± 0.07	1.65	± 0.02	42.88	± 0.3	0.32	50.71	13.88	13.05	± 0.10	44.3	± 0.3
3.0%	22.87	± 0.08	1.60	± 0.01	33.79	± 0.12	0.33	56.44	12.47	12.92	± 0.06	43.8	± 0.2
3.2%	21.90	± 0.07	1.70	± 0.04	31.82	± 0.2	0.31	57.25	10.22	12.55	± 0.08	42.6	± 0.3
3.4%	22.39	± 0.08	1.64	± 0.14	32.82	± 0.3	0.32	56.83	7.79	12.74	± 0.10	43.2	± 0.3
3.7%	22.13	± 0.08	2.26	± 0.05	29.14	± 0.2	0.23	61.51	8.51	13.63	± 0.08	46.2	± 0.3
4.1%	24.04	± 0.10	3.22	± 0.06	39.88	± 0.3	0.16	51.56	7.58	12.42	± 0.10	42.2	± 0.3
4.4%	23.77	± 0.08	5.30	± 0.08	40.08	± 0.3	0.10	51.46	7.38	12.28	± 0.11	41.7	± 0.4

Plateau age (Ma):	no plateau		Plateau steps:		^{39}Ar %:		%	
Normal isochron age (Ma) from all steps:	41.89	± 0.22	Initial $^{40}Ar/^{36}Ar$ =	314.7	± 1.3	MSWD:	7.83	

Table B.5: $^{40}Ar/^{39}Ar$ age data table-2

	Inverse isochron age (Ma) from all steps:			41.96	±	0.22		Initial $^{40}Ar/^{36}Ar$ =			315.7	±	1.3	MSWD:		7.74			
	Total gas age (Ma):			44.43	±	0.09													
Laser output#	$^{40}Ar/^{39}Ar$			$^{37}Ar/^{39}Ar$			$^{36}Ar/^{39}Ar$			K/Ca	$^{40}Ar^*$	$^{39}Ar_K$	$^{40}Ar^*/^{39}Ar_K$			Age(±1s)			
							(x10 $^{-3}$)				(%)	fraction (%)				(Ma)			
Sample ID: GER-2 gm	*Laboratory ID: 1254*						*Irradiation ID: PO-9*												
J=	*(1.8871 ± 0.0024) x 10 $^{-3}$*																		
1.5%	390.62	±	2.41	1.05	±	0.12	1205.73	±	8.47	0.50	7.87	2.93	30.75	±	1.36	101.98	±	4.40	
1.8%	156.67	±	0.57	2.13	±	0.07	443.50	±	2.33	0.25	15.60	5.75	24.47	±	0.57	81.62	±	1.85	
2.1%	39.86	±	0.19	5.89	±	0.13	83.52	±	0.79	0.09	38.62	5.09	15.45	±	0.24	51.98	±	0.79	
2.4%	24.61	±	0.14	8.75	±	0.10	49.49	±	0.46	0.06	42.82	5.69	10.60	±	0.17	35.81	±	0.56	
2.7%	20.40	±	0.09	5.76	±	0.10	37.04	±	0.25	0.09	48.07	9.60	9.84	±	0.08	33.28	±	0.28	
2.9%	29.64	±	0.11	7.72	±	0.12	69.05	±	0.35	0.07	32.55	7.30	9.70	±	0.09	32.79	±	0.32	
3.1%	21.97	±	0.09	6.29	±	0.11	42.32	±	0.26	0.08	44.81	8.64	9.89	±	0.09	33.43	±	0.30	
3.3%	18.34	±	0.08	8.84	±	0.25	32.00	±	0.25	0.06	51.80	6.89	9.56	±	0.09	32.32	±	0.31	
3.5%	17.22	±	0.10	9.07	±	0.14	27.43	±	0.55	0.06	56.69	6.57	9.82	±	0.18	33.21	±	0.59	
3.7%	15.35	±	0.05	6.28	±	0.12	20.09	±	0.16	0.08	64.21	9.87	9.90	±	0.06	33.46	±	0.22	
3.9%	18.42	±	0.06	6.28	±	0.07	30.16	±	0.22	0.08	53.87	8.68	9.96	±	0.08	33.68	±	0.26	
4.1%	18.42	±	0.06	6.28	±	0.07	30.16	±	0.22	0.08	53.87	8.68	9.96	±	0.08	33.68	±	0.26	
4.4%	21.58	±	0.12	6.12	±	0.12	39.93	±	0.57	0.09	47.03	6.88	10.19	±	0.17	34.44	±	0.58	
4.7%	11.53	±	0.08	4.18	±	0.08	7.42	±	0.12	0.13	83.71	7.43	9.68	±	0.08	32.72	±	0.26	
	Plateau age (forced) (Ma):			33.62	±	0.13		Plateau steps:			9th to 13th		^{39}Ar %:	40.7	%				
	Normal isochron age (Ma) from plateau:			32.69	±	0.61		Initial $^{40}Ar/^{36}Ar$ =			308.7	±	7.1	MSWD:		0.58			
	Inverse isochron age (Ma) from plateau:			32.68	±	0.61		Initial $^{40}Ar/^{36}Ar$ =			308.7	±	7.1	MSWD:		0.58			
	Total gas age (Ma):			39.18	±	0.20													
Laser output#	$^{40}Ar/^{39}Ar$			$^{37}Ar/^{39}Ar$			$^{36}Ar/^{39}Ar$			K/Ca	$^{40}Ar^*$	$^{39}Ar_K$	$^{40}Ar^*/^{39}Ar_K$			Age(±1s)			
							(x10 $^{-3}$)				(%)	fraction (%)				(Ma)			
Sample ID: GE-12 gm	*Laboratory ID: 1256*						*Irradiation ID: PO-9*												
J=	*(1.8822 ± 0.0024) x 10 $^{-3}$*																		
1.5%	1369.44	±	7.22	0.000	±	0.139	4582.10	±	25.10	7363.06	0.10	0.52	1.41	±	2.24	4.79	±	7.62	
1.7%	558.22	±	162.68	0.015	±	0.043	1808.82	±	527.15	36.09	3.26	1.14	18.18	±	5.51	60.85	±	18.13	
1.9%	80.66	±	0.32	0.005	±	0.009	242.50	±	1.05	111.64	10.24	7.12	8.26	±	0.17	27.88	±	0.56	
2.1%	28.88	±	0.07	0.002	±	0.005	73.00	±	0.41	212.04	24.53	13.47	7.08	±	0.11	23.94	±	0.38	
2.3%	18.26	±	0.05	0.001	±	0.005	38.17	±	0.68	525.67	37.58	11.39	6.86	±	0.20	23.20	±	0.68	
2.5%	14.83	±	0.05	0.000	±	0.004	28.89	±	0.19	119807.28	41.84	8.46	6.20	±	0.06	20.99	±	0.19	
2.7%	13.08	±	0.04	0.005	±	0.007	23.07	±	0.11	103.36	47.34	6.42	6.19	±	0.03	20.95	±	0.12	
2.9%	11.19	±	0.05	0.000	±	0.007	16.70	±	0.12	82556.30	55.44	5.84	6.20	±	0.04	20.99	±	0.14	
3.1%	9.58	±	0.03	0.006	±	0.008	12.09	±	0.13	90.84	62.34	6.24	5.97	±	0.04	20.22	±	0.15	
3.3%	8.64	±	0.03	0.000	±	0.006	9.17	±	0.13	1865.05	68.32	6.79	5.91	±	0.04	19.99	±	0.14	
3.5%	8.17	±	0.03	0.005	±	0.006	8.04	±	0.09	98.49	70.66	7.38	5.78	±	0.03	19.55	±	0.12	
3.7%	7.91	±	0.03	0.008	±	0.006	6.82	±	0.05	65.00	74.25	9.07	5.87	±	0.03	19.87	±	0.10	
3.9%	8.20	±	0.03	0.015	±	0.006	7.73	±	0.23	36.24	71.87	8.45	5.89	±	0.07	19.94	±	0.25	
4.1%	9.60	±	0.05	0.013	±	0.009	12.38	±	0.11	40.00	61.51	4.30	5.91	±	0.04	19.99	±	0.14	
4.3%	12.97	±	0.04	0.000	±	0.016	23.83	±	0.32	32240.59	45.14	2.31	5.85	±	0.10	19.82	±	0.33	
4.5%	19.83	±	0.08	0.080	±	0.041	42.94	±	1.01	6.54	35.38	1.10	7.01	±	0.30	23.72	±	1.02	
	Plateau age (forced) (Ma):			19.84	±	0.06		Plateau steps:			10th to 14th		^{39}Ar %:	36.0	%				
	Normal isochron age (Ma) from plateau:			19.47	±	0.26		Initial $^{40}Ar/^{36}Ar$ =			309.5	±	8.9	MSWD:		1.53			
	Inverse isochron age (Ma) from plateau:			19.48	±	0.26		Initial $^{40}Ar/^{36}Ar$ =			309.3	±	8.9	MSWD:		1.52			
	Total gas age (Ma):			22.00	±	0.15													
Laser output#	$^{40}Ar/^{39}Ar$			$^{37}Ar/^{39}Ar$			$^{36}Ar/^{39}Ar$			K/Ca	$^{40}Ar^*$	$^{39}Ar_K$	$^{40}Ar^*/^{39}Ar_K$			Age(±1s)			
							(x10 $^{-3}$)				(%)	fraction (%)				(Ma)			
Sample ID: MEK-1 kf	*Laboratory ID: 1257*						*Irradiation ID: PO-9*												
J=	*(1.9025 ± 0.0025) x 10 $^{-3}$*																		
1.6%	43.98	±	1.20	0.001	±	0.773	105.76	±	3.69	754.9	28.20	0.25	12.40	±	0.78	42.17	±	2.62	
2.0%	12.25	±	0.09	0.00	±	0.11	0.98	±	0.23	5196.0	97.60	1.71	11.96	±	0.11	40.68	±	0.38	
2.2%	11.61	±	0.09	0.00	±	0.11	1.07	±	0.23	5351.9	97.26	1.76	11.29	±	0.12	38.43	±	0.39	
2.4%	11.47	±	0.08	0.00	±	0.09	0.81	±	0.16	7026.4	97.89	2.32	11.22	±	0.09	38.21	±	0.31	
2.6%	11.38	±	0.07	0.00	±	0.06	0.79	±	0.10	10192.0	97.92	3.37	11.14	±	0.08	37.94	±	0.26	
2.8%	11.36	±	0.06	0.02	±	0.04	0.83	±	0.07	30.8	97.83	6.25	11.11	±	0.06	37.82	±	0.20	
2.9%	11.39	±	0.04	0.00	±	0.02	0.19	±	0.04	231.9	99.52	9.34	11.33	±	0.04	38.56	±	0.14	

Table B.6: $^{40}Ar/^{39}Ar$ age data table-3

3.0%	11.27	±	0.03	0.07	±	0.02	0.33	±	0.03	7.2	99.18	12.07	11.18	±	0.03	38.04	±	0.12
3.1%	11.21	±	0.03	0.00	±	0.02	0.03	±	0.04	301.3	99.92	10.21	11.20	±	0.03	38.12	±	0.12
3.2%	11.40	±	0.05	0.02	±	0.05	0.11	±	0.11	33.1	99.72	3.73	11.37	±	0.06	38.70	±	0.22
3.4%	11.30	±	0.08	0.04	±	0.06	0.41	±	0.14	13.9	98.96	3.06	11.19	±	0.09	38.08	±	0.30
3.7%	11.27	±	0.07	0.00	±	0.05	0.20	±	0.11	10918.0	99.46	3.62	11.21	±	0.08	38.15	±	0.26
4.0%	11.20	±	0.05	0.00	±	0.04	0.00	±	0.09	12495.2	100.00	4.15	11.20	±	0.06	38.11	±	0.19
4.3%	11.30	±	0.04	0.000	±	0.013	0.12	±	0.02	44741.3	99.67	14.86	11.26	±	0.04	38.32	±	0.16
4.6%	11.34	±	0.05	0.014	±	0.008	0.10	±	0.02	36.6	99.75	23.31	11.31	±	0.05	38.50	±	0.16

Plateau age (Ma):	38.28	±	0.07	Plateau steps:	9th to 15th	^{39}Ar %:	62.9	%		
Normal isochron age (Ma) from plateau:	38.20	±	0.15	Initial $^{40}Ar/^{36}Ar$ =	246.7	±	250.4	MSWD:		0.88
Inverse isochron age (Ma) from plateau:	38.01	±	0.15	Initial $^{40}Ar/^{36}Ar$ =	970.9	±	404.0	MSWD:		1.12
Total gas age (Ma):	38.24	±	0.06							

Laser output#	$^{40}Ar/^{39}Ar$			$^{37}Ar/^{39}Ar$			$^{36}Ar/^{39}Ar$ (x10 $^{-3}$)			K/Ca	$^{40}Ar^*$ (%)	$^{39}Ar_K$ fraction (%)	$^{40}Ar^*/^{39}Ar_K$			Age(±1s) (Ma)		
Sample ID: GE7 gm	Laboratory ID: 1290			Irradiation ID: PO-10														
J=	*(1.8752 ± 0.0073) x 10 $^{-3}$*																	
1.4%	242.93	±	4.05	1.78	±	0.70	787.60	±	13.94	0.30	3.26	0.63	7.93	±	1.79	26.70	±	6.00
1.7%	45.24	±	0.47	2.62	±	0.22	108.42	±	1.30	0.20	28.92	2.92	13.11	±	0.33	43.91	±	1.09
2.2%	17.78	±	0.19	2.22	±	0.13	19.14	±	0.37	0.24	68.88	5.32	12.26	±	0.17	41.11	±	0.60
2.4%	14.60	±	0.12	1.81	±	0.09	10.43	±	0.17	0.29	79.68	11.03	11.65	±	0.12	39.06	±	0.41
2.6%	14.42	±	0.08	1.37	±	0.07	9.69	±	0.13	0.38	80.71	14.34	11.65	±	0.09	39.08	±	0.32
2.8%	15.85	±	0.14	1.12	±	0.11	14.50	±	0.18	0.47	73.26	12.53	11.62	±	0.12	38.99	±	0.43
3.0%	16.99	±	0.13	1.41	±	0.10	17.77	±	0.25	0.37	69.44	9.27	11.81	±	0.13	39.60	±	0.45
3.2%	16.89	±	0.15	1.45	±	0.14	18.68	±	0.24	0.36	67.69	8.69	11.44	±	0.14	38.40	±	0.48
3.5%	18.86	±	0.20	2.22	±	0.12	25.70	±	0.34	0.24	60.29	8.49	11.39	±	0.17	38.21	±	0.59
3.8%	18.38	±	0.10	6.51	±	0.10	27.60	±	0.25	0.08	58.06	12.48	10.72	±	0.10	35.99	±	0.36
4.1%	18.29	±	0.12	11.86	±	0.20	27.07	±	0.26	0.04	61.11	14.28	11.27	±	0.12	37.82	±	0.43

Plateau age (Ma):	38.97	±	0.17	Plateau steps:	4th to 9th	^{39}Ar %:	64.4	%		
Normal isochron age (Ma) from plateau:	39.41	±	0.50	Initial $^{40}Ar/^{36}Ar$ =	287.1	±	9.9	MSWD:		1.04
Inverse isochron age (Ma) from plateau:	39.40	±	0.50	Initial $^{40}Ar/^{36}Ar$ =	287.5	±	9.9	MSWD:		1.06
Total gas age (Ma):	38.50	±	0.14							

Laser output#	$^{40}Ar/^{39}Ar$			$^{37}Ar/^{39}Ar$			$^{36}Ar/^{39}Ar$ ($x10^{-3}$)			K/Ca	$^{40}Ar^*$ (%)	$^{39}Ar_K$ fraction (%)	$^{40}Ar^*/^{39}Ar_K$			Age(±1s) (Ma)		
Sample ID: GE1 gm	*Laboratory ID: 1291*			*Irradiation ID: PO-10*														
J= (1.8715 ± 0.0073) x 10 $^{-3}$																		
1.4%	1006.48	±	12.96	10.41	±	2.61	3360.56	±	54.48	0.05	0.40	0.16	4.03	±	11.68	13.59	±	39.22
1.7%	190.96	±	3.44	5.87	±	0.91	593.54	±	12.83	0.09	7.45	0.53	14.29	±	2.85	47.72	±	9.38
2.0%	70.99	±	1.24	3.75	±	0.53	221.50	±	5.59	0.14	7.27	0.97	5.18	±	1.34	17.43	±	4.48
2.2%	31.29	±	0.48	4.27	±	0.25	83.23	±	2.02	0.12	21.70	1.96	6.81	±	0.58	22.90	±	1.96
2.4%	20.56	±	0.19	2.81	±	0.15	50.81	±	1.03	0.19	27.33	3.85	5.63	±	0.30	18.95	±	1.02
2.6%	16.26	±	0.11	2.34	±	0.11	33.73	±	0.26	0.22	39.24	8.88	6.39	±	0.11	21.50	±	0.38
2.8%	11.06	±	0.09	1.67	±	0.06	16.66	±	0.15	0.31	56.27	22.63	6.23	±	0.07	20.97	±	0.24
3.0%	7.07	±	0.05	1.28	±	0.04	4.64	±	0.05	0.41	81.87	32.06	5.79	±	0.05	19.49	±	0.18
3.2%	7.45	±	0.05	1.22	±	0.06	5.63	±	0.20	0.43	78.77	13.29	5.87	±	0.07	19.77	±	0.26
3.5%	10.25	±	0.08	3.35	±	0.14	16.32	±	0.49	0.16	55.13	6.31	5.67	±	0.16	19.07	±	0.55
3.8%	11.73	±	0.14	9.17	±	0.25	22.54	±	0.66	0.06	49.00	3.87	5.79	±	0.23	19.47	±	0.78
4.3%	11.11	±	0.09	10.70	±	0.28	20.71	±	0.58	0.05	52.21	5.48	5.85	±	0.19	19.68	±	0.64

Plateau age (Ma):	19.55	±	0.14	Plateau steps:	8th to 12th	^{39}Ar %:	61.0	%		
Normal isochron age (Ma) from plateau:	19.56	±	0.24	Initial $^{40}Ar/^{36}Ar$ =	295.4	±	8.9	MSWD:		0.74
Inverse isochron age (Ma) from plateau:	19.56	±	0.24	Initial $^{40}Ar/^{36}Ar$ =	295.6	±	8.9	MSWD:		0.74
Total gas age (Ma):	20.14	±	0.15							

Laser output#	$^{40}Ar/^{39}Ar$			$^{37}Ar/^{39}Ar$			$^{36}Ar/^{39}Ar$ (x10 $^{-3}$)			K/Ca	$^{40}Ar^*$ (%)	$^{39}Ar_K$ fraction (%)	$^{40}Ar^*/^{39}Ar_K$			Age(±1s) (Ma)		
Sample ID: GD-2 gm	Laboratory ID: 1292			Irradiation ID: PO-10														
J=	*(1.8652 ± 0.0073) x 10 $^{-3}$*																	
1.4%	1679.65	±	42.11	6.98	±	6.24	5593.75	±	149.11	0.08	0.60	0.09	10.20	±	19.75	34.07	±	65.36
1.7%	351.56	±	9.40	5.80	±	1.40	1145.13	±	32.76	0.09	2.88	0.37	10.18	±	5.11	34.01	±	16.91

Table B.7: $^{40}Ar/^{39}Ar$ age data table-4

2.0%	117.72	±	2.31	4.22	±	0.89	379.77	±	9.49	0.12	3.98	0.65	4.70	±	2.46	15.77	±	8.23
2.2%	56.28	±	0.90	3.57	±	0.43	145.86	±	3.58	0.15	23.14	1.28	13.05	±	1.00	43.49	±	3.30
2.4%	19.25	±	0.21	1.74	±	0.13	23.21	±	0.84	0.30	64.74	3.18	12.48	±	0.29	41.59	±	0.98
2.6%	15.48	±	0.12	1.23	±	0.10	11.23	±	0.20	0.43	78.99	5.20	12.24	±	0.12	40.80	±	0.43
2.8%	12.61	±	0.09	1.22	±	0.03	3.54	±	0.06	0.43	92.41	23.52	11.66	±	0.09	38.91	±	0.32
3.0%	12.47	±	0.06	1.29	±	0.05	2.61	±	0.10	0.41	94.59	24.25	11.81	±	0.07	39.39	±	0.27
3.2%	12.36	±	0.06	1.30	±	0.06	1.97	±	0.07	0.40	96.09	14.01	11.89	±	0.06	39.66	±	0.26
3.5%	12.13	±	0.08	2.55	±	0.09	2.63	±	0.08	0.21	95.23	11.33	11.57	±	0.08	38.62	±	0.31
3.9%	11.98	±	0.10	3.74	±	0.09	2.74	±	0.06	0.14	95.71	16.12	11.49	±	0.10	38.35	±	0.36

Plateau age (Ma):	39.37	±	0.16	Plateau steps:	7th to 9th	^{39}Ar %:	61.8	%			
Normal isochron age (Ma) from plateau:	39.79	±	0.53	Initial $^{40}Ar/^{36}Ar$ =	227.4	±	67.6	MSWD:	1.10		
Inverse isochron age (Ma) from plateau:	40.34	±	0.53	Initial $^{40}Ar/^{36}Ar$ =	156.1	±	67.3	MSWD:	0.11		
Total gas age (Ma):	38.99	±	0.16								

Laser output#	$^{40}Ar/^{39}Ar$			$^{37}Ar/^{39}Ar$			$^{36}Ar/^{39}Ar$ ($x10^{-3}$)			K/Ca	$^{40}Ar^*$ (%)	$^{39}Ar_K$ fraction (%)	$^{40}Ar^*/^{39}Ar_K$			Age(±1s) (Ma)		
Sample ID: KO1 gm	*Laboratory ID: 1293*			*Irradiation ID: PO-10*														
J= (1.8655 ± 0.0073) x 10^{-3}																		
1.4%	428.90	±	4.18	0.00	±	0.72	1379.34	±	14.10	487.59	3.98	0.55	17.08	±	2.62	56.73	±	8.55
1.7%	100.07	±	1.27	1.19	±	0.33	297.50	±	3.87	0.44	11.34	1.66	11.36	±	0.71	37.92	±	2.34
2.0%	66.16	±	0.51	1.20	±	0.16	199.69	±	1.63	0.44	10.03	4.09	6.64	±	0.34	22.27	±	1.12
2.2%	27.67	±	0.25	1.39	±	0.13	75.88	±	0.71	0.38	18.52	5.62	5.13	±	0.22	17.21	±	0.73
2.4%	18.77	±	0.13	1.01	±	0.08	45.54	±	0.36	0.52	28.01	9.53	5.26	±	0.12	17.66	±	0.41
2.6%	13.26	±	0.07	1.19	±	0.08	27.82	±	0.18	0.44	38.07	15.69	5.05	±	0.08	16.96	±	0.28
2.8%	9.75	±	0.07	1.17	±	0.06	16.36	±	0.14	0.45	50.88	16.64	4.96	±	0.07	16.67	±	0.24
3.0%	8.31	±	0.04	1.13	±	0.07	11.61	±	0.12	0.47	59.37	14.49	4.94	±	0.05	16.57	±	0.18
3.2%	7.26	±	0.05	1.79	±	0.13	7.90	±	0.14	0.29	69.52	9.75	5.06	±	0.06	16.98	±	0.21
3.5%	10.37	±	0.07	2.52	±	0.14	17.97	±	0.23	0.21	50.26	7.70	5.22	±	0.09	17.53	±	0.31
3.9%	6.97	±	0.04	5.19	±	0.16	9.19	±	0.12	0.10	66.70	14.29	4.66	±	0.05	15.67	±	0.19

Plateau age (Ma):	16.91	±	0.10	Plateau steps:	4th to 10th	^{39}Ar %:	79.4	%			
Normal isochron age (Ma) from plateau:	16.61	±	0.18	Initial $^{40}Ar/^{36}Ar$ =	302.9	±	2.4	MSWD:	1.37		
Inverse isochron age (Ma) from plateau:	16.62	±	0.18	Initial $^{40}Ar/^{36}Ar$ =	302.8	±	2.4	MSWD:	1.39		
Total gas age (Ma):	17.55	±	0.12								

Laser output#	$^{40}Ar/^{39}Ar$			$^{37}Ar/^{39}Ar$			$^{36}Ar/^{39}Ar$ ($x10^{-3}$)			K/Ca	$^{40}Ar^*$ (%)	$^{39}Ar_K$ fraction (%)	$^{40}Ar^*/^{39}Ar_K$			Age(±1s) (Ma)		
Sample ID: KO-4 gm	*Laboratory ID: 1294*			*Irradiation ID: PO-10*														
J= (1.8667 ± 0.0073) x 10^{-3}																		
1.4%	63.60	±	0.69	0.66	±	0.20	187.77	±	2.02	0.80	11.94	1.34	7.60	±	0.55	25.48	±	1.82
1.7%	17.86	±	0.09	0.38	±	0.03	24.16	±	0.19	1.39	59.79	10.41	10.68	±	0.08	35.71	±	0.30
2.0%	14.09	±	0.09	0.68	±	0.03	9.09	±	0.09	0.77	81.13	18.12	11.43	±	0.08	38.18	±	0.31
2.2%	13.13	±	0.08	1.10	±	0.05	6.47	±	0.09	0.48	85.97	9.13	11.30	±	0.08	37.75	±	0.30
2.4%	12.47	±	0.08	1.15	±	0.08	5.21	±	0.11	0.46	88.27	6.84	11.02	±	0.08	36.82	±	0.30
2.6%	12.26	±	0.10	1.22	±	0.09	5.09	±	0.13	0.43	88.41	5.19	10.85	±	0.11	36.24	±	0.38
2.9%	11.40	±	0.08	1.63	±	0.11	4.74	±	0.14	0.32	88.74	4.90	10.12	±	0.09	33.85	±	0.32
3.2%	12.01	±	0.10	1.37	±	0.12	6.39	±	0.11	0.38	85.06	7.91	10.23	±	0.10	34.19	±	0.34
3.5%	11.75	±	0.06	2.12	±	0.07	5.65	±	0.08	0.25	87.12	12.23	10.25	±	0.06	34.27	±	0.25
3.8%	11.41	±	0.08	4.10	±	0.12	5.58	±	0.07	0.13	88.32	17.95	10.11	±	0.07	33.80	±	0.28
4.1%	10.78	±	0.09	9.62	±	0.39	5.13	±	0.14	0.05	93.06	4.64	10.10	±	0.11	33.77	±	0.38
4.4%	11.09	±	0.18	13.38	±	0.67	6.29	±	0.42	0.04	92.89	1.34	10.39	±	0.22	34.74	±	0.75

Plateau age (forced) (Ma):	34.01	±	0.14	Plateau steps:	7th to 11th	^{39}Ar %:	47.6	%			
Normal isochron age (Ma) from plateau:	33.47	±	0.63	Initial $^{40}Ar/^{36}Ar$ =	329.7	±	39.5	MSWD:	0.78		
Inverse isochron age (Ma) from plateau:	33.13	±	0.64	Initial $^{40}Ar/^{36}Ar$ =	350.9	±	39.8	MSWD:	0.71		
Total gas age (Ma):	35.40	±	0.09								

#100% corresponds to 50W output of CO_2 laser. All the errors indicate 1 sigma error. $^{40}Ar^*$ means radiogenic ^{40}Ar.

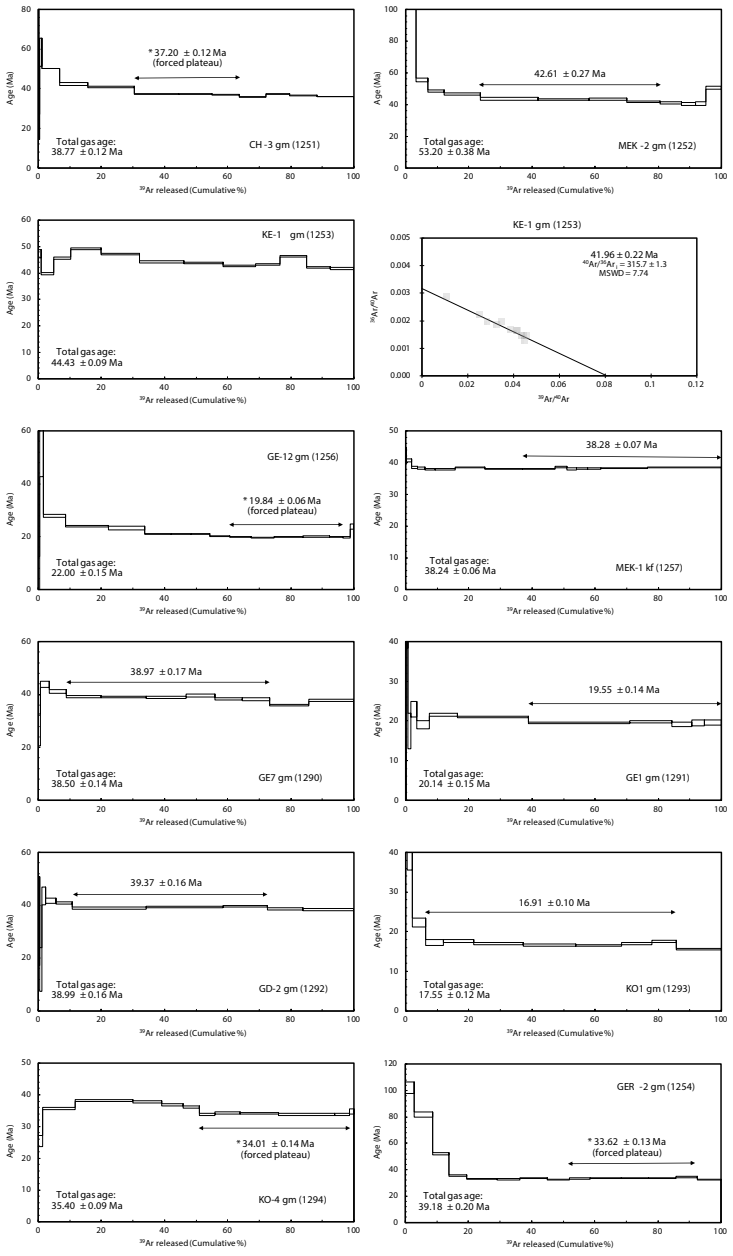

Figure B.1: Age spectrum

Eidesstattliche Erklärung

Hiermit versichere ich, dass meine Dissertation "Cenozoic magma-assisted continental rifting and crustal block rotations in an extensional overlap zone between two rift segments, Southwest Ethiopia, East Africa" selbständig verfasst wurde und dass keine anderen Quellen und Hilfsmittel als die angegebenen benutzt wurden.

Potsdam, den 26. Juni 2023,

_____

(Asfaw Erbello Doelesso)